Modelling of solar magnetic fields using cellular automata models

Thesis

UNRESTRICTED

Faculty of Science, The Open University

Modelling of Solar Magnetic Fields using Cellular Automata Models.

Christopher Peter Brockwell B.Eng M.Sc.

Submitted for the degree of Ph.D.

June 2003

Submission date: 17 February 2003
Award date: 10 June 2003

ProQuest LLC.
789 East Eisenhower Parkway
P.O. Box 1346
Ann Arbor, MI 48106 – 1346

Modelling of Solar Magnetic Fields using Cellular Automata Models.

Christopher Peter Brockwell B.Eng M.Sc.
June 2003

Faculty of Science, The Open University
Submitted for the degree of Ph.D.

Solar activity, including flares, CMEs, sunspots, global field reversal and, consequential to these, particle acceleration and X-ray emission result from the complexity of the atmospheric magnetic fields. These fields are driven into complex topologies by the continual stochastic photospheric motions and granulation flows. Significant energy is stored in the magnetic field however magnetic reconnection provides a mechanism for the relaxation and simplification of the field and release of this energy. Reconnection is capable of providing the observed plasma heating, field reorganisation and particle acceleration, although the relationship between reconnection and flaring is not yet understood. It is clear however that the field topology is key. Given flare-size self-similarity, the short time-scales of hard X-ray emission and the observed apparent self-organisation, flaring models (Lu & Hamilton 1991) have been constructed based upon self-organised criticality ('SOC') with minimal physics and have produced plausible flare-size distributions. The model by MacKinnon, Macpherson & Vlahos (1996) however assumed only local flare-triggering and made no statements regarding flare physics. This model reproduced the broad statistical features of flares yet without any implicit SOC.

We speculate that the observed Solar activity arises from the self-interaction of the magnetic field, flux emergence/submergence and reconnection without the necessity for invoking SOC or power-law distributed convective flows. Our first model was a simple 1-D cellular automata ('CA') containing only formalised field connectivity, reconnection and flux emergence/submergence. The model produced self-similarity in flare-sizes over four orders of magnitude. The following model built upon the first and included more realistic physics with continuous parameter values. The model gave power-law distributions in field density and flare-sizes (up to seven orders of magnitude) without inclusion of SOC or power-law forcing. The results were robust and insensitive to details of the reconnection mechanism. We derive analytical explanations for the observed rapid decay curves of impulsive-phase X-ray emission and consider that the flares produced represent presently unresolvable reconnection events. It was found that, similar to large Solar flares, large events are rarely concurrent.

Now that the carcus of the thesis has been laid to rest I should first state my mea culpa that the remaining errors in this work are entirely my own.

These three and a bit years were tremendous fun and a very positive experience. I learnt a lot, especially from Andrew, and was exposed to many fun and interesting things.

My supervisor and friend Andrew Conway, PhD papa to Ben and I, looked after me way beyond the call of duty and his patient and generous guidance and attention is very much appreciated. When we met at the interview I immediately liked him and we worked well together from the beginning having many stimulating discussions. Despite occasional chair-fumbling I hope I was a good student. Andrew has a great deal of integrity and is all that an academic, and a human being, should be. I can't recall him ever speaking without saying something worthwhile, whether at work, Coffee Club or in bed. Andrew is self-effacing, egoless, and has a rare quality of unknowingly inspiring great loyalty and friendship. Ben and I would unhesitatingly fight for Andrw's good name, if ever required. His ideas and energy helped the project a hugely. I hope to see him on the hills in the future, where I hope, probably in vain, to punish him for being so perfect.

The Mopadave (*aka* Dave Lott) and Lisacat Gorgeous Strontium Bitch (*aka* Lisa Blake) were my roommates and chums. We did a lot of playing and laughing. There was also crossbow shooting, paintballing, robot building and Xmas artwork. Two outstanding characters, both irrepressible. The Mopa is an enigma, a fiery S.O.B., generous and a good listener, despite seasoning his conversation with mentions of the 'furious fist'. Lisacat has her own way of doing things and will annoy you intensely, but nevertheless put herself out for you. Unique individuals who taught me a few things. To keep Stronty happy I'd better quickly thank a few furred friends : Super Indie Discount Night(Indie)-Lulu-Henble-Bindle(Bindy), Staty(LeStat)-Bean(Beany, Boon, the Boon) and Spunky-Pucklebunny-Wufflechops (I thought that one up). I shall miss our time together a great deal (although not Mopa's Charlatans and Neil Diamond CDs).

I would like to thank Professor Barrie Jones for being my second supervisor. Barrie wasn't involved directly in the project but took an interest and provided plenty of welcome and entertaining tales over coffee.

Thanks to Hannah Quaintrell for giving me support, food, shelter and MASSIVE encouragement during most of the writing up period and after, when rigor mortis set in. She put up with my endless whining and carried out the emotional triage while supplying roast dinners and pre-recorded BBC history programs. She kept me sane during the countless exhumations of the thesis corpse during early-to-mid 2003 and provided expert Linux/Latex help. Hugs and kisses.

My Mum has always believed in and encouraged me a great deal, and throughout my life Dad has constantly nurtured the fascination with science which we share. Thanks to you both.

My alter-ego, Sylvain, who went AWOL to Paris in 2002, provided a lot of necessary silliness. The mad Frenchman has a unique sense of humour. Our breakfasts, beginning early and stretching into the late morning, would leave me replete and exhausted. Chocolate would feature in every facet of the breakfast : croissants, cocoa, on toast and au naturel. Sylvain, toujours tu es bon et je suis ton

chou poilu.

My PhD little brother, Ben(*aka* Benjy), made it necessary to build The Sign - a traffic light system for controlling noise and ingress/egress. In time he learned to respect the sign although a great deal of training was required - mainly aversion therapy relying upon my frequent bellowing of 'BEGONE!'. Returning the favour, Ben taught me the essential principles of time-keeping. Forever my PhD brother, Ben is a wonderful warm cuddly bearlike man - immensely strong with with the hands of a masseur and good strong lips. (It's like having your own pet manatee!) A big thanks for all the distractions Bro - both welcome and unwelcome.

Joe Shawcross was my chins and dips buddy. Lunchtimes, we pushed each other, and together enjoyed Dave's gentle swaying/twitching actions on the bars, finding them amusing and profoundly relaxing. Keep at it and maybe one day you can graduate from the 'mummy' to the 'daddy' chin bar? Thanks also for the help with the '12 days'.

Thanks to DJ $\star$ for tolerating a difficult flatmate, and to John for leading us on the robot.

Thanks to Craig (*aka* Bilbo(Bilbus)) for being my IDL guru and teaching me an immense amount of IDL and Linux, always at short notice and with immense patience. Our many stimulating non-work conversations were and continue to be highly enjoyable, not the least of which was our joint devising of an absurdly complex virtual-particle self-interaction for a journal club talk.

When my computer decided not to play ball, Wiggly and Geoff, despite always being extremely busy, never hesitated to take the time to bail me out, even reinstalling the OS on my machine where necessary.

The good people of Coffee Club, many of whom have now left the OU (Mark Sullivan, Andy G and Babs et al.) deserve a thank you for the pleasure of their company, the morning and afternoon distractions, and tolerating my no-shoes policy.

I should apologise to the Open University security guards who, during the small hours in the department, were occasionally shocked by my unusual postures and sudden movements in the kitchen area, made while waiting for the kettle to boil...

The boys of Van Halen often unknowingly filled the silence of the physics department corridors during the small hours, maintaining my sanity and keeping at bay the creatures of the night.

Thanks to the makers of 'King of the Hill' for their wisdom. Propane rules! Let he who has ears listen.

Thanks to my punchbag for taking occasional beatings and relieving frustration.

That brings me on to my martial arts buddy Niall with whom each week, during 2001, 2002 and 2003, I spent a few hours engaging in mutual grasping, shoving and butting. A few hours each week away from it all and learning from each other doing stuff we both love. Cheers mate. What's the next flow drill?

Thanks to the horses all around MK, and their tacit acceptance of my fruit and veg. (Better that than my meat and veg.) Thanks also to all the manatees, wherever they may be, including the late but (formerly) very beautiful Star, who passed away in Hommosassa Springs during 2002 but will

not be forgotten.

No animals were harmed during the writing of this thesis, although several humans did get slightly roughed up.

For Mum and Dad.

CONTENTS

LIST OF FIGURES

LIST OF TABLES

Symbols

Symbol	Quantity	Value	Units
A	area		m^2
A_{grid}	cross-sectional area of the grid (continuous model)	10^6	m^2
B	Plasma Beta		
a	input node of neural network		
B	magnetic field density		G
B_0	initial magnetic field density		G
b	input node of neural network		
c	output node of neural network		
C_A	Alfven speed		$m\ s^{-1}$
C_s	sound speed		$m\ s^{-1}$
d	diffusion rate of magnetic field		$m^2\ s^{-1}$
D	duration of a reconnection event		s
E	total energy of cell, or energy released		J
E	error in neural network evaluation		
$\underline{E}$	electric field (vector field)		V
E_{int}	integrated energy of reconnection event (less background)		J
$\dot{E}$	energy flux		$J\ s^{-1}$
$\dot{E}_{peak}$	peak energy-release rate of reconnection		$J\ s^{-1}$
$g(x)$	input activation function of neural network		
$h(s)$	height at cell s in sand-pile model		
i	consecutive number of cell in model by MacKinnon, Macpherson & Vlahos (1996)		
k_B	Boltzmann's constant	1.381×10^{-23}	$J\ K^{-1}$
l	thickness of current sheet		m
L	cell (or other) length, or characteristic length scale		m
L_{init}	cell length at commencement of run		m
L_{max}	maximum cell length allowed before cell division occurs		m
L_{min}	minimum cell length allowed before removing cell from grid		m

Symbols

Symbol	Quantity	Value	Units
M	mass		kg
M_{cz}	mass of Solar convective zone		kg
M_{in}	Mach number of inflow plasma in Sweet-Parker model		
m_p	mass of proton	1.673×10^{-27}	kg
m_e	mass of electron	9.11×10^{-31}	kg
n	number density		m^{-3}
N	total number of particles, or number of cells		
N_{cells}	total number of cells in grid		
p	probability		
P	pressure		Pa
P_c	central Solar pressure		Pa
$P(N)$	probability of obtaining an event of size N		
r	radius		m
R_{cz}	depth of Solar convective zone		m
R_{mag}	magnetic Reynolds number		
s	consecutive number of site in sand-pile model		
t	time, or timescale		s
$t_{em/sub}$	replacement timescale of emergence/ submergence	typically 1000	s
T	temperature		K
T	observing time		s
T_c	central Solar temperature		K
T_{cz}	temperature at base of Solar convective zone		K
$T_{e,\odot}$	effective temperature of photosphere	5785	K
δt	discrete time interval (time-step)	$\frac{1}{500}$	s
δt	flare waiting time		s
V	volume		m^3
v	velocity		$m\ s^{-1}$
W	width of grid	10^3	m
w_a, w_b	input weight connections of neural network nodes		

Symbols

Symbol	Quantity	Value	Units
x_i	state of cell i in model by MacKinnon, Macpherson & Vlahos (1996)		
X	Solar hydrogen mass fraction		
X_s	value of vector field at cell s in model by Lu & Hamilton (1991)		
Z_s	gradient at cell s in sand-pile model		
Z_c	critical gradient in sand-pile model		
α	generic constant		
ϵ	small change in a value		
γ	ratio of specific heat capacities	5/3	
ΔN	increment to particle number in emergence cell		
ζ	random number		
η	noise level, or magnetic diffusivity		$m^2\ s^{-1}$
κ	emergence/submergence proportion	typically 0.1	
λ	spectral index of power-law distribution		
μ_0	permeability of a vaccuum	1.257×10^{-6}	$H\ m^{-1}$
ν	number of items (usually cells)		
ξ	energy density (magnetic or thermal)		$J\ m^{-3}$
ρ	density		$kg\ m^{-3}$
ρ_c	central Solar density		$kg\ m^{-3}$
σ	Stefan-Boltzmann constant	5.67×10^{-8}	$W\ m^{-2}\ K^{-4}$
τ	half-life		s
ϕ	magnetic flux		Mx
ψ	noise level in pressure field		
∇	Del operator		

Superscripts/Subscripts

ar	active region
background	background level of grid
bound	cell boundary
cell(s)	cell(s) within grid of model
co	coronal
curr	cell currently under consideration
deficit	loss from model compared with sum obtained at beginning of run
diff	diffusion
em	emerging flux cell
er	ephemeral active region
grid	grid
i	consecutive cell number
in	inflow
init	at beginning of run of model
int	integrated energy released
left	cell boundary wall closest to origin
mag	magnetic
model	within the model
next	adjoining cell in direction away from the origin
out	outflow
peak	peak energy release rate
p	proton

Superscripts/Subscripts

ph	photospheric
poly	polygon
prev	adjoining cell in direction towards the origin
right	cell boundary wall furthest from origin
realloc	reallocation of emergence/submergence sites
rec	pertaining to magnetic reconnection
sub	submerging flux cell
th	thermal, or thermodynamic
typical	typical value
unipolar	unipolar region
/	new recalculated value
·	rate of change with respect to time
⊙	Solar

Definitions of Commonly Used Terms

1-D	one-dimensional
2-D	two-dimensional
3-D	three-dimensional
avalanche	causally related relaxation events occurring in an SOC system
AR	active region
CME	coronal mass ejection
ER	ephemeral active region
field lines	magnetic field lines
flux	magnetic flux (ϕ)
flux density	magnetic field density (B)
frozen-in condition	charged fluid with high magnetic Reynolds number, i.e. negligable diffusion of field
GOES	Geostationary Operational Environmental Satellite
ICE	International Cometary Explorer spacecraft
Isliker effect	systematic biasing effect described by Isliker & Benz (2001)
log	logarithmic (base 10)
loop	closed magnetic field line (usually between two cells in a model)
MDI	Michelson Doppler Imager
MHD	magneto-hydrodynamics
normalised frequency	the probability density function of a plot (used on the y-axis)
peak flux	peak photon count rate of a Solar flare
P.D.F.	probability density function
reconnection	magnetic reconnection

Definitions of Commonly Used Terms

SMM	Solar Maximum Mission
SOC	self-organised criticality
SOHO	Solar and Heliospheric Observatory
typical initial conditions	initial parameters for a plot using :
	10^3 cells
	cell length = 10^4 m
	standard reconnection mechanism
	emergence/submergence turned on
	cell fraction for emergence/submergence, $\kappa = 0.1$
	flux replacement timescale, $t_{\mathrm{em/sub}} = 10^3$ s
	noise level, $\frac{\psi}{P}$ = zero
UV	ultraviolet radiation
YOHKOH	'sunbeam', Japanese Solar imaging satellite
ZAMS	zero-age main sequence

Chapter 1

Introduction.

"I asked him what the other books were about, the twenty-three previous ones, and he said that he thought one of them was about owls."
Richard Brautigan.

"Hello?
Yeah, it's me. I wanna give you some good frequencies. 172, 2.6, 2245
Yeah?
3032, 400
400?
Yeah.
I'm coming over.
Do that.
I'll be there in two seconds."
Röyksopp.

The purpose of this thesis is to present cellular automata models of the Solar surface activity together with the data produced and make where possible comparisons with real data. These models embody realistic 1-D fluid behaviour, emergence and submergence of magnetic flux and magnetic reconnection. They consist of simplified grids of cells with limited physical laws. There is enough physics, we believe, to usefully capture the salient behaviour of the Solar magnetic flux, yet not too much for the models to place too great a charge upon computing resources.

The questions we will try to address are as follows :

- How do power-law flux density distributions arise?
- How do power-law event-size distributions arise?
- Do we see sufficient dynamic range and appropriate power-law indexes in the model-generated data?
- Can features of flaring events be obtained with this model?
- How do the results depend on the details of the reconnection mechanism?
- What is the relevance of self-organised criticality?

1.1 Solar Activity and Properties of the Atmosphere.

The Solar atmosphere, whether atomic, as in the photosphere, or ionised, as in the chromosphere, transition region and corona, consists of material where thermodynamic pressure and magnetic pressure compete for dominance. The ratio of these can be characterised by the Plasma B :

$$\begin{aligned} \mathrm{B} &= \frac{\text{particle pressure}}{\text{magnetic pressure}} \\ &= \frac{n\, k_{\mathrm{B}}\, T}{\left(\frac{B^2}{2\mu_0}\right)} \\ &\approx \frac{C_{\mathrm{s}}^2}{C_{\mathrm{A}}^2} \end{aligned}$$

where : $C_{\mathrm{A}} = \frac{B}{\sqrt{\mu_0\, \rho}}$ and $C_{\mathrm{s}} = \sqrt{\frac{P\, \gamma}{\rho}}$

Thus, when B > 1, the gas pressure dominates over the magnetic pressure (also, any changes in density will be equilibrated by sound waves rather than slower Alfven waves). If we move radially outwards through the Solar atmosphere, we find that magnetic field density varies such that B > 1 in the photosphere at the base of the magnetic carpet, B << 1 in the mid corona, then B > 1 in the upper corona (Gary 2001). Our continuous model, explained in chapter 3, takes into account both the magnetic and thermodynamic components of pressure, therefore it is unnecessary to make any assumptions in the continuous model regarding Plasma B. The model incorporates simplified fluid behaviour intended to represent the photospheric velocity field and magnetic reconnection parameterised to represent the photosphere and corona.

The photosphere is the visible surface of the Sun. The corona is a hot tenuous region extending outwards from the Sun in all directions with no definite edge. The corona radiates thermally and non-thermally in extreme ultraviolet, soft and hard X-rays. The transition region is a layer of the Solar atmosphere which lies between the photosphere and hotter corona and is characterised by a steep temperature gradient, the temperature rising from the photosphere to the corona.

The term 'magnetic carpet', as discussed by Parnell (2001), refers to the complex magnetic field topology attached to the photosphere and extending through the photosphere and into the corona. The term originated when magnetogram images produced by the MDI ('Michelson Doppler Imager') instrument on board the SOHO ('Solar and Heliospheric Observatory') spacecraft were used to produce maps, such as figure 1.1, showing the approximate 3-D geometry of the photospheric and coronal magnetic field. The field connectivity has been derived by calculating potential-field solutions to the observed spatial distribution of magnetic charges across a magnetogram image.

By assuming that everywhere there is a 'potential field' structure we mean that we assume there are no currents, or current sheets, within the field. This assumption cannot be valid because non-parallel field will inevitably produce intervening current-sheets and diffusion regions, however it does allow us to determine from magnetogram images a simplified picture of the magnetic field structures and so obtain an idea of the types of field topologies present. These potential-field calculations also assume that plasma B $<<$ 1 throughout the whole of the mid-corona and upper-corona. Gary (2001) explains that this assumption is not likely to always be valid. We recall that plasma B reflects the ratio of gas pressure to magnetic pressure. Moving radially outwards along a magnetic field line from the photosphere, we are likely to find that this ratio varies from : B $>$ 1 in the photosphere, to B $<<$ 1 in the mid-corona, to B $>$ 1 in the upper corona. It is well known that B $>$ 1 where $r > 2R_{\odot}$, however there is a great deal of evidence that B $>$ 1 at relatively low coronal heights (Gary & Alexander 1999 and Hiei & Hundhausen 1996). Gary (2001) infer that the spreading of loop cusp material at a height of ≈ 0.23 reflects the dominance of Solar wind gas pressure over magnetic pressure at that height. This implies that B$\approx$1 at this height. The open field lines above loop cusps are thought to have advected gas away and therefore to be rarefied and to have B $<<$ 1. Gary (2001) construct a model using a variety of fits for gas and magnetic pressures and stretching of loops. They find that the general features of the model results are unchanged for a range of values for magnetic field density between a photospheric magnetic field density of 2.5 kG and, at the other extreme, 150 G. At first B $>$ 1 then becomes B $<<$ 1. For upper coronal loop cusps, B $>$ 1 will occur again at a height of $few \times 10^2$ Mm.

Let's now consider the thermal and magnetic energy densities inside the photosphere and corona

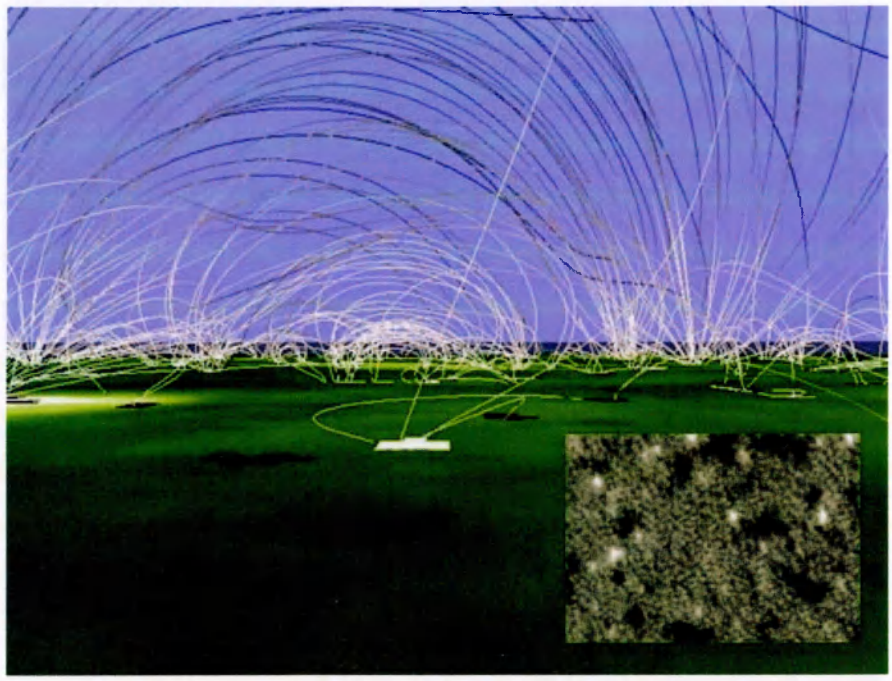

Figure 1.1: The Solar magnetic carpet, including magnetogram from which the potential-field topology was calculated. SOHO Consortium.

assuming the following typical parameter values (Zirin 1989 and Roberts 1999) :

$$\begin{aligned} n_{\rm ph} &= 10^{23}\ {\rm m}^{-3} \\ T_{\rm ph} &= 5800\ {\rm K} \\ B_{\rm ph} &= 1,\ 10 \text{ and } 50\ {\rm G} \\ n_{\rm co} &= 10^{15}\ {\rm m}^{-3} \\ T_{\rm co} &= 10^{6}\ {\rm K} \\ B_{\rm co} &= 1 \text{ and } 100\ {\rm G} \end{aligned}$$

and also,

$$\begin{aligned} m_{\rm p} &= 1.673 \times 10^{-27}\ {\rm kg} \\ m_{\rm e} &= 9.11 \times 10^{-31}\ {\rm kg} \end{aligned}$$

Now, we know :

$$\xi_{\rm th} = \frac{3}{2} n k_{\rm B} T$$

$$\xi_{\rm mag} = \frac{B^2}{2\mu_0}$$

Location	Type	B [G]	ξ [J m^{-3}]	P [N m^{-2}]
photosphere	thermal		1.2×10^4	8×10^3
photosphere	magnetic	1	4.0×10^{-3}	4.0×10^{-3}
photosphere	magnetic	10	0.4	0.4
photosphere	magnetic	50	9.9	9.9
photosphere	magnetic	3000	3.6×10^4	3.6×10^4
corona	thermal		2.1×10^{-2}	2.8×10^{-2}
corona	magnetic	1	4.0×10^{-3}	4.0×10^{-3}
corona	magnetic	100	40	40

Table 1.1: Calculated typical photospheric and coronal pressures and energy densities, both thermal and magnetic.

$$P_{\mathrm{mag}} = \frac{B^2}{2\mu_0}$$

$$P_{\mathrm{th,ph}} = nk_{\mathrm{B}}T$$

$$P_{\mathrm{th,co}} = 2nk_{\mathrm{B}}T$$

We remember that whereas we can consider the photosphere to be an atomic gas, in the corona electrons and protons are dissociated therefore there is a particle pressure contribution from both electrons and protons.

Table 1.1 shows the energy densities and pressures, thermal and magnetic, for the corona and photosphere based upon the values we have assumed above. Thus, we see that in the photosphere thermodynamics dominates the magnetic field except where the field density reaches $2 \leftrightarrow 3 \times 10^3$ G, which occurs only in sunspots. In the corona the reverse is the case. For the purposes of our continuous model, described in chapter 3, we can therefore neglect neither the magnetic nor thermal components of the energetics or the pressure forces, but must take account of both in our model dynamics.

Lawrence, Cadavid & Ruzmaikin (2001) found that the appearance of the photosphere in visible light is dominated by the granular and supergranular structures $\sim 1 \leftrightarrow 2 \times 10^6$ m and $\sim 2 \leftrightarrow 4 \times 10^7$ m, respectively. Granules have a lifetime of $\sim$ 18 minutes and the granular material has a velocity of perhaps $1 \leftrightarrow 2 \times 10^3$ m s^{-1}. Granules are caused by the underlying convective motions and are destroyed by fragmentation, decay and merger with other granules. Zirin (1989) describes the Solar photospheric magnetic field in the following terms. The magnetic field structure has several

components. The underlying quiet network is mixed in polarity although often unipolar at the poles and has a field density of $2.5 \leftrightarrow 3$ G (Parnell 2001). Active regions are characterised by bright plage, sunspots and loops. The field density of sunspots may be $2 \leftrightarrow 3 \times 10^3$ G. Ephemeral magnetic regions number in the thousands and appear everywhere on the Sun although usually near neutral lines. By contrast, sunspots usually appear at low latitudes. Ephemeral regions persist for approximately a day and are usually simple dipoles, contrasting with the far more complicated structures of active regions. Ephemeral regions may produce one small flare each. There are also chaotic regions of post-active region flux known as 'unipolar magnetic regions'. Magnetic loop structures, observable because of the X-ray and extreme UV emitted by hot plasma confined in gyro-rotation to the field lines, extend from active regions and ephemeral regions into the corona. Large features such as active regions are thought to originate at the base of the convective zone, whereas small features such as ephemeral regions may have their origins in small scale motions near the surface (Parnell 2001). Flares tend to occur along neutral lines between antiparallel flux regions and where the field within active regions becomes twisted and sheared. The canonical figure for the energy of a large flare is 10^{25} J, most of which will be generated within ~ 100 s. A common informal categorisation of flares is as follows :

flares	$10^{23} \leftrightarrow 10^{25}$ J
microflares	$10^{20} \leftrightarrow 10^{23}$ J
nanoflares	$10^{17} \leftrightarrow 10^{20}$ J

Parker (1988) proposed that the X-ray emission from the corona is created by immense numbers of unobservably small reconnection events (nanoflares). These are localised impulsive energy bursts caused by the constant random convection-driven motion of flux-tube footpoints which complicates the field and leads to current sheets and reconnection. We can think of flares in this scheme as consisting of superpositions of many nanoflares. Kaufmann et al. (1980) go further and suggest that the nanoflares represent a 'quantisation' of flare energy release.

Let's now consider flare size distribution data.

Hard X-ray data was obtained by the Hard X-Ray Burst Spectrometer ('HXRBS') on the Solar Maximum Mission ('SMM') spacecraft and by the X-ray spectrometer aboard the International Cometary Explorer ('ICE') spacecraft during long-term Solar flare observations. Statistical studies of the HXRBS data (Crosby, Aschwanden & Dennis 1993) and the ICE data (Bromund, McTiernan & Kane 1993) reveal power-law distributions in the peak count rate (C), total duration (D) and peak photon flux (F). Peak energy flux (E) and total energy (W) in accelerated electrons were also calculated using a single power-law photon spectrum and a thick-target interaction model. The power-law

distributions, as shown in table 1.2, extend for several decades. The threshold values result from instrument sensitivity and therefore give no information regarding the minimum event size. The two studies show slightly different power-law gradients, however this may be attributable to differences in instrument sensitivity or to differing methods of electron energy estimation.

	C (s^{-1})	D (s)	F (ph cm^{-2} s^{-1})	E (erg s^{-1})	W (erg)
Solar Maximum Mission (Crosby, Aschwanden & Dennis 1993)					
gradient	-1.73 ± 0.01	-2.17 ± 0.05	-1.59 ± 0.01	-1.67 ± 0.04	-1.53 ± 0.02
threshold	30	200	1.5	10^{27}	3×10^{28}
International Cometary Explorer spacecraft (Bromund, McTiernan & Kane 1993)					
gradient	-	-2.40 ± 0.04	-1.86 ± 0.01	-1.92 ± 0.02	-1.67 ± 0.02
threshold	-	100	4	2×10^{27}	10^{29}

Table 1.2: Characteristics of the distributions of hard X-ray flare parameters. Data was obtained by the Hard X-Ray Burst Spectrometer on the Solar Maximum Mission spacecraft (Crosby, Aschwanden & Dennis 1993) and by the X-ray spectrometer aboard the International Cometary Explorer spacecraft (Bromund, McTiernan & Kane 1993).

The SMM and ICE data shows typical Solar flare event-size distributions. However it has been well known since Datlowe, Elcan & Hudson (1974) that the size-distribution of flares follows power-laws when counted by peak photon flux during the soft X-ray impulsive phase of the flares. Many later studies have confirmed this for peak photon flux together with various other proxies for flare size, such as integrated energy (Wheatland 2000). Aschwanden, Dennis & Benz (1998) provide a useful tabulation of many studies which obtained distributions of peak flux for Solar flares and give the power-law indexes found. That paper shows that most studies completed during the last decade fint the spectral index of the peak flux distributions in the hard and soft X-ray bands are : $\sim 1.5 \pm 0.2$.

We should clarify the meaning of the term 'power-law'. If we collect data of events where the size of each of these events is s, we will bin these events in order to obtain the likelihood of finding events

of size s. We can divide the event count within each bin by the width of that bin in order to obtain the probability density function ('P.D.F.'), $P(s)$. Let us suppose that :

$$P(s) = \alpha\ s^{-\lambda}$$

where e is the base of natural logarithms, λ is the spectral index and α is a constant. The distribution is said to be of 'power-law' form. If we then plot a graph of $\log(s) - v - \log(P(s))$ we will find that the distribution lies along a straight line. The spectral index ('power-law index') is the gradient of the distribution.

Miroshnichenko, Mendoza & Enriquez (2001) analyzed data between 1955 and 1996 in order to determine accurate distributions of event-sizes. Considering only protons with energies greater than 10 MeV, and events above the rate of 1 p.f.u (proton $\mathrm{cm}^{-2}\ \mathrm{s}^{-1}\ \mathrm{sr}^{-1}$), they found 320 events associated with identified flares. Considering the integrated energy released from these events they found the events to have a power-law distribution with a gradient of $1.37\ \pm\ 0.05$ over the whole range of proton intensities : $1.0\ \leftrightarrow\ 10^5$ p.f.u. Considering only a subgroup of 159 events associated with magnetospheric storms, they found that this subgroup exhibited double power-law distributions. The two exponents for these were 1.00 ± 0.04 and 1.53 ± 0.03, below and above 10^3 p.f.u., respectively.

In this section we have explained something of the general nature and behaviour of the Solar surface plasma and magnetic fields. The following sections within the Introduction will focus more closely upon specific physics, phenomena and models.

1.2 Variation of $|B|$ with the Solar Cycle.

The Solar photospheric magnetic field appears to exist in a power-law distribution. Schrijver & Harvey (1989) analysed magnetic field maps for the period 1975 to 1984 and generated magnetic field density distributions for six snapshots during this period. Schrijver & Harvey (1989) used synoptic magnetic field maps produced from smoothed $1''$-resolution daily magnetograms, since within any small area of the photosphere for which we have magnetogram data we would not expect a complete absence of magnetic flux antiparallel to the vector of the mean flux.

The magnetic field distributions determined by Schrijver & Harvey (1989) and the times associated with each are given in figure 1.2. This plot shows normalised distributions of field density where the x-axis is in units of Gauss and both axes are log-log.

These distributions all consist of two regimes. There is a fairly flat lower region which undergoes a transition into a clearly power-law region at higher flux levels. The six distributions run roughly from Solar minimum through maximum to another minimum. We can distinguish the distributions without

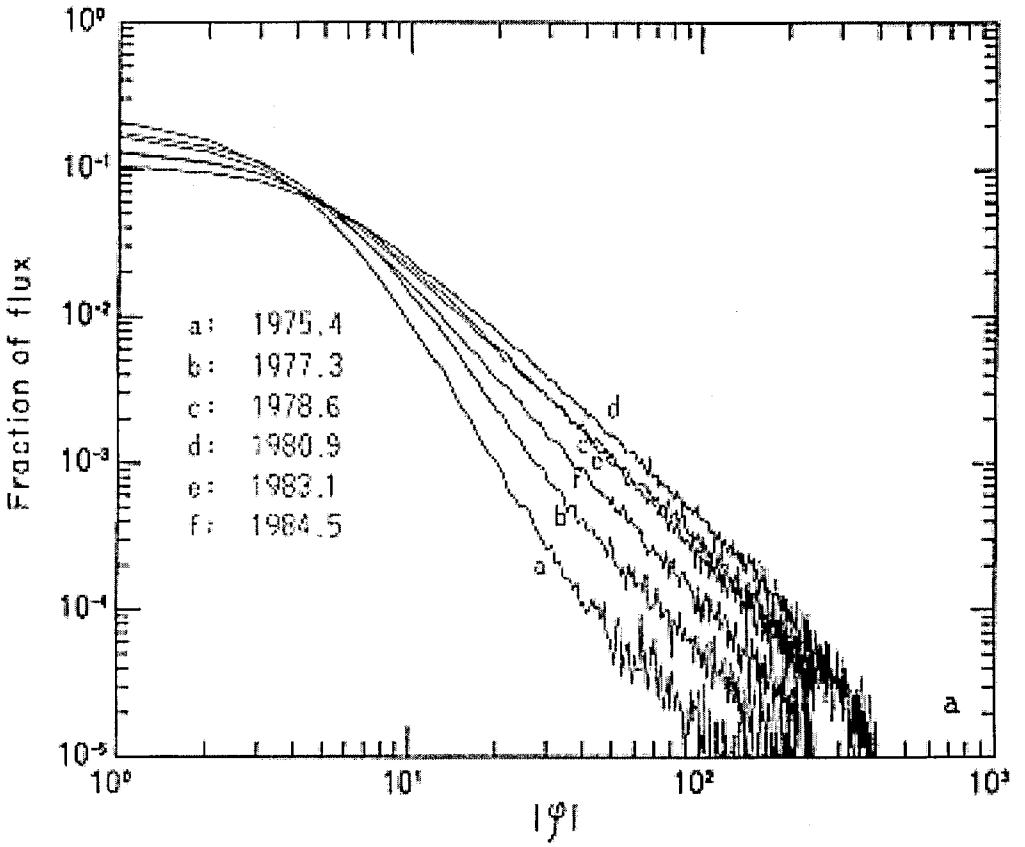

Figure 1.2: P.D.F. of $|B|$ (despite the use of ϕ in the figure) at different times in the Solar cycle. Bin-size = 1 G. Time interval 'd' represents Solar maximum. (Schrijver & Harvey 1989).

difficulty and there is an unequivocal flattening of the P.D.F. moving towards Solar maximum, followed by a steepening again after maximum. Also, there is a progressive movement of the position of the roll-over from approximately 2-4 G at Solar minimum to 3-6 G at maximum.

We will consider this data in more detail later in section 5.4 when discussing the results from the model.

1.3 Power-law Structure of Magnetic Regions.

Meunier (1999) have analysed the fractal nature of the Solar surface magnetic field and found that the area and perimeter of regions exceeding particular magnetic flux density thresholds can be described by fractal dimensions. The two plots shown in figure 1.3 were generated from full disc magnetogram data. To generate the upper plot they identified regions with magnetic field density greater than 40 G then calculated area, linear size and perimeter for each region. Plotting perimeter against area on logarithmic axes they found the slope of the best-fit line. Twice this value is equal to a measure of fractal dimension called the Hausdorff dimension. Thus :

$$d_1 = 2\,\frac{\Delta \log \mathrm{P}}{\Delta \log \mathrm{A}}$$

The more complex and denticulate a magnetic region the closer will the value of the Hausdorff dimension (d_1) be to 2. A perfect circle or square will give a value of 1. The value of the Hausdorff dimension for figure 1.3 lies between 1 and 2.

The lower plot was generated by plotting area against linear size on logarithmic axes. Thus :

$$d_2 = \frac{\Delta \log \mathrm{A}}{\Delta \log \mathrm{L}}$$

The slope of this graph is equal to another measure of fractal dimension. The more complex and denticulate the region is the smaller this value will be, and will equal 2 for non-fractal regions. The lower plot of figure 1.3 gives a value for this measure of approximately 2.0, thus indicating a non-fractal field distribution. The reason for using two different methods of calculating fractal dimension is that each of the two methods are only indicators of how denticulate a region is.

1.4 'Frozen-In Condition' and Magnetic Reconnection.

We have seen that the magnetic field dominates energetically in the upper Solar atmosphere extending from the transition region into and including the corona. For an ideal MHD plasma Ohm's law gives us :

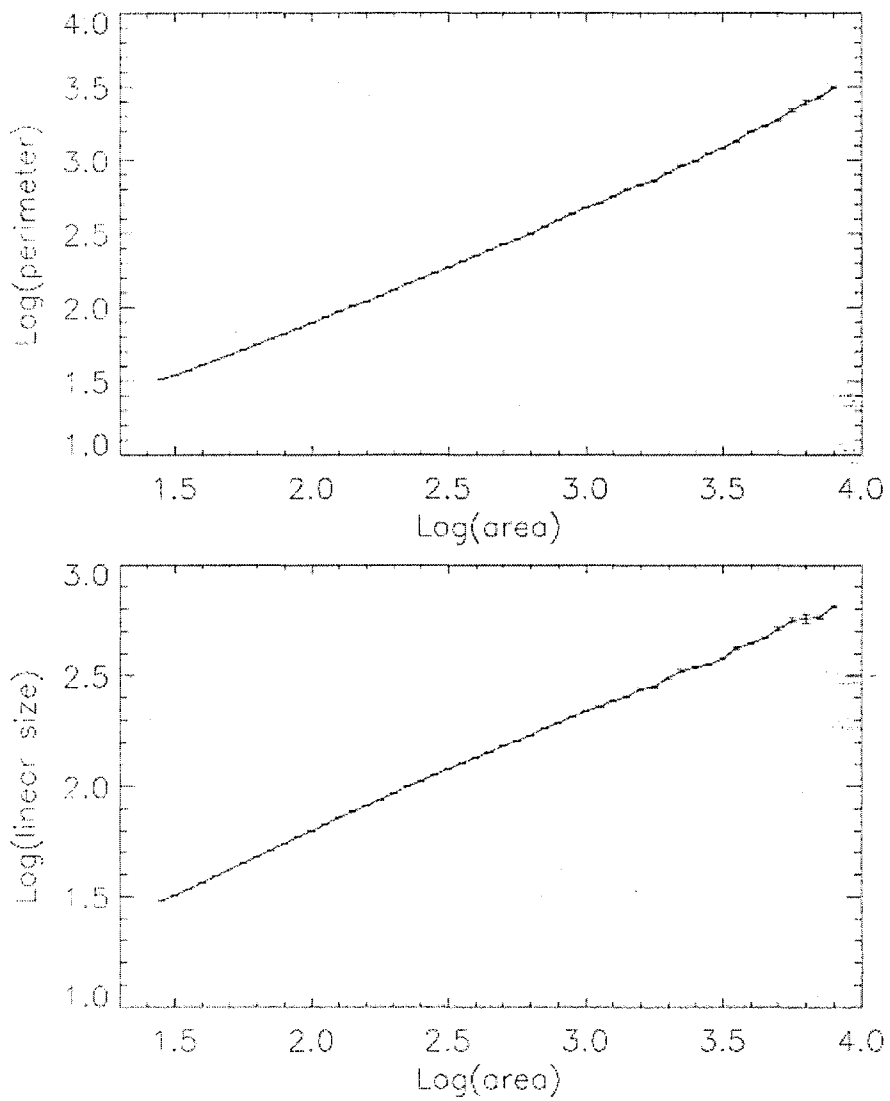

Figure 1.3: Top: Average perimeter P versus the area A for data set of full-disk magnetograms for a threshold of 40G and area larger than 30 pixels; bin-size = 0.05. Bottom: similar relation between L and A. Units of A, P and L are pixels. Meunier (1999).

$$\underline{E} + \underline{v} \times \underline{B} = 0$$

Here, $\underline{E}$ is the electric field.

Ohm's law in a more general form :

$$\frac{\partial \underline{B}}{\partial t} = \nabla \times (\underline{v} \times \underline{B}) + \eta \, \nabla^2 \underline{B} \tag{1.1}$$

The first term on the right-hand side of equation 1.1 represents advection of field lines and the second term represents diffusion of flux across plasma. Taking the ratio of these two terms gives us the following, where $R_{\rm mag}$ is the magnetic Reynolds number, v a velocity term, L a characteristic length-scale and η the magnetic diffusivity of the plasma :

$$\begin{aligned} R_{\rm mag} &= \frac{\nabla \times (\underline{v} \times \underline{B})}{\eta \, \nabla^2 \underline{B}} \\ &= \frac{\text{advective term}}{\text{diffusive term}} \\ &= v \, L/\eta \end{aligned}$$

For Solar and astrophysical plasmas L is large therefore the advection term dominates and diffusion is negligible. This means that plasma and magnetic field are fixed together. This is known as the 'frozen-in condition'. Flux cannot diffuse readily through the plasma but must flow with it (or vice versa depending on the value of the Plasma B). The only relative motion allowed between the plasma and field is (1) gyro-rotation of electrons and protons around field lines and (2) motion along the field lines, the superposition of which implies a spiralling motion along field lines. For an electron velocity of 10^6 m s^{-1} and a field density of 10 G we would expect a gyro-radius of $\sim 6 \times 10^{-3}$ m.

Thus, we have an important result for space plasma physics : like beads on a string, elements of plasma attached to a field line remain attached to that field line throughout any subsequent motion. This means that topologically different regions of flux cannot interpenetrate. Figure 1.4 shows a 2-D section through two topologically different and distinct regions of magnetic field : (1) a closed island/plasmoid, and (2) open parallel field. While these regions may change their field density and number density distributions and distort their shapes, they may not change their topologies, cross over or interpenetrate.

Considering the case of a magnetic field in a static atmosphere of fully ionised hydrogen, Dere (1996) obtain an expression giving the time-scale of resistive diffusion of flux.

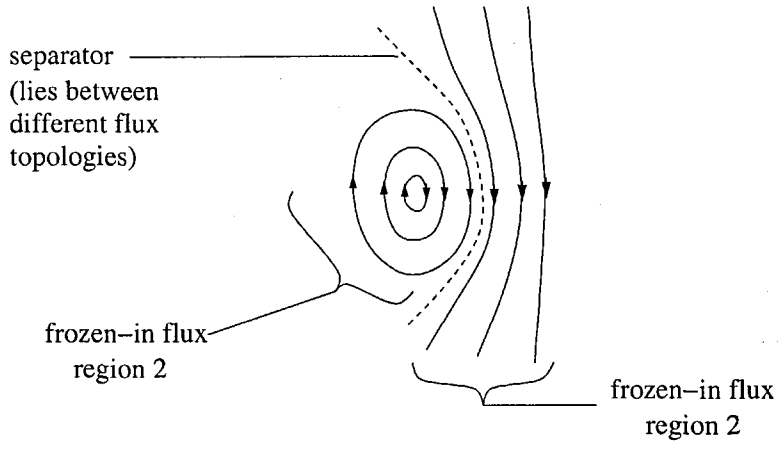

Figure 1.4: Illustration of frozen-in condition. Two topologically distinct regions of magnetic field.

In the purely diffusive regime, Ohm's law (equation 1.1) becomes :

$$\frac{\partial \underline{B}}{\partial t} = \eta \, \nabla^2 \underline{B}$$

After performing a dimensional analysis of this, we arrive at :

$$\frac{B}{T} = \frac{\eta B}{L^2}$$

where T is the characteristic time-scale of the diffusion.

Further, we have :

$$T = \frac{L^2}{\eta}$$

Spitzer (1962) gives :

$$\eta = 5.2 \times 10^7 \ \ln(A) \ T^{-3/2} \ \mathrm{m^2 \ s^{-1}}$$

If we consider $\tau \approx T$ and substitute for η we obtain :

$$\tau_{\mathrm{diff}} = L^2/d \tag{1.2}$$

where :

$$d \approx 10^{13.1} \ T^{-3/2} \ \mathrm{cm^2 \ s^{-1}}$$

$\tau_{\mathrm{diff}} = L$ is the time-scale for resistive diffusion of magnetic flux and d is the diffusion rate. Thus, magnetic field variations over the length scale L, are destroyed over the timescale τ.

Dere (1996) find that for a typical coronal active region of size 3×10^7 m and temperature 2×10^6 K, $\tau \approx 6 \times 10^{15}$ s. The early impulsive phase of a flare, which may release of the order of 10^{25} J, will typically take place in ~ 100 s. Clearly the reorganisation of a magnetic field by diffusion is far too slow to explain the topological changes in field structure required for the dynamic behaviour of the Solar atmosphere.

In order therefore for reorganisation of the Solar magnetic field to occur, the frozen-in condition must break down. This is where magnetic reconnection must be brought in. Additional to the problem of explaining mechanisms for fast energy release and field reorganisation, there is another significant difficulty which has not yet been satisfactorily resolved. Although the temperature of the Solar photosphere is around 5800 K, the far more tenuous and expansive corona, extending out several Solar radii, has temperatures of typically several hundred thousand to several million Kelvin. Amongst other theories, including some which invoke MHD waves, it is believed that magnetic reconnection is responsible for heating the coronal and transition region plasma (Jardine 1992).

It was realised in the early sixties that magnetic reconnection is necessary for the fast energy release occuring in the large-scale and rapid field organisation we observe during flaring activity and CMEs.

The 'Sweet-Parker model' (Sweet 1958) was probably the earliest serious model for magnetic reconnection where anti-parallel flux is being pushed together by external bulk movement of field. The model, shown in figure 1.5 is 2-D and steady-state, like the later Petschek model, and consists of a thin current sheet between anti-parallel fiux. After reconnection, plasma exits the current sheet at the Alfven speed, C_{A}. To preserve the current sheet there must be an inflow of flux at velocity v_{in} such that the outward diffusion of the field in the current sheet is exactly balanced. Thus, we have :

$$v_{\mathrm{in}} = \frac{\eta}{l}$$

where $l \equiv$ thickness of the current sheet and v_{in} is assumed to be small compared with C_{A}. By considering mass continuity of the plasma flow we obtain :

$$L\, v_{\mathrm{in}} = l\, C_{\mathrm{A}}$$

also, we have :

$$M_{\mathrm{in}} = \frac{v_{\mathrm{in}}}{C_{\mathrm{A}}}$$

where $L \equiv$ length of the current sheet. Further algebraic manipulation using these relationships will give :

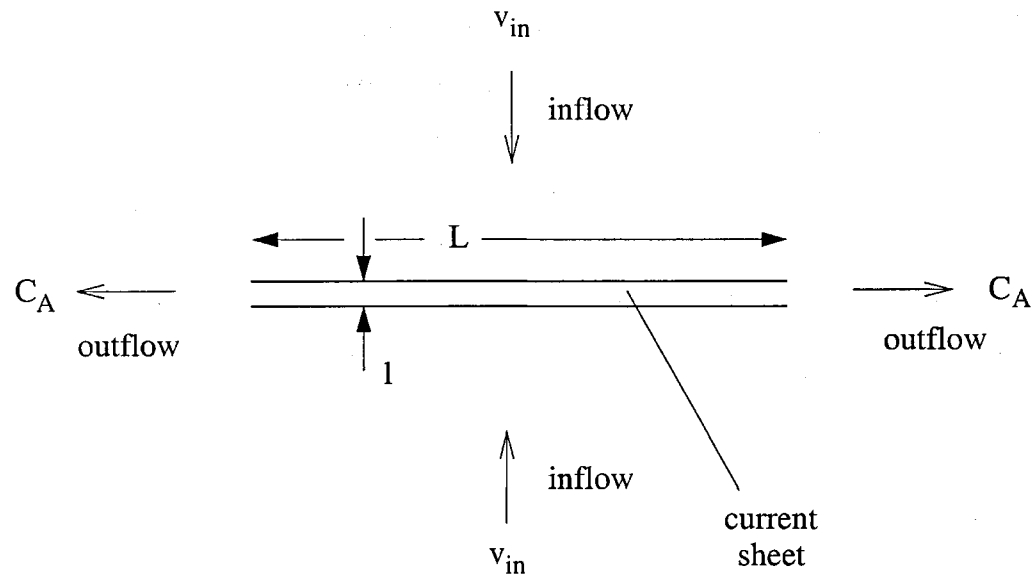

Figure 1.5: 'Sweet-Parker' reconnection model showing inflow and outflow of flux through diffusion region (Sweet 1958).

$$M_{\rm in} = \frac{1}{\sqrt{R_{\rm mag}}}$$

where $M_{\rm in} \equiv$ inflow Mach number.

In the typical Solar plasma we are considering here, the magnetic Reynolds number, $R_{\rm mag}$, will be large (see section 1.4) therefore we expect $M_{\rm in}$ to be small. Given that $R_{\rm mag} = Lv_{\rm in}/\eta$ and $v_{\rm in} = \frac{\eta}{l}$, it follows that :

$$\frac{L}{l} = \sqrt{R_{\rm mag}}$$

Given that $R_{\rm mag}$ will be large, $\frac{L}{l}$ will be small and when L is considered to be the global length scale of a typical flare the current sheet in the Sweet-Parker model will be long and thin with $M_{\rm in} \sim 10^{-3} \leftrightarrow 10^{-6}$. Given a typical coronal value for $C_{\rm A}$ of $\sim 10^5$ m s^{-1} we therefore have values of $v_{\rm in}$ which are far too low to explain flare observations. Thus, although the Sweet-Parker model has been confirmed experimentally (Yamada 1998), the reconnection takes place too slowly to account for Solar flares and a faster mechanism is required. Although controversial, a model which answers this problem is the 'Petschek model'.

The current model for simple 2-D reconnection was suggested by Petscheck (1964). We suppose that bulk movements push together Solar plasma such that flux with a substantial anti-parallel component comes into contact. Because of the non-zero resistivity of the plasma, a current sheet will exist across the region where the field lines reverse. Within this region the magnetic Reynolds

number, R_{mag}, will be sufficiently small such that field lines will be able to diffuse. Figure 1.6 shows a 2-D schematic representation of the Petschek model (Petscheck 1964). The diffusion region is shown by the shaded box. Thus, the field lines can reconnect into a new continuous pattern about the null point within the diffusion region. The thickness of the diffusion region must be in the order of tens of metres in order to generate the necessary field gradients (Foukal 1990) therefore we cannot expect to be able to directly observe the diffusion region itself. This model incorporates Alfven waves piled into shocks across the inflow regions which convert energy stored in the magnetic field into thermal energy (Jardine 1992). Tension in the newly-reconnected field lines post-reconnection accelerate the plasma away from the diffusion region at the Alfven speed (Jardine 1992).

In this model, the diffusion region constitutes in effect a miniature Sweet-Parker model, and it is no longer necessary therefore to assume that the length of the diffusion region is comparable to the size of the system. We can therefore allow v_{in} to approach C_{A}, which gives us a much higher rate of reconnection than that allowed in the Sweet-Parker model. Nevertheless, the Petschek model is not widely accepted. This is partly because of the semi-qualitative nature of the analysis. The magnetic field strength should decrease outwards along the direction of propagation of the incoming Alfven wave (or slow shock), which implies that the field to the outside of that region should be bowed away from the diffusion region, rather than being straight. The Petschek model assumes, amongst other things, that the magnetic field density outside the current sheet is independent of distance from the neutral line (Petschek & Thorne 1967).

Biskamp (1986) performed a numerical experiment and found, contrary to the Petschek model, that when the rate of inflowing plasma was increased magnetic flux accumulated in front of the diffusion region and the rate of reconnection scaled only as per the slow reconnection predicted by the Sweet-Parker model, although the inflow velocity exceeded that allowed by the Sweet-Parker model.

Petscheck (1964) assumes the length of the diffusion region to be a free parameter and consequently chooses the smallest possible length in order to produce the highest possible reconnection rate. In fact, as explained by Kulsrud (2003), this length is not a free parameter but is constrained by the requirement of constant resistivity. Where the resistivity is held constant it is a consequence that the size of the diffusion region will be the same as that of the whole reconnection region, and therefore we would find that the Petschek mechanism gives a reconnection rate no faster than that predicted by the Sweet-Parker mechanism.

Priest & Forbes (1992) were able to explain the results of Biskamp (1986) and show that it was his assumption of constant resistivity that resulted in his findings that the rate of reconnection was

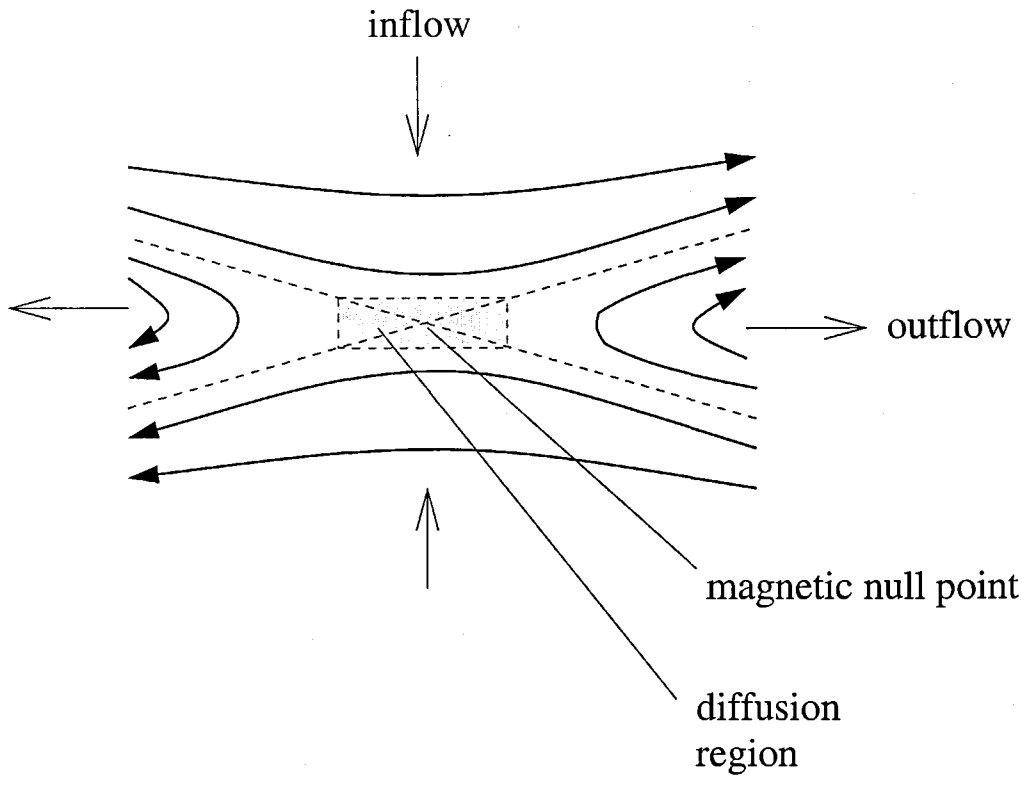

Figure 1.6: Current reconnection model ('Petschek model'), showing inflow and outflow of flux through diffusion region. Petscheck (1964)

no greater than that of the Sweet-Parker model. They were able to show that numerical simulations using suitable and reasonable boundary conditions are able to produce the fast reconnection predicted by the Petschek mechanism.

Certainly, fast reconnection under the Petschek scheme has never been achieved in numerical simulations, except by increasing the resistivity in the diffusion region in a way not universally agreed to be valid.

Figure 1.7 illustrates the standard 2-D flare model, based upon magnetic reconnection. The field topology in this cartoon model is one of several possible alternative speculative field topologies. Let's briefly consider the important features of this model. First, reconnection accelerates the ejected plasma away into the upper corona to typical velocities of $10^5 \leftrightarrow 10^6$ m s^{-1} where it merges with the Solar wind. Second, the production of reconnected field accelerates charged particles along the field lines down to the footpoints of the loop. Along the way these particles heat the loop material trapped along the field lines in the corona, chromosphere and photosphere and eventually impact with and heat photospheric material. The existence of these fast particles is inferred from observations of impulsive bursts of hard X-rays generated in the corona and/or chromosphere and/or photosphere.

The model shown in figure 1.7 is undoubtedly a highly simplified version of the actual process and remains a controversial idea although there is general agreement regarding the broad features : magnetic reconnection, ejected plasma, fast particle streams leading to impulsive hard X-ray bursts.

Simulations have shown that in terms of flow rates the Petschek model gives dynamically sensible results for the forced convergence of anti-parallel flux regions.

Thus, it is believed that the continual stochastic photospheric motions and granulation flows force a continuous and random braiding of the intense flux-tubes which thread the photospheric surface and are believed to be constituents of magnetic concentrations. This braiding stores energy in the magnetic field and creates conditions for complex current sheets. Fast non-thermal electrons and protons are observed to be associated with flaring events, and powerful electric fields generated may be responsible for acceleration of these particles. We have discussed the Petscheck and Sweet-Parker models here as simple models of reconnection, however we must clarify that where there is complex braiding of flux-tubes, there will not be a simple structure of current sheets. Therefore simple Petschek model reconnection will not take place. Reconnection need not occur in a simple current sheet geometry, but can occur within a region where the field is sheared, leading to tearing-mode instability. Braided and twisted flux tubes are also likely to exhibit pinch, kink and helical instabilities. The topology of the field and current sheets may have very complex geometries.

Magnetic reconnection provides a mechanism for the relaxation and simplification of this complex field. There is also evidence that reconnection is responsible for flaring activity. Demoulin et al. (1993) studied magnetic field topology within several active regions and, after calculating potential fields (magnetic field where there are no currents) from magnetogram data, compared these diagrams with flare loops. By performing these studies Demoulin et al. (1993) tentatively showed that the evolution of the magnetic fields is caused by reconnection.

Moore, LaRosa & Orwig (1995) take this standard flaring model and address a problem associated with it. In order to do this they consider a large eruptive flare which occurred on April 24/25 1984. Reconnection taking place during the flare causes three events, according to the model : (1) acceleration of electrons and plasma heating to precipitate hard and soft X-ray emissions; (2) creation of an arcade of coronal flare loops with two footpoints attached to a pair of separating flare ribbons; (3) an intense flux rope located above the reconnection site is further wrapped in flux which forms a plasmoid, unattached to the photospheric field, and which is driven (possibly constituting a coronal mass ejection ('CME')) into interplanetary space. The is no accepted model of the electron heating of the plasma by reconnection. The problem is that the shocks which sit above and below the reconnection site, and which the accelerated electrons flow through, can heat the plasma to

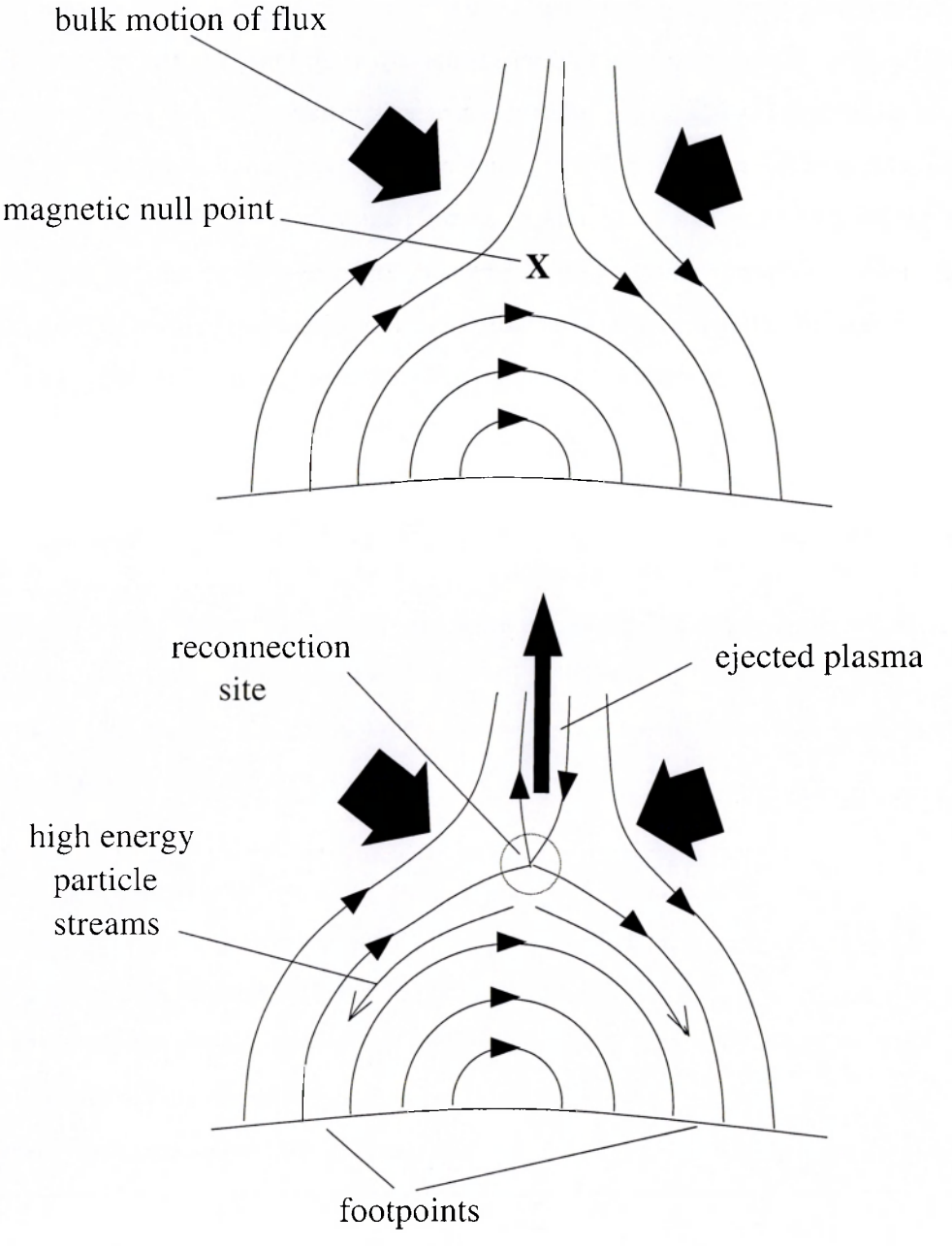

Figure 1.7: Standard flare model.

only a few keV at the most. Electrons with energies of > 25 keV must be produced at a high rate ($\sim 10^{36}$ s^{-1}) to produce the observed hard X-ray (> 25 keV) emission during the impulsive phase of flares. Moore, LaRosa & Orwig (1995) suggest and test a modified form of the standard model. The modification consists of the inflowing field not being laminar but instead being turbulent. Moore, LaRosa & Orwig (1995) find that their model allows the acceleration of ambient electrons to energies of ~ 25 keV by Fermi acceleration. More generally, they find that the morphology of the 1984 flare accords with their model. The model turbulent wall required to power the heating of the plasma fits comfortably within the observed flare. This energy required is of the order of $\sim 10^{25}$ J. Taking the observed length of the two flare ribbons at the peak of the explosive phase to be ~ 65000 km, the width of the pre-flare channel to be ~ 5000 km and the average field strength to be 1000 G, they calculate that the preflare turbulent wall could have contained $\sim 2 \times 10^{25}$ J. Thus, with suitable modification it is clearer still that the general features of the standard flare model are correct.

1.5 Relevance of MHD.

The behaviour of the Solar atmosphere is an expression of the release of energy stored in the magnetic field. For the purposes of this study we are concerned with the field of the photosphere out into the corona. The footpoints of loops visible in TRACE images are anchored in the magnetic carpet. We have seen how the frozen-in condition requires that reorganisation of the field is achieved through magnetic reconnection. The question is : how can we use this understanding to develop useful models?

By considering the plasma as a conducting fluid within the presence of a magnetic field we can use MHD to analyse and model the dynamical behaviour and equilibria of plasma. MHD allows us to describe a conducting collision-dominated (therefore Maxwellian) fluid through which are threaded magnetic field lines. This field may be produced by current flowing in the fluid, externally imposed or a combination of these. The MHD description is macroscopic and statistical and consists of an amalgamation of fluid mechanics and electromagnetism and incorporates conservation principles in respect of mass, momentum, energy and magnetic flux.

The equations of MHD are as follows : mass continuity, adiabatic equation of state, momentum continuity, Ampere's law, Faraday's law, div $\underline{B} = 0$ and resistive Ohm's law (Dendy 1993).

MHD is a powerful technique, and has for instance successfully explained in general terms many effects ranging from the dynamo effect, where a field arises spontaneously in a rotating conducting planetary body, to the varied problems associated with magnetic confinement of hot plasma in prototype thermonuclear fusion reactors. MHD is useful for examining evolution of idealised magnetic

plasma configurations where there are a small number of null points and simple magnetic topology, very often using symmetrical geometrical arrangements. MHD is capable of describing the propagation of Alfven, sound and magnetosonic waves, where Alfven waves propagate across and along magnetic field lines and magnetosonic waves are a combination of sound waves and Alfven waves.

There are a number of workers in the field making different approaches to the problem of exploring the effect of magnetic reconnection in a variety of realistic Solar atmospheric environments. The most popular is the use of MHD where a magnetic configuration is set up with specific initial conditions and is evolved. Of course, these models are highly simplified idealisations and cannot yet approach the variety and randomness of the real Solar atmosphere. An example of this work is Galsgaard & Roussev (2002). These models attempt to incorporate increasing numbers of important physical features such as gravity, stratification, three-dimensionality and multiple null points and current sheets.

MHD is however incapable so far of performing accurate 3-D simulations with large numbers of null points and complex current sheets, and certainly is nowhere near being able to deal with the full range of length scales from that of the reconnection diffusion region in Solar plasmas to that of large flares : a few metres (Foukal 1990) to 10^8 m, respectively. Such capabilities are necessary if MHD is to explain the behaviours we observe in the Solar atmosphere, including flares, CMEs, sunspots, plage, poleward migration of sunspot pairs, tornadoes and coronal heating.

Hesse (1995) have discussed magnetic reconnection in generic cases with a particular interest in investigating the relevance of the integral of the parallel electric field along field lines. they showed that reconnection is most likely to occur where there are helical structures of magnetic field. Such structure are referred to in the literature as 'flux ropes'. They used detailed MHD simulations to model the formation of current sheets and flux ropes and the consequent acceleration of these flux ropes by the outflow from reconnection. They showed that the formation of helical field lines and of large regions of parallel flux are obtained, as expected, where there is a sheared magnetic field configuration and the loop footpoints are converging. Hesse (1995) showed that sensible scaling of the model up to coronal sizes would result in particle acceleration in the GeV range.

1.6 3-D MHD Simulations of Black Hole Accretions disks.

It is thought that magnetic fields play important roles in many astrophysical systems, often being a mechanism for energy release by reconnection or transport of angular momentum.

Machida & Matsumoto (2003) used MHD to model black-hole accretion disks and the role of magnetic reconnection therein. We would expect differential rotation to stretch and compress field in

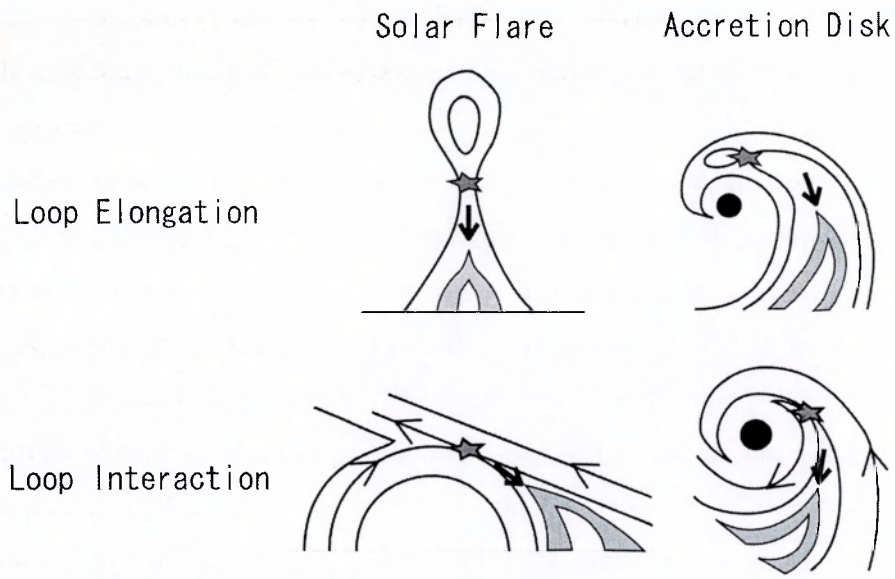

Figure 1.8: Schematic comparing magnetic reconnection in Solar flares and accretion disks. Machida & Matsumoto (2003)

the inner region of a disk. Current sheets should form and the field will be subject to magnetic reconnection. Tajima & Gilden (1987) and Sano & Inutsuka (2003) have carried out MHD simulations of the formation of current sheets and magnetic reconnection in accretion disks. These models showed quasi-periodic energy release. Mineshiga (1994) used a simple cellular automaton model incorporating self-organised criticality and obtained self-similar flaring behaviour. Kawaguchi, Mineshige & Machida (2000) performed MHD simulations of accretion disks and successfully reproduced the self-similar behaviour in the time-domain which we observe in black-hole candidates. Machida & Matsumoto (2003) modelled not only magnetic field topology and energy release by reconnection, but also ratio of gas pressure to magnetic pressure (plasma B) and density, radial velocity, angular momentum and other parameters. Figure 1.8 illustrates schematically two types of reconnection process analogous between Solar flares and accretion disks. Interactions taking place in accretion disks may be able to release more energy than those in the Solar corona for the reason that rotational energy is an additional source of magnetic energy. Figure 1.9 shows the magnetic field lines of the disk distorted by differential rotation. Machida & Matsumoto (2003) found that gravitational potential energy of the accreting gas was converted into magnetic energy and that following the infall of dense blobs of gas, reconnection would occur in the newly rarefied material. Reconnection also occurs where current sheets interact. X-ray emission by reconnection in the model was compared to that of Cygnus X-1. In both the soft X-ray 'shot' is time symmetric. In the model, hard X-ray emission occurs impulsively after the peak of the soft X-rays has passed.

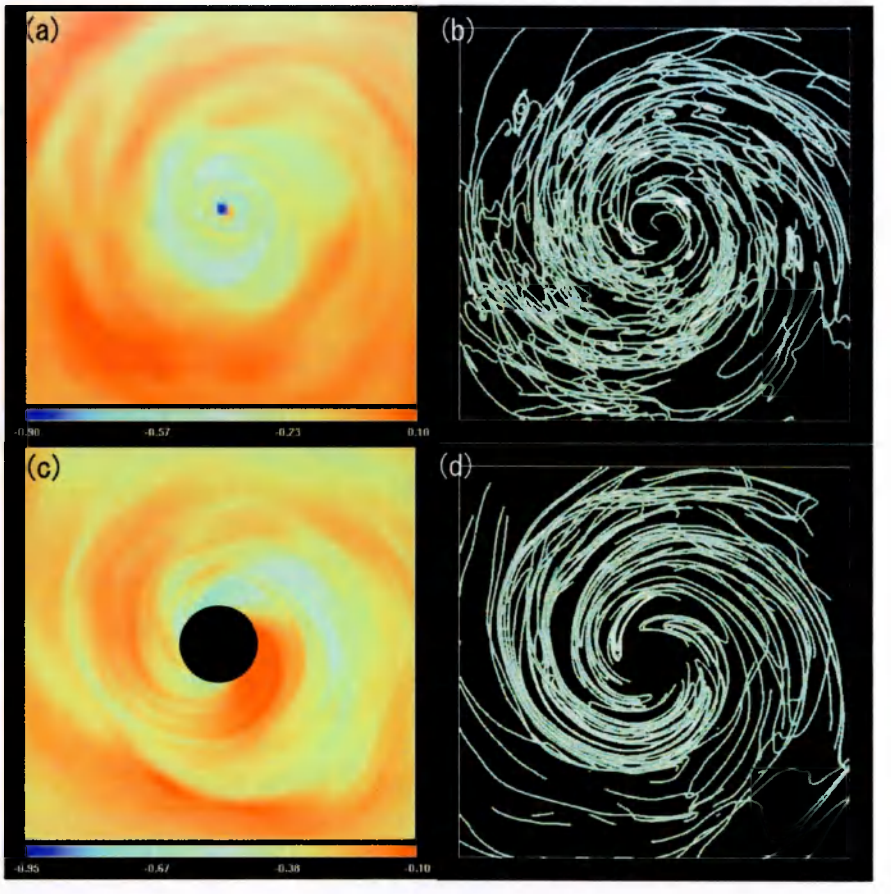

Figure 1.9: Magnetic field lines and equatorial density distribution of accretion disk projected onto the equatorial plane. Images a,b : global structure inside $r = 60$. Images c,d : inner region inside $r = 10$. Machida & Matsumoto (2003)

1.7 Self-Organised Criticality, Power-Law Behaviour and Sand-piles.

The world and the wider universe are replete with systems, natural or otherwise, exhibiting temporal or spatial power-law behaviour. For example : size of animal bodies across species, sizes of lunar impact craters, magnitude of biological extinctions, quasar hard X-ray bursts and city-sizes. Processes which produce objects or behaviour with power-law distributions are said to be 'self-similar'. As we can see from the above list, these behaviours can be self-similar in space or time (turbulence is a self-similar phenomena in both space and time). Bak, Tang & Wiesenfeld (1987) and Bak, Tang & Wiesenfeld (1988) have found that the dynamics of self-similar phenomena tend to be associated with a temporal behaviour known as '$1/f$ flicker noise', where the power spectrum $P(f)$ as a function of the frequency f scales as $P(f) = 1/f^a$ where the exponent a is close to 1. Examples of $1/f$ noise include current flow through resistors, traffic flow, speech, river flow rates and stock exchange indices

(Sornette 2000). $1/f$ flicker noise is not really noise but temporal self-similarity of the system. It seems that spatial self-similarity and 1/f flicker noise are signatures of systems which exist in a state of self-organised criticality ('SOC'). It does not follow however that systems which exhibit spatial self-similarity and 1/f flicker noise are necessarily SOC.

The classic example of an idealised system exhibiting SOC is the 'sand-pile', as explored by Bak, Tang & Wiesenfeld (1988).

Figure 1.10 shows the sand-pile model. In the 1-D case we use a space which is open to the right with an infinite wall to the left. We can visualise this more easily by thinking of the model as half of a symmetric pile of sand. A 1-D array of integers specifies the height of consecutive sites along a grid. Units are dropped in turn at random locations and the model is allowed to evolve in accordance with simple rules.

Where the gradient at site s is Z_s, we have :

$$Z_s \equiv h(s) - h(s+1)$$

Given this expression for Z_s, each time that the height at site s is incremented by one unit the effect is that :

$$Z_s \rightarrow Z_s + 1$$

$$Z_{s-1} \rightarrow Z_{s-1} - 1$$

This is shown in figure 1.10. Just like a sand-pile there is a critical gradient, Z_c, above which an adjustment is made to the heights of site s and $s+1$: one unit is subtracted from site s and added to site $s+1$.

When $Z_s > Z_c$:

$$Z_s \rightarrow Z_s - 2$$

$$Z_{s\pm1} \rightarrow Z_{s\pm1} + 1$$

We can see that the increment in value of Z_{s+1} and Z_{s-1} may precipitate further events. The size of an 'avalanche' is the sum of the number of events following from the deposition of one unit upon a randomly selected site. An avalanche, and the events of which it is constituted, represent a form of relaxation of the system.

Thus, we find that from arbitrary initial conditions the system evolves towards a state where the gradient everywhere is just below the critical gradient. The critical state is an attractor for the system. This is the 'minimally stable state' and the system is said to have reached 'criticality'.

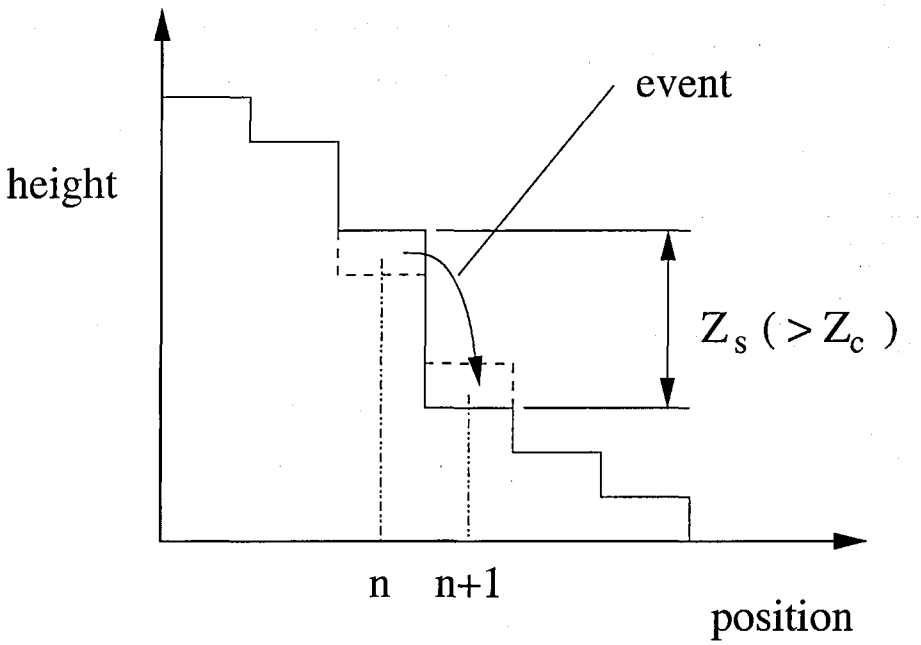

Figure 1.10: Sand-pile model. Shows the relocation of one unit caused by an event. Bak, Tang & Wiesenfeld (1988)

Following the attaining of criticality, the avalanches of the sand-pile will be of power-law distribution as a consequence of there being no intrinsic scale. Avalanches of any size are possible up to the size of the model and it is not possible to infer from one avalanche the details of the following one. The power-law distributions follow from the lack of any natural physical scale in the system and the behaviour is said to be 'scale-invariant'. Exploring 2-D and 3-D sand-piles using exactly the same principles, Bak, Tang & Wiesenfeld (1988) found qualitatively identical scale-invariance.

The expressions 'scale-invariant', 'scale-free', 'self-similar' and 'power-law distribution' mean essentially the same thing and we will use them interchangeably in the text.

Thus, we see that sand-pile models naturally produce time-series of events in power-law distributions. Some models or systems which exhibit power-law distributions may be easily characterised as sand-piles however many may not. Also, some power-law behaviours are products of SOC while others are not. Using terminology introduced near the beginning of this section, the presence of spatial self-similarity and 1/f flicker noise are not direct evidence of SOC. In other words, we can't necessarily expect there to be SOC wherever we find power-laws (Sornette 2000). However, it appears that SOC is often very swiftly invoked to provide convenient theoretical explanations for power-laws.

For an example of a phenomenon where it has been conjectured that SOC may be responsible, accretion disks around some galactic objects produce X-ray flares in power-law distributions. (Mineshiga 1994) suggest that this effect is produced by reconnection in disks threaded with tightly

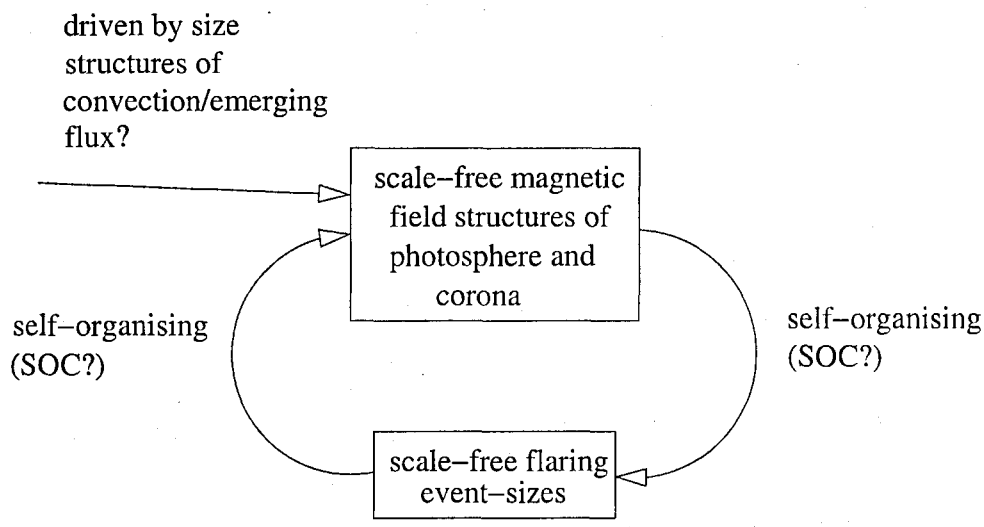

Figure 1.11: Schematic of possibilities for self-organisation of Solar atmosphere.

wound field lines . The concept is that reconnection occurs at a critical threshold and locally heats the disk plasma, thus producing the observed X-rays. Perhaps using a similar mechanism to the production of CMEs, the reconnection reorganises the disk field into the existing disk plus a new topologically distinct region of field. This new region forms into a plasmoid which detaches from the disk, carrying away angular momentum thus allowing further inflow of material.

We see in chapter 2 that Solar flares show power-laws in their distributions of proxies for size, including peak duration, photon count rate, peak energy flux and total energy. These distributions extend over several decades. This data provides a basis for comparison with the synthetic data produced by our models. The models which form the main subject matter of this thesis do not explicitly include SOC behaviour, however we will consider in chapter 5 whether SOC is indirectly responsible for power-laws in our results and whether the models contain elements of SOC.

Considering the real Solar atmosphere, there are several possibilities for the origin of the scale-invariance of the flaring events and size of the flux regions (see section 1.3 below) :

- SOC in the self-interaction of the magnetic carpet and photospheric plasma through reconnection and flux emergence/submergence.
- Solar atmospheric 3-D magnetic field is self-organising into scale-free structures without SOC.
- Solar atmosphere scale-free field is driven directly by scale-free granulation/supergranulation flows from convective zone.

We illustrate these relationships in figure 1.11.

SOC/sand-pile modelling is increasingly a common and popular method for the production of scale-free behaviour in models. We will shortly see an example of a sand-pile model devised to model Solar flaring behaviour.

1.8 Cellular Automata Models.

In contrast with the hegemony of MHD modelling of Solar magnetic field behaviour, our models in this work are cellular automata ('CA') models. CA models are an approach which allows simplification of a problem to its dynamical essence and therefore extended evolution of a model without too onerous use of computer time. The simplification naturally means that physics which is explicitly incorporated into full physical simulations, for example MHD, must be neglected or parameterised for inclusion in a CA. In addition to reduced number-crunching a benefit of this is that if realistic results are obtained by the CA model then it may be true that the detail of the parameterised physics is not an important part of producing the actual physical features of the system.

The study of CAs was initiated by Wolfram (1984). CA models are dynamical systems which are discretized in time and space. The model will evolve through a series of discrete time-steps and will consist spatially of a lattice/grid of cells. We will use 'lattice' and 'grid' interchangeably in this work. Each cell will have one or more parameters associated with it. The updating of the grid each time-step, which is performed simultaneously on all cells, will proceed according to local rules of interaction between neighbouring cells. Non-local interactions are also allowed although the rules of these interactions must be precisely specified. Thus, in general the state of each cell will depend upon the states of itself and its neighbours in the previous time-step. A CA model may be completely deterministic or may include stochastic elements, such as the sand-pile models of Bak, Tang & Wiesenfeld (1988) or forest fire models. CA models have been used to usefully model fluid dynamics, disease aetiology and progress, Maxwell's equations, traffic flows and ecosystems.

The most relevant models previous to this work are those of Lu & Hamilton (1991) and MacKinnon, Macpherson & Vlahos (1996), both of which are CA models.

Following the idea mentioned in section 1.1 that flares are composed of many simultaneous nanoflares Lu & Hamilton (1991) suggest that this postulated nanoflaring behaviour might result from self-organisation of these fundamental units of energy release. Through SOC a flare could be regarded as an avalanche of nanoflares. The model by Lu & Hamilton (1991) is essentially a 3-D sand-pile consisting of a 3-D vector field within a regular lattice. The model makes no statements about the detailed physical origin of flaring events. This is not to say that there is no physics as such within their model. Rather, the physics is embodied within the rules of the model insofar

as magnetic field is represented by the 3-D vector field, and reconnection events are considered be avalanches within a 3-D grid which result in redistribution of the tension within the vector field into the surrounding 3-D lattice.

The local gradient $\nabla|X_s|$ at any site s is defined as the discrepancy between the field at that site X_s and the mean of its six neighbours, $X_{\rm nn}$:

$$\nabla|X_s| = X_s - \frac{1}{6}\sum_{\rm nn} X_{\rm nn}$$

Each time-step the vector field is incremented at a randomly located site by the addition of a random vector. There is a critical gradient, X_c and when addition of a random vector causes a local gradient to exceed this critical gradient then adjustment of the local lattice must occur to reduce the offending local gradient to a value below the critical gradient. Some of the magnitude of the local vector is redistributed to neighbouring sites. Specifically, the rules for the adjustment are as follows :

$$X_s \rightarrow X_s - \frac{6}{7}\nabla|X_s|$$

$$X_{\rm nn} \rightarrow X_{\rm nn} + \frac{1}{7}\nabla|X_s|$$

Thus, although the adjustment reduces the local gradient, it will also increase the gradients in the immediately surrounding cells and so create the possibility that these gradients will exceed the critical gradient. Therefore the initial adjustment is capable of triggering further adjustments. If that is the case then still within the same time-step further adjustments must be carried out and so forth until all gradients are less than critical.

By following these rules the scheme is implicitly conservative of the modulus of the vector field. If we consider X in this model to be equivalent to B then the vector field X represents the magnetic field of the Solar atmosphere and avalanches can be considered to represent Solar flares. By producing a time series of avalanches the model is used to simulate a time-series of Solar flares.

This model is essentially a sand-pile, constructed completely around SOC behaviour, and will move from arbitrary initial conditions to a minimally stable state. Lu & Hamilton (1991) found that the model produced events with power-law distributions in the event-size distributions. MacKinnon & Macpherson (1997) when running this model in a $40 \times 40 \times 40$ grid found that the power-law behaviour persisted over almost five orders of magnitude and that the system robustly settled to the same mean vector field values regardless of whether the model was begun with under-critical, near-critical or over-critical values. MacKinnon & Macpherson (1997) explored this model further, incorporating a facility for remote triggering of avalanches. They found that remote triggering of one

or two sites simultaneously did not alter the event-size distributions, however higher levels of remote triggering destroyed the distributions.

MacKinnon, Macpherson & Vlahos (1996) took a further step back from realistic physics and created a simple CA model without making any statements about the detailed physical origin of flares. The model features the idea that the likelihood of flaring at a site is more favourable if one or more neighbours are presently flaring. We have a 1-D grid where each cell, i, has three possible states :

$$x_i = \begin{cases} 0 & \text{(quiescent)} \\ 1 & \text{(flaring)} \\ 2 & \text{(flared)} \end{cases}$$

All sites begin with $x = 0$. Each time-step each cell is considered and if the state of cell i is $x_i = 0$, and the neighbours of cell i, $(i-1)$ and $(i+1)$ are such that : $x_{i-1} = 0$ and $x_{i+1} = 0$ then there is a probability, p_0 that cell i will change state : $x_i \rightarrow 1$. If however $x_{i-1} = 1$ or $x_{i+1} = 1$ then there is a probability p_1 $(p_1 > p_0)$ of $x_i \rightarrow 1$.

Thus, if a cell x_i has neighbours neither of which have flared, a change in state of $x_i \rightarrow 1$ represents potentially the initiation of an avalanche, where an avalanche is a series of spatially and temporal connected changes of cell-states from 0 to 1. Continuing the analogy with Solar flares, the size of an avalanche is equal to the number of flaring sites within the avalanche. This assumes that each cell flaring is identical, which of course is the case within the model. Where $x_i = 1$ the state of this cell will then be set to 2. Thus $(x_i = 1) \rightarrow (x_i = 2)$.

This means that following the initiation of an avalanche the probability of it being of size N is :

$$P(N) = N p_1^{N-1}(1-p_1)^2$$

In order to avoid arbitrary choice of the value of p_1 and to draw analogy with the expectation that the probability of a flare commencing, given that a nearby flare is presently occurring, will vary across the Sun, MacKinnon, Macpherson & Vlahos (1996) considered p_1 to be a random variable with a flat distribution over $0 \leftrightarrow 1$. They then integrate $P(N)$ over all values of p_1. This gives :

$$\begin{aligned} \overline{P}(N) &= \int_0^1 P(N) \mathrm{d}p_1 \\ &= \frac{2}{(N+1)(N+2)} \end{aligned}$$

$$\propto N^{-2} \qquad \text{as} \quad N \to \infty$$

This power-law index in the avalanche size of -2 is similar to the observed index of flare sizes (-1.5) although not the same. MacKinnon, Macpherson & Vlahos (1996) argue that if a model with the same principles is constructed in 2-D or 3-D then the increased number of possibilities for interaction and triggering between neighbouring cells will reduce the index and bring it closer to -1.5. However, Litvinenko (1998) used branching theory methods to prove that the distribution of avalanche sizes produced by this model is independent of dimension. Also, we might hope that the introduction of non-local triggering of avalanches into this model might move the index closer to -1.5. Non-local triggering however represents a partial increase in the dimensionality of the model therefore the result of Litvinenko (1998) will also foreclose the bringing about of a more favourable power-law by this method.

This model does not require the criticality which the sand-pile model of Lu & Hamilton (1991) explicitly depends upon but instead the one free parameter, p_1, is allowed to take all possible values. Neither is there a need for an explicit conservation law in this model. Like Lu & Hamilton (1991), this model contains no explicit physics, yet its achievement lies in showing that by supposing only that flares are self-organising processes, we can reproduce the broadest statistical feature of flares (power-law distribution with an index close to observations).

We mentioned earlier that Parker (1988) suggested that there are many unobservably small flaring events occurring, which he termed 'nanoflares'. Some researchers have proposed that a continuous background flux of energy released from the magnetic field by nanoflares may be responsible for maintaining the coronal temperature at its level of $few \times 10^6$ K (Parker 1983, Parker 1989, Berger 1993). Hudson (1991) found that if the generally-accepted power-law index of $\sim 1.5 \pm 0.2$ for flare peak energy flux is extrapolated downwards below the observable level then the contribution to coronal heating by nanoflares is insufficient. Further, they found that the energy balance of the corona would be met if the spectral index for the nanoflares is ~ -4. Georgoulis & Vlahos (1996) suggested that below the presently observable minimum flare peak flux, the Solar flare spectral index may increase substantially. If this were so then nanoflaring may indeed be sufficient to maintain the high coronal temperature. Georgoulis & Vlahos (1996) proposed a sand-pile model consisting of a 3-D lattice with a scalar field representing local values of a magnetic field. As in the model of Lu & Hamilton (1991) there is random loading of the field and a relaxation process which occurs when local field gradient exceeds a threshold. The relaxation can occur both isotropically and anisotropically. The introduction of the anisotropic element into the model has the effect of producing a peak flux P.D.F. consisting of a broken power-law. At the upper end of the distribution the spectral index

is $\sim -1.73 \pm 0.05$ whereas at the lower end of the distribution the spectral index is $\sim -3.26 \pm 0.2$. They found that a similar broken power-law was found for flare duration and total flux. Georgoulis & Vlahos (1996) find that the steeper lower end of the distribution contributed more than 90% of the energy released. Georgoulis & Vlahos (1996) concluded that this result supports the hypothesis of coronal heating by nanoflare energy release. In the future more sensitive instrumentation might reveal a region of the peak flux flare distribution with a spectral index steep enough to indicate that nanoflaring is indeed largely responsible for coronal heating.

1.9 Interpreting Solar Flare CA Models as Discretized MHD equations.

We have already discussed MHD and a few CA Solar flare models. The advantages of the CA approach are that we assume there is insensitivity to precise details of the local processes, and therefore we gain no insights into the local behaviour over short time-scales, however we are able to gain an appreciation of the global behaviour over longer time-scales. Classical physical models however, such as MHD models, may elucidate the local processes but offer little help in understanding global dynamics (Isliker et al. 1998).

Instead of accepting a stark choice between either the MHD approach (Galsgaard & Roussev 2002) or the cellular automata approach (Lu & Hamilton 1991) there is perhaps another way of modelling Solar flares. Isliker et al. (1998) considered the model of Lu & Hamilton (1991) and recast that model as a set of discrete MHD equations. Lu & Hamilton (1991), in creating their model, found a general type of system (sand-pile models) which produced the type of dissipative avalanche behaviour observed in Solar flares. By contrast Isliker et al. (1998) have taken a useful model (Lu & Hamilton 1991) and discovered the continuous system which corresponds to that model. In their paper it is clear that in doing so they have also founded a general approach for achieving this.

Basically, the model of Lu & Hamilton (1991) has been recast as the solution to a discretized partial differential equation ('PDE') :

$$\frac{\partial B(x,t)}{\partial t} = \eta \nabla^2 B(x,t) + S(x,t)$$

where we have :

$$\begin{aligned} B &\equiv \text{magnetic field} \\ x &\equiv 3-\text{D space} \\ t &\equiv \text{time} \end{aligned}$$

$$\eta \equiv \text{diffusivity}$$

$$S \equiv \text{source (driving) term}$$

This equation consists of a diffusion term and a source term and is equivalent to the usual continuous induction equation of MHD. The diffusion only occurs when an instability threshold is met. The source term provides the random driving of the vector field.

This recasting allows for the interpretation of the CA model of Lu & Hamilton (1991) by examining the continuous PDE.

The PDE has a stable mode and an unstable mode. During the stable mode the equation reduces to :

$$\frac{\partial B(x,t)}{\partial t} = S(x,t)$$

and describes behaviour in a convective regime.

If the Laplacian, $|\nabla^2 B|$, exceeds a certain threshold then the induction equation reduces to :

$$\frac{\partial B(x,t)}{\partial t} = \eta \nabla^2 B(x,t)$$

which represents behaviour in the diffusive regime. The time-scale of the source term, S, is much longer than that of the diffusive process, and the term is therefore neglected.

As Isliker et al. (1998) explained, this approach is based upon assumptions : (1) every instability (flare) has the same diffusion time and length-scale; (2) diffusion occurs within a bounded region of the same size for each instability, and (3) the convective term can be replaced by a simple random driving function.

This approach produces in effect a hybrid model, where we understand the physics explicitly, but we can also see that the global behaviour is an avalanche phenomenon.

Isliker et al. (1998) considered how the approach may be carried further after the introduction of meaningful units into the model :

1. We can enquire as to whether the level of diffusion required for SOC in the model is physically reasonable.

2. We can calculate the magnetic energy released during avalanches.

3. we can compare the released energy with the input from the driving.

They also consider how the CA model may be made more physical by the modification of the CA rules. Thus, we can see that by following this approach the rules of CA Solar flare models in general may be improved by inclusion of insights from MHD.

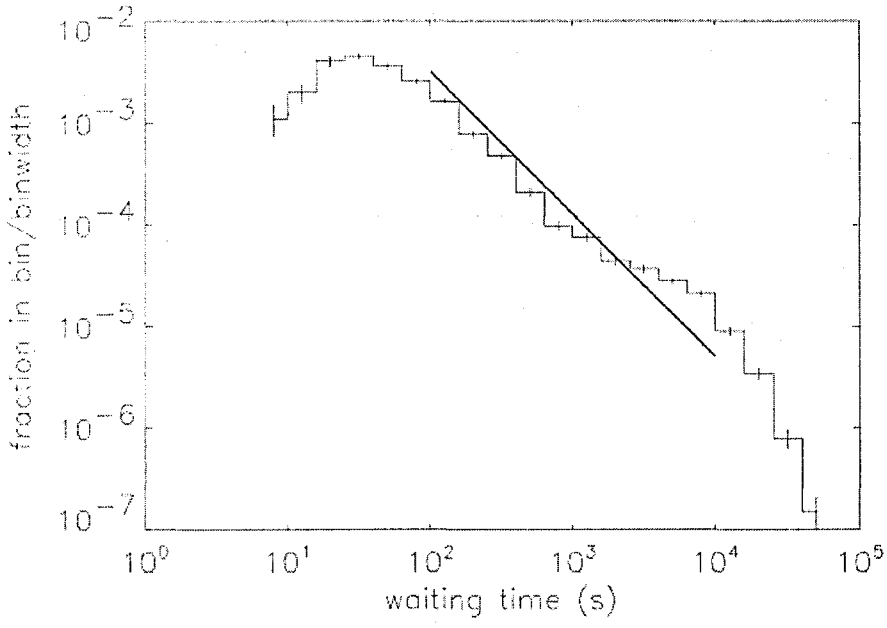

Figure 1.12: Waiting-time distribution for the ICE flare data. A power-law fit for the range $10^2 \rightarrow 10^4$ s is shown. Wheatland, Sturrock & McTiernan (1998)

Isliker et al. (1998) have shown that a simple CA model may be equivalent, and understood in terms of, a physically meaningful classical model. Given that each of these provides insights that the other cannot, Isliker et al. (1998) hope that this work may eventually lead to the creation of models explicitly incorporating these two approaches and capable therefore of illuminating both the local and global behaviour.

1.10 Solar Flare Waiting-Time Distributions.

We have already noted the property of self-similarity of Solar flares as evidenced by the power-law nature of flare-size distributions (Crosby, Aschwanden & Dennis 1993, Bromund, McTiernan & Kane 1993 and Pearce, Rowe & Yeung 1993). Let us now consider the waiting-times between flares. Wheatland, Sturrock & McTiernan (1998) analysed the waiting-times amongst eight years of hard X-ray burst data obtained by ICE. They considered the time of an event to be the time of peak-flux. Figure 1.12 shows the distribution of waiting-times obtained from this data. The plot suffers from a deficit of larger waiting-times owing to gaps in the data. Additionally, there are likely to be small events lost because their peak fluxes were swamped by emission from previous events. This may be responsible for the turn-over below $\approx$ 30 seconds. There appears to be a power-law fit over $10^2 \leftrightarrow 10^4$ seconds (gradient $\approx$ -1.4).

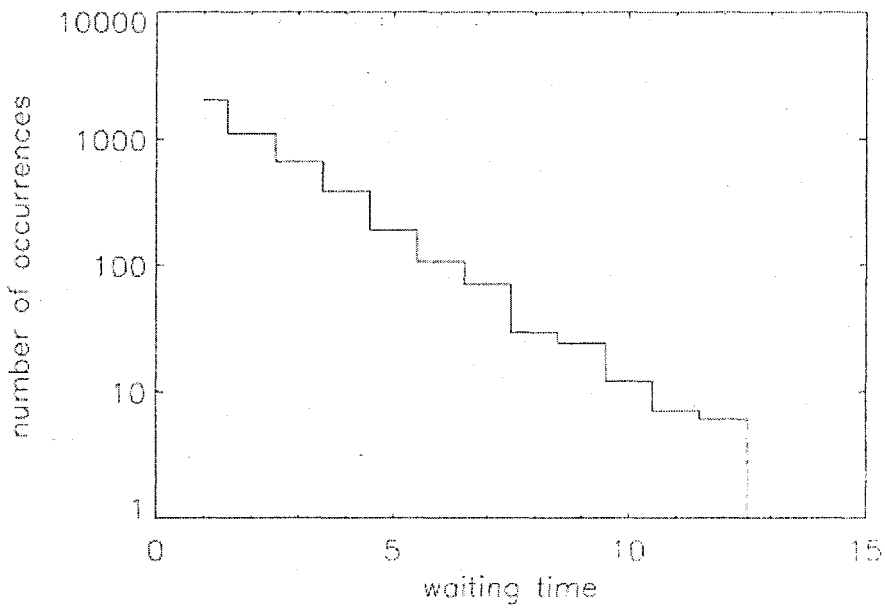

Figure 1.13: Waiting-time distribution for the avalanche model. The x-axis is in units of the time step of the model. Wheatland, Sturrock & McTiernan (1998)

Now, considering sand-pile models, there is no memory of the previous avalanche contained within the present avalanche and therefore the events/avalanches generated by sand-pile models are independent events. Wheatland, Sturrock & McTiernan (1998) explain that sand-pile models represent Poisson processes and therefore the distribution of waiting-times between events in a sand-pile model will follow an exponential law :

$$P(\Delta t) = \alpha e^{-\alpha \Delta t}\left(1 - \frac{\Delta t}{T}\right)$$

where we have,

$$\begin{aligned} \Delta t &\equiv \text{waiting} - \text{time} \\ \alpha &\equiv \text{constant} \\ T &\equiv \text{observing time} \end{aligned}$$

Wheatland, Sturrock & McTiernan (1998) used the 2-D sand-pile model of Bak, Tang & Wiesenfeld (1987) to generate a waiting-time distribution for 10^5 time-steps of the model. During this time there were almost 5000 events. Figure 1.13 shows this distribution, clearly exponential, thus confirming their derivation of the above waiting-time PDF.

Wheatland, Sturrock & McTiernan (1998) compared their analysis of ICE hard X-ray burst data

with the sand-pile-derived simulated data and found an over-abundance of short waiting-times. These short waiting-times suggest that occurrence of one event is likely to trigger another event which will therefore follow the first closely. The short waiting times thus imply inter-dependence of events.

It appears thus that hard X-ray bursts are not independent and that sand-pile modelling is incapable of explaining this inter-dependence of small events. Given that the ICE data which they used contained no spatial resolution, Wheatland, Sturrock & McTiernan (1998) comment that it would be interesting to use data obtained by an instrument with spatial distribution, such as that obtained from YOHKOH, to determine whether the events following short waiting-times and their preceding events originate from the same area of the Sun (this is called 'sympathetic flaring').

Suggesting a simple 1-D MHD model, Galtier (2000) was able to produce a distribution of waiting-times (gradient $\approx$ -2.3) compatible with the observed waiting-time distributions determined by Boffetta et al. (1999) (gradient $\approx$ -2.4). The model of Galtier (2000) treats loops as magnetic lines and events are generated as shocks. Each burst of Joule dissipation signals an event, and thus waiting-times are considered to be times between these dissipation events. The model is able to reproduce other Solar flare properties, such as peak flux distribution.

Figure 1.13 shows the distribution obtained for waiting-times. Galtier (2000) takes the view that the plot shows that events are not independent, and that the recovery of the power-law gradient compatible with the results of Boffetta et al. (1999) indicates that non-local interactions are important in MHD phenomena. Galtier (2000) explains that the 'overlapping of dissipative events appears as a natural property of the 1-D MHD model', and that this fact, together with obtaining the correct power-law index and the 'strong time-correlation of flares' should be tests for all flare models : tests which sand-pile models are not generally able to pass.

1.11 Statistical Prediction using Artificial Neural Networks.

Most of the work we discuss in the Introduction represents attempts to determine, or test, theories of mechanisms which explain the energy release processes occurring in the corona and/or photosphere. When these processes, such as flux emergence, or reconnection in coronal loops, are observed by our instruments, that data may not contain in itself all the information necessary to explain the underlying mechanisms. There will probably also be noise and other statistical randomness within the data (Conway 1998). Some researchers have therefore considered whether, in a statistical sense, Solar behaviour might be understood in terms of itself rather than always assuming the existence of an underlying cause.

Sunspot number is a simple proxy for the level of Solar activity and consists of a time series. In

fact, the sunspot number, recorded daily since 1848, is the longest continually-recorded time series. As explained by Conway (1998), accurate prediction of sunspot number would be useful in many ways, including (1) Solar satellite mission-planners need to know when Solar maximum will occur, and (2) Solar storms can damage satellites and terrestrial electrical systems and therefore protective measures would ideally be based upon accurate and timely foreknowledge.

During the period since 1848, the Solar magnetic field has exhibited an eleven-year periodicity. At 'Solar minimum' there is a clearly definable, generally poloidal, global field. There is a gradual change to a more active and disrupted field, flares and coronal mass ejections ('CME') occurring more frequently and higher daily sunspot numbers. Five or six years after Solar minimum, the field is highly disordered and energetic. This is 'Solar maximum'. During the following five or six years there is a gradual calming of the field and a return to Solar minimum. The polarity of the global field post-maximum is however opposite to that of the pre-maximum phase. Thus, every approximately eleven years there is a field reversal, and the Solar cycle can be regarded as a cycle of twenty-two years periodicity. This periodicity is known as the 'Solar cycle'.

Conway (1998) has taken the sunspot number and applied neural network techniques to the problem of predicting the profile of the rise and fall of the sunspot number during the next (now present) maximum (cycle 23). Such techniques are used in the following way. Let us suppose we have a time series of a single output of a system, $t_0, \ldots t_k$, and we are interested in predicting further values of this parameter, $t_{k+1}, t_{k+2}, \ldots$. We can input into our neural network the known time series up to and including t_k and expect it to give us predicted values for this parameter, $t_{k+1} \ldots$. Thus, the predictions are based entirely upon the already known time series and are not derived from any knowledge of the underlying physics.

Neural network techniques may vary considerably in detail but all are broadly similar in operation. We take one output node and a number of input nodes.

Let a, b be the input nodes, and c the output node. Also, w_a and w_b are the input weight connections of these nodes (see figure 1.14). The state of the neural network is contained within the values of the input weight connections. Initially, values for these are chosen fairly arbitrarily then the network is trained by exposing it to input values (the 'training set'), comparing its output to observed values, calculating the error and iteratively changing the input weight connections until this error is minimised. At some point during this minimisation we will find that, when compared with some other independent data set, the error reaches a minimum then begins to increase. This occurs when the input weight connections pass their optimum values. The neural network has begun to lose its generalisation ability and is learning the training set too closely, in the same way that a

schoolchild, having learned examples of solutions to mathematical problems by rote, would be unable, upon taking a difficult examination, to adapt to the new problems requiring solution. If he/she had instead gained an understanding of general principles then he/she would be able to tackle the new problems in a meaningful way.

The value of the output node is given by: $c = g(w_a + w_b)$ where $g(x)$ is the 'input activation function', increasing with x but saturating to finite values as $x \to \pm\infty$.

We calculate the error using a least-squares method :

$$E = \sum_{i=0}^{N} \left(c\left(a_i, b_i\right) - C_i\right)^2$$

We carry out the following procedure :

1. Randomly choose values for w_a, w_b.
2. Evaluate $c(a_i, b_i)$ for all i (table 1.3 shows example values).
3. Evaluate error, E.
4. At present point (w_a, w_b) evaluate :

$$\frac{\partial E}{\partial w_a} \quad \text{and} \quad \frac{\partial \mathrm{E}}{\partial \mathrm{w_b}}$$

5. For small change, ϵ, calculate new values of w_a and w_b :

$$w_a \to w_a - \frac{\partial E}{\partial w_a}\,\epsilon$$
$$w_b \to w_b - \frac{\partial E}{\partial w_b}\,\epsilon$$

6. return to point 2 until values of w_a and w_b have converged such that E is minimised.

Conway (1998) clarifies that there has been some limited success in making predictions using neural networks, however these techniques suffer from a number of inherent problems, such as systematic delays in the predicted times of peak sunspot number. Prior to this work there had only been 13 complete Solar cycles and the capability for training the neural networks was limited by this insufficiency. Feed-forward neural networks used by Conway (1998) made predictions of the year 2000/2001 Solar maximum based upon sunspot numbers throughout cycles 20 and 21. The quoted uncertainties of these predictions had a confidence of 80%.

As explained by Conway (1998), we cannot be certain that the Solar cycle is a stationary time series rather than a temporary transitional part of a longer time-scale chaotic behaviour. If this is the

i	a_i	b_i	$C_i(a,b)$
0	8	9	7
0	8	9	7
1	2	7	3
2	6	4	3
⋮	⋮	⋮	⋮
N	8	9	1

Table 1.3: Example training set for a neural network. Example values: i; input nodes: a, b; observed values: C.

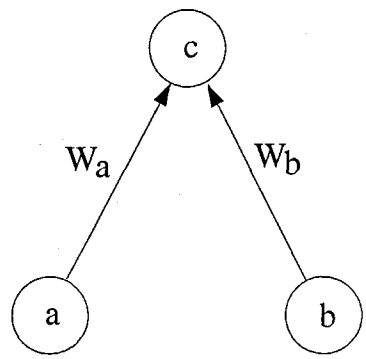

Figure 1.14: Schematic diagram of simple neural network. Input nodes: $a, b.$; output node: c; input weight connections: W_a and W_b.

case then we cannot expect artificial neural networks to be able to predict future sunspot numbers well, or at all. Certainly, given the difficulty in obtaining correct predictions from neural networks, it may be the case that the time series will be found to be non-stationary.

We might wonder whether predictive techniques not based upon any understanding of the underlying physics but instead upon historic time series are able to make better predictions than intuitive guessing by human beings? In fact, Conway & Brown (1999) made a non-rigorous attempt to answer this question. Briefly, they gave a series of training data sets to seven individuals who attempted to make predictions. Individually, the standard of the human predictions varied, though none surpassed the neural network method. The individuals were also averaged to produce a prediction by 'committee', and this also was found to be no better than predictions by neural network.

1.12 Isliker Effect.

Isliker & Benz (2001) explored a systematic biasing of data which has some bearing on the understanding of our data in this present work.

Isliker & Benz (2001) performed an analysis of narrow-band radio spikes during a Solar flare. They took this very high resolution data and artificially worsened the temporal and frequency resolution. They then showed that the values of the peaks obtained will not coincide with the actual peaks within the time-series and that this will give erroneous distributions for low and high flux values. In particular, this error arises where we are attempting to obtain peak flux values from time-series data and the peak flux values are in a power-law distribution. The time-series is integrated or sampled using low temporal or frequency resolution.

Isliker & Benz (2001) also provide an analytical explanation of the dependency of the biased peak flux distributions upon the temporal/frequency resolution used.

In qualitative terms the reason for this bias is that the actual peaks within the data will invariably lie between the time/frequency points where the data was sampled/integrated and the sampled/integrated data cannot therefore give the true locations of these peaks. Thus, there is likely to always be a discrepancy between the magnitude of the true peaks and the measured peaks.

More specifically, Isliker & Benz (2001) found that the biased distribution may be near to the true distribution apart from two effects :

1. At high values of peak flux, there is a change from power-law to exponential distribution, i.e. a faster fall-off at high flux values.

2. At low values of peak flux the true distribution is extended into a completely artificial, elongated and relatively flat region.

These are illustrated schematically in figure 1.15.

As we will see later, the continuous model (described in chapter 3) generates a time-series of energy release rate data at the rate of one value per time-step. This is then sampled by taking every tenth value and it is from this time-series that event-size distributions are produced. We would therefore expect the Isliker effect to cause a biassing of the distribution profiles.

The effect will also cause a distortion of our distributions of cell parameters, such as B and ϕ. The reason for this is less obvious but we shall explain why this is the case. In the continuous model in respect of any particular parameter a single value only attaches to each cell, where each cell represents a 1-D section of fluid with finite length. In real fluid we would find a continuum of values whereas in the model this single value is assumed to encapsulate the complete range of values for

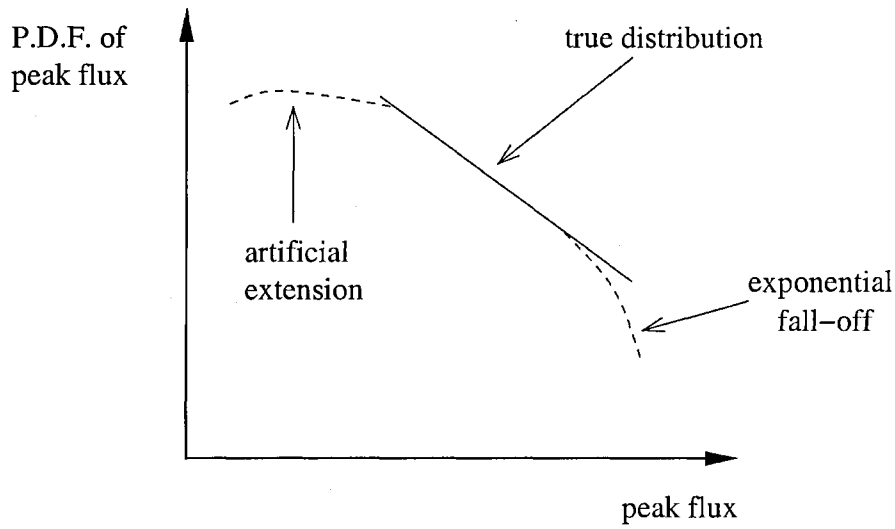

Figure 1.15: Schematic of systematic biasing effects found by Isliker & Benz (2001).

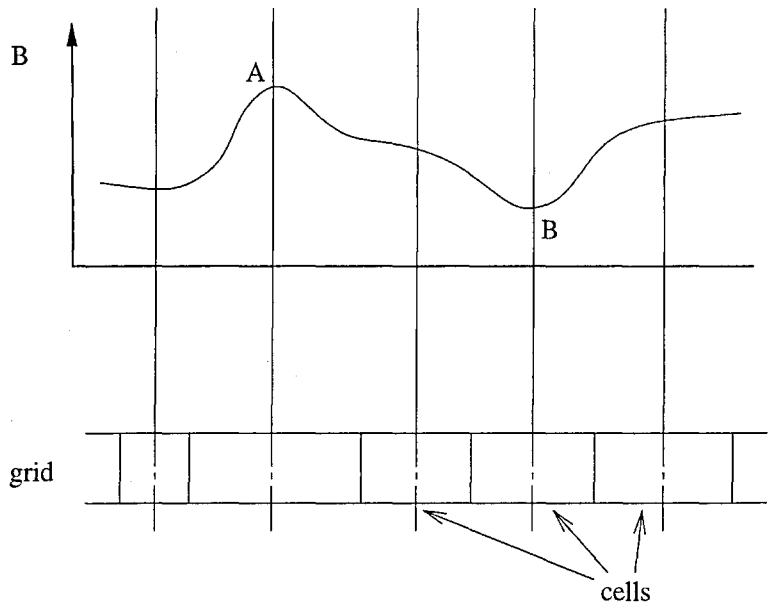

Figure 1.16: Schematic of relationship of Isliker effect to cell parameter values. Isliker & Benz (2001).

the cell in question. If we assume that there is a real continuous fluid underlying the CA grid then figure 1.16 illustrates the problem for the magnetic flux density. The values which the model uses will in some sense be related to the values at the intersections between the curve and the centre-lines of the cells. The field density at point A clearly gives an over-estimate whereas that at point B gives an under-estimate. In a sense the parameter values represent a sampling of the true underlying field and will therefore be subject to the effect discussed by Isliker & Benz (2001).

Chapter 2

Discrete Model.

"I guess one of the reasons that I've never been a very good private detective is that I spend too much time dreaming of Babylon."
Richard Brautigan.

2.1 Introduction.

MacKinnon, Macpherson & Vlahos (1996) and others have used 1-D lattice models with highly simplified physics and/or highly formalised behaviour. Few of these models, however, explore the relevance of the magnetic field connectivity. In this chapter we present the discrete model which we developed in order to explore this aspect of the magnetic field. The discrete model consists of a 1-D lattice and includes a simple field connectivity, whereby each cell is either connected to another cell or unconnected. Figure 2.1 illustrates this idea. An idealised form of reconnection occurs between cells and new field connectivity is generated in order to simulate the emergence of magnetic flux occuring within the photosphere. Other than these, there are no features within the structure of the model. We allow the model to run and we count the rate at which reconnection events occur within the model. We also take snapshots of the lattice when a steady-state has been reached. We produce distributions of event-sizes and loop-sizes. We can thus investigate the importance of the field connectivity to the distributions of events and size structure of the field.

We will here describe this model in detail and present the results generated by it. We will compare these results with Solar behaviour and finally, leading us into the next chapter, touch upon

the limitations of this model.

Now, we should firstly address the meaning of discrete and continuous in this context. The model consists of a finite number of interacting cells however, we are not concerned with the model being discrete in this sense. Rather, by 'discrete' we imply an absence of parameters attached to the cells which take non-integer values. Each cell is identical and has only two features : attachment to a magnetic field line and a velocity. 'Discrete' here means that (1) the attachment to a field line takes one of five states, and (2) the velocity of a cell does not vary along the cell (there is no notion of cell length) but is a single value attached to the whole cell. In chapter 3 we will make clear in what sense the continuous model is 'continuous'.

While the continuous model is Lagrangian, this present discrete model is Eulerian. This distinction is explained more fully in section 3.2.2. Eulerian in the present model implies that the cell boundaries are fixed in absolute space and do not follow the motion of fluid moving around the model. Our points of reference are not attached to bundles of fluid, but rather we consider that fluid moves across the points at which we record data in our model. These points are the footpoints of the field lines. In fact, this classification is misleading here since there is no notion of fluid motion occurring within the model but only of magnetic flux emerging, and disappearing through reconnection or submergence.

The discrete model is built upon the premise that the topology of the atmospheric magnetic field, ranging from the magnetic carpet (Parnell 2001) to the coronal field, and its self-interaction, is the most important determinant of its magnetic reconnection and energy-release events. Also, we expect that the photospheric footpoint of any field line will be tied to the Solar gas and be passively dragged by the photospheric convective motions until moved into a supergranular boundary where the field line will eventually meet and annihilate with oppositely-directed flux (Simon, Title & Weiss 2001). Thus, moving within the photospheric surface velocity field produced by convection, we expect the part of the field lines existing above the photosphere to become increasingly knotted and braided as a function of time. Current sheets will appear between regions of opposite magnetic polarity and consequently the 'frozen-in condition' (see the Introduction) will break down allowing magnetic reconnection to occur between these regions of opposite polarity magnetic flux.

The model is designed to be as simple as possible for clarity and understanding of the bare bones of the problem. The discrete model is comprised of only two aspects : a velocity field and magnetic connectivity.

2.2 Magnetic Connectivity and Reconnection.

Magnetic field lines are connected to the cells, and each line may be open or closed. 'Open' lines connect to only a single cell, whereas 'closed' lines connect pairs of cells. Each field line, whether open or closed has a direction associated with it and this direction has two states : upwards or downwards. Where we have a closed field line, for continuity of direction along the line, the direction (we call this 'polarity') of the line will appear to be upwards at one end and downwards at the other.

Each cell in the model is connected to a field line in one of the following ways :

- connected to a closed field line with 'upwards' polarity.
- connected to a closed field line with 'downwards' polarity.
- connected to an open field line with 'upwards' polarity.
- connected to an open field line with 'downwards' polarity.
- not connected to any field lines.

We can accept having unconnected cells in the model for the following reasons. Let us consider instruments performing observations of Solar flaring activity, such as the Reuven Ramaty High Energy Solar Spectroscopic Imager ('RHESSI'), for instance. We would expect that there would be small flares which fall below the time resolution of the instrument and could never therefore be resolved despite high spatial resolution. Thus, there will be a succession of (spatially small) short-lived events which go unobserved.

Figure 2.1 shows a snapshot of a section of the grid during a model run and we can see the connectivity described, shown by many closed field lines and nested loops. All loops are adjacent or nested with no crossing lines. Field lines in real 3-D space cannot cross therefore we do not allow crossing of field lines in this model. The model is 1-D in the sense that it consists of a 1-D lattice of cells, however there is non-local connectivity between cells, and this indicates dimensionality greater than one, but less than two.

When the model is allowed to run, an annihilation process analogous to reconnection is allowed to occur between adjacent cells of antiparallel magnetic flux. As mentioned in section 2.3, reconnection may only occur between cells i and $i+1$ when $v_i - v_{i+1} > 0$. This process is illustrated in figure 2.2. Adjacent cells which have anti-parallel flux are deemed to become connected to each other and their partners become connected to each other. If the antecedent field lines consisted of two loops, the configuration will change to two different loops using the same cells, as we can see in figure 2.2. Then (still within the same time-step) the new loop formed from the two initially adjacent cells

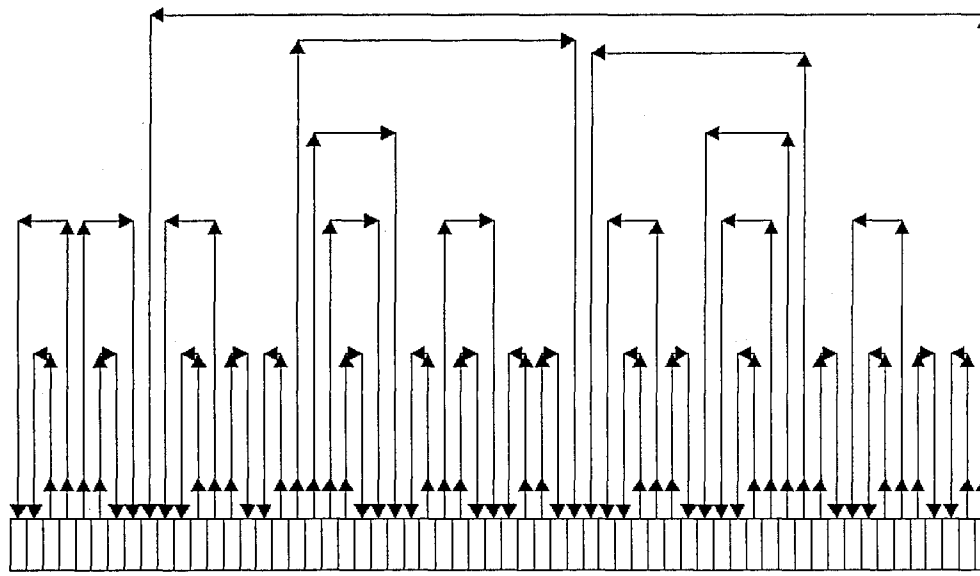

Figure 2.1: Example section of the grid during a run. Shows connectivity of field lines.

will be deleted. The cells will thus become unconnected. This is equivalent to the annhilation and submergence of magnetic flux and is shown in part (c) of figure 2.2. On the actual Sun, we find that submergence of magnetic flux occurs at sites of cancellation by reconnection (Harvey et al. 1999). For this reason in the model we will submerge a new closed field line created by reconnection. Where we have reconnection between an open field line and a loop, the process will produce a new loop, and the point of attachment of the open field line will change. The loop will then submerge. This is illustrated in figure 2.3. Similarly, two adjacent open field lines will reconnect with one another then submerge, as shown in figure 2.4. A detail we have not yet mentioned is that the occurrence of reconnection is conditional upon the velocity field. This will be explained later. Where one loop (or open field line) reconnects with another loop (or open field line) we will call this a 'reconnection event' and it represents a unit of energy-release.

Thus, we have simplified the problem of studying the connectivity of the Solar magnetic field. Physics has been stripped away and reduced to simple local rules governing the behaviour of the cellular automata.

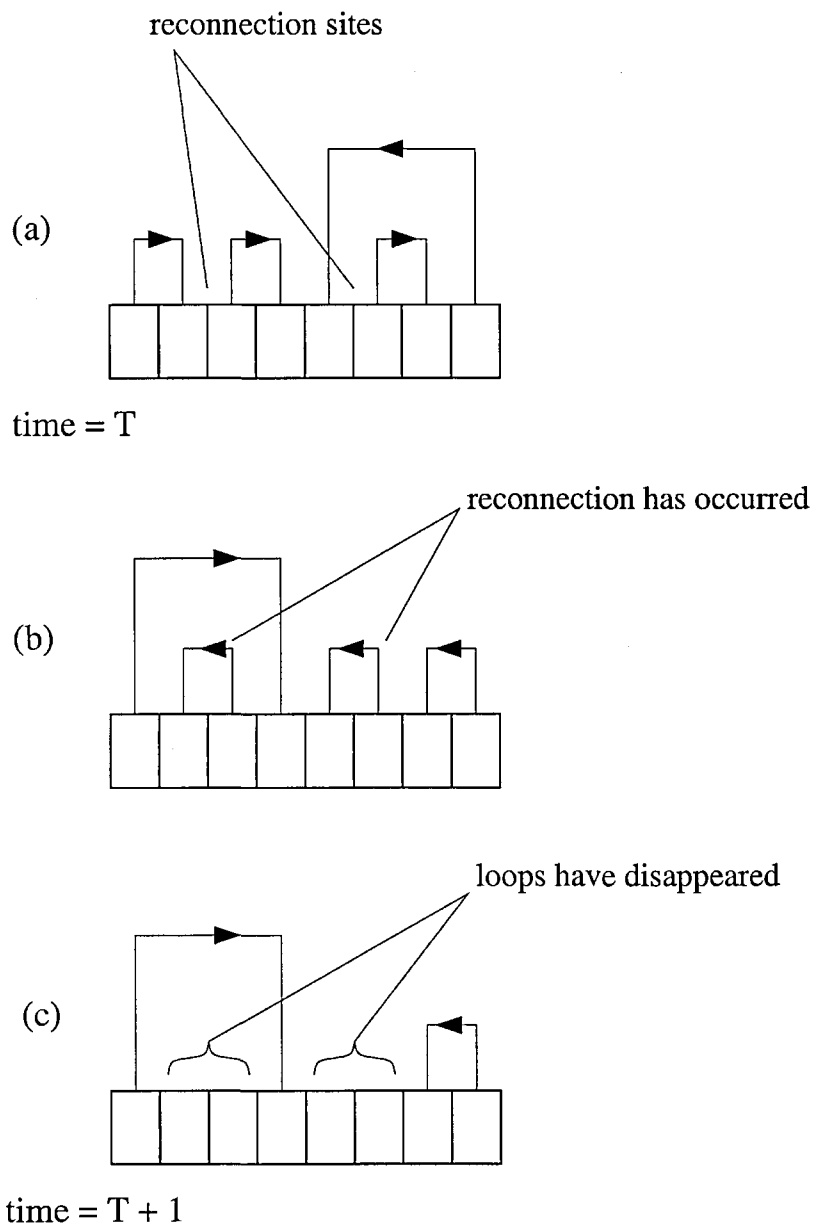

Figure 2.2: Formalised magnetic reconnection process (loop - loop).

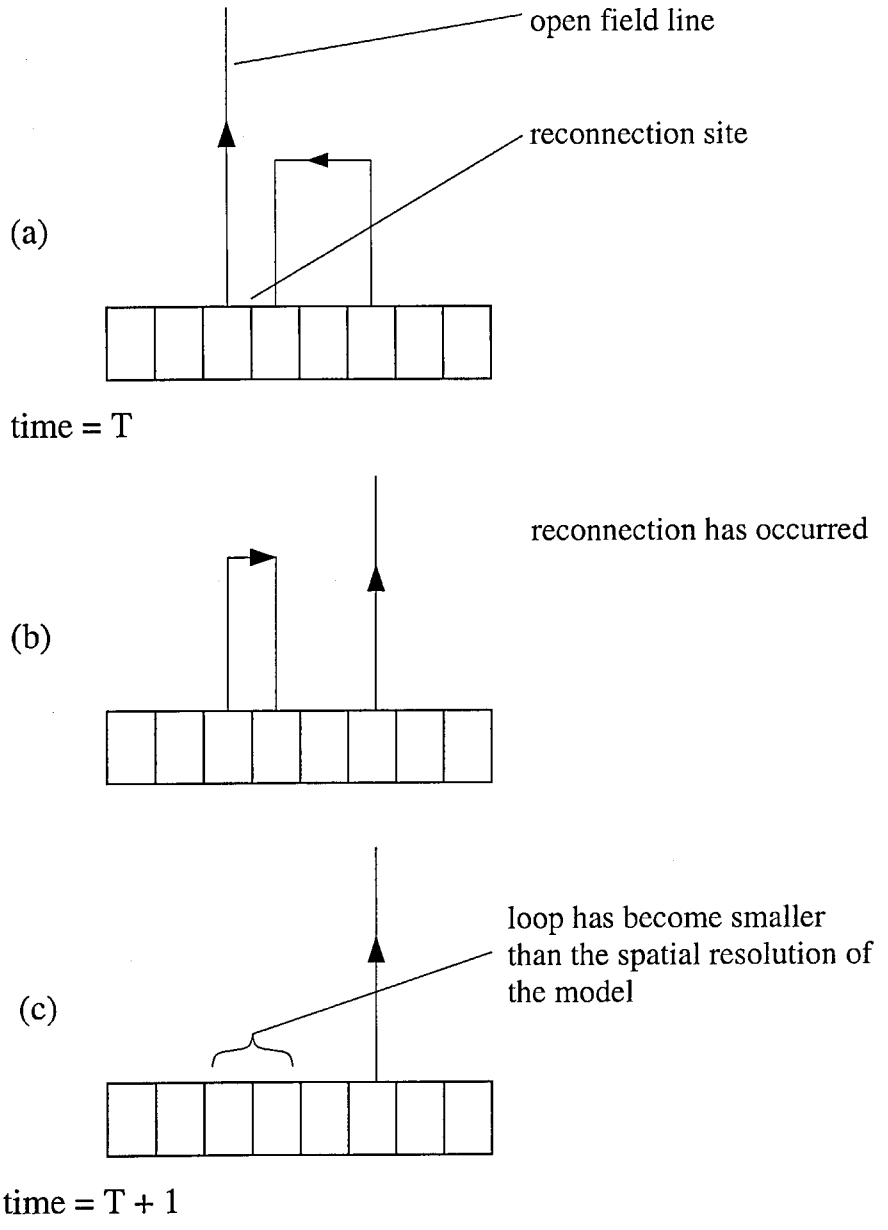

Figure 2.3: Formalised magnetic reconnection process (loop - open field line).

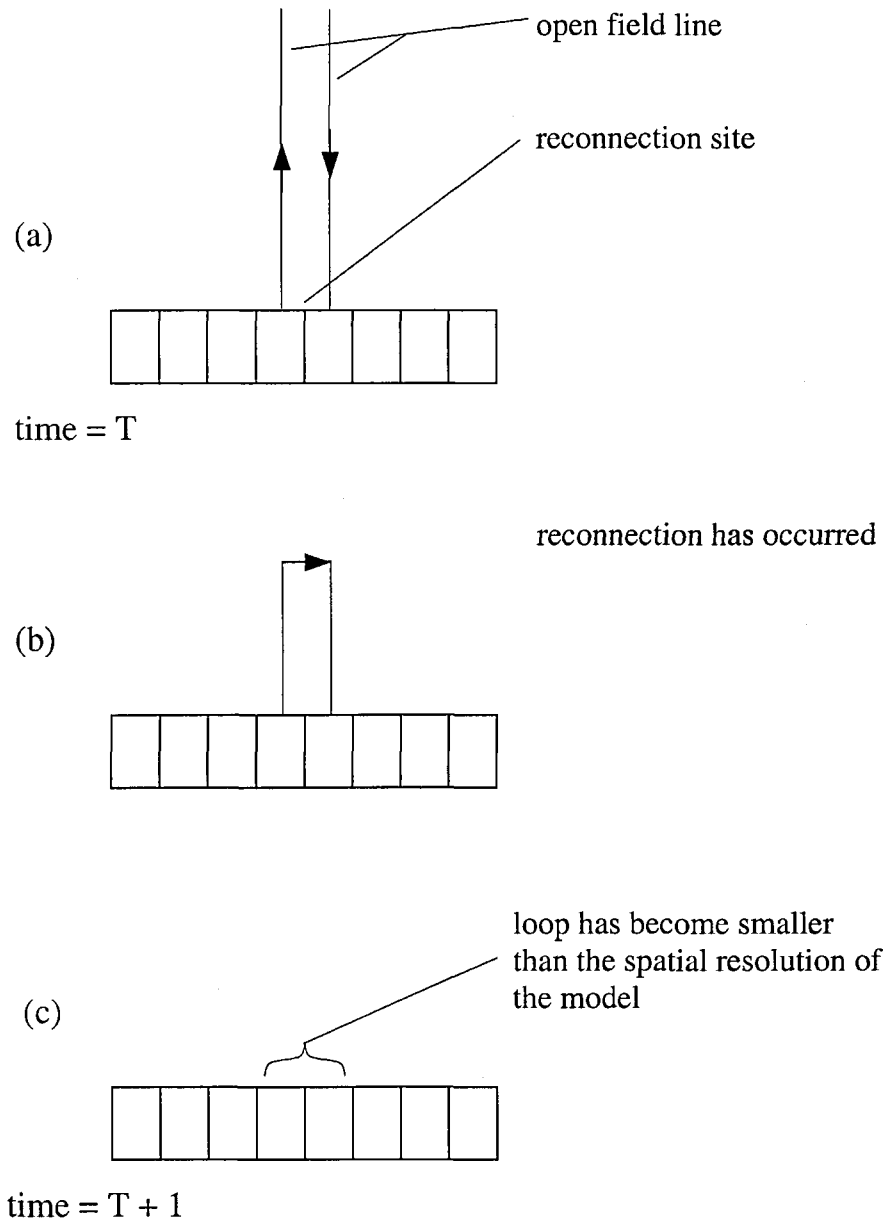

Figure 2.4: Formalised magnetic reconnection process (open field line - open field line).

2.3 Velocity field

The model is strictly 1-D and therefore cells cannot exchange positions or move relative to one another. Therefore in order to represent the confluence and separation of magnetic flux we establish a velocity field within the model. The way that this is achieved is as follows. A velocity is assigned to each cell of the model. This value is randomly generated in the range $-1 \leftrightarrow +1$ according to a uniform random distribution and represents motion parallel with the grid. Cell i has velocity v, defined such that $v > 0$ indicates motion towards cell $i+1$. Thus, we find that $v_{\rm i} - v_{\rm i+1} > 0$ indicates that cells i and $i+1$ are approaching one another. We take the view that compared with a state where $v_{\rm i} - v_{\rm i+1} < 0$ (cells i and $i+1$ are separating) the fact of the two cells converging enhances the likelihood of magnetic reconnection occurring between them. This idea is incorporated into the model by making reconnection between cells i and $i+1$ conditional upon $v_{\rm i} - v_{\rm i+1} > 0$. The velocity field is evolved with time and this is accomplished by re-assigning random values to each cell every timestep.

2.4 Emergence of Magnetic Flux.

Each time-step, after the reconnection process has been performed, a number of closed field lines sufficient to maintain the grid with its initial complement of field lines are introduced into the grid. The footpoints of the lines are given random locations and random polarity. Again, no field lines are allowed to cross. Given that the reconnection of field lines depends upon their polarity and proximity, this emergence and submergence of field lines represents stochastic excitation of the grid. By analogy with the Solar magnetic field there is conservation of magnetic flux with fresh flux appearing randomly across the surface.

2.5 Initial State.

Prior to running the model is given an initial state. 75% of the cells are deemed to be attached to a field line, of which 5% are open field lines. The locations of the open lines are random, as are the pairings of the remaining cells. The random generation of pairings follows the rule that the field lines must not cross. It is necessary to leave 25% of the cells initially free from field lines otherwise the finding of an intial state becomes a non-trivial problem.

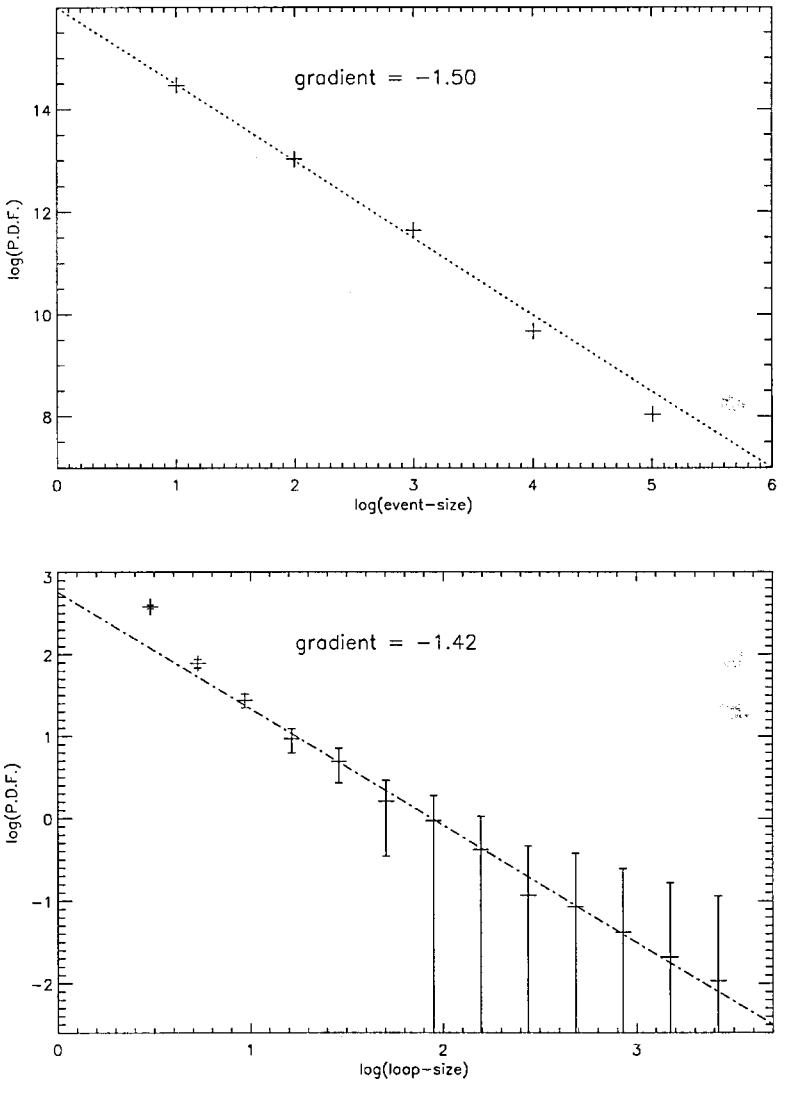

Figure 2.5: Top: probability density function of event-sizes (number of reconnection events occuring per time-step); y-axis gives log(normalised frequency); error bars are too small to be visible; bin-size = 1. Bottom: probability density function of loop-lengths; y-axis gives log(normalised frequency); bin-size = 0.245 .

2.6 Running the Model and Results.

The model consists of 5000 cells. In choosing this number of cells we have balanced the running time with the need for a sufficient number of cells for viable data when counting loop-sizes and number of reconnection events.

During a run we count the number of reconnection events which take place during every successive period of 100 time-steps and consider this to be the 'event-size'. Therefore we are assuming that events are correlated over model timescales of at least 100 time-steps. There is no physical length scale embedded in the model therefore if this were real data we would assume that the reconnection events represented are proximate enough for our instruments to only detect the total energy-release in a given time interval. Alternatively, we might consider that the physical region is sufficiently small that we would expect only a single event at any one time. Thus, we create a time-series of the energy-release rate. Also, if we stop the run at a point after it has settled to a steady state where the energy-release rate has become approximately a stationary time-series, we can count the number of loops of various lengths and thus obtain a size distribution for these. Thus, we can produce probability density functions for both loop-size and event-size. Figure 2.5 shows these. Regarding the upper plot, the quantity of data was sufficient for the error bars to be sufficiently small that they are not visible on this plot. Regarding the lower plot, the left-most point at log(loop-size)=0.48 appears to suffer from an edge effect and we have therefore ignored it in the line-fitting. During any individual run, the relatively few number of cells results in poor statistics, hence the large error bars which resulted. The line-fitting was performed using the least-squares method. It is known that Solar flaring events follow power-laws in distribution (Crosby et al. 1998, Datlowe, Elcan & Hudson 1974, Aschwanden, Dennis & Benz 1998), the index of which depends on the particular parameter considered. Thus, this highly simplified model is capable of producing power-laws extending over several orders of magnitude in both event-sizes and in loop-size within the grid.

Events produced by the model are of discretized size and by definition have a minimum size of two cells. Theoretically, the maximum event-size equals the length of the grid, though this is unlikely to be reached. Thus there is no intrinsic length-scale other than the minimum event-size and quanta of length (one cell), and we therefore expect that the distribution of event-sizes would be power-law, which is what we see.

There is another reason why we might expect to find power-law distributions produced by this model. In the context of this present model let's recall our discussion of self-organised criticality in the Introduction. In general terms, for SOC we require that the system consists of units which are driven by some form of stochastic forcing, the existence of a threshold, and that when the threshold

is exceeded there is a redistribution or adjustment. In the discrete model we appear to satisfy these requirements : (1) the positions of cells with oppositely-directed field lines are randomly driven by the flux emergence process, (2) a qualification for the occurrence of reconnection, the threshold in effect, is that of the flux between two adjacent cells being anti-parallel, and (3) when reconnection occurs there is a reorganisation of the field lines resulting in a cancellation of the two reconnecting oppositely-direct field lines. It is arguable that the structure of the model exhibits SOC behaviour and produces power-law distributions for this reason.

This extremely simple model has displayed behaviour consistent with the broad properties of Solar activity. However, it has limitations insofar as there is no realistic fluid behaviour or thermodynamic properties and the reconnection has no notion of time-scale or length-scale. Also the intrinsic scale (one cell) and units of energy release are discrete. It is in the spirit of trying to take this model to a more useful level, with enhanced comparability to real observations, that the continuous model was developed, which we will describe in chapter 3.

Chapter 3

Continuous Model.

"I bought me a Chevy
it's as big as a whale
and it's about to set sail."
The B52's.

"If I didn't dream of fish I dreamed of money."
John Fante.

3.1 Introduction.

As discussed in the Introduction, a variety of models, such as those of Macpherson & MacKinnon (1997) and Lu & Hamilton (1991), have been developed to explore ideas of triggering of flares. These particular models, and others in the field use simple 1-D, 2-D or 3-D lattices and highly simplified physics. By contrast, magnetohydrodynamics produces highly detailed physical simulations of the behaviour of plasmas. There thus seems to be a lacuna in this modelling schema which we have attempted to fill with the 'continuous model' presented in this chapter. There are in fact few models which use simple lattices and simple, but plausibly realistic parameterised physics. We have attempted here to minimise the physical rules, but still to maintain plausible physicality. The continuous model consists of a 1-D lattice of cells containing atomic gas. Gas does not move across cell boundaries but instead the cells will adiabatically expand and contract, the boundaries remaining

tied to the gas. As explained later, this is a Lagrangian approach. The key features of the model are : fluid behaviour of the 1-D lattice, flux emergence and submergence and parameterised reconnection. The model contains and models thermodynamic properties, magnetic flux, flux density and energy released by parameterised reconnection. There are also other features such as thermal cooling of the top surface of the lattice and addition of noise to the pressure field. Mass, energy and magnetic flux are conserved quantities.

The previous chapter presented and explained the first model, the discrete model. We discussed the limited dynamic range and physicality of the model. The simplicity of the concept was however one of its appeals, and it is practical to begin with a highly simplified model in order to capture the main behaviours of a complex system.

The continuous model was created from the need to extend the dynamic range and features of the discrete model. The model is continuous spatially although discrete temporally, evolving through a succession of discrete time-steps. The continuous model uses continuous values for all parameters. This allows event-sizes to take dynamic ranges of many orders of magnitude. The continuous model also differs from the discrete model in that meaningful physical units are introduced and the cellular automata rules are more physical and consistent with 1-D fluid laws.

In order to remove avoidable edge effects we use a periodic grid. This also allows the preservation of the total length of the grid. The grid is a 1-D layer of cells 1 km wide and 1 km deep. The model works by treating the motion of the cells as obeying simple, but sufficient, 1-D compressible-fluid dynamical laws. The material is considered to compress adiabatically and radiate thermally from it's top surface. There is simplified magnetic flux attached to each cell, represented by a single variable, the magnetic flux density, which represents a flux level averaged over each entire cell. Fluid material, with attached magnetic flux, may flow into and out of cells. The physical details of magnetic reconnection are not addressed in the model.

UV and soft X-ray images from The Transition Region and Coronal Explorer ('TRACE') spacecraft have shown us that reconnection may be occurring not only in the photosphere but also up in the transition region and corona (Saba, Gaeng & Tarbell 2002). At first sight there is a difficulty here in that the photosphere drives the footpoints of loops, where they are located in the magnetic carpet, and pushes them to the edges of super-granular boundaries where they meet oppositely-directed magnetic flux with which they annihilate (Simon, Title & Weiss 2001). The continuous model however models only the motions and magnetic field of the photosphere. This is not a problem because the mass density and energetics of the photosphere far outweigh those of the corona, except where the magnetic field density is high, therefore we consider the fluid motions of only the photosphere.

Recapping, in the Introduction we found that :

$$\begin{aligned} \xi_{\text{th,ph}} &= 1.2 \times 10^{4} \text{ J m}^{-3} \\ \xi_{\text{th,co}} &= 2.1 \times 10^{-2} \text{ J m}^{-3} \\ \xi_{\text{mag,ph}} &= 4.0 \times 10^{-3} \leftrightarrow 3.6 \times 10^{-4} \text{ J m}^{-3} \\ \xi_{\text{mag,co}} &= 4.0 \times 10^{-3} \leftrightarrow 40 \text{ J m}^{-3} \end{aligned}$$

also, we know that :

$$\begin{aligned} \rho_{\text{ph}} &\approx 10^{-4} \text{ kg m}^{-3} \\ \rho_{\text{co}} &\approx 10^{-11} \text{ kg m}^{-3} \end{aligned}$$

Perhaps we should begin by outlining some important features of the continuous model prior to launching into the detailed workings.

3.2 Features and Capabilities of Model.

3.2.1 Physical Parameters of Cells.

- magnetic flux density and polarity, B.
- total number of hydrogen atoms, N.
- length, L.
- temperature, T.
- pressure, P.
- number density of hydrogen atoms, n.
- Alfven speed, C_{A}
- cell boundary velocities, $V_{\text{L}}, V_{\text{R}}$

Figure 3.1 illustrates the cell concept within the model.

Amongst the physical parameters listed above, the following are duplicated in both an 'old' and a 'new' form within the code : $B, L, P, n, V_{\text{L}}, V_{\text{R}}$. The sections, or 'modules' of the model use values contained in the 'old' forms of the variables to obtain the 'new' values. Towards the end of each time-step the 'new' values are loaded into the 'old' versions of the variables ready for utilisation during the next time-step.

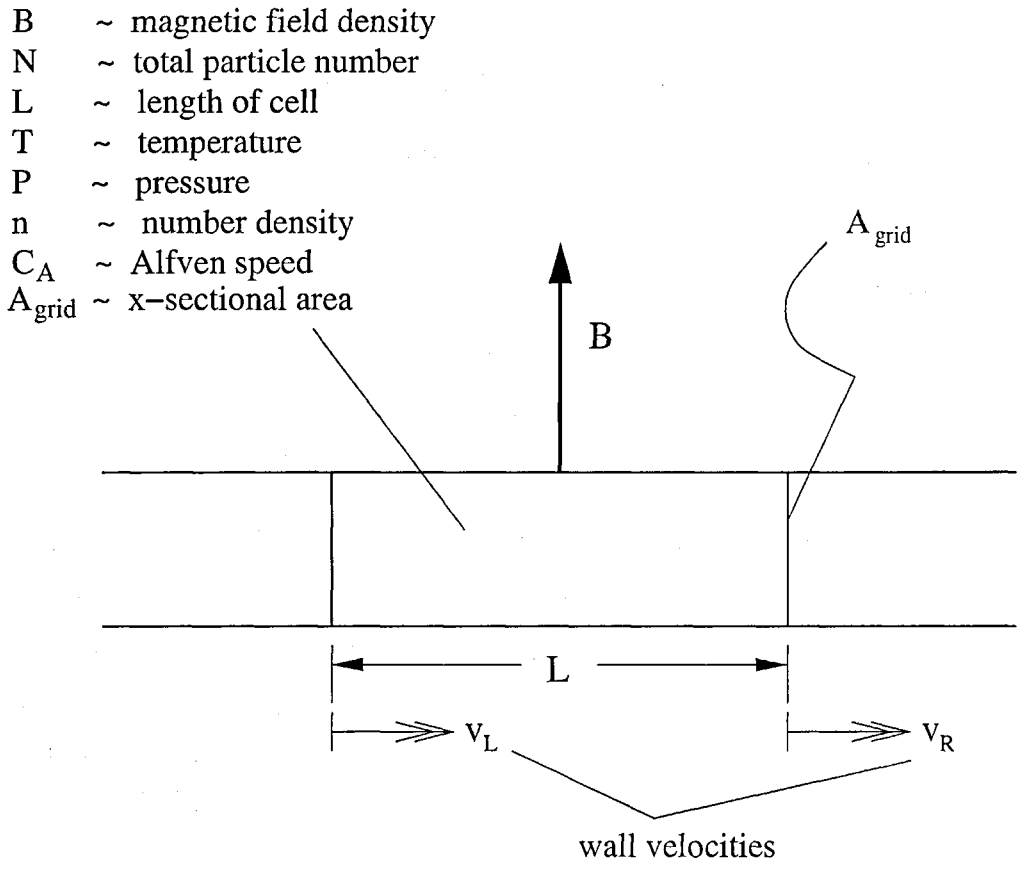

Figure 3.1: Schematic of a typical cell.

3.2.2 One-Dimensional Fluid Laws.

Similarly to the discrete model the continuous model uses a 1-D grid of cells. The model is Lagrangian in type which means that the cell boundaries move with the fluid, the cells moving and changing size to suit. This is in contrast to an Eulerian model where the boundaries or the points at which data is known remain fixed relative to some static framework. The Eulerian approach simplifies the obtaining of data from real fluid systems, since we need only station measuring instruments at fixed known positions, however, this does not give us information on the evolution of any particular parcel of fluid. The Lagrangian is more useful in the sense that the point of origin of our data moves with the fluid and thus we have time-dependent data on the evolution of a given bundle of fluid. An example would be allowing instruments to float along within a fluid flow, providing pressure and temperature data. However, a Lagrangian grid of data points will not remain evenly distributed, and we must constantly redefine our measurement sites. In our present model the high value of the magnetic Reynolds number means that the magnetic field lines restrict bulk movement, diffusion and conduction across the field lines. The model field lines are considered to be perpendicular to the grid

therefore conduction and motion are not possible across cell boundaries. Thus, the cell boundaries are frozen into the fluid and the model embodies a Lagrangian method, assuming that the magnetic flux and fluid move together within the same velocity field. This is consistent with the approach used by Simon, Title & Weiss (2001) where their 'corks' floated passively within the 2-D velocity field of the photospheric fluid. Simon, Title & Weiss (2001) describe the process of the passive migration of flux tubes into the network between supergranules where they eventually undergo annihilation with oppositely directed field.

In our continuous model the fluid within the cells follows simple 1-D fluid dynamical behaviour, using a simple equation of motion. This process is explained in detail later.

To utilise the simplicity and efficiency of the cellular automata approach each cell uses a single parameter for each cell property. These properties are : magnetic flux density, number of particles, length, temperature, pressure, particle number density, sound speed and Alfven speed. Were we to use a real physical fluid we would find a continuum of values for each of these properties except for particle number. In the model we treat these cell parameters as averages of a range of values. This means that each time-step the properties of the whole of the fluid within each cell are updated simultaneously in a single action. The distance between neighbouring cell boundaries - in other words the cell length - must always satisfy the condition of being greater than the distance a sound pressure wave travels in a single time-step. Therefore the cells' thermodynamic properties cannot equilibrate within a time-step and so cell boundaries are adjusted independently. However we can justify this apparent unphysicality by ensuring that all the cell parameters change smoothly in time. The change in values between each time-step must be small. The necessary checking procedures ensuring the maintenance of this condition are explained later.

Cell boundaries cannot be adjusted independently if the distance between two neighbouring cell boundaries becomes less than the distance a sound pressure wave can travel in a single time-step. If this condition occurs then changes in cell boundary velocities will not be smooth.

Thus, we require :

$$C_{\rm s}\ \delta t << L_{\rm i}$$

where :

$$C_{\rm s} \equiv \text{sound speed}$$

$$\delta t \equiv \text{one time} - \text{step (1/500 s)}$$

We know :

$$C_s = \sqrt{\frac{k_B T \gamma}{m}}$$

$$\sim 8.9 \times 10^3 \text{ m s}^{-1}$$

where :

$T = 5785$ K

$m \sim m_p$ (atomic hydrogen)

Now, coming back to our determination of the minimum size of a cell, our model time-step is $1/500$ of a second, thus we can see that

$$C_s \, \delta t \sim 8.9 \times 10^3 \text{ m s}^{-1} \times \frac{1}{500} \text{ s}$$

$$\sim 18 \text{ m}$$

Thus, cells' sizes cannot become arbitrarily small. We can see that the model should not allow the existence of cells with length less than : few $\times$ 10 m. However, there are other reasons related to numerical instabilities in discrete-time models causing us to postulate a minimum cell size greater than this. Apart from the problems associated with repositioning cell boundaries which are close to very small cells, there is also a danger of numerical instability where a cell is allowed to become small. Any changes in the material content of a cell caused by emergence or submergence of magnetic flux must be small compared with the level of material within the cell i.e. $\Delta\phi << \phi$. The model evolves through the passing of discrete time-steps and so, like any temporally discrete numerical simulation, the changes in the parameter values between one time-step and another must remain small in order to retain relatively little divergence between the model and a real physical system (this occurs where the length of a cell is too small. The cell must be removed and we explain this below). This requirement is additional to the requirement for smoothness in time which was elucidated above. When a cell is undergoing submergence of magnetic flux it is clear that when the cell has almost disappeared there is a point when the change in magnetic flux is comparable to the amount of flux contained within the cell, and thus $\Delta\phi << \phi$ will not be preserved.

To avoid numerical instability the grid must also remain smooth in space, i.e. the disparity in parameter values between adjacent cells must remain small.

We will consider the sequence of processes for the resizing of cells and the adjustment each time-step of cells' thermodynamic properties. This sequence includes details of 1-D fluid laws, an equation

of motion for each cell and also a mechanism for removing cells which endanger the stability of the model because of their small size.

Sequence of processes :

1. calculate new lengths.
2. remove dangerously small cells.
3. calculate new number densities.
4. calculate new pressure.
5. calculate new boundary velocities.
6. calculate new temperatures.

It is necessary to have a mechanism within the model for snipping out cells which have become too small. Following the removal of such a cell, the space within the grid formerly occupied by the excised cell is attributed equally to the two neighbouring cells. We explained earlier why cell length must exceed $C_s\ \delta t$ and showed that this distance is $\sim$ few $\times$ 10 m. On this basis, it was decided that cell length must not slip below 100 m. Where this happens, the cell in question is removed from the grid. Importantly, this length is small compared with the typical initial cell length of 10^4 m.

The parameters attributed to each cell apply to the whole space within that cell, and we should therefore consider the parameter values to be averages for each cell, as mentioned above. No resolution is possible below the size of the cell. Exactly what the value is of this resolution during the running of the model is not easily quantifiable, but we will take it to be the initial cell size (i.e. the length of the cells at the commencement of a run) and thus it remains constant throughout the evolution of a run. It is not a good idea for us to allow arbitrarily large cells to grow during a run, since we are then in effect allowing the resolution of the data to become coarser. Therefore, there is a feature of the model which detects a large cell and splits it into pairs of smaller cells. The size above which no cell is allowed to exist is 1.5 times the mean initial cell size. Thus, there are good practical reasons for only allowing cells within this Lagrangian scheme to exist with lengths within a specific range.

The time evolution of the model is discrete in time, in intervals of 0.002 s. During each iteration of the model, the functions of the program operate upon the parameter values calculated from the previous iteration.

We will now consider the exact process of calculating cell parameter values as occurs each time-step.

1. New cell length.

   Given the old cell length (calculated during the previous time-step) we can calculate the new cell length. For a given cell,

   $$L' = L - \delta t \; \Delta V$$

   where $\Delta V \equiv V_{\rm L} - V_{\rm R}$

2. Remove small cells.

   As discussed at the beginning of this section it is important to remove small cells around the size of $\sim$ few $\times$ 10 metres or less. The specific level is chosen for the continuous model is 100 metres. These cells are removed from the grid, and the cells either side are extended equally into the space previously occupied by the cell. If the cell removed was formerly the site of emergence or submergence of magnetic flux then this will be deemed to continue in another cell in the grid, randomly selected.

3. New number density.

   Given the old cell number density, we can calculate the new number density. Total number of particles, N, will be changed by the emergence/submergence processes, thus,

   $$n' = \frac{N}{A_{\rm grid} \; L'}$$

4. New pressure.

   The total pressure within each cell consists of two components : magnetic, $P_{\rm mag}$ and thermal, $P_{\rm th}$.

   $$P_{\rm total} = P_{\rm mag} + P_{\rm th} \tag{3.1}$$

   Where :

   $$P_{\rm mag} = \frac{B^2}{2\mu_0} \tag{3.2}$$

   and

   $$P_{\rm th} = n k_{\rm B} T \tag{3.3}$$

We assume that cells undergo reversible adiabatic expansion and contraction :

$$\begin{aligned} P_{\text{th}}V^{\gamma} &= \text{constant} \\ &= P'_{\text{th}}V'^{\gamma} \end{aligned} \tag{3.4}$$

Let's explain the mechanism for adjustment of cell pressure :

(a) Subtract P_{mag} from total pressure to obtain thermodynamic pressure. (See equation 3.1). The reason for this is that in the next step we will adjust the thermodynamic pressure in accordance with the adiabatic relation. Now, this relation (equation 3.4) does not apply to magnetic pressure, therefore we must subtract the magnetic component from the total pressure prior to using the adiabatic relation.

$$P_{\text{th}} = P_{\text{total}} - P_{\text{mag}} \tag{3.5}$$

(b) Calculate new thermal pressure assuming a reversible adiabatic equation of state, using new cell length i.e. use equation 3.4. The adiabatic identity, equation 3.4, holds only for the thermodynamic pressure. P_{th} and P_{mag} are not coupled (see equations 3.2 and 3.3).

$$P'_{\text{th}} = P_{\text{th}}\left(\frac{L}{L'}\right)^{\gamma} \tag{3.6}$$

(c) Calculate new P_{mag} and new total of thermal and magnetic pressures.

$$P'_{\text{mag}} = \frac{(B')^2}{2\mu_0}$$

We know :

$$P'_{\text{total}} = P'_{\text{th}} + P'_{\text{mag}}$$

Therefore we have :

$$P'_{\text{total}} = P\left(\frac{L}{L'}\right)^{\gamma} + \frac{(B')^2}{2\mu_0}$$

5. New boundary velocity.

We are interested (each time-step) in finding the new boundary velocities in order that the cell boundaries can be repositioned. New boundary velocities consequently give the necessary information for re-sizing the cells and calculating new number density, pressure and magnetic field density. Regarding the mechanism for finding the new velocity of a sample cell boundary,

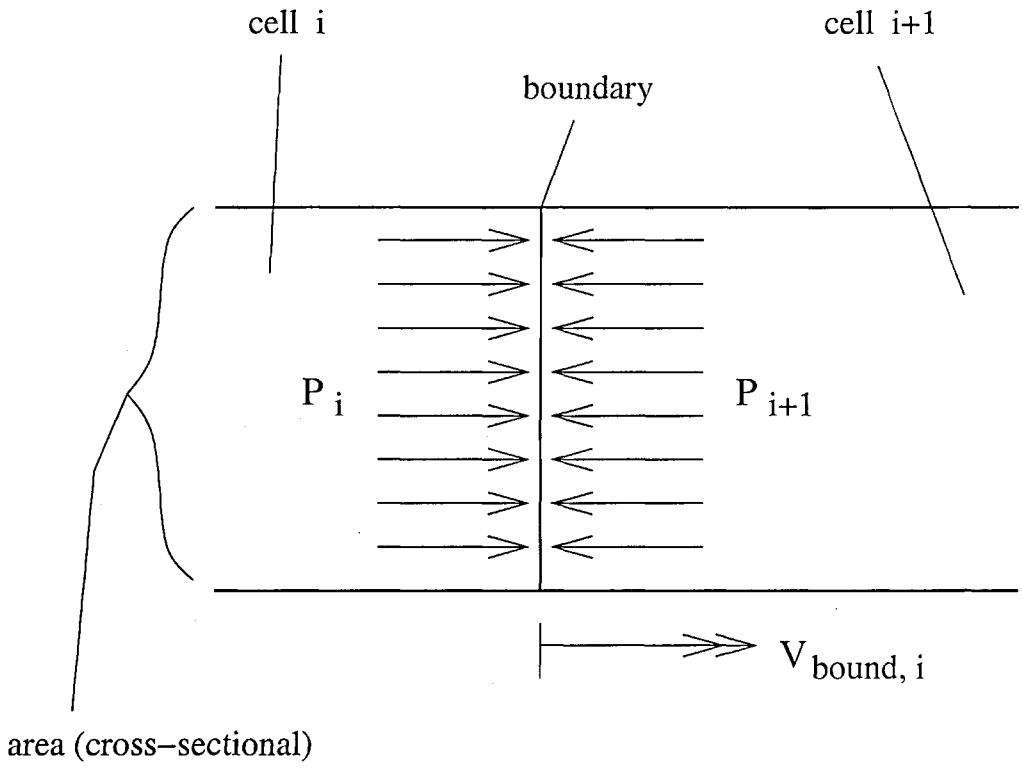

Figure 3.2: Schematic of cell boundary.

let's consider figure 3.2. We need to apply the equation of motion to determine the acceleration of the boundary produced during one timestep :

$$\frac{\Delta V_{\text{bound}}}{\delta t} = \frac{\Delta P_{\text{bound}}\, A_{\text{grid}}}{M_{\text{bound}}}$$

We can immediately see problems here. To obtain ΔP what pressure values will we take, and what mass, M, shall we use? Were we to consider the acceleration of a cell boundary, we can see that in the limit the pressures immediately adjacent to a cell boundary on both sides of it will be equal, and M will be zero. What then are we to do? Our solution is to suppose the existence of a notional cell which straddles this boundary and we locate this cell's walls in the same longitudinal positions as the centres of the true cells on each side of the boundary. Figure 3.3 illustrates this notional cell with a dotted line. We next find the mass of the notional cell by simply summing half the mass of each cell either side of the boundary.

Regarding the notional cell straddling the boundary, we calculate the change in velocity of that boundary. To do this we use the net impulse resulting from the pressures upon the walls of the notional cell. These walls are deemed to be situated along the centre-lines of the actual cells either side of the boundary.

Thus, we have :

$$V'_{\text{boundary,i}} = V_{\text{boundary,i}} + \left(\frac{\delta t \left(P_{\text{i}} - P_{\text{i+1}} \right)}{m_{\text{p}} \left(n_{\text{i}} \frac{L_{\text{i}}}{2} + n_{\text{i+1}} \frac{L_{\text{i+1}}}{2} \right)} \right)$$

$(P_{\text{i}} - P_{\text{i+1}})$ is the net pressure force acting upon the notional cell, while the denominator is the mass of the notional cell (neglecting mass of electrons). We can see that the cross-sectional area of the grid has cancelled out across the fraction. This calculation is carried out simultaneously for every boundary along the grid.

An earlier conceived alternative method for the calculation of the mass was to interpolate the number density of the notional cell at the site of the boundary under consideration. This number density would be interpolated between those of the two adjacent cells, where number densities were assumed to be correct at their centres. However, this method was found to be unsatisfactory giving inappropriately high or low values for the number density where the two cells were of sufficiently different lengths and number densities. This is shown in figure 3.4. Therefore, the interpolation method was abandoned in favour of simply taking half the mass of each adjoining cell.

Given that the model is a 1-D system there is no momentum transfer between regions by shearing or frictional or turbulent dissipation.

6. New temperature.

   Given the new pressure, length, and total cell particle number (post-emergence/submergence) we can calculate the new cell temperature.

$$T' = \frac{P' A_{\text{grid}} L'}{N k_{\text{B}}}$$

3.2.3 Simplified Magnetic Field and Reconnection.

The magnetic field within each cell is represented by a single parameter, B, which has magnitude and sign. Within the formalism of the model, reconnection occurs at the boundaries between cells with oppositely signed magnetic flux and depletes the cells' magnetic energy by a calculated value. This process is described in detail in section 3.3.

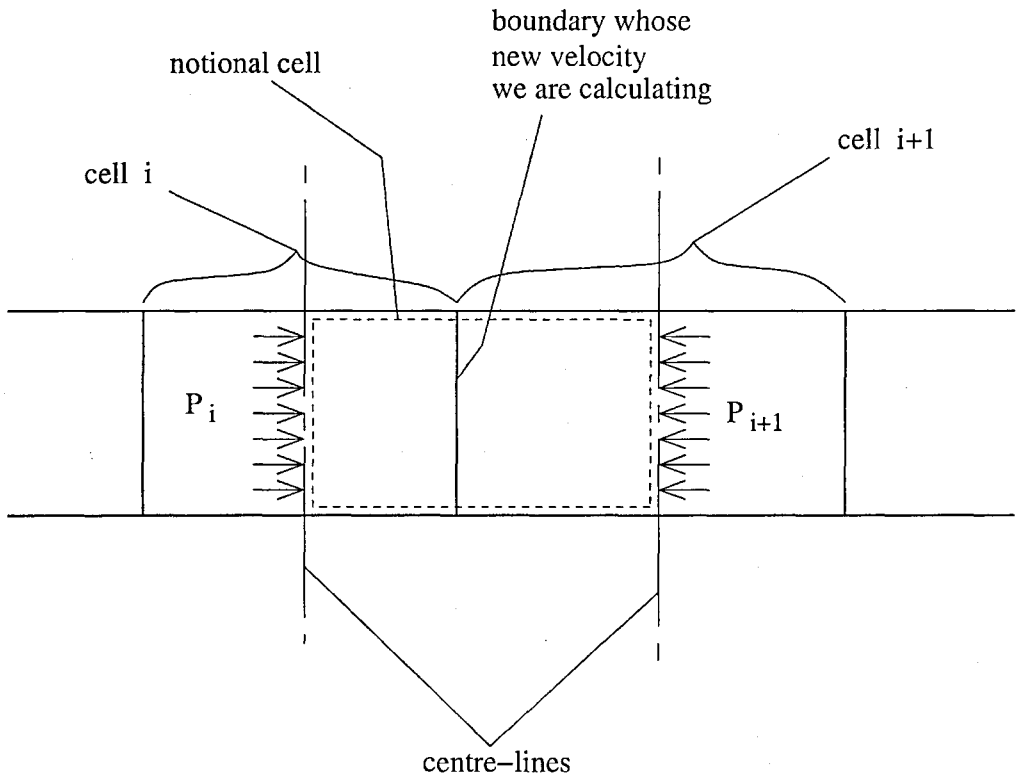

Figure 3.3: Mechanism for calculation of new cell boundary velocities.

3.2.4 Emergence and Submergence of Magnetic Flux.

In a real fluid we would expect transfer of momentum by turbulence or friction caused by shearing between adjacent fluid layers. We can introduce some sense of this behaviour into the model by providing a mechanism for the removal of fluid (with magnetic field attached) from one part of the grid and its introduction to another region. This operates as a mechanism for transfer of momentum. This effect is a non-local communication which raises the dimensionality of the model to greater than unity. We may also think of this emergence and submergence of magnetic flux as representing the result of convective motions in the fluid, where the grid represents the layer at the top of the convective zone. This feature is necessary as regions of fluid, which due to their magnetic field have the potentiality for undergoing magnetic reconnection, cannot ordinarily flow together in this 1-D model without requiring tremendous compression of gas. The emergence/submergence facility can represent inflows and outflows that push and 'suck' regions together.

3.2.5 Conservation of Magnetic Flux, Energy and Mass.

Although we believe that Solar radiative output has increased by a few percent during the last few hundred million years, over timescales relevant to our present work (seconds to minutes) there is no

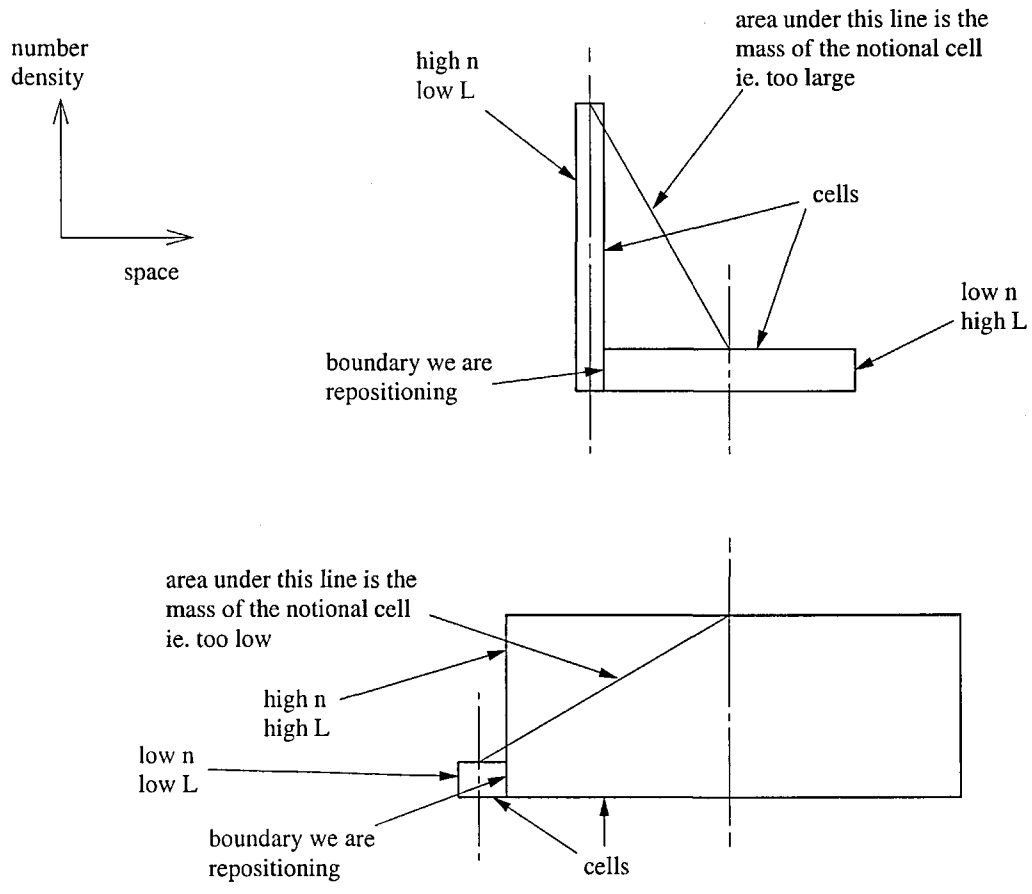

Figure 3.4: Cell n and L configurations which render interpolation method inaccurate.

bulk change in the properties of the Solar surface. Large flaring events may significantly deplete the energy stored within the magnetic field, however in general an equilibrium is maintained. The model therefore is designed to ensure near constancy in the levels of magnetic flux.

3.2.5.1 Conservation of Magnetic Flux.

Let's consider the parts of the model which produce changes in the magnetic flux within cells. There are three such modules, described below.

Figure 3.5 shows the order of these modules. The boxes described as 'various' represent any and all of the other parts of the model. Because they do not produce changes to the magnetic fluxes we are presently unconcerned with them.

First, before the commencement of a run of the model, the total magnetic flux within the grid is summed. This value is remembered throughout the run.

1. Magnetic reconnection.

   The reconnection function carries out an appreciation for each cell as to whether magnetic

reconnection can occur and if so, then the energy release by reconnection and the changed level of magnetic flux within the cell are calculated. Thus the magnetic flux contained within a cell is depleted.

2. Removal of small cells.

   Cells with length below 100 metres are removed in order to avoid a particular class of numerical instabilities, as explained in section 3.2.2. The flux within such cells disappears from the model.

3. Emergence/submergence of magnetic flux.

   The emergence and submergence process conserves magnetic flux. The order of play is submergence first then emergence. The submergence is carried out upon the whole grid then emergence is carried out upon the whole grid. Following emergence the total flux within the grid is summed and this is compared with a figure equal to the total flux existing at the commencement of the run. Any deficit in flux in the present state of the grid is divided between all the cells undergoing flux emergence, and the magnetic field density of these cells is increased to account for this deficit. Details of this process are given in section 3.3.2.

   Thus, a constant level of total magnetic flux within the grid of the model is ensured. In the long term the magnetic field density of the photosphere is constant. Also, we would expect a close similarity between the emerging and submerging flux because submerged flux must emerge again at the surface due to the convective motions. The reconnection process, both in the Sun and the model, conserves total flux, therefore we must ensure that the model emerged flux matches the submerged flux.

3.2.5.2 Conservation of Energy.

Let us consider now those parts of the model which produce changes in the total energy of the grid. There are four such modules, described below. Figure 3.6 shows the order of these modules. The boxes described as 'various' represent any and all of the other parts of the model. Because they do not produce changes to the energy, thermal or magnetic, we are presently unconcerned with them.

1. Magnetic reconnection.

   Within the model the magnetic reconnection process reduces magnetic field density, and hence magnetic energy stored within cells.

   We expect some of the energy released in real Solar magnetic reconnection to go into heating of the photosphere. Highly energetic electrons and protons will travel along the magnetic field

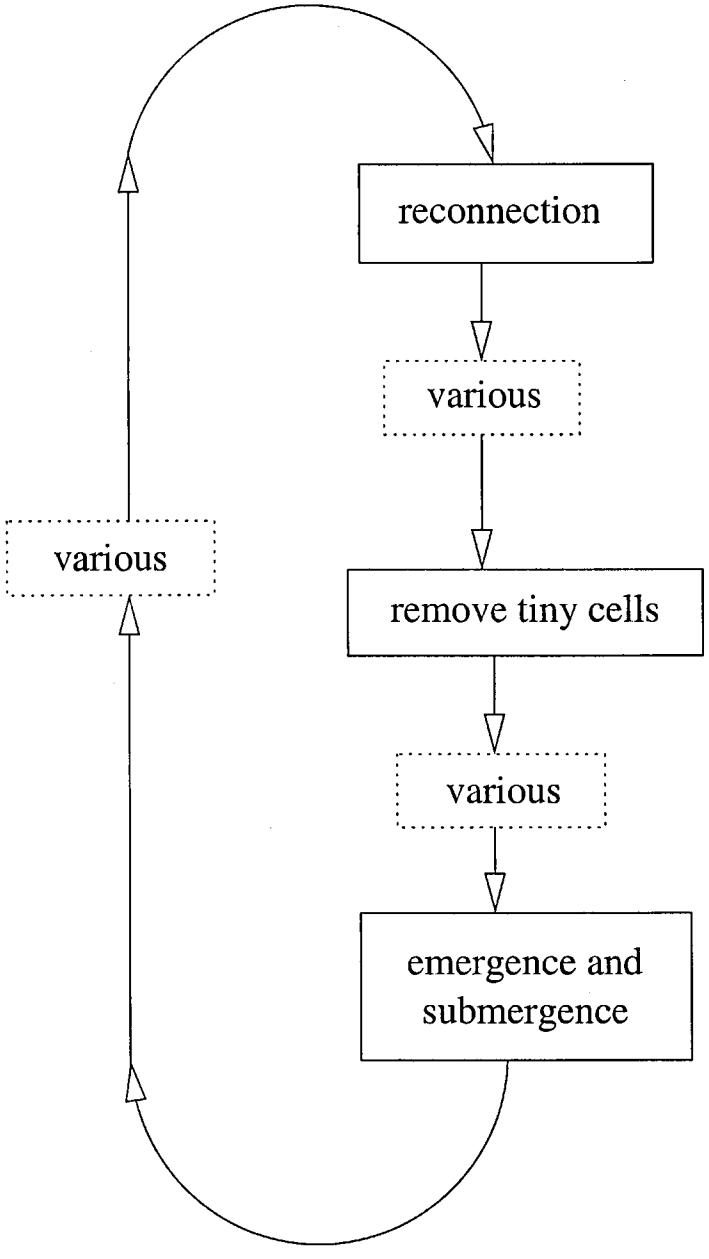

Figure 3.5: Modules relevant to conservation of magnetic flux.

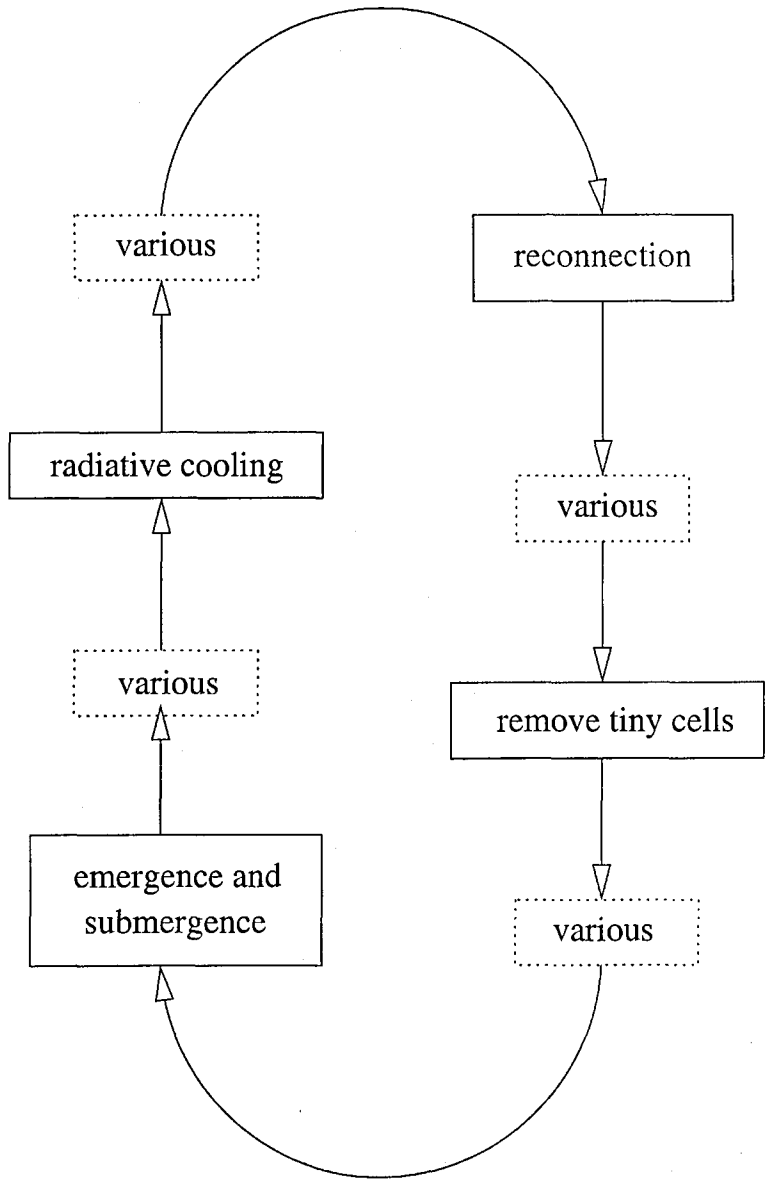

Figure 3.6: Modules relevant to conservation of energy.

lines from a reconnection site, situated perhaps at the top of a loop, and impact into the dense photospheric material, heating it. Therefore, within the model there is a facility for heating the cell material using energy released by reconnection.

2. Removal of small cells.

   As we have seen, cells with length below 100 metres are removed in order to avoid a type of numerical instability. Because the material is considered to submerge and disappear from the model, the magnetic energy and thermal energy within the removed cell are lost from the grid.

3. Emergence/submergence of magnetic flux.

   The submergence process removes material from cells. The total thermal energy within each cell is given by $\frac{3}{2}Nk_{\mathrm{B}}T$ therefore the thermal energy reduces pro rata such that it remains in proportion with the amount of material remaining in a cell. Similarly, the magnetic flux contained within the cell is reduced pro rata such that the new level of flux is in proportion with the new reduced amount of material within the cell.

   Regarding temperature of emerging magnetic flux, all the material disappearing from submerging cells is put into emerging cells at the same temperature at which it is submerged. This means that the thermal energy is actively conserved during the emergence and submergence. Similarly, the magnetic field density is raised in the emerging cells in order to maintain the total magnetic flux of the grid at the level of the magnetic flux at the commencement of the run. Thus, the total magnetic energy of the grid is conserved.

4. Radiative cooling of cells.

   The grid is assumed to exist within an ambient black-body radiation field at a temperature of 5785 K ($T_{\mathrm{e},\odot}$ given by Karttunen et al. (1996)), and there will therefore be a net energy flux through the notional top surface of each cell. The grid has a width of 10^3 m. The particular value is unimportant, however in accordance with Stefan's Law[1] we nevertheless need a value for width in order to perform the updating calculations)

   The photosphere radiates strongly at various wavelengths including IR, optical, UV and X-ray. In our model radiative cooling acts as a negative feedback effect, restoring the temperature of each cell to 5785 K.

[1] Stefan's law gives the total energy flux, E, radiated at all wavelengths by a black-body at a given temperature, T :

$$\dot{E} = \sigma T^4$$

3.2.5.3 Conservation of Mass

Let us consider now those parts of the model which produce changes in the total mass of the grid.

Figure 3.7 shows the order of these modules. The boxes described as 'various' represent any and all of the other parts of the model. Because they do not produce changes to the mass we are presently unconcerned with them.

1. Removal of small cells.

   As explained in section 3.2.2, cells with length below 100 metres are removed from the model. The material within these cells disappears from the model.

2. Emergence/submergence of magnetic flux.

   At the commencement of a run the total mass of the grid is summed and this value is remembered throughout the run as a benchmark for comparison. Each time-step cells which are designated during that time-step for the submergence of magnetic flux have their N parameter reduced by the designated amount. Similarly, those cells designated for emergence of magnetic flux have their number of particles incremented, thus increasing their mass. There are equal numbers of submergence and emergence cells therefore the net change of mass will be zero. However, during the time-step and prior to the emergence and submergence, the module responsible for removing small cells may have carried out its function. If this is the case then we expect that there will be a deficit in the total grid mass as compared with the record of the initial total mass. The mass deficit, equal to the mass of the lost cells, is divided equally between the cells undergoing flux emergence. Their total particle numbers are increased by this figure.

   Thus, mass conservation is ensured by the forced emergence of an amount of material required to maintain constant total mass equal to the initial total mass.

3.2.6 Not Tied to Any Particular Length Scale.

We have flexibility within the model to choose different initial cell lengths providing that the requirements regarding minimum cell size mentioned in section 3.2.2 are satisfied. If these requirements are not satisfied then we expect numerical instability to occur. Thus, cell lengths must significantly exceed the minimum level of 100 m.

The initial cell length is effectively the resolution of the model and therefore smaller cells mean a higher effective resolution to the model. Increasing the cell length for a constant size of the entire grid means fewer cells and therefore poorer data. Fewer cells also implies fewer cell-cell interactions and

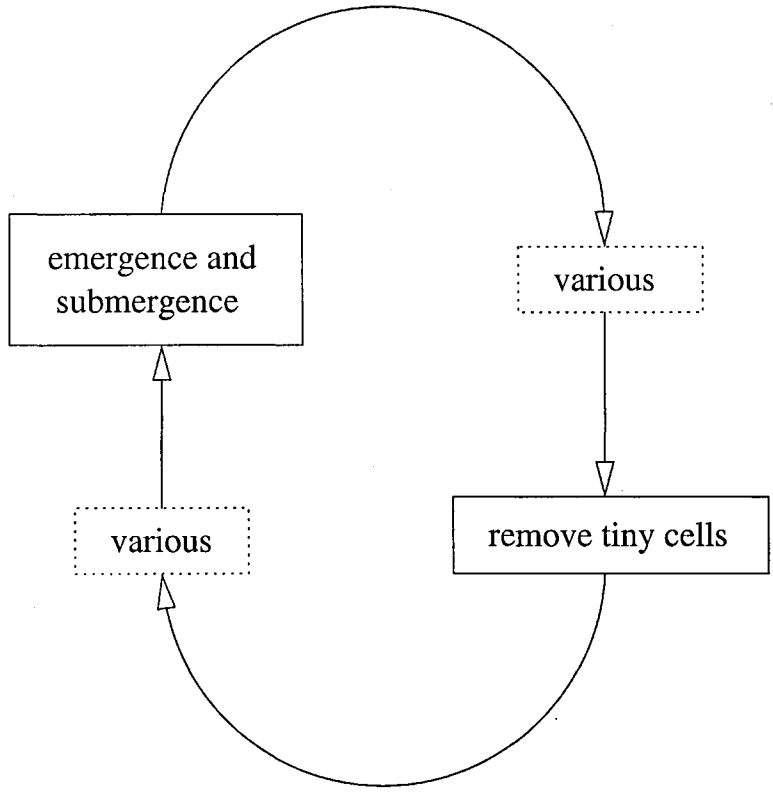

Figure 3.7: Modules relevant to conservation of mass.

sites with potentiality for reconnection. Similarly, smaller cells mean more cells, which improves our data, but makes the computation more CPU-intensive. In the extreme case a spatially continuous and infinitely detailed model would obviously provide no limit upon the number of reconnection sites, however this is technically unfeasible and would defeat the purpose of using a CA model. There is thus a trade-off between data/resolution and practicality. A balance must be struck, and consequently we have chosen to use an initial cell length of 10^4 metres. For purposes of comparison however, we perform additional runs with initial cell length of 5×10^3 m.

3.2.7 Radiative Cooling of Simulated Solar surface.

Our model incorporates conservation of magnetic flux and energy. We know that the temperature of the Solar photosphere is in a steady state and radiates strongly at various wavelengths, in particular IR, optical, UV and X-ray. In fact, the total Solar radiation flux is $\sim 4 \times 10^{26}$ W (Karttunen et al. 1996). The model simulates radiative cooling by black-body emission from the surface of the grid. For the maintenance of an equilibrium it is assumed that there is an ambient background into which the upper surface of the cells radiate at a temperature of 5785 K ($T_{e,\odot}$ given by Karttunen et al. (1996)). Given that the radiation energy flux is proportional to σT^4, the radiative effect behaves as

negative feedback (strongly linked to the temperature) and tends to return the temperature to 5785 K, and also therefore acts as a negative feedback upon the thermodynamic pressure, of each cell.

In the introduction we saw that the photospheric thermal energy density is $\sim 1.2 \times 10^4$ J m^{-3} (table 1.1) whereas the coronal thermal energy density is $\sim 2.1 \times 10^{-2}$ J m^{-3} (table 1.1). Given the far greater thermal energy density of the photosphere, we can neglect radiative losses from the corona and chromosphere and need only account within the model for radiative cooling of the photosphere. Besides, given the high magnetic Reynolds number of the corona, hot particles trapped inside magnetic structures within the corona may only travel along such field lines, and so will follow the field lines until they impact into the denser photospheric material, where they will radiate non-thermally in the UV and X-ray bands until reaching equilibrium with the photospheric gas.

3.2.8 Introducing Noise into the Pressure Field.

In order that we can explore the effect of noise in the model there is a facility for its addition to the pressure field.

For each cell we have:

$$P' = P\,(1 + \zeta)$$

where ζ is a uniformly distributed random number in the range : $\pm\eta$.

This noise is added to the pressure values for each cell every 500 time-steps (1 second).

η is a parameter we typically give the value $\eta = 0.001$. In the Earth's atmosphere, we know that typically $\frac{\Delta P}{P} \sim 0.001$ therefore in the absence of any Solar $\frac{\Delta P}{P}$ data we will not use noise greater than this.

3.2.9 Reversible Adiabatic Expansion of Cells.

As mentioned above in section 3.2.2, expansion and contraction of cells occurs over a timescale assumed to be short compared with the heat transfer timescale. Because of the high gas pressure in the photosphere it is difficult to bring gas together for reconnection therefore we expect reconnection to mainly take place in the corona. In the Solar atmosphere we know that the magnetic Reynolds number is much greater than unity, and therefore the plasma is effectively tied to the magnetic field lines. This makes heat transfer across the field lines slow and justifies our assumption of reversible adiabatic expansion. To properly be able to use the relation $P_i V_i^{\gamma} = constant$ we need to assume not only that cell expansion is adiabatic but also that it is slow enough for the process to be represented by a curve on a P-V diagram, i.e. a point on the curve represents the state of the whole cell. This means that all the material within each cell is in the same thermodynamic state. This is achieved

if we can assume expansion/contraction is quasi-static. We can justify this if our time-step is small enough that the process is smooth.

In the model, by analogy with the high magnetic Reynolds number of the Solar plasma, heat transfer between cells due to conduction or mixing is not possible. Given the model time-step of $\frac{1}{500}$ seconds we can assume adiabatic reversible adiabatic expansion/contraction.

3.2.10 Typical Initial Model Parameter Values.

Let us clarify typical values for the various parameters associated with the initial state of the model run.

3.2.10.1 Number of Cells.

Typically, the model will commence with 10^3 cells. The determining factor here is time for completion of the run.

3.2.10.2 Number of Time-Steps.

Typically, the duration of a run is 3×10^6 time-steps. To ensure that we lose the memory of the initial conditions, data will only be reported after the first 10^6 time-steps, thus giving 2×10^6 time-steps of data, equivalent to 4000 seconds.

Figures 3.8 and 3.9 show the time series of the energy release for a run using a combination of initial parameters which will hereafter be referred to as 'typical', as per the Definition of Commonly Used Terms given at the beginning of the thesis.

Figure 3.8 shows the time series covering the period from the beginning of the model run to 3×10^6 timesteps (6000 s), whereas figure 3.9 shows the time series covering the period from 10^6 timesteps to 3×10^6 timesteps (2000 s to 6000 s).

It can clearly be seen that very soon after beginning the run of the model there are some high peaks followed by a gentle decline which merges into the steady state around 10^6 timesteps (2000 s). For this reason event-size, and other, distributions are calculated from data produced between 10^6 and 3×10^6 timesteps (2000 s and 6000 s).

3.2.10.3 Reconnection Method.

Simplified formalised reconnection between cells of anti-parallel magnetic flux is represented within the model, and is the method for releasing the magnetic energy within the cells. This release is manifested as events which are counted towards event-size distributions. The reconnection method

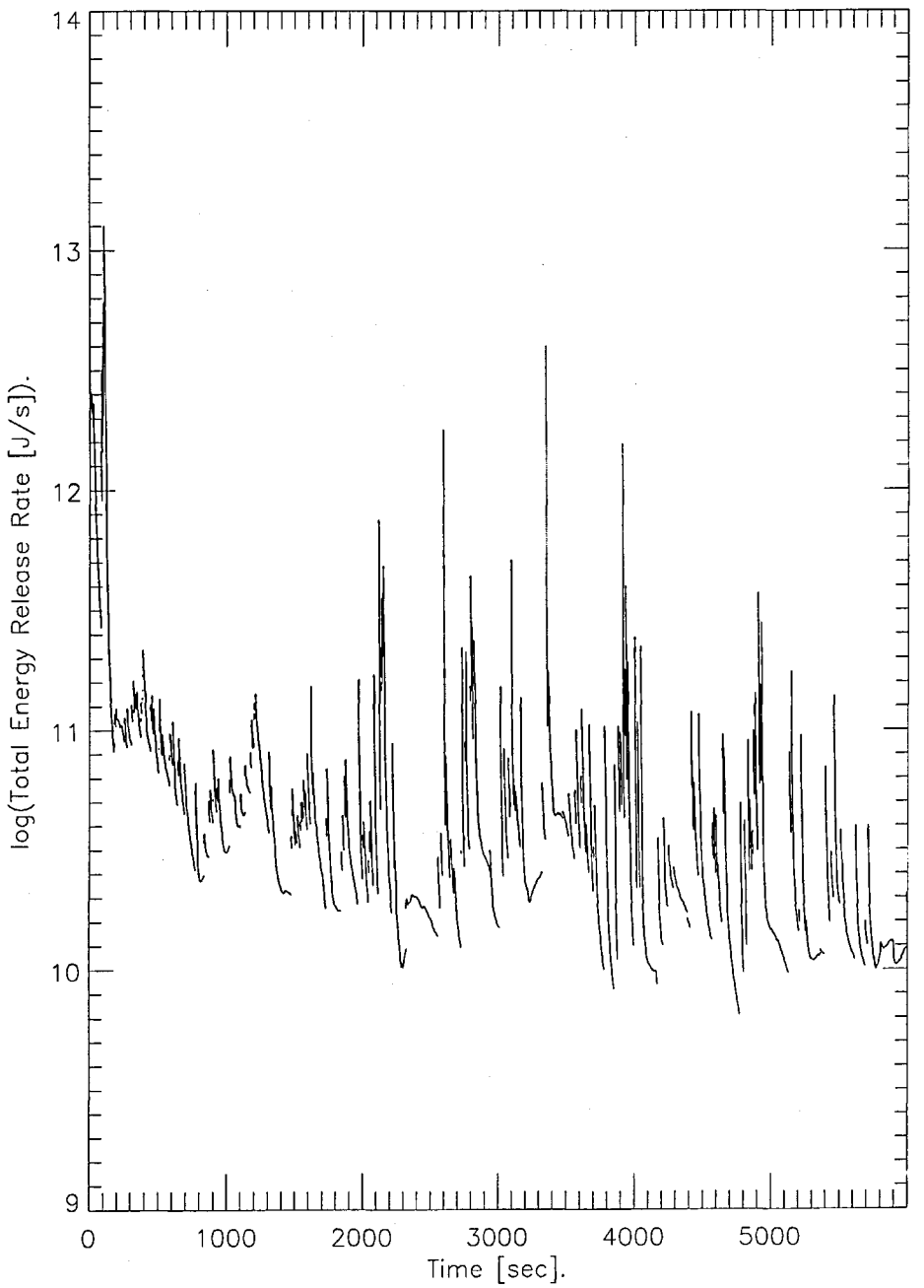

Figure 3.8: Time series of total model and maximum magnetic reconnection energy release for period 0 timesteps to 3×10^6 timesteps.

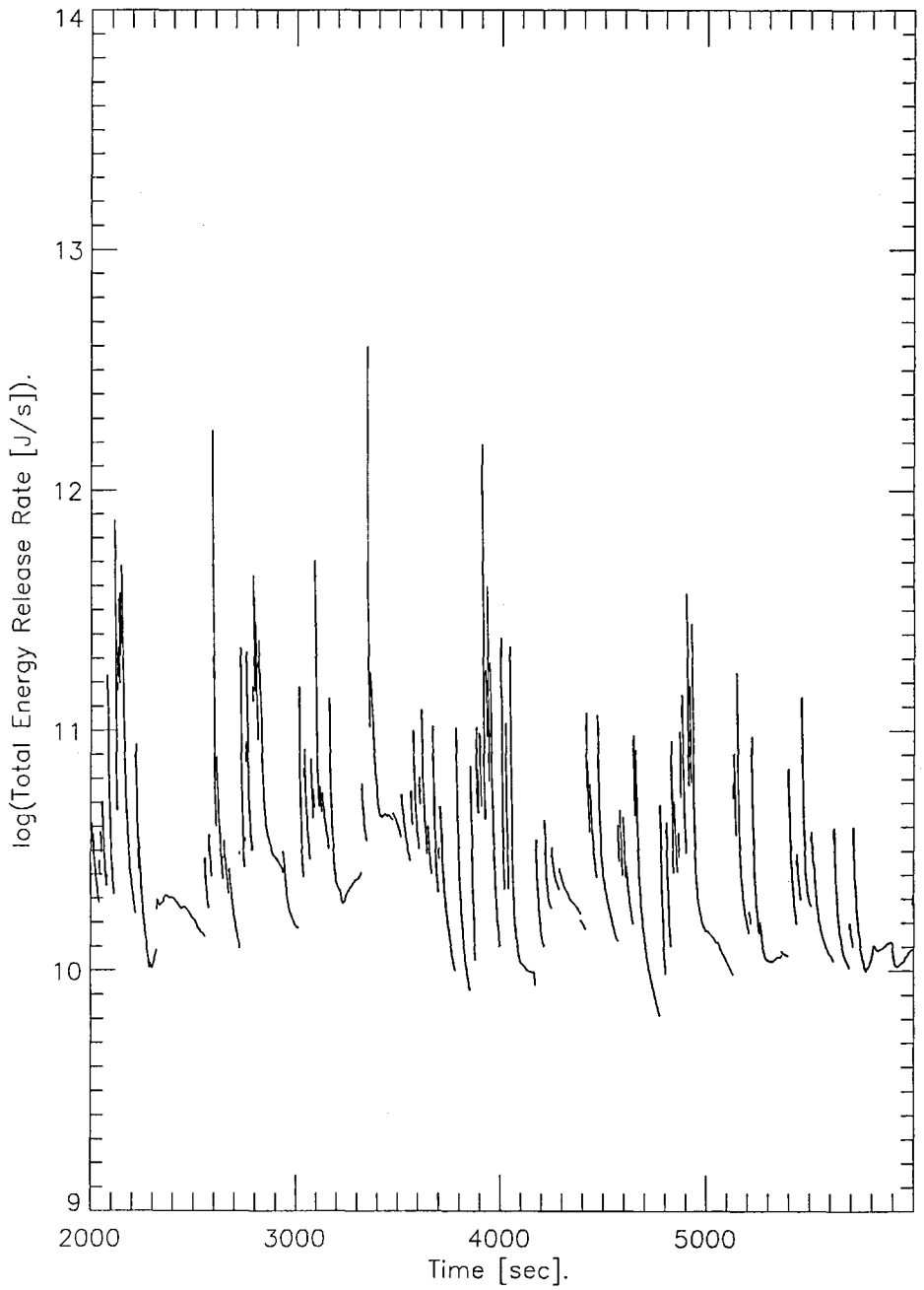

Figure 3.9: Time series of total, and maximum, model magnetic reconnection energy release for period 1×10^6 timesteps to 3×10^6 timesteps.

is explained in detail in section 3.3. The reconnection may be turned on and off, and the detail of the reconnection module itself may be tinkered with. There are several variants explored by this model and these are detailed in section 3.3.

3.2.10.4 Emergence/Submergence of Magnetic Flux.

The standard model has the emergence and submergence set up such that the rate of material transfer into or out of a cell is equal to the initial mean cell mass per 10^3 seconds. In section 3.3.2 we show that this rate of material transfer gives a rate of flux emergence within two orders of magnitude of observed values. Lawrence, Cadavid & Ruzmaikin (2001) find a typical coherence time of 1200 seconds for the granular scale : the smaller of the two distinct size scales which they find for photospheric cellular flows, $\sim 2 \times 10^6$ m.

We typically enable 10% of the cells in the model to be undergoing emergence or submergence at any time ($\kappa = 0.1$ in section 3.3.2).

Further details may be found in section 3.3.

3.2.10.5 Time-step (δt).

After some experimentation, a discrete time interval of 1/500 s was settled upon. This is a compromise between the need to overcome the tendency to numerical instability (increasing at larger δt) and considerations of scarcity of CPU-time. This matter is discussed in section 3.4.

3.2.11 Typical Initial Cell Parameter Values.

Now, let us clarify typical values for the various parameters associated with the initial state of the cells.

3.2.11.1 Magnetic Flux Density (and polarity), B.

B varies through the Solar atmosphere as follows :

large sunspot	-	4×10^3 G
typical sunspot	-	$2 \leftrightarrow 3 \times 10^3$ G
intense photospheric flux tube	-	$1 \leftrightarrow 2 \times 10^3$ G
active region	-	few $\times$ 100 G
corona	-	$1 \leftrightarrow 100$ G
quiet region	-	1 G

(lecture notes from introductory Solar physics course (Roberts 1999).)

The standard model run generates a flat random distribution of magnetic field density in the range ± 100 G. The model does not allow sufficient orders of magnitude of the size range of cells which would be necessary to accurately simulate the full range of features from quiet network to intense flux tubes within the same run.

We are also able to generate magnetic field density values in a random power-law distribution. The highest (negative) power-law index we can use without onset of catastrophic numerical instability is -1. Figure 3.10 shows the distribution of $|B|$ for 10^3 cells, generated by a power-law (index = -1) random distribution for the run described in section 3.4.4.4 (figures 3.28 and 3.29).

We needed to investigate the evolution of the size distribution of unipolar flux regions (see section 4.2.5), therefore a run was made where the magnetic polarity of cells in the initial state alternated from one cell to the next along the grid. The cells have the same initial length therefore all unipolar regions are of length equal to one cell length (usually 10^4 m). Thus, the initial distribution of sizes of unipolar regions in this case is a delta function at the initial cell length.

The power-law distribution of magnetic field density is used to determine whether an initial power-law distribution of magnetic field density forces the event-size distributions to also be power-law in nature.

3.2.11.2 Temperature, T.

Given that the temperature at the photosphere is thought to be approximately 5785 K (Karttunen et al. (1996) gives the effective temperature of the photosphere, $T_{e,\odot} = 5785\ K$, where $T_{e,\odot}$ is the temperature calculated assuming a perfectly thermal wavelength distribution), an initial temperature of 5785 K is attributed to each cell. Also, for the purpose of calculating the radiative cooling effect of the grid, we assume a background temperature at this level.

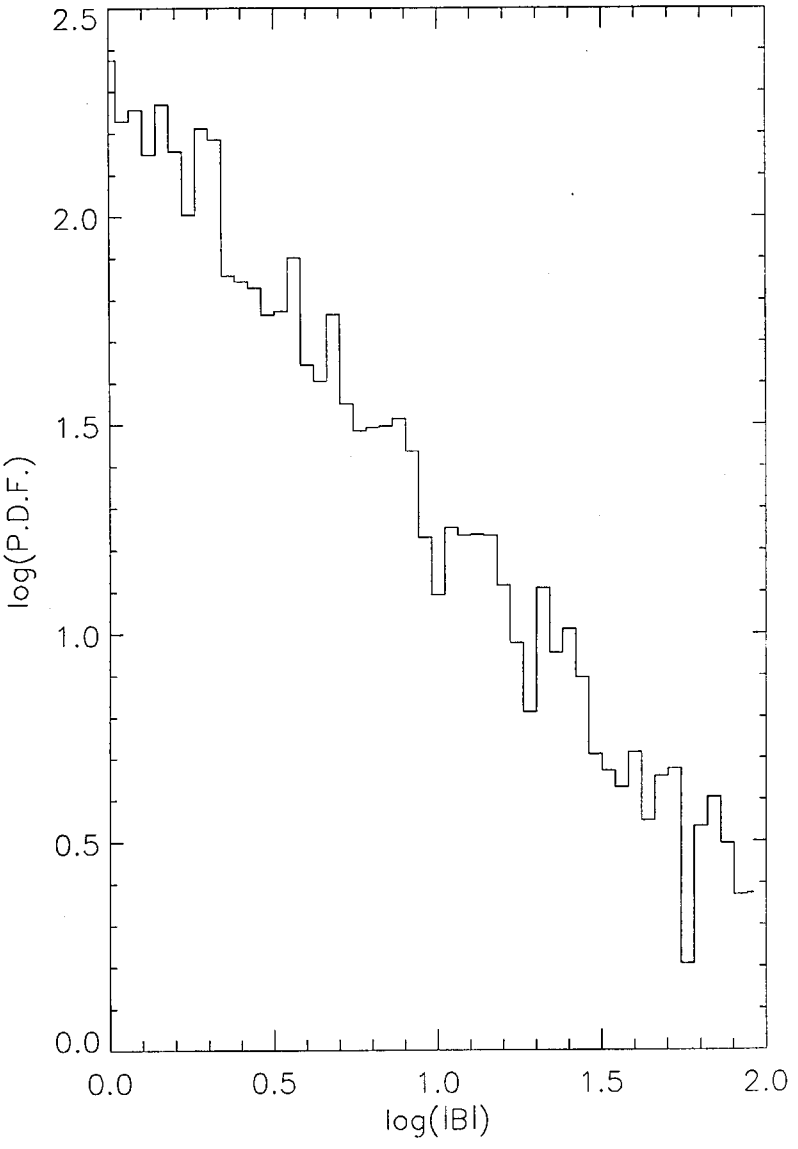

Figure 3.10: Plot of values of $|B|$ for 10^3 cells where $|B|$ is distributed in a power-law with index = -1. $1 < |B| < 100$. Bin-size = 0.04.

3.2.11.3 Total particle number, N.

We know $N = nA_{\text{grid}}L$ and we take typically $N = 10^{32}$ particles (neutral hydrogen atoms).

3.2.11.4 Number Density, n.

Particle number density varies through succesive layers of the Solar atmosphere :

$$\begin{aligned} \text{lower corona} &\sim 10^{14} \leftrightarrow 10^{15}\ \text{m}^{-3} \\ \text{chromosphere} &\sim 10^{15} \leftrightarrow 10^{18}\ \text{m}^{-3} \\ \text{photosphere} &\sim 10^{23}\ \text{m}^{-3} \end{aligned}$$

(lecture notes from introductory Solar physics course (Roberts 1999).)

For the initial values of the number density through the grid we use the photospheric value 10^{23} m^{-3} for each cell. The photospheric gas will largely be un-ionised therefore we consider it to be atomic.

3.2.11.5 Pressure, P.

Now, as expressed in section 3.2.2, total pressure is comprised of thermal and magnetic components. As explained above, the photospheric material is treated as atomic gas. There is therefore only a single contribution of $k_{\text{B}}T$ from each hydrogen atom. If it was ionised, there would be twice the thermal pressure since both electrons and hydrogen ions would contribute.

Thus, we have :

$$\begin{aligned} P &= P_{\text{th}} + P_{\text{mag}} \\ &= nk_{\text{B}}T + \frac{B^2}{2\mu_0} \end{aligned}$$

which will typically take values in the range $8009 < P < 8049$ Pa, given :

$$\begin{aligned} n &= 10^{23}\ \text{m}^{-3} \\ T &= 5785\ \text{K} \\ B &= -100\ \text{G} \leftrightarrow +100\ \text{G} \end{aligned}$$

Our typical pressures are thus of the same order as that taken by Gary (2001), where he uses a photospheric gas pressure of 1250 Pa at a photospheric scale height of 250 km.

3.2.11.6 Length, L.

The typical initial value is 10^4 metres. Section 3.2.2 explains why the cell length must have a minimum size. Where cells fall below 100 metres they are removed from the model, as explained earlier. An initial cell length of 10^4 metres allows a significant amount of submergence of magnetic flux to occur before this minimum is reached.

Alternatively, initial cell length might be given a random value with a uniform distribution in the range $10^2 \leftrightarrow 10^4$ m. Unfortunately unavoidable numerical instability results when this approach is made.

3.2.11.7 Alfven Speed, C_A.

Alfven speed is a function of $|B|$ and the density of the medium, ρ :

$$C_A = \frac{B}{\sqrt{\mu_0 \rho}}$$

Let us consider the initial values in the model, given a mean modulus value of the magnetic field density of 50 G and the mass density $\rho = nm$ where $n = 10^{23}$ m^{-3} and $m = m_p$. We will neglect mass of electrons.

We find that initially $C_A \sim 340$ m s^{-1}

3.2.11.8 Cell Boundary Velocities, V_L, V_R.

Initially these are zero.

3.3 Detailed Description of some Specific Modules of the Model.

Figure 3.11 shows the ordering of the main processes of the model through the time-step. The model passes through this loop once per time-step.

We will now describe the detailed operation of some of these processes. We will address the major previously undescribed parts of the model. Only unduplicated information will be included.

3.3.1 Loading New Values into Old Values.

In order to use an iterative scheme with discrete time-steps it is vital that each time-step the functions of the program operate upon the values generated during the previous time-step to generate the new values. Correspondingly, these new values will then be the subject of the calculations during the

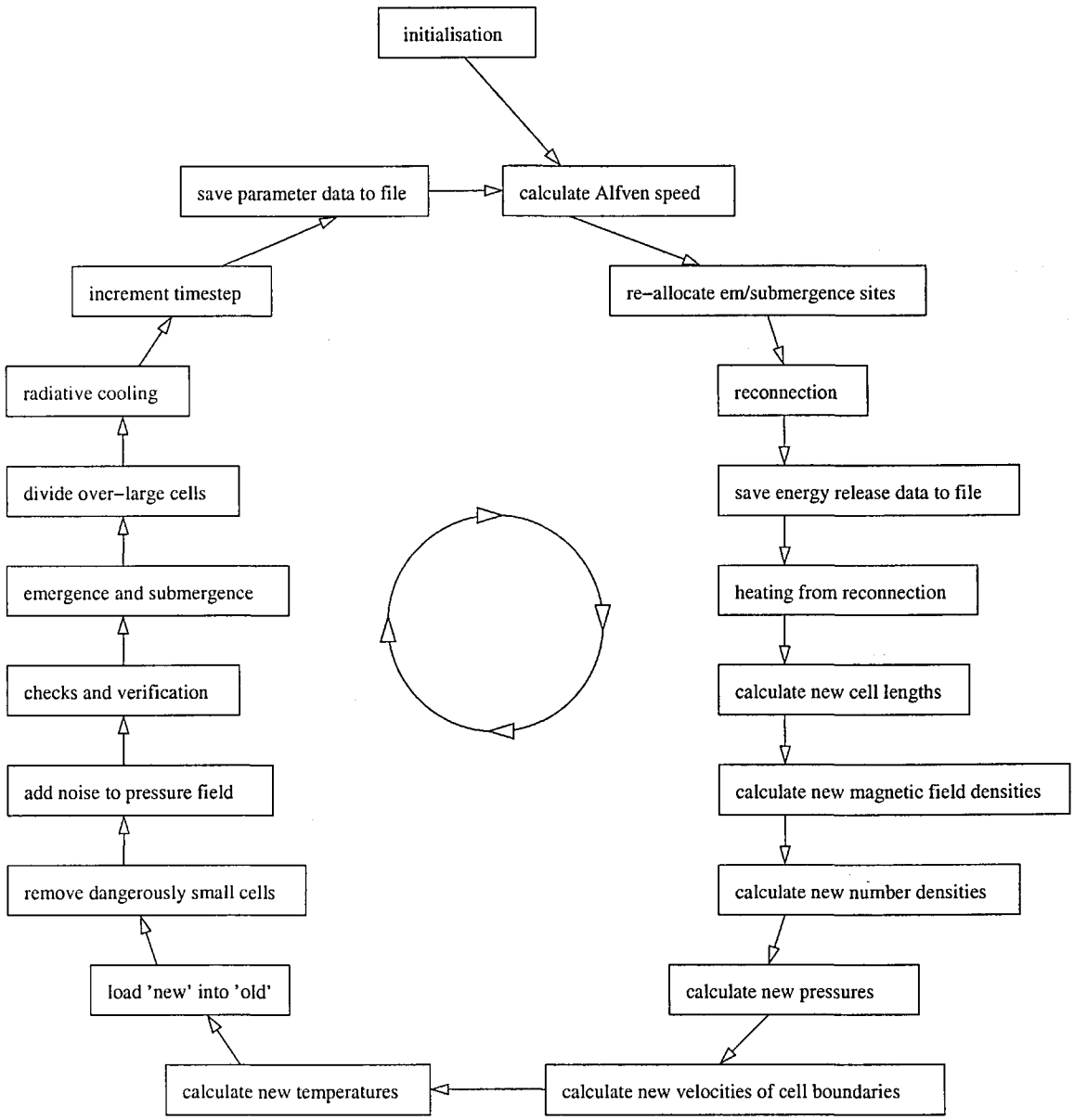

Figure 3.11: Flowchart showing ordering of modules and processes within the cycle of the model. Each loop represents one time-step.

following time-step. Also, some parameters are used for several different functions during each time-step therefore the code must remember the old value. Thus, the code holds both old and new values of cell parameters. During each time-step new cell parameters are generated from the old values, following which these new values are over-written on the old values, in readiness for the generation of further new values from these now old values.

3.3.2 Emergence/Submergence of Magnetic Flux.

On the actual Sun, we find that submergence of magnetic flux occurs at sites of cancellation by reconnection (Harvey et al. 1999). We also find that magnetic flux is capable of submergence and that submergence, which will occur even during the growth phase of active regions, is a strong process comparable to emergence (Rabin, Moore & Hagyard 1984).

Calculations by Simon, Title & Weiss (2001) show that the total Solar unsigned magnetic flux would decay through self-annihilation within a few days without the existence of a process for continual renewal. It is well known that bipolar magnetic flux emerges at a rate of $\sim$ few $\times 10^{22}$ Mx day^{-1}, and our model also features renewal of flux by emergence.

Each time-step submergence takes place across the entire grid, followed by flux emergence (if the emergence/submergence feature is turned on). Then the total flux within the grid is summed and this is compared with the total flux existing at the commencement of the run. Any deficit in flux is divided between all cells undergoing flux emergence, and the magnetic field density of these cells is increased to exactly account for this deficit.

The emergence/submergence feature may be turned on or off, and also the rate of emergence and submergence can be altered by varying two parameters. The first parameter is the replacement timescale of emergence/submergence, given as $t_{\mathrm{em/sub}}$. This tells the model how fast it must move material into flux emergence cells and out of submergence cells. Specifically, $t_{\mathrm{em/sub}}$ gives the number of seconds which would be taken to emerge or submerge M_{init}, the average mass of cells at the commencement of the run. Given that the observed timescale of overturning of material on the Sun at the granular ($\sim 2 \times 10^6$ m) level is something less than 20 minutes (Lawrence, Cadavid & Ruzmaikin 2001), the typical value used in the model is 10^3 seconds. Given that we must maintain conservation of mass, this flow rate is the same for each cell whether material is ingoing or outgoing.

Second, the emergence/submergence proportion, given as κ, tells the model what fraction of cells in the grid are involved in emergence and submergence. As the total number of cells in the model moves up or down the number of cells undergoing emergence/submergence will change pro rata. The typical value for this parameter is 0.1. Alternative values representing higher rates of flux emergence explored in the model are 0.2 and 0.4. For example, if there are 10^3 cells in a run and $\kappa = 0.1$ then there will initially be 50 cells undergoing emergence of magnetic flux and the same number undergoing submergence.

For the simplification of maintaining the conservation of mass, energy and magnetic flux, cells undergoing emergence or submergence are considered to act as a pair such that the same amount of material leaving one cell in a pair is added to the other cell at the same temperature.

Let us now make a calculated guess at the emergence rate of Solar magnetic flux.

Schrijver et al. (1997) and Hagenaar (2001) estimate a total Solar ephemeral region magnetic flux emergence rate of $\sim 7 \times 10^{22}$ Mx day^{-1} and $\sim 5 \times 10^{23}$ Mx day^{-1} respectively. We will take the most up-to-date estimate by Hagenaar (2001) of $\sim 5 \times 10^{23}$ Mx day^{-1}.

We will assume that this flux emergence occurs evenly across the Solar surface. Given that the area of the Solar surface, $A_\odot = 1.5 \times 10^{18}$ m^2, we have :

$$\dot{B}_\odot = \frac{5 \times 10^{23} \quad \text{Mx day}^{-1}}{1.5 \times 10^{18} \quad \text{m}^2}$$

$$= 3.9 \quad \text{G s}^{-1}$$

Let us calculate, on the other hand, the emerging flux within a typical cell in the continuous model. The replacement timescale of emergence/submergence, $t_{\text{em/sub}}$, will typically be 10^3 seconds. Consequently, the number of particles emerged into a cell each time-step, $t_{\text{em/sub}}$, is calculated by :

$$\Delta N = \overline{N} \, \frac{\delta t}{t_{\text{em/sub}}}$$

where :

$$\overline{N} \equiv \text{mean of } N_{\text{i}}$$

Typically, for a cell of length 10^3 m we will have $N = 10^{32}$. Thus, we take :

$$\overline{N} = 10^{32} \text{ particles}$$

$$t_{\text{em/sub}} = 10^3 \text{ s}$$

and we know $\delta t = 0.002$ s

This gives $\Delta N = 2 \times 10^{26}$ particles per time-step.

So, each time-step our emerging cell gains $\sim 2 \times 10^{26}$ particles to add to its reservoir of $\sim 10^{32}$ particles. Because the magnetic field is attached to the cell material, we can assume the proportion of magnetic field remaining after each time-step is the same as the proportion of particles remaining.

Thus, to calculate the new magnetic field density given the proportional removal of particles, we have :

$$B' = B\left(1 + \frac{\Delta N}{N}\right)$$

and

$$\begin{aligned} \Delta B &= B' - B \\ &= \frac{B\Delta B}{N} \\ &= 10^{-4}\ \mathrm{G} \end{aligned}$$

where $\Delta B \equiv$ change in magnetic field density.

For the typical magnetic field density let's assume a single uniform value of : $B = 50$ G

This gives us :

$$\begin{aligned} \dot{B}_{\mathrm{model}} &= \frac{\Delta B}{\delta t} \\ \dot{B}_{\mathrm{model}} &= 10^{-4}\ \mathrm{G}\ (\mathrm{time-step})^{-1} \\ &= 5.0 \times 10^{-2}\ \mathrm{G\ s^{-1}} \end{aligned}$$

Thus, to summarise, we have calculated :

$$\begin{aligned} \dot{B}_{\odot} &= 3.9\ \mathrm{G\ s^{-1}} \\ \dot{B}_{\mathrm{model}} &= 5.0 \times 10^{-2}\ \mathrm{G\ s^{-1}} \end{aligned}$$

The rate of change of magnetic flux produced by the model lies within two orders of magnitude of the figure believed for the sun.

We have arrived at this figure for the rate of change of magnetic flux produced by the model by designating the values of three parameters :

- $\kappa = 0.1$

  Thus, at any given time 1 in 20 cells are undergoing flux emergence. (add this to the 1 in 20 undergoing submergence to give the value of κ). The value of this parameter should not be too high otherwise the flux emergence/submergence will dominate the changing values of magnetic flux density. Rather, we wish the flux emergence to be present yet allow cells to persist sufficiently for magnetic reconnection to affect the magnetic flux densities. Also, there is a danger of numerical instability if κ is much higher than 0.1.

- $t_{\mathrm{em/sub}} = 10^3$ s

  As explained above, this value represents 1 cell-mass of material emerging or submerging within 10^3 s, which is in agreement with the observed timescale for flux emergence (Lawrence, Cadavid & Ruzmaikin 2001).

- Typical magnetic flux density, $B = 50$ G.

  This value lies somewhere in the range between coronal values ($B_{\rm co} \approx 1 \leftrightarrow 100$ G) and quiet region values (1 G).

Although we have chosen appropriate-seeming values for these parameters we can see a serious discrepancy between $\dot{B}_{\odot}$ and $\dot{B}_{\rm model}$. For this derivation we have assumed that the flux emergence taking place within cells within the model lattice is equivalent to that taking place within all the ephemeral regions but spread evenly over the whole Solar surface. Our model lattice may be closer to the quiet regions of the photosphere, in which case we have arrived at an unreasonably low estimate of $\dot{B}_{\rm model}$. We would be advised to allow emergence in a greater proportion of cells than the 1-in-20 we have supposed.

Let's run through a brief description of the process of emergence and submergence before we consider it in detail. The first action carried out is to calculate, given a particular value of the timescale of emergence/submergence, the number of particles which must be transferred per time-step into an emerging cell.

Next, each cell undergoing submergence has its complement of particles reduced by this number. The new values of number density, magnetic field density and pressure are calculated using, respectively, new particle number and volume, a pro rata reduction of magnetic field density in proportion with the reduction in particle number, and the ideal gas law.

When the submerging cell has so few particles that the present subtraction of particles causes its mass to drop below zero, the cell is removed from the grid. A replacement cell for the continuation of submergence of magnetic flux is randomly selected and the two cells adjoining the removed cell are deemed to expand equally into the space formerly occupied by the submerged cell. The length, magnetic field density, number density and pressure of these cells are recalculated, given the new cell lengths.

Next, the present mass of the grid is summed and compared with the total mass remembered from the commencement of the run. The deficit is divided by the number of cells undergoing emergence of magnetic flux and this amount of mass is added to these emerging cells. This ensures conservation of mass. The new value of number density is calculated given the new particle number. Given that $E_{\rm th} = \frac{3}{2} N k_{\rm B} T$ the new value of temperature is calculated assuming equilibration of (1) the cell material prior to emergence and (2) the new emerged material, which enters the cell with the same temperature as the cell from which it is considered to have submerged. The particle pressure parameter is calculated according to the Ideal Gas Law. The new magnetic field density of each cell is calculated, as described later in this section.

Let's describe the flux submergence process in further detail. This process is carried out prior to emergence. We showed earlier how we determine the number of particles ΔN emerging into or submerging from a cell during a time-step. The number of particles within a submerging cell is diminished by ΔN :

$$N' = N - \Delta N$$

The magnetic Reynolds number is high and so the field is attached to the plasma material. Therefore magnetic flux is lost in the same proportion as the plasma. The new number density and pressure (thermal and magnetic pressure components) are then calculated :

$$B' = B\left(1 - \frac{\Delta N}{N}\right)$$

and

$$n' = \frac{N'}{L\ A_{\text{grid}}}$$

and

$$P'_{\text{total}} = \frac{N' k_{\text{B}} T}{L\ A_{\text{grid}}} + \frac{(B')^2}{2\mu_0}$$

Let's now describe in detail the flux emergence process. The number of particles increases by ΔN in cells designated for the receipt of emerging magnetic flux :

$$N' = N + \Delta N$$

Consequently, the number density and temperature are recalculated :

$$n' = \frac{N'}{L\ A_{\text{grid}}}$$

Each emergence cell is paired with a submergence cell, meaning that (for the energy conservation) the temperature of the material emerged into a cell is deemed to emerge at the temperature of the submerging cell.

Thus, calculating new temperature of a cell, we have : thermal energy of a cell after emergence equals a weighted sum of its thermal energy prior to emergence plus the thermal energy of the emerged material.

Equivalently,

$$E'_{\text{cell,th}} = E_{\text{cell,th}} + E_{\text{em,th}}$$

Hence,

$$\frac{3}{2}\ N'_{\text{cell}}\ k_{\text{B}}\ T'_{\text{cell}} = \frac{3}{2}\ N_{\text{cell}}\ k_{\text{B}}\ T_{\text{cell}} + \frac{3}{2}\ \Delta N\ k_{\text{B}}\ T_{\text{em}}$$

Rearranging,

$$T'_{\rm cell} = \frac{N_{\rm cell}\, T_{\rm cell} + \Delta N\, T_{\rm em}}{N'_{\rm cell}}$$

where,

$$T_{\rm em} \equiv \text{temperature of emerging material}$$

Also, we calculate new pressure :

$$P' = \frac{N' k_{\rm B} T'}{L\, A_{\rm grid}} + \frac{B^2}{2\mu_0}$$

The new values of magnetic field density are now calculated according to a method which ensures conservation of magnetic flux. We mentioned earlier that the model sums the total flux within the grid at the beginning of the model and remembers this figure. Let us remember that by this point in the time-step the reconnection and submergence of magnetic flux has already occurred. Thus, the magnetic flux within each cell is in a depleted state. The total magnetic flux within the grid is summed and subtracted from the initial total magnetic flux, $\Phi_{\rm grid,init}$, which the model remembers. The result, $\Phi_{\rm grid,lost}$, which represents the total loss of magnetic flux (caused by reconnection and submergence) during the time-step is then divided equally between the cells which are emerging magnetic flux.

Thus, we have $\Delta\Phi$ for each emergence cell. The new magnetic field density within each of the emerging cells is calculated according to these steps :

1. Sum flux within model and subtract from remembered initial flux to arrive at total flux deficit.

$$\Phi_{\rm grid} = \sum \Phi_{\rm i} = \sum (B_{\rm i}\, L_{\rm i}\, W)$$

$$\Phi_{\rm grid,lost} = \Phi_{\rm grid,init} - \Phi_{\rm grid}$$

2. Divide flux deficit equally between cells emerging flux.

$$\Phi_{\rm em} = \frac{\Phi_{\rm grid,lost}}{\nu_{\rm cells}}$$

3. Calculate new magnetic field density for each emerging flux cell.

$$B' = B + \frac{\Phi_{\rm em}}{L\, W}$$

3.3.2.1 Regular Flux-Collision Imposed upon the Model.

An element of randomness is introduced by the decision process which designates the locations of cells undergoing emergence and submergence of magnetic flux. Each time-step, a test is conducted to determine whether the locations of emergence/submergence sites should be re-allocated. If the

re-allocation occurs the new sites of emergence and submergence are determined randomly. Also, the time allowed to elapse between successive re-allocations is itself random. Specifically, each time-step there is a random 1 in 10^5 chance of the re-allocation occurring. In practice this means that the waiting-time between successive re-allocations will be randomly distributed with a mean of $\sim 8 \times 10^4$ time-steps, giving approximately 25 randomly distributed re-allocations during a typical model run.

The Solar convective motions in the photosphere cause the emergence, spreading, collision and consequent submergence of material at the top of the photosphere. Flux tubes gather at the edges of convection cells which results in regions of greater magnetic flux density.

It seemed interesting to construct a form of the model such that the material was actively forced to emerge, spread, collide and submerge repeatedly throughout the grid in regular units (many units in order to average the statistics). This is done by alternating the sites of emergence and submergence along the grid and ensuring that these sites are regularly spaced (in terms of physical distance within each interval). The positions of the emergence and submergence cells is fixed at the commencement of a run such that there are 20 cells in each interval (between sites of emergence of magnetic flux). This corresponds to the distance, d, as shown in figure 3.12. However, once the model is running, while remaining the same physical distance, the interval may consist of a greater, or lesser, number of cells than 20 owing to the emergence and submergence of fresh magnetic flux which causes enlargement and shrinkage of cells. The physical positions of the emergence and submergence sites must remain fixed, therefore re-setting of the position of flux emergence and submergence must occur frequently to maintain these positions. Therefore, each time-step there is a random $\frac{1}{100}$ probability of the re-allocation occurring. In this case the typical waiting-time between re-allocations of the emergence and submergence sites is only ~ 100 time-steps.

Figure 3.13 shows how the forced alternation of emergence and submergence sites produces definite regions of collision.

Compare this to the alternating submergence and emergence caused by the photospheric granulation and illustrated schematically in figure 3.14. Typical length-scales would be few $\times 10^6$ m (Lawrence, Cadavid & Ruzmaikin 2001).

The main purpose of designing this particular specialised configuration of the model is to make comparisons with the unadulterated model using randomly determined locations of emergence/submergence and see what effect the imposition of an emergence/submergence field has upon the results.

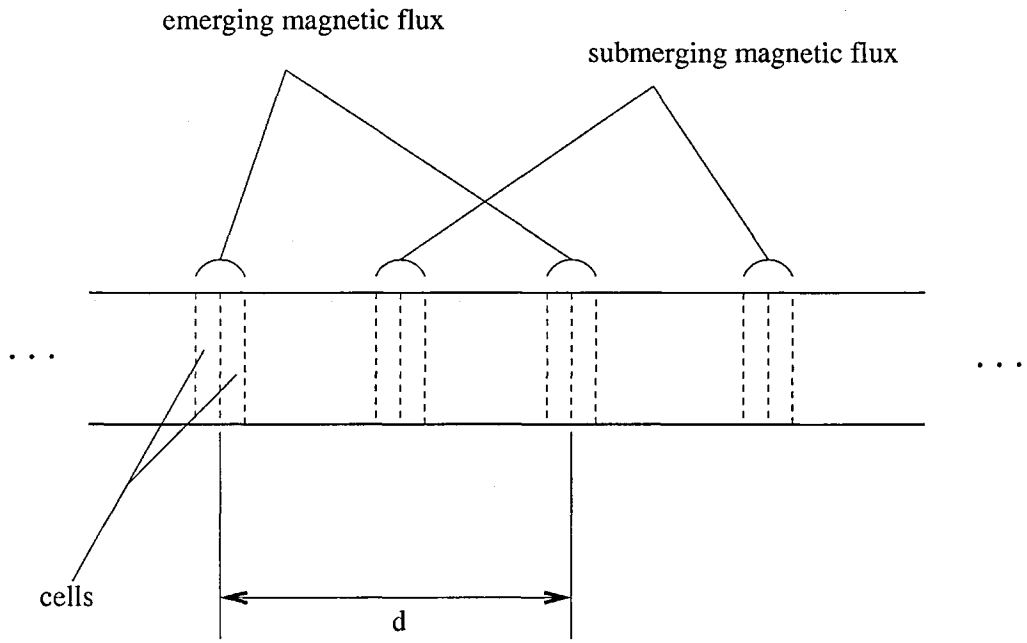

Figure 3.12: Detail of model grid for flux-collision configuration of the model.

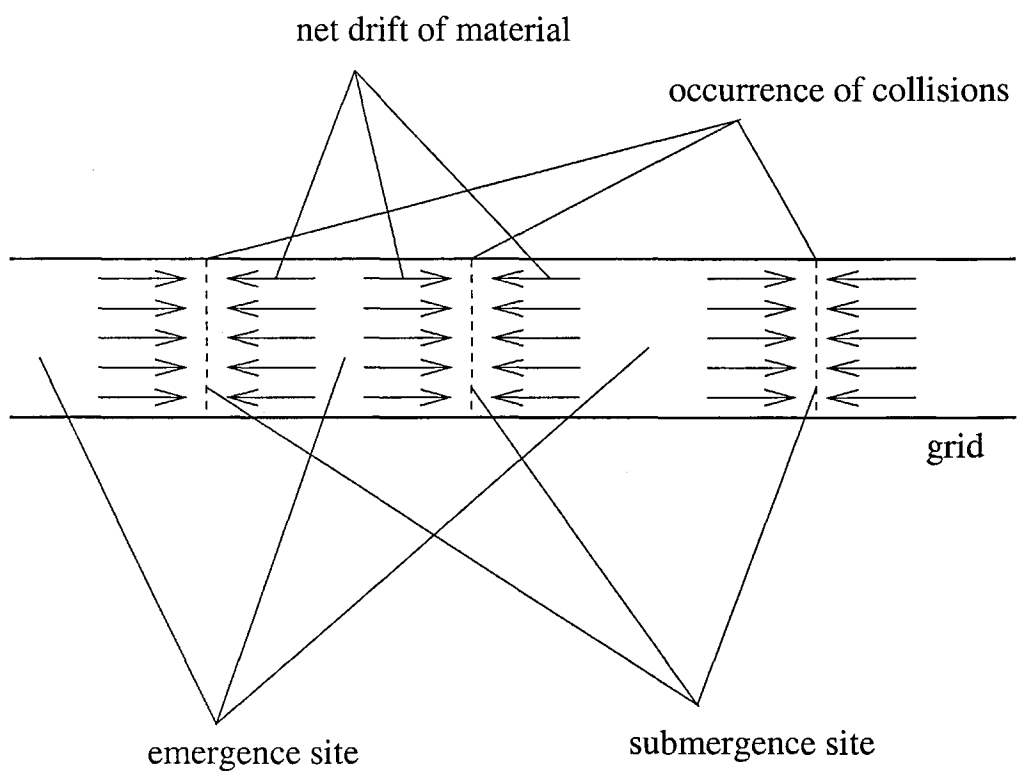

Figure 3.13: Drift of cell material caused by alternating emergence and submergence in collision model.

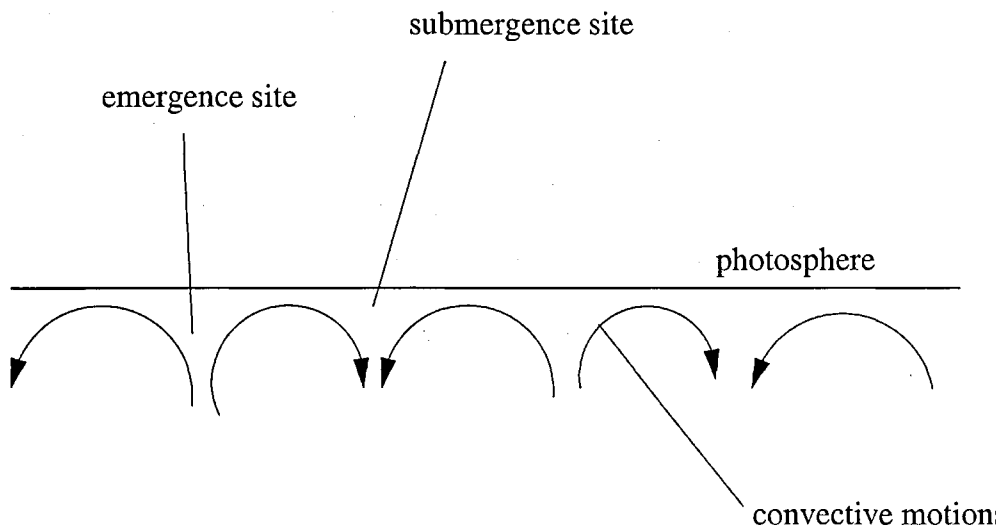

Figure 3.14: Schematic of Solar granulation.

3.3.3 Calculate Alfven Speed.

The Alfven speed within each cell is necessary for the calculation of energy release through magnetic reconnection, therefore prior to running the reconnection module, Alfven speed is calculated for each cell in the grid according to :

$$C_{\mathrm{A}} = \frac{|B|}{\sqrt{\mu_0\,\rho}}$$

3.3.4 Reconnection.

Reconnection is the method by which magnetic energy is released in the grid and this occurs at the boundaries between pairs of cells. Further, reconnection is only allowed at each site where opposite polarity magnetic fluxes meet. Each time-step the grid is scanned for such sites, and at these places the reconnection mechanism performs its task. Where reconnection takes place at a boundary the energy release occurring in each cell is calculated. Thus, after the whole grid has been scanned for reconnection each cell will contain a parameter describing the total magnetic energy released within that cell during the reconnection process. This parameter has one component from reconnection taking place with each of the cell's neighbours (one or both of these components may be zero).

The reconnection method which we will here describe at length is the one usually used in the model, and will henceforth be referred to as 'standard'.

We will now run through the details of this method and consider a generic pair of cells, i and $i+1$, which have anti-parallel magnetic flux.

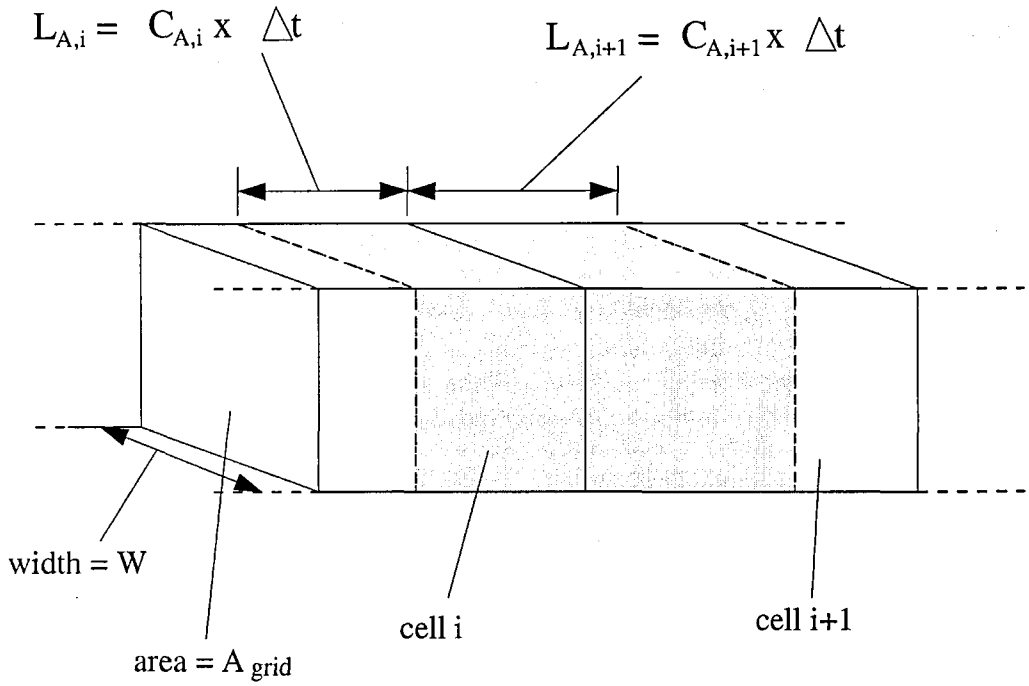

Figure 3.15: Schematic of reconnection about a cell boundary.

1. Dere (1996) find that the Alfven speed more appropriately accounts for the rate of reconnection than the timescales of resistive diffusion or tearing-mode reconnection. Therefore, we consider that during one time-step the amount of magnetic flux available for reconnection is determined by the Alfven speed. Either side of the boundary, we calculate the distance equal to the Alfven speed multiplied by the time-step. These distances are shown by arrows in figure 3.15. Let us note that although we use $A_{\rm grid} = 10^6$ m^2 and $W = 10^3$ m these values have no effect on our conclusions since we might have set these equal to unity, in which case our calculated energy would be per unit cross-sectional area of the grid.

2. For either cell, if this distance exceeds the cell length :

$$L_{\rm i,Alf} > L_{\rm i} \quad \text{or} \quad L_{\rm i+1,Alf} > L_{\rm i+1}$$

then we set this distance equal to the cell length.

3. Next, we calculate the amount of flux represented contained within this length for each cell. We use

$$\Phi_{\rm i,Alf} = L_{\rm i,Alf} W B_{\rm i}$$

4. Magnetic flux within the two interacting cells annihilates therefore the same amount of flux within each cell must be destroyed during the reconnection process. Thus, we compare

$\Phi_{\mathrm{i,Alf}}$ and $\Phi_{\mathrm{i+1,Alf}}$ and set them both equal to the value of the smaller of these. These parameters represent the flux available for reconnection.

5. Thus, we have now calculated available flux within the two cells either side of the boundary. Now, the magnetic flux for each cell is divided by the magnetic field density of each cell (B_{i} and $B_{\mathrm{i+1}}$) to give us equivalent lengths, $L'_{\mathrm{i,Alf}}$ and $L'_{\mathrm{i+1,Alf}}$, inside which the reconnection occurs. Thus,

$$L'_{\mathrm{i,Alf}} = \frac{\Phi_{\mathrm{i,Alf}}}{W L_{\mathrm{i,Alf}}}$$

6. We are now in a position to calculate the energy released by the reconnection. The model assumes that all of the magnetic energy is released in the volume spanned by $L'_{\mathrm{i,Alf}}$ in cell i and $L'_{\mathrm{i+1,Alf}}$ in cell $i+1$ is released.

$$E_{\mathrm{i,rec}} = \frac{B_{\mathrm{i}}^2 L'_{\mathrm{i,Alf}} A_{\mathrm{grid}}}{2\mu_0} \quad \text{and} \quad E_{\mathrm{i+1,rec}} = \frac{B_{\mathrm{i+1}}^2 L'_{\mathrm{i+1,Alf}} A_{\mathrm{grid}}}{2\mu_0}$$

The value $E_{\mathrm{i,rec}}$ is added to the energy release parameter of cell i, and $E_{\mathrm{i+1,rec}}$ to that of cell $i+1$.

7. Next, we calculate the pre-reconnection magnetic energy stored in cell i and i+1.

$$E_{\mathrm{i,total}} = \frac{B_{\mathrm{i}}^2 L_{\mathrm{i}} A_{\mathrm{grid}}}{2\mu_0} \quad \text{and} \quad E_{\mathrm{i+1,total}} = \frac{B_{\mathrm{i+1}}^2 L_{\mathrm{i+1}} A_{\mathrm{grid}}}{2\mu_0}$$

and use the above-calculated values of energy-released to calculate post-reconnection magnetic energy remaining in the two cells :

$$E'_{\mathrm{i,total}} = E_{\mathrm{i,total}} - E_{\mathrm{i,rec}} \quad \text{and} \quad E'_{\mathrm{i+1,total}} = E_{\mathrm{i+1,total}} - E_{\mathrm{i+1,rec}}$$

8. Given the remaining magnetic energy in the cells, we must now calculate new B for each cell :

$$B'_{\mathrm{i}} = \sqrt{\frac{2E'_{\mathrm{i,total}}\,\mu_0}{L_{\mathrm{i}} A_{\mathrm{grid}}}} \quad \text{and} \quad B'_{\mathrm{i+1}} = \sqrt{\frac{2E'_{\mathrm{i+1,total}}\,\mu_0}{L_{\mathrm{i+1}} A_{\mathrm{grid}}}}$$

Thus, the model has calculated, (1) the energy released with respect to the boundaries on each side of each cell, and (2) the new reduced magnetic flux.

As explained earlier when we run the model we have the expectation of a single event occuring at any one time. Therefore, the reconnection module scans the grid each time-step after having performed the reconnection process and locates the cell within which the greatest energy release has occurred. We must consider this to be the location of the reconnection event. Also, the total energy released in the grid is summed each time-step.

During the useful period of a run (10^6 to 3×10^6 time-steps (see section 3.2.10.2)) reconnection data, described below, is saved to file every 10 time-steps.

Thus, we are able to compare the total energy released in the whole grid with that released in the biggest event. Part of the justification for considering that only one event occurs and characterising it as the site of greatest energy release is that we find that the profiles of the total energy release and the greatest energy release are highly correlated, and that the total grid energy release can be characterised as a superposition of the energy released from the single largest reconnection event plus a background level. This is demonstrated in section 3.6.2. Also, in general there is typically only one large flaring event taking place on the Sun itself at any given time. Energy released within other cells is much smaller and behaves like noise additional to the far greater contribution of the single greatest event in the grid.

During this interval of from 10^6 time-steps to 3×10^6 time-steps, data is saved to file every 10 time-steps. The change over 10 time-steps (0.02 s) will be small. The saved data consists of : location in the grid of maximum energy release, value of that energy release and value of the total grid energy release. Thus, the reconnection mechanism produces three time-series. We will explain later how this is processed to give us event-size distributions.

We should note that this mechanism for representing reconnection in the model can obviously be altered as we see fit in order to determine what differences the details of the reconnection mechanism makes to the distributions produced. There are some particular variants used in the model. These are :

- Threshold.

  A threshold is introduced which must be exceeded for reconnection to occur. The modulus of the disparity between the values of the magnetic field densities of two adjacent cells must exceed 50 G or 20 G for reconnection to be allowed. As before, the magnetic flux of the two adjacent cells must be anti-parallel. In the Introduction we described self-organised criticality (SOC) and learnt that SOC requires the existence of a gradient which, when exceeded, results in the occurrence of an avalanche with a power-law distribution. The addition to reconnection of a threshold criterion may introduce an element of SOC into the model.

- Completely randomised energy release.

  The calculated energy release which takes place between two adjacent cells is multiplied by a random number, ζ, uniformly distributed in the range $0 < \zeta < 1$. We recall that a single parameter value for a given cell represents an average of the magnetic field density for that cell, yet we would expect there to be a continuum of values throughout the cell, and also unresolved

anti-parallel flux. We can consider this random element as reflecting this unresolved field, which would increase, reduce or curtail the reconnection in a way undeterminable by the model.

- Partially randomised energy release.

  The energy release, E, calculated for each cell by the unaltered reconnection mechanism is multiplied by a random number, ζ, uniformly distributed in the range $0.9 < \zeta < 1.1$.

We can imagine that any number of similar alternative methods might be used instead, each a variation on this theme. However, the purpose of the model is not to attempt a complete and accurate physical description but to obtain the statistical essence of the problem. Thus, the method used satisfies the essential prerequisites insofar as there is a linear dependency upon the magnetic energy density and also upon the Alfven speed in the material (itself dependent upon magnetic field density).

3.3.5 Checking Procedures.

There are modules which perform the function of confirming that there is no obviously unphysical behaviour occurring. Such behaviour would show that the model has broken down and can no longer be relied upon. In particular, if any cell shows negative length or pressure then the model ceases running.

Since the size resolution can be taken to be approximately the mean cell length, we must prevent cells from growing to arbitrary lengths. For this reason, cells found to have length equal to or greater than 1.5 multiplied by the initial mean cell length of the grid are divided into two identical cells each with half the length and particle number of the original single cell. These cells retain the same magnetic flux density, number density and temperature of the original.

To justify the model being temporally discrete we must ensure that changes in the parameter values are smooth. The emergence/submergence module ensures smoothness in N, and thus also in n. Smoothness in P is dependent upon smoothness in L, since Volume $\propto L$ and $P' = P\left(\frac{V}{V'}\right)^{\gamma}$. Also, smoothness in B is dependent upon smoothness in L because $B' = B\left(\frac{L}{L'}\right)$. We have $T' = \frac{P'}{nk_B}$, therefore smoothness in T also depends upon smoothness in L. Thus, to confirm smoothness in L the model checks that changes in the velocities of the cell boundaries are smooth. In particular, the model will halt if the change in velocity of any cell boundary is greater than 1/10 of that boundary's velocity.

We cannot rely upon our 1-D fluid laws unless the bulk motion within the grid is always subsonic (i.e. $V_{\text{i,boundary}} << C_s$). Therefore the model will check each time-step that we have :

$$V_{\mathrm{i,boundary}} < \frac{1}{10} C_{\mathrm{s}}$$

3.3.6 Updating Magnetic Field Densities.

Remembering that the parameters within a cell represent idealised averages of parameters along the entire length of the cell, the model must calculate the new magnetic field density within a cell to reflect the re-sizing of the cell and conservation of magnetic flux within that cell.

Thus,

$$B' = B\left(\frac{L}{L'}\right)$$

3.3.7 Flexibility in Implementation.

So, we can see that there are many ways in which we can introduce variations to the basic model. Some of these are :

- add noise to the pressure distribution. We can vary the level of this perturbation.
- use power-law (random) initial magnetic field density distributions instead of flat (random) distribution.
- introduce random factors into the calculation of magnetic energy release.
- make alterations to the detail of the reconnection mechanism.
- introduce different methods of counting energy release events.
- use a variety of initial cell lengths.
- use different sized grids (number of cells).
- switch reconnection off.
- switch emergence/submergence off.
- change parameter values of emergence/submergence of magnetic flux (fraction of cells undergoing this process, κ, and replacement time-scale, $t_{\mathrm{em/sub}}$).

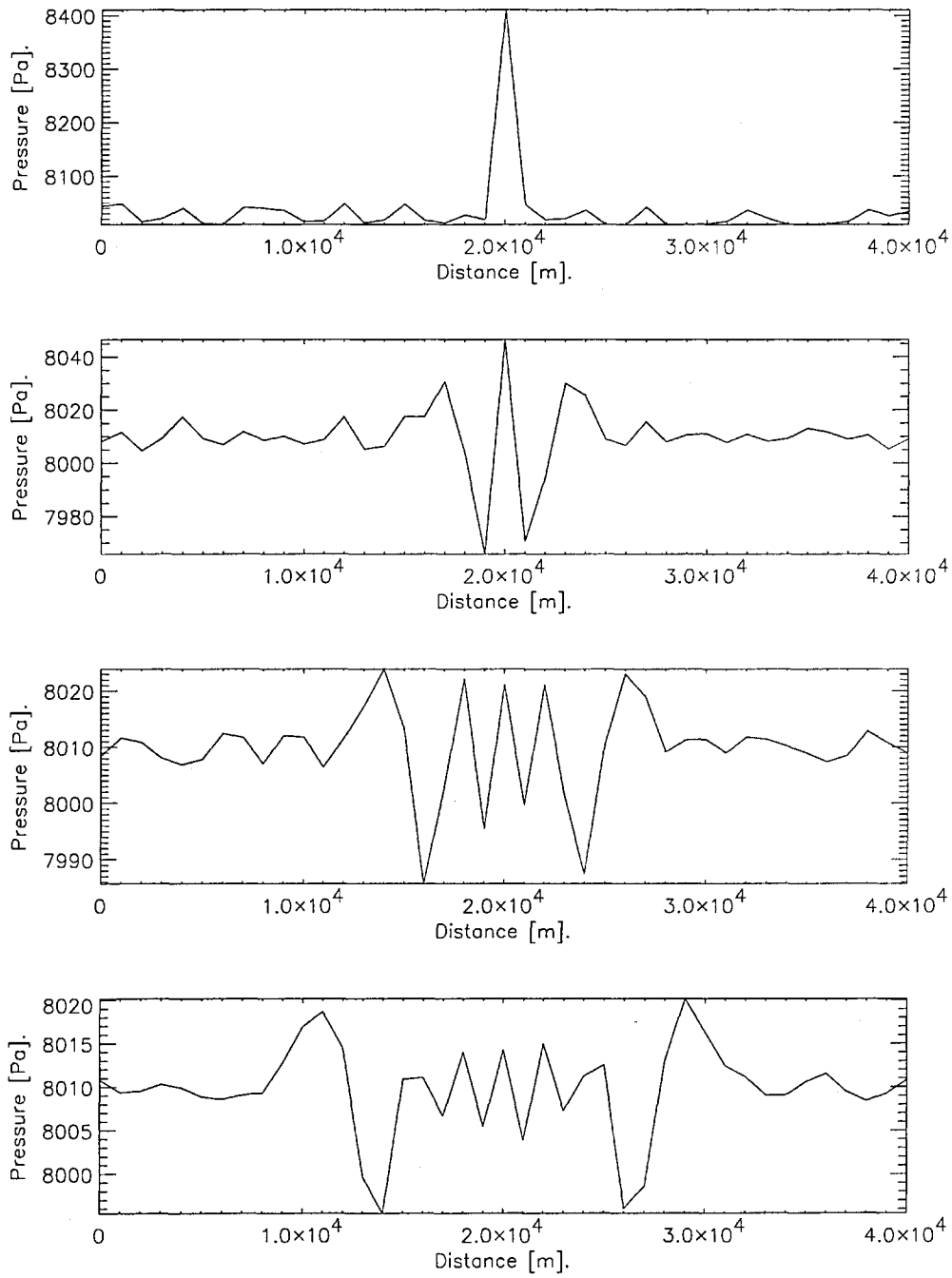

Figure 3.16: Demonstration of fluid behaviour in 1-D grid.

3.4 Validation of Correct Functioning, Assumptions, Stability and Sensitivity Analysis.

3.4.1 Correct Fluid Behaviour.

We can show that the 1-D fluid behaviour of the model is accurate by demonstrating correct propagation of pressure waves at the sound speed of the fluid.

In figure 3.16 we have a simple run, without reconnection or emergence/submergence. There are 100 cells each of length 10^3 m. There is an initial perturbation in the pressure field of +5% in a cell near the centre position. The images shown are at intervals of 200 time-steps, equivalent to 0.4 s. We can see that the waves propagate approximately sinusoidally and can make an estimate of sound speed :

$$\sim 7.5 \times 10^3 \text{ m s}^{-1}$$

Let us compare this with that calculated in section 3.2.2 from the thermodynamic properties of the fluid :

$$\sim 8.9 \times 10^3 \text{ m s}^{-1}$$

We can be pleased that the sound speed within the model grid is close to the value we would expect from a real physical fluid with the same properties. Thus, we find that the model behaves like a real fluid closely enough for our purposes.

3.4.2 Steady-State.

Where the parameter values and initial state are such that the model does not become numerically unstable the model enters a steady state. In every case it is found that the parameters settle into values which are not unphysical. Thus the particular values of these parameters provide persuasive evidence that the model is operating sensibly. The representative example of the model having settled into a steady state which we present in this section is one where our initial conditions and parameters are what we consider to be typical - a benchmark against which the results generated by other model runs may be compared. These parameters in the initial state take the typical values as given in the Definition of Commonly Used Terms given at the beginning of the thesis.

Table 3.1 compares initial conditions against evolved stable cell parameter values. The rightmost column gives settled stable values. There is a small deviation around these values.

We define :

$$\sum M \equiv \text{total grid mass}$$
$$\sum L \equiv \text{total grid length}$$
$$\sum \phi \equiv \text{total grid magnetic flux}$$
$$N_{\text{cells}} \equiv \text{number of cells}$$

Mean temperature has been weighted by number of particles, N, within each cell.

Thus the total mass and magnetic flux remain unchanged. As we have explained earlier, the model ensures that there is conservation of mass and magnetic flux. The total length of the grid remains unchanged. Were this not the case we could not trust the 1-D fluid laws within our model. The evolved settled number of cells settles to a value only marginally higher than the inital value and the remaining cell parameters are all also very close to the initial values. The mean cell boundary velocity is only 3.31 m s^{-1} compared with the mean of the absolute values of cell boundary velocites, 254 m s^{-1}, therefore the cells within the grid are not accelerating but remain stable. It is clear therefore that the grid settles into a steady equilibrium state.

3.4.3 Assumptions.

Let us itemise the assumptions made in the model.

- expansion/contraction of cells is reversible and adiabatic.
- bulk motion is always subsonic.
- photospheric material is unionised atomic gas, and we therefore do not need to consider a pressure contribution from electrons.
- it is meaningful to summarise in a single average value the whole range of values of each cell parameter within each cell, and it is acceptable that we can neglect smaller unresolved concentrations.
- for the reconnection mechanism to be meaningful we assume that magnetic reconnection propagates at the Alfven speed.
- radiative cooling mechanism is based upon the assumption that the top surface of the grid radiates a black-body spectrum.
- background temperature of 5785 K.
- there is no net change in the total magnetic flux within cells.

Parameters	Initial Values ($t = 0$)	Evolved Values ($t = 6000$ s)
$\sum M$	1.673×10^8 kg	1.673×10^8 kg
$\sum L$	10^7 m	10^7 m
$\sum \phi$	4.780×10^{15} Mx	4.780×10^{15} Mx
N_{cells}	10^3 cells	1175 ± 25 cells
$\overline{P}$	8023.3 Pa	8138 Pa
σ_P	13.70 Pa	323.8 Pa
$\overline{n}$	10^{23} m^{-3}	1.003×10^{23} m^{-3}
σ_n	0.0 m^{-3}	6.9×10^{21} m^{-3}
$\overline{T}$	5800 K	5868 K
σ_T	0 K	694 K
$\overline{L}$	10^4 m	8510 m
σ_L	0.0 m	2448 m
$\overline{B}$	0.02 G	7.0 G
σ_B	55.9 G	188 G
$\overline{\lvert B \rvert}$	47.80 G	74.6 G
$\overline{v_{\text{bound}}}$	0.0 m s^{-1}	3.31 m s^{-1}
$\sigma_{v_{\text{bound}}}$	0.0 m s^{-1}	304 m s^{-1}
$\overline{\lvert v_{\text{bound}} \rvert}$	0.0 m s^{-1}	254 m s^{-1}

Table 3.1: Comparison of initial and evolved model parameters in a steady state (note that $\sigma \equiv$ standard deviation).

3.4.4 Sensitivity Analysis.

The figures in this section all use the same axes-ranges for ease of comparison. Each run of the model starts with the cells having a specific length allocated, usually 10^4 m, and a random uniform distribution of magnetic field density in the range $-100 \leftrightarrow +100$ G (giving $\overline{|B|} = 50$ G). We can thus easily calculate the mean absolute initial magnetic field density and mean initial cell flux for each run. Where we include in the text plots showing the distributions of unipolar region sizes, magnetic flux density and magnetic flux, we have found it useful to also draw vertical dotted lines showing these mean initial values (L_{unipolar}, B, ϕ).

When plotting log-log distributions of magnetic field density and magnetic flux we have found that in the region above the initial levels (marked by dotted lines) where at the commencement of the run there were zero bin counts, there are often power-laws produced. These regions represent magnetic flux processed by the model and so we shall fit lines to only points lying above the dotted lines.

We will produce plots on log-log or log-linear axes giving distributions of cell parameters, such as magnetic field density and magnetic flux, where the y-values will give 'log(P.D.F.)'. 'P.D.F.' refers to 'probability density function'. This means that our data has been counted into bins then normalised according to the width of each bin. In other words, for each bin the number of counts is divided by the width of the bin. This figure then gives us the y-value for that bin.

Where lines are fitted to plotted points, the least-squares method will be used.

3.4.4.1 Effect of Noise upon the Model.

We would like to determine the effect that a degree of stochastic excitation has on the model. Perhaps the results are robust with respect to noise? Perhaps we need noise to obtain nice ordered power-law (or otherwise) distributions? Perhaps noise will complicate any nice ordered results?

Noise may be introduced into any of the cell parameters. We already have a system (emergence and submergence of magnetic flux) for continuously changing the magnetic flux within cell. Therefore we instead introduce noise into the thermodynamic properties of the model. Pressure embodies within it number density and temperature therefore noise is introduced into the pressure field. If we consider the pressure at any point on the surface of the Earth at sea level as a stationary time-series we rarely find pressure differences from the mean greater than one part in a hundred. One part in a hundred would represent a severe atmospheric disturbance. We will therefore restrict the noise applied to less than or equal to one part in a hundred.

The noise is applied every 500 timesteps. This equates to one second of model time. When this

occurs each cell in the grid individually has noise added to its pressure level. For cell i this addition takes the form of :

$$P_i' = P_i \times (1 + \alpha_i)$$

α is a multiplier which is random and uniformly distributed within the following ranges, depending on the particular run chosen :

- $-0.001 \leftrightarrow +0.001$
- $-0.005 \leftrightarrow +0.005$
- $-0.01 \leftrightarrow +0.01$

We can run the model for each of these three noise regimes with the typical initial parameter values, as per the Definition of Commonly Used Terms given at the beginning of the thesis.

Figure 3.17 compares distributions of magnetic flux density for runs without noise and each of the three noise levels. The plots show power-law-like distributions although the gradients vary.

Figure 3.18 compares distributions of magnetic flux for runs without noise and each of the three noise levels. Again, the plots show power-law-like distributions although the gradients vary.

Figure 3.19 compares distributions on log-linear axes of sizes of unipolar regions for runs without noise and each of the three noise levels. Data at the high end of these four plots is poor resulting in the large error bars, and the apparent turn-over at the far bottom end of the plots might be due to edge effects.

Figures 3.20 and 3.21 compare distributions of event-sizes counted by peak release rate and integrated energy release, respectively. The distributions are reasonable power-law-like distributions and there is no substantial difference in either the gradients or positions of the profiles between each of the different noise levels, although the x-ranges vary.

On balance, there is no indication of substantial dependence of the distributions upon the noise level.

3.4.4.2 Arbitrary Parameters.

The model contains parameters which are not meaningful in physical terms and yet are unfortunately necessary for the operation of the model. The values of these parameters are not derivable from observations but instead must be chosen by us. Therefore it needs to be true that the general properties of the results have very little dependency upon the particular values of these parameters.

Minimum Cell Size.

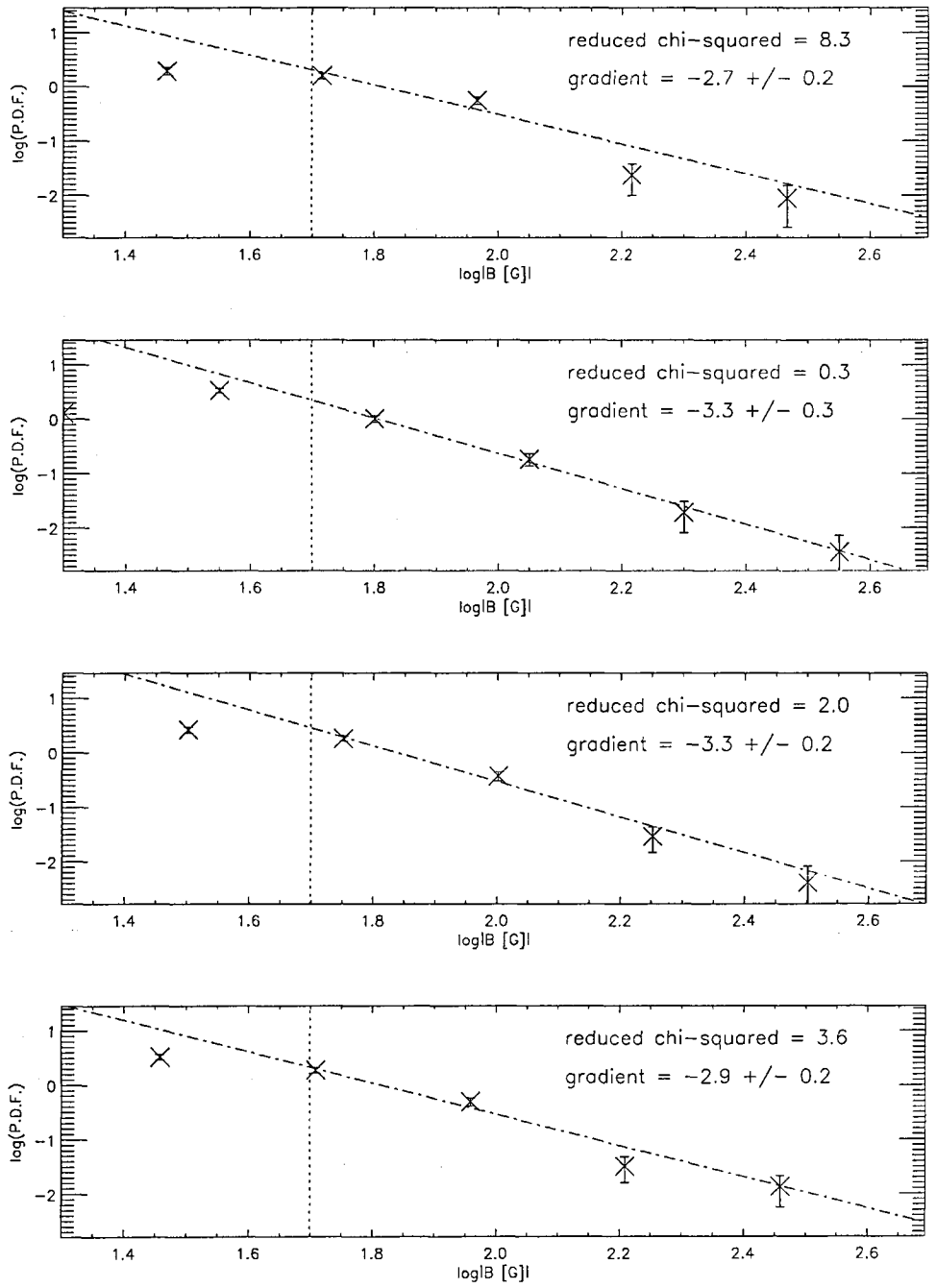

Figure 3.17: Distributions of magnetic flux density in runs comparing different noise levels; 10^3 cells; bin-size = 0.25. Dotted lines mark mean initial magnetic field density. Initial cell length = 10^4 m. Top: run without noise. Second: $\frac{\psi}{P} = 0.001$. Third: $\frac{\psi}{P} = 0.005$. Fourth: $\frac{\psi}{P} = 0.01$.

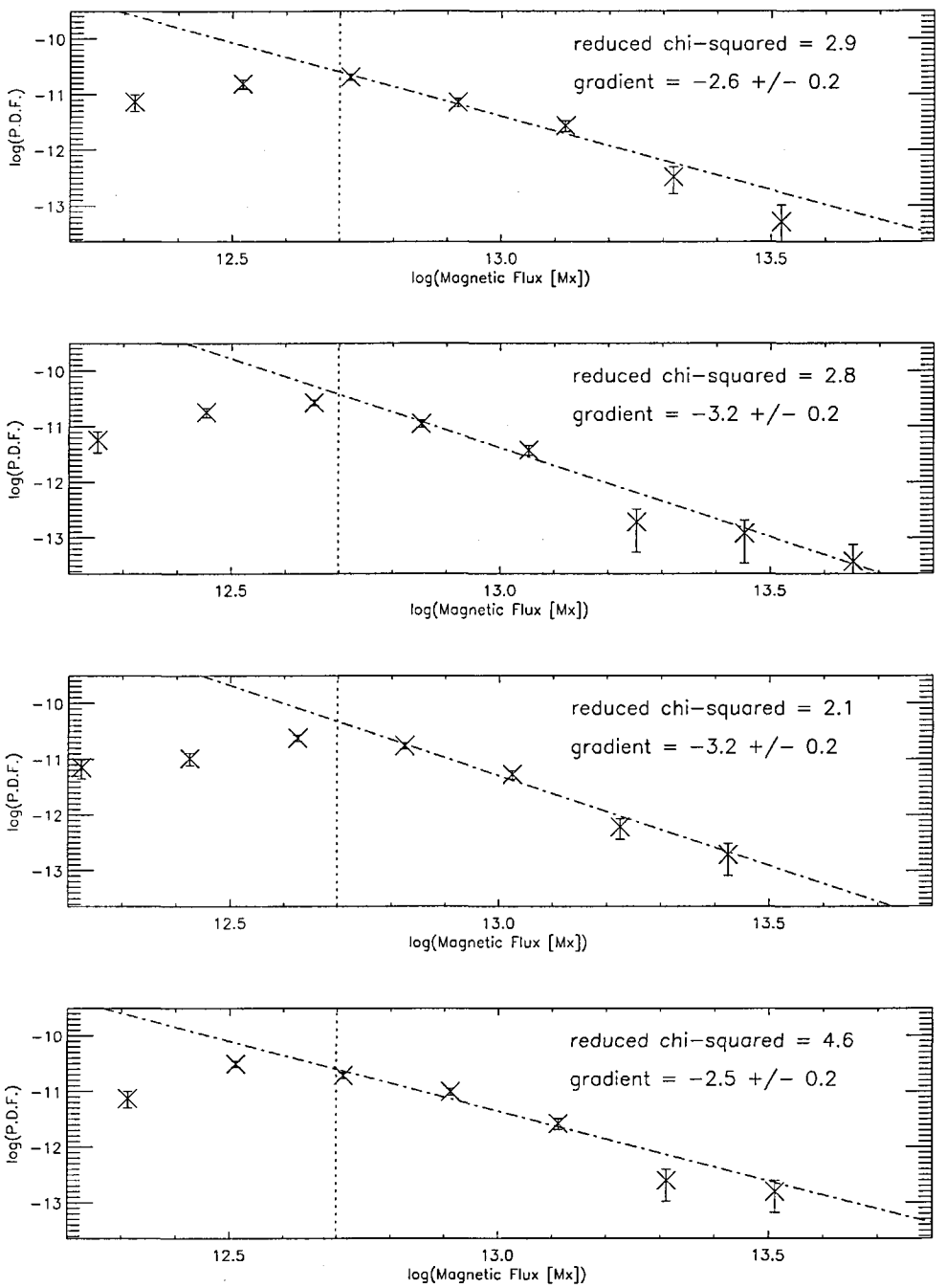

Figure 3.18: Distributions of magnetic flux in runs comparing different noise levels; 10^3 cells; bin-size = 0.25. Dotted lines mark mean initial magnetic flux. Initial cell length = 10^4 m. Top: run without noise. Second: $\frac{\psi}{P} = 0.001$. Third: $\frac{\psi}{P} = 0.005$. Fourth: $\frac{\psi}{P} = 0.01$.

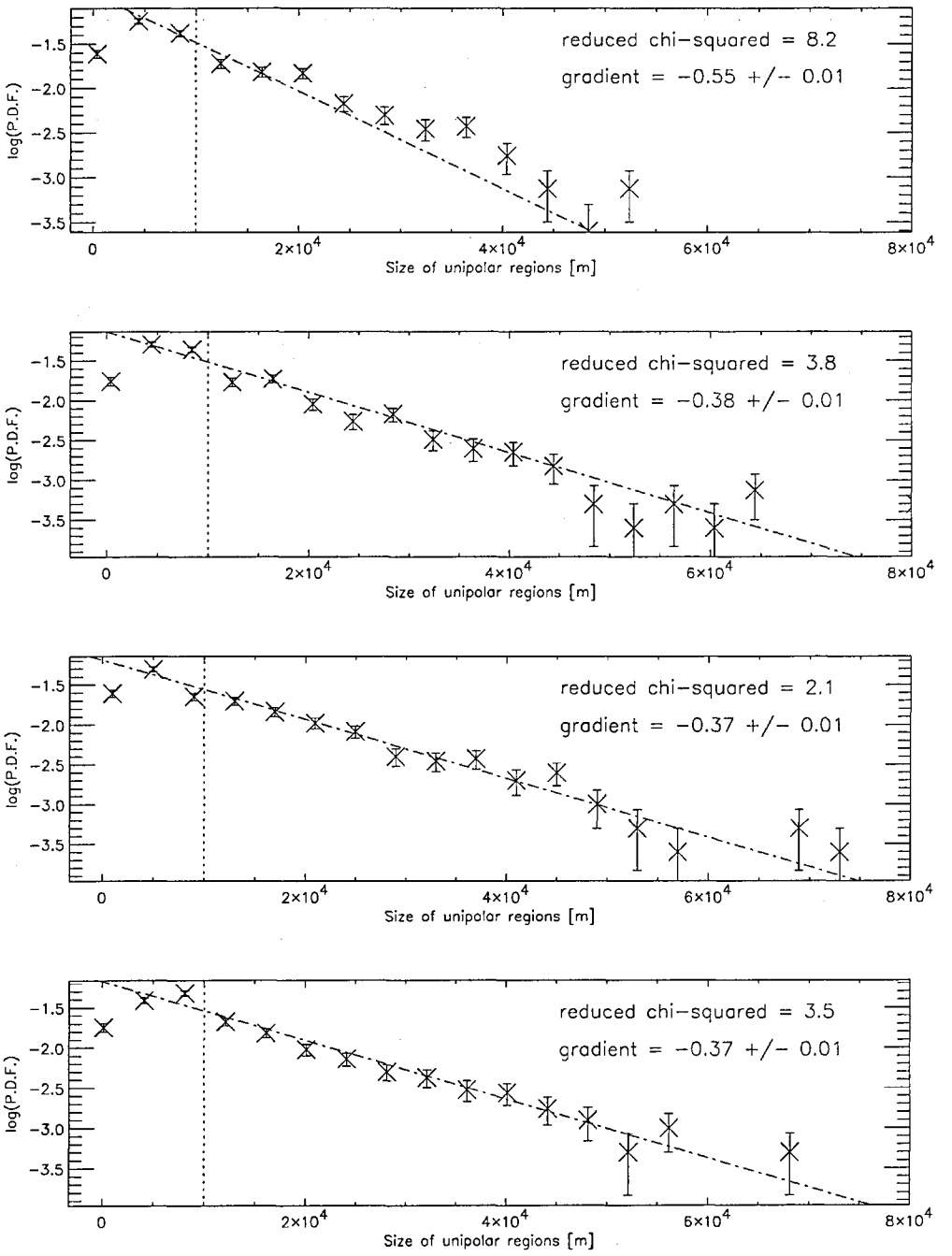

Figure 3.19: Distributions of unipolar region sizes in runs comparing different noise levels; 10^3 cells; bin-size = 0.25. Dotted lines mark initial unipolar region length. Initial cell length = 10^4 m. Top: run without noise. Second: $\frac{\psi}{P} = 0.001$. Third: $\frac{\psi}{P} = 0.005$. Fourth: $\frac{\psi}{P} = 0.01$.

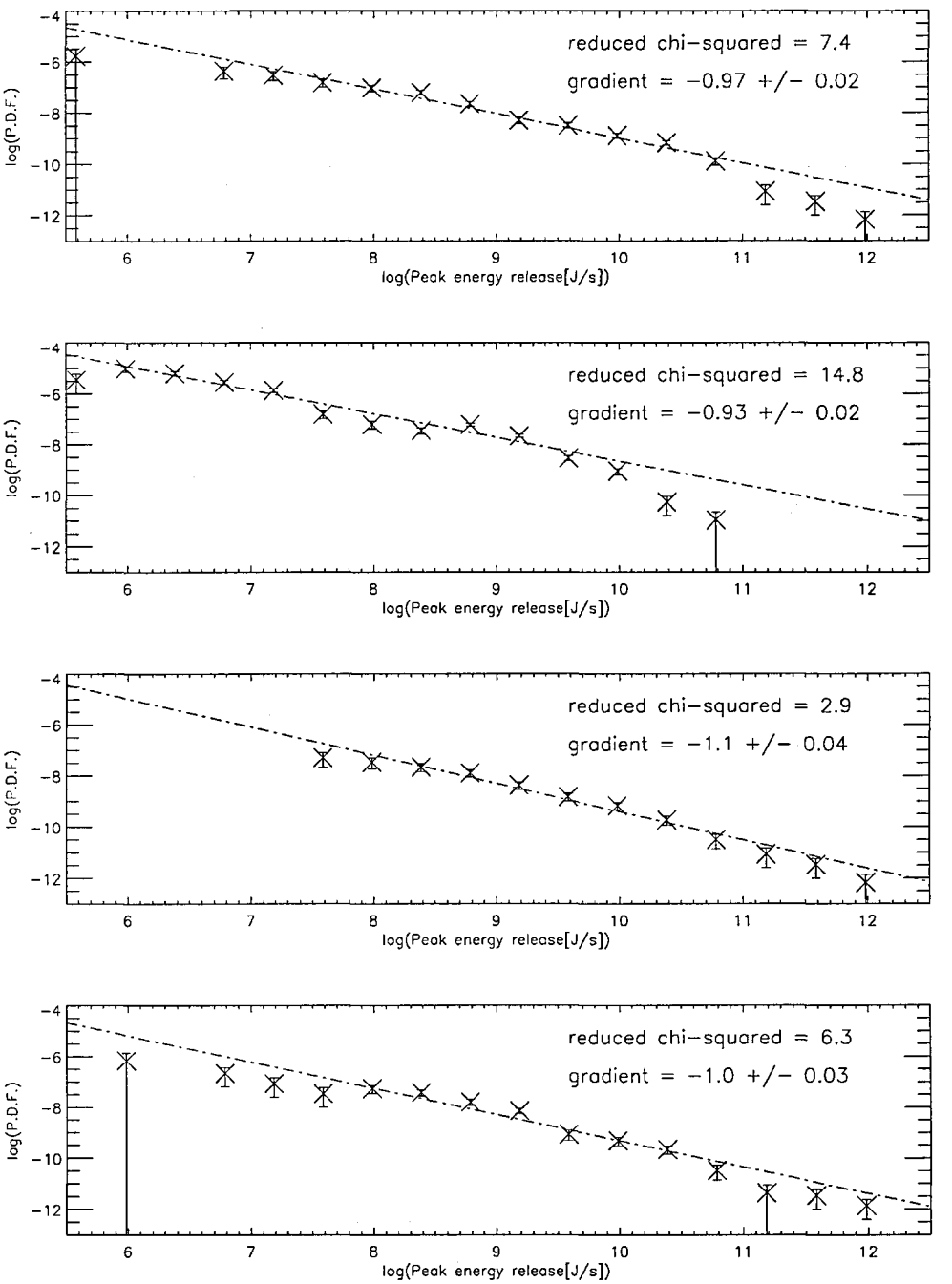

Figure 3.20: Distributions of event-sizes comparing different noise levels; counted by peak energy release method; 10^3 cells; bin-size = 0.4; initial cell length = 10^4 m. Top: No noise. Second: $\frac{\psi}{P} = 0.001$. Third: $\frac{\psi}{P} = 0.005$. Fourth: $\frac{\psi}{P} = 0.01$.

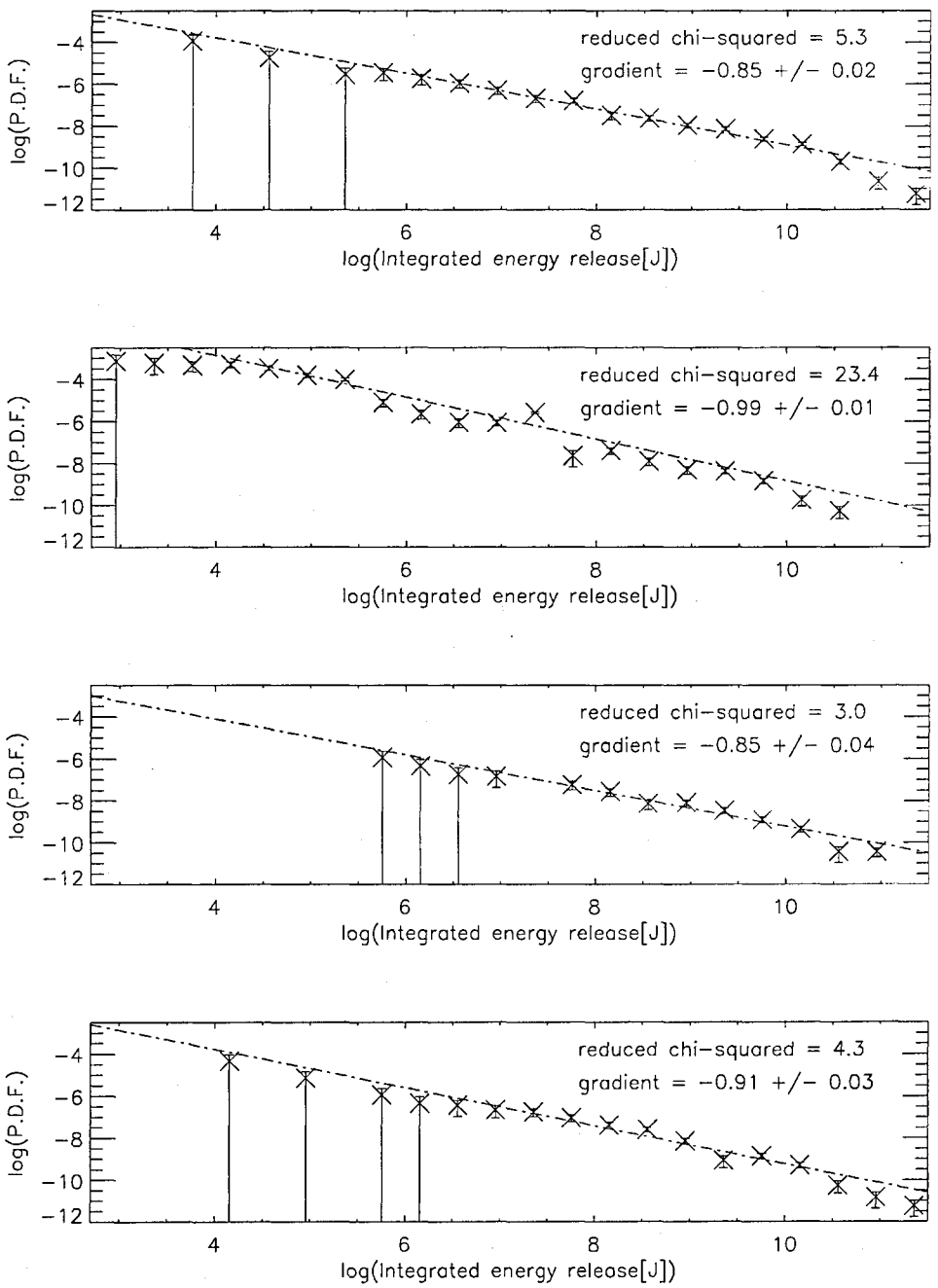

Figure 3.21: Distributions of event-sizes comparing different noise levels; counted by integrated energy release method; 10^3 cells; bin-size = 0.4; initial cell length = 10^4 m. Top: No noise. Second: $\frac{\psi}{P} = 0.001$. Third: $\frac{\psi}{P} = 0.005$. Fourth: $\frac{\psi}{P} = 0.01$.

Figure 3.22 shows us event-size distributions counted by peak energy release rate for three runs :

1. a run using typical initial conditions (as defined earlier), (minimum cell length is 100 m)
2. a run using typical initial conditions (as defined earlier), where the minimum cell length is 200 m
3. a run using typical initial conditions (as defined earlier), where the minimum cell length is 500 m

Figure 3.23 shows us event-size distributions counted by integrated energy release for the same runs as figure 3.22.

Considering first figure 3.22, we can see that the three plots are the same shape and cover the same approximate range. There is an approximately power-law region between 10^8 J s^{-1} and 10^{11} J s^{-1} with a small dip near the upper end of this range. We also see the points turn over at the lower end of the plots, from approximately 10^8 J s^{-1} and below. We cannot trust that the end regions are reliable because we expect these to manifest edge effects. The gradients of the more reliable parts of the plots, lying between 10^8 J s^{-1} and 10^{11} J s^{-1}, are approximately equal.

Considering now the plots produced using integrated energy release (figure 3.23), we can see that these three plots are also generally the same shape over the same approximate range. These are approximately power-law between 10^7 J and 10^{11} J. The three plots seem to have a slight but sharp break in their gradients at approximately 10^{11} J. The gradient above this point is slightly steeper than below. There are a few small deviations above and below this line.

It does not appear that changing the minimum cell length has a significant effect upon the peak or integrated energy release therefore we should trust our runs using a value of 100 metres for the minimum cell length. These event-size distributions are close to power-law or power-law-like and are in the same positions with similar ranges.

Maximum Cell Size.

We recall that typically we will use a value for the maximum cell length of 1.5 multiplied by the initial cell length. This means that when a cell expands to this size it will be divided into two equal cells. For comparison we have also performed runs using maximum cell lengths of 1.2 and 2.0 multiplied by initial cell length.

The first plots on figures 3.24 and 3.25 show event-size distributions for the typical initial conditions and model parameters using a value for the maximum cell length parameter of 1.5 multiplied by the initial cell length. The second figures show event-size distributions for a run using a value for the maximum cell length parameter of 1.2 multiplied by the initial cell length. The third figures

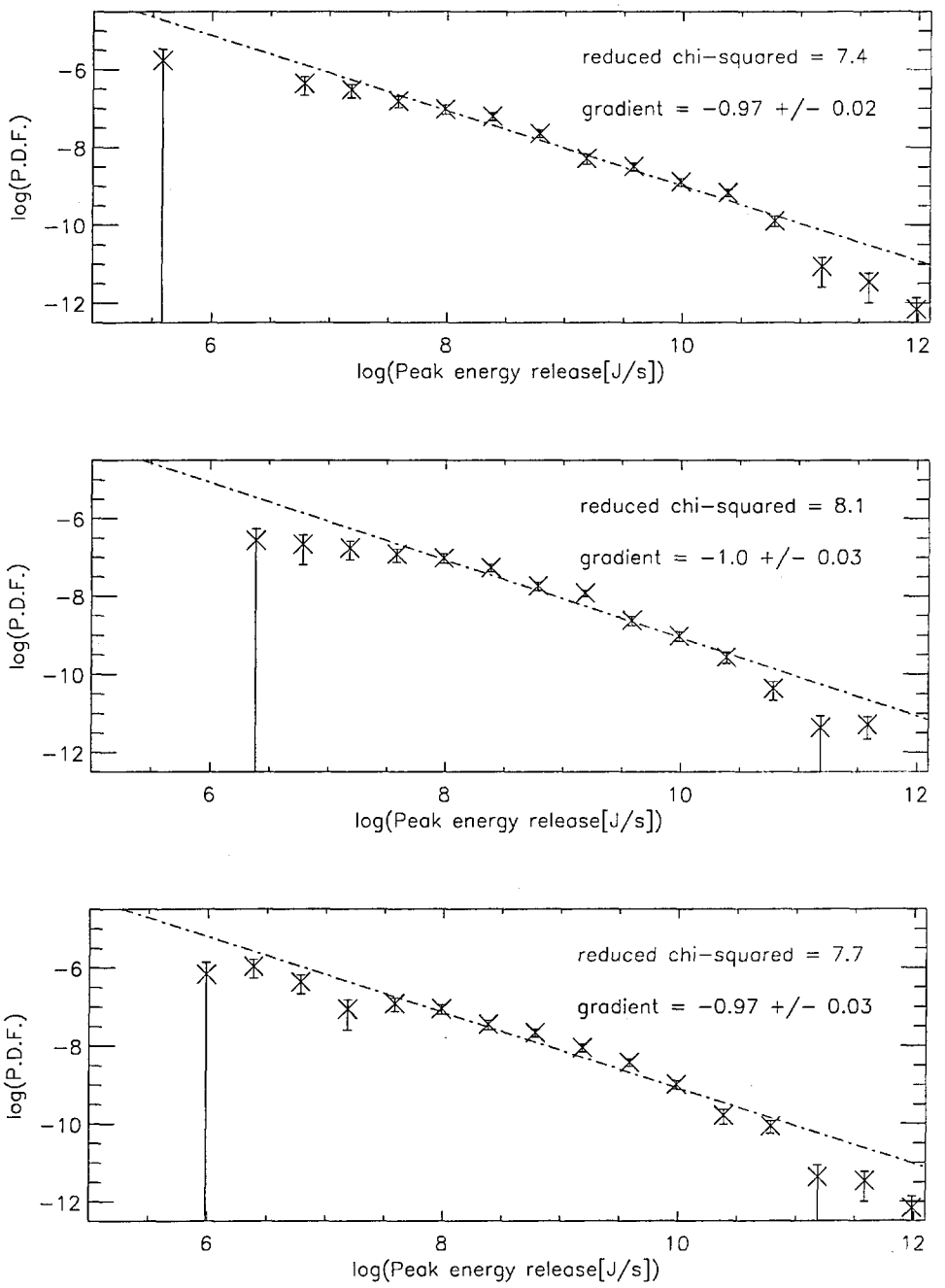

Figure 3.22: Distribution of event-sizes, counted by peak energy release rate. Log-log axes; 10^3 cells; initial cell length = 10^4 m; bin-size = 0.4. First: typical model parameters (minimum cell length = 100 m). Second: minimum cell length = 200 m. Third: minimum cell length = 500 m.

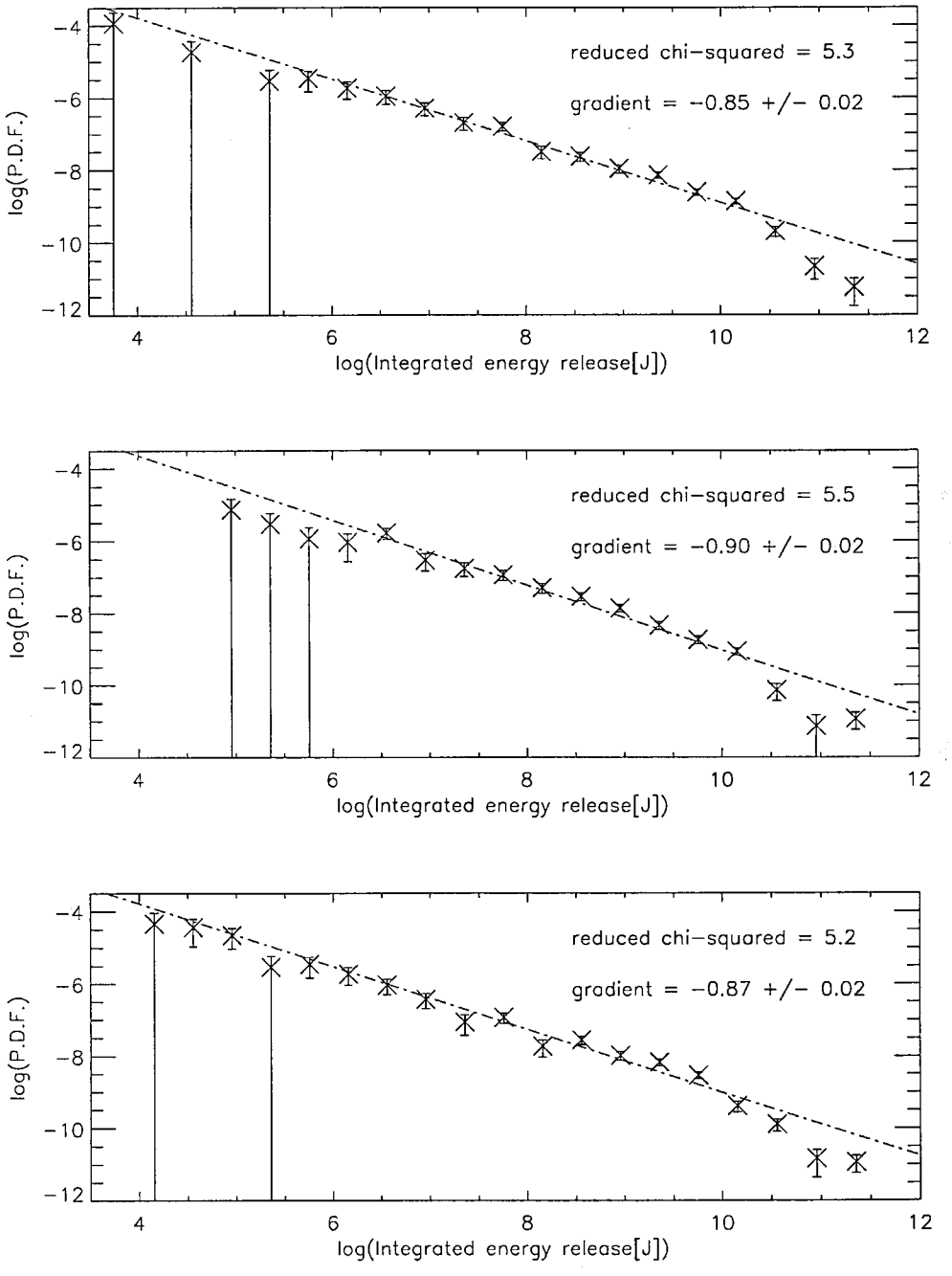

Figure 3.23: Distribution of event-sizes, counted by integrated energy release. Log-log axes; 10^3 cells; initial cell length = 10^4 m; bin-size = 0.4. First: typical model parameters (minimum cell length = 100 m). Second: minimum cell length = 200 m. Third: minimum cell length = 500 m.

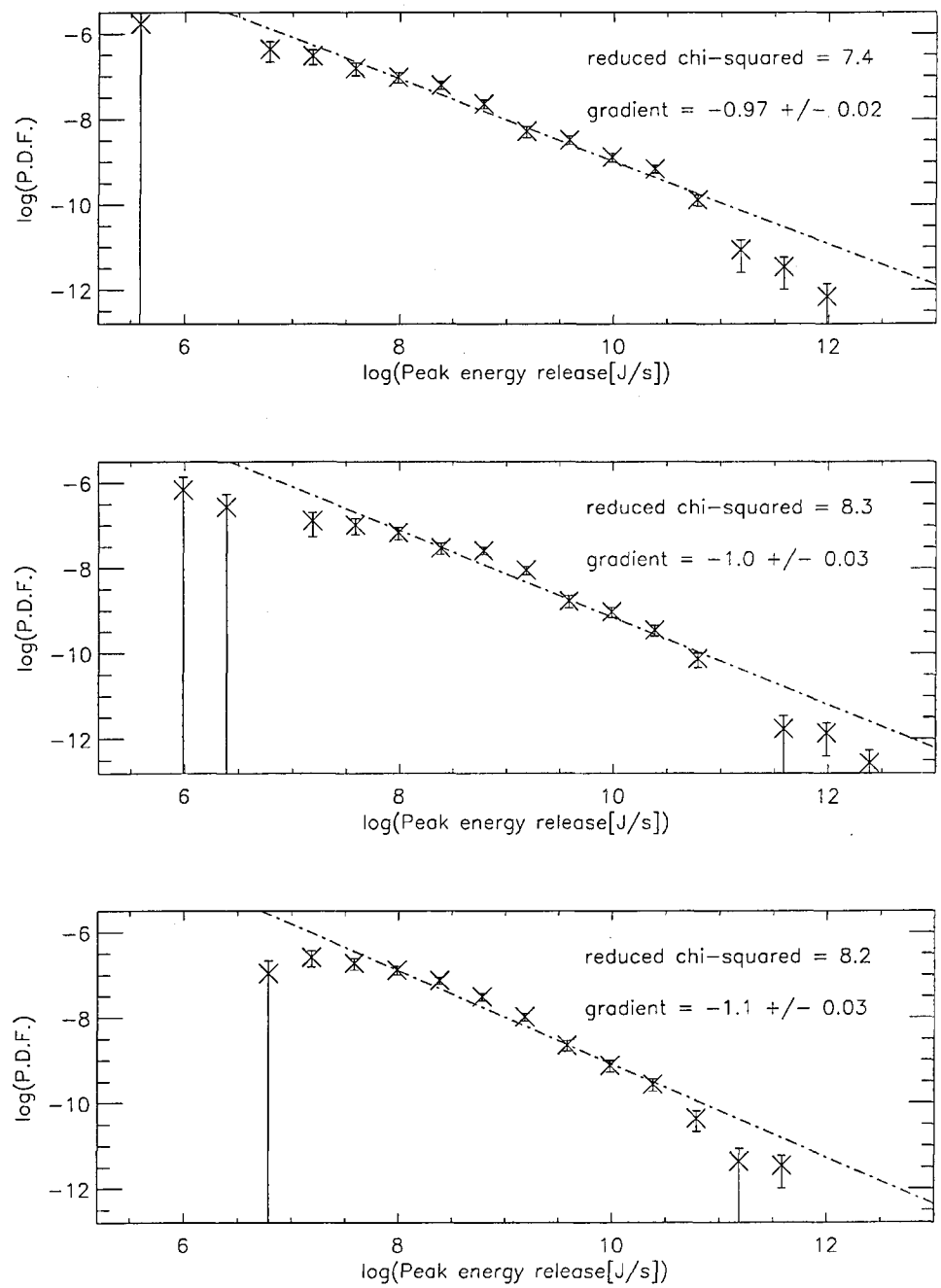

Figure 3.24: Distribution of event-sizes, counted by peak energy release rate. Log-log axes; 10^3 cells; initial cell length = 10^4 m; bin-size = 0.4. First: typical model parameters (maximum cell length = 15000 m). Second: maximum cell length = 12000 m. Third: maximum cell length = 20000 m.

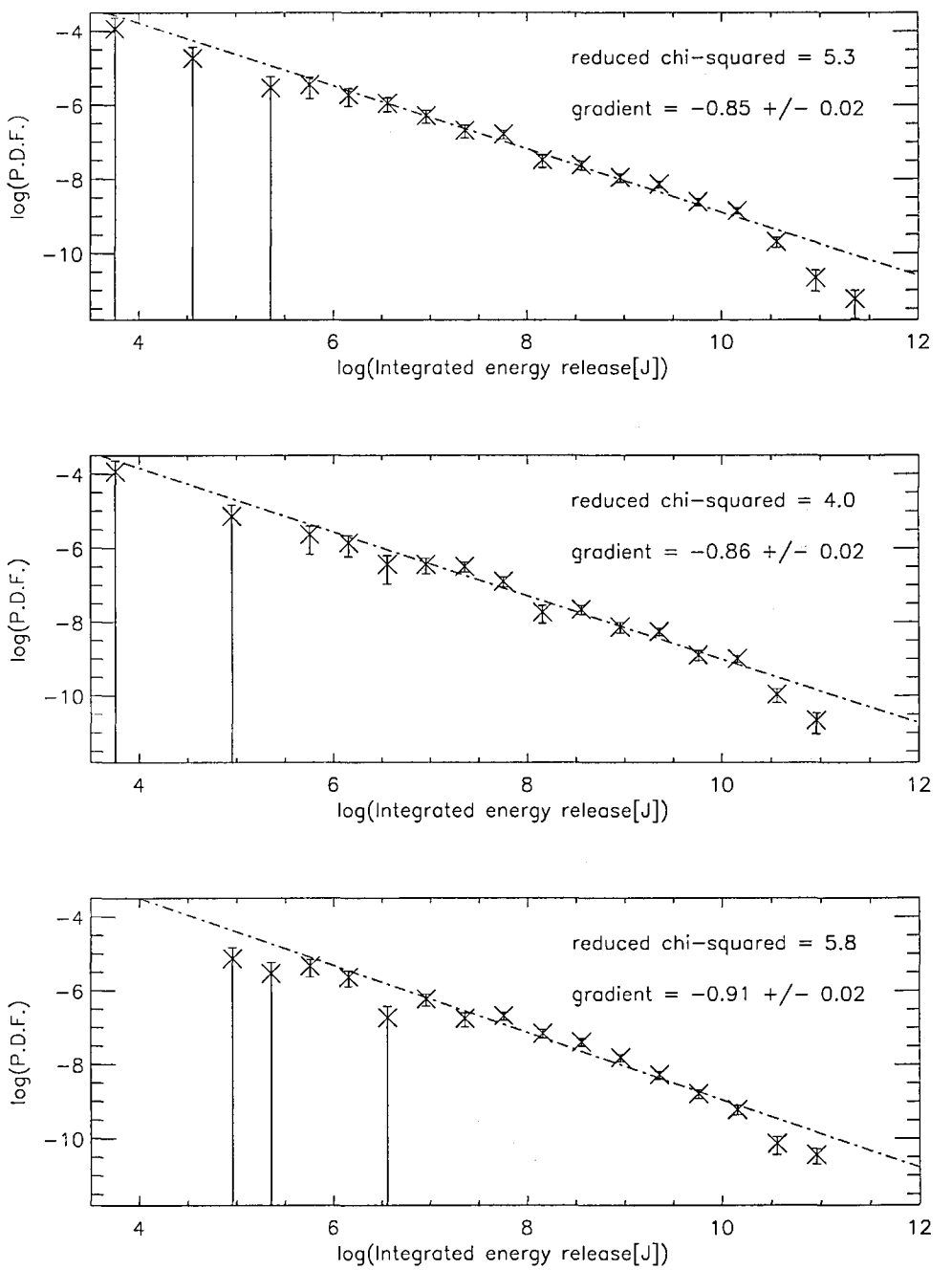

Figure 3.25: Distribution of event-sizes, counted by integrated energy release. Log-log axes; 10^3 cells; initial cell length = 10^4 m; bin-size = 0.4. First: typical model parameters (maximum cell length = 15000 m). Second: maximum cell length = 12000 m. Third: maximum cell length = 20000 m.

show event-size distributions for a run using a value for the maximum cell length parameter of 2.0 multiplied by the initial cell length.

Considering first the plots showing peak energy release (figure 3.24), we can see again that the profiles are of the same form and cover the same range. There is an approximately power-law region between $10^{5.5}$ J s^{-1} and 10^{11} J s^{-1}. All three plots have a slight dip at a varying position between $10^{8.5}$ J s^{-1} and $10^{9.5}$ J s^{-1}. The gradients of these plots are very similar. We see the usual turn-over at the lower end of these three plots, which may be caused at least in part by the Isliker effect.

Regarding figure 3.25, which shows the integrated energy release distributions, the plots all have very similar profiles, approximately power-law between 10^6 J and 10^{11} J with a few deviating points. The gradients are very similar.

We believe that these distributions are sufficiently similar that we can treat the model as not greatly dependent upon the maximum cell length.

Heating of Material by Magnetic Reconnection.

We expect that the Solar magnetic reconnection makes a contribution towards heating of the photospheric gas. Energetic protons and electrons accelerated by reconnection will gyrate around field lines while travelling along them until the particles impact into the denser photospheric material, heating it by the conversion of kinetic energy into thermal. We do not however know the level of this heating effect in the Sun. We have designed the model to incorporate this heating effect.

Now, for a given cell we have :

$$E_{\rm rec} \equiv \text{ magnetic energy released in a cell during one time} - \text{step}$$

Let's consider the thermal energy of the cell's particles. We know :

$$E_{\rm th} = \frac{3}{2}\, N\, k_{\rm B}\, T$$

Therefore, for constant N :

$$\delta E_{\rm th} = \frac{3}{2}\, N\, k_{\rm B}\, \delta T$$

and :

$$\delta T = \frac{2}{3}\frac{\delta E_{\rm th}}{N\, k_{\rm B}}$$

Now, let's suppose $\delta E_{\rm th} = \alpha \times E_{\rm rec}$ where α is a constant. Therefore :

$$\delta T = \frac{2}{3}\frac{\alpha\, E_{\rm rec}}{N\, k_{\rm B}} \tag{3.7}$$

Using typical values and setting α equal to 0.5 :

$$E_{\rm rec} = 8.0 \times 10^6 \text{ J}$$

$$N = 10^{32} \text{ particles}$$

Thus, we have :

$$\delta T \sim 1.9 \times 10^{-3} \text{ K} \quad \text{per time} - \text{step}$$

In the model we assume even heating of the gas and that it can equilibrate completely within the duration of each time-step. We can do this provided that the change in cell temperature is smooth. We have already addressed the matter of smooth adjustment of thermodynamic properties in section 3.2.2.

For comparison and testing of the robustness of the model to different values of α we conducted four different runs of the model. Each of these used the same 'typical' initial parameters, as per the Definition of Commonly Used Terms given at the beginning of the thesis.

1. Run where there is no contribution to heating of gas by energy release from magnetic reconnection ($\alpha = 0$).

2. Run where there is a contribution to heating of gas equal to exactly half the energy released by magnetic reconnection ($\alpha = 0.5$).

3. Run where there is a contribution to heating of gas equal to whole of energy released by magnetic reconnection ($\alpha = 1$).

4. Run where the contribution to heating of gas is equal to whole of energy released by magnetic reconnection multiplied by ζ where : $\zeta \equiv$ uniformly distributed random number in the range $0 \leftrightarrow 1$.

Regarding figures 3.26 and 3.27, the four plots on each figure show data produced by these four runs, in the same order as the list above. Figure 3.26 shows event-size distributions counted by peak energy release rate. Figure 3.27 shows event-size distributions counted by integrated energy release.

Comparing the peak energy release rate plots with each other (the plots on figure 3.26) we see that these have very similar profiles and cover the same approximate ranges. Between approximately 10^7 J s^{-1} and 10^{11} J s^{-1} the profiles are nearly power-law in form with similar gradients. There is the usual turn-over at the lower end, perhaps caused, or enhanced by the Isliker effect.

Turning to the integrated energy released plots (figure 3.27), again these plots have no substantive differences and are approximately power-law with a slightly exponential shape. they cover approximately the same range of 10^6 J to 10^{11} J and have similar gradients.

The distributions are all power-law-like in profile, covering similar ranges of x-values and y-values. Between different regimes of heating of the cell material, there is sufficient similarity in the event-size distributions to suggest that there is little dependency upon the detail of the heating mechanism. The most supportable conclusion is that we should not include heating derived from reconnection.

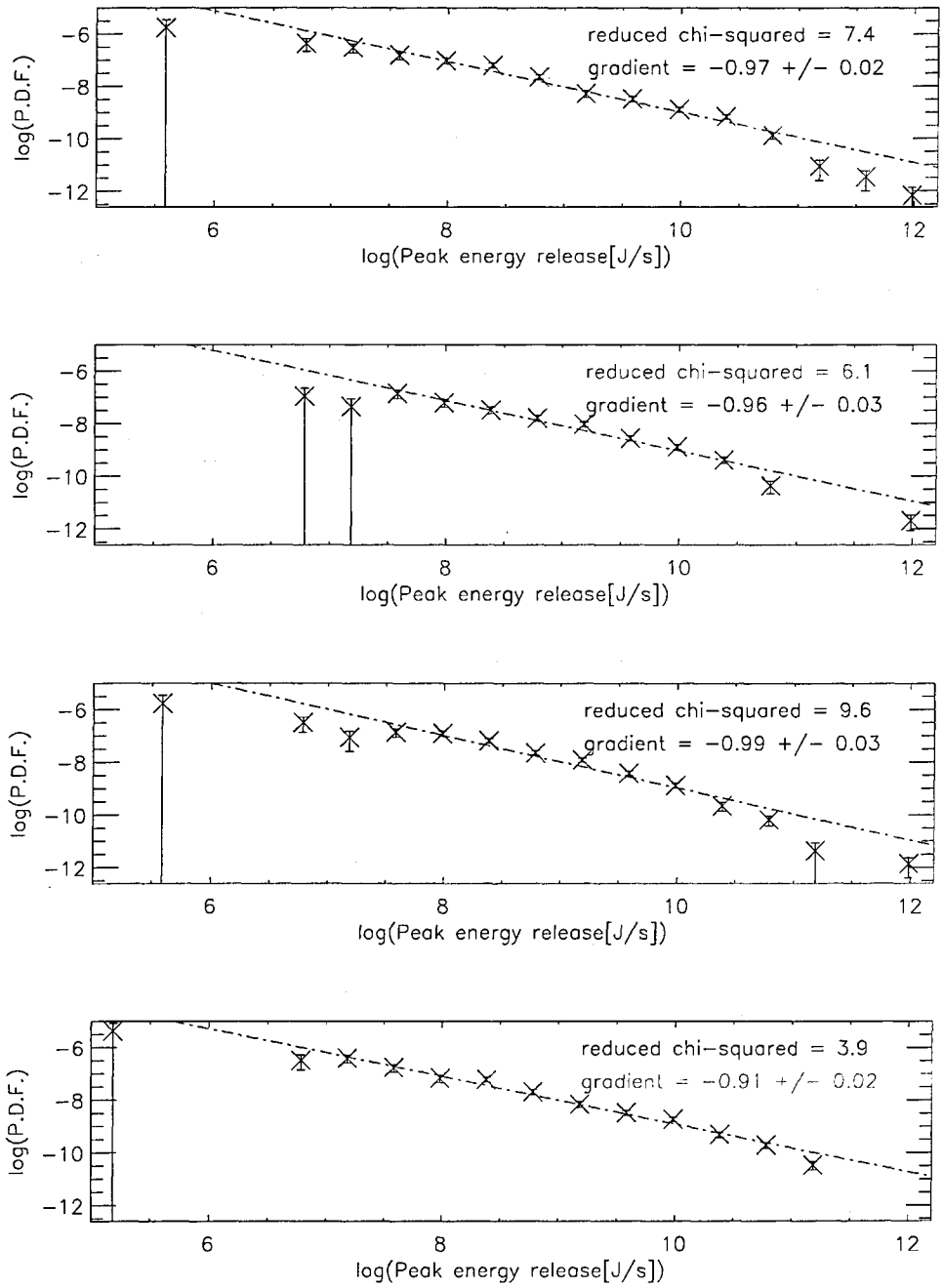

Figure 3.26: Distribution of event-sizes, counted by peak energy release rate. Log-log axes; 10^3 cells; initial cell length = 10^4 m; bin-size = 0.4. First: typical model parameters (no heating of cell material by energy released in reconnection). Second: heating of cell material by half energy released in reconnection. Third: heating of cell material by entirety of energy released in reconnection. Fourth: a random fraction (uniformly distributed in the range $0 \leftrightarrow 1$) of the whole of the energy released by magnetic reconnection is channelled into heating the gas.

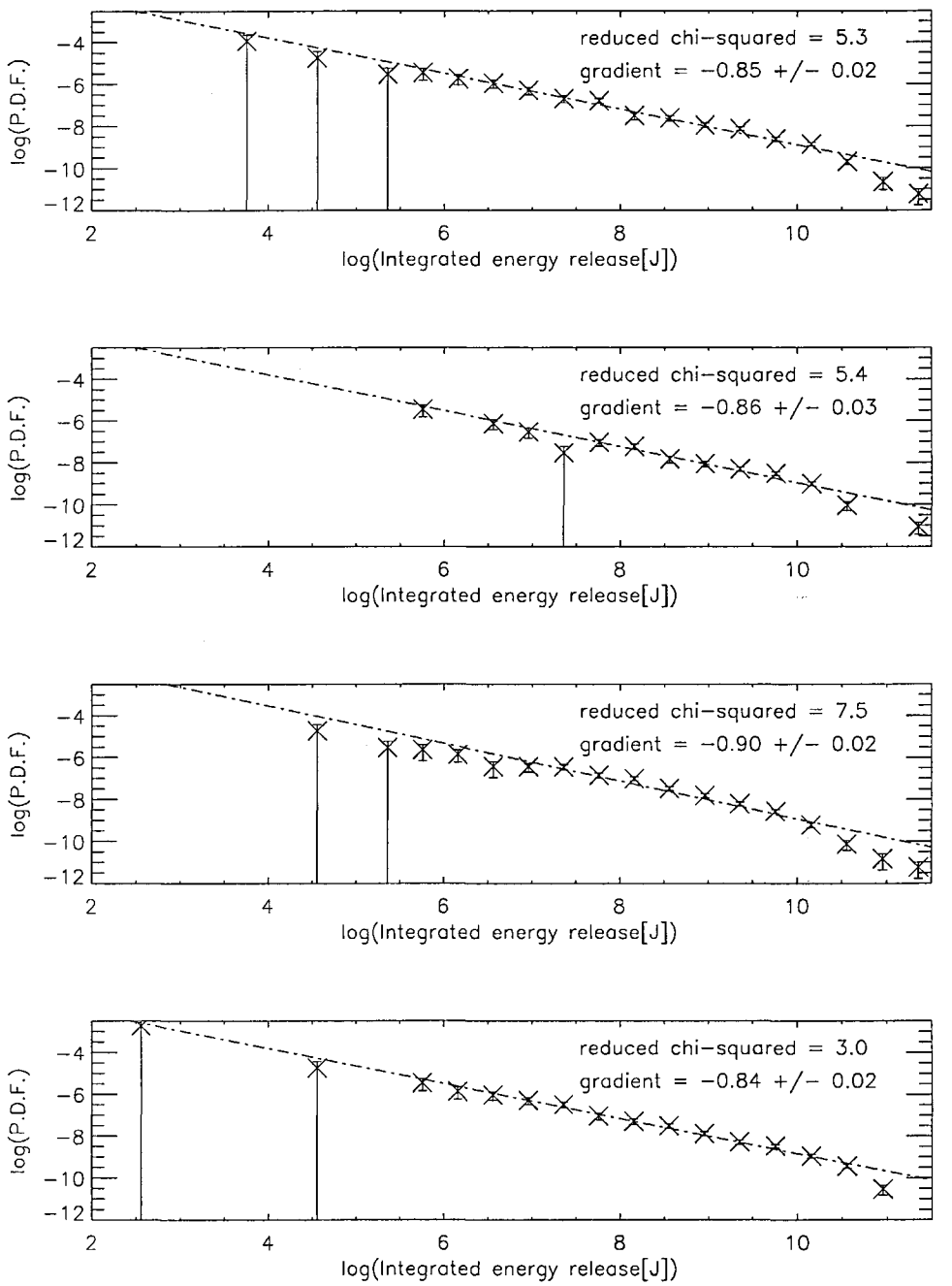

Figure 3.27: Distribution of event-sizes, counted by integrated energy release. Log-log axes; 10^3 cells; initial cell length = 10^4 m; bin-size = 0.4. First: typical model parameters (no heating of cell material by energy released in reconnection). Second: heating of cell material by half energy released in reconnection. Third: heating of cell material by entirety of energy released in reconnection. Fourth: a random fraction (uniformly distributed in the range $0 \leftrightarrow 1$) of the whole of the energy released by magnetic reconnection is channelled into heating the gas.

Summary.

We note that the data in the first plot of each of figures 3.22, 3.24 and 3.26 is identical and pertains to a run using minimum cell length of 100 m, maximum cell length of 15000 m and zero heating of the cell material from the energy of reconnection (i.e. $\alpha = 0$). These three figures show event-size distributions counted by peak energy release rate. Each of these three figures demonstrates a different class of deviations from these model parameter values of $L_{\text{cell,min}}$, $L_{\text{cell,max}}$ and α, respectively. Remembering that the first plot of each of these three figures represents the same data, we can therefore evaluate the effects in the distributions produced by these variants on the values of $L_{\text{cell,min}}$, $L_{\text{cell,max}}$ and α.

Similarly, the three figures 3.23, 3.25 and 3.27, give the distributions of event-sizes corresponding to the same runs (and therefore model parameter values) as figures 3.22, 3.24 and 3.26.

Thus, considering the peak energy release rate and the integrated energy release event-size distributions separately, the plots are all power-law-like and cover similar x and y ranges. They are all in similar positions on the graphs, indicating that each may represent a subset of an underlying distribution. In summary, there are no substantial differences between any of the plots on these three figures, either in the profiles or ranges of the binned data, and our model is robust in terms of minimum cell length, maximum cell length and heating by reconnection.

We conclude the following :

1. the particular values of minimum cell length, $L_{\text{cell,min}}$ (100 m, 200 m and 500 m) are all sufficiently small compared with typical cell lengths (10^4 m) that within this range the model has no significant dependency upon the particular value selected. All further runs will use the value $L_{\text{cell,min}} = 100$ m.

2. the particular values of maximum cell length, $L_{\text{cell,max}}$ ($L_{\text{cell,init}} \times$ 1.2, 1.5 and 2.0 (for a value of $L_{\text{cell,init}} = 10^4$m)) are such that the model has no significant dependency upon the particular value selected within this range. All further runs will use the value $L_{\text{cell,max}} = 1.5 \times L_{\text{cell,init}}$

3. the particular heating level of the cell material by the energy of reconnection (α = 0, 0.5, 1.0, random) is insufficient to produce any significant dependency of the model upon the particular value selected. All further runs will incorporate zero heating.

3.4.4.3 Radiative Cooling.

We recall that the top surface of the grid radiates with a black-body spectrum into a background which has a temperature of 5785 K. We tested whether the exponent of temperature ($\dot{E} = \sigma T^a$,

where $a = 4$) is important, or perhaps the model is robust to any reasonable value of the exponent. In fact, it was found that the model is stable only within the range : $3.5 < a \leq 5.0$.

A surprising result, which we have investigated fully. We suspected that this may result from a resonance with another parameter also raised to a power in the range $3 \leftrightarrow 5$ however this is not the case. Certainly, T^a features nowhere else in the model.

We are trying to make a model of Solar surface behaviour as faithful to the reality as possible. We should therefore hope that any real physics coded into the model is not inconsistent with the operation of the model.

3.4.4.4 Initial Magnetic Field Distribution.

We should investigate the dependency of the results upon the initial field density P.D.F.s. We have so far run the model using a random flat distribution of magnetic density ($\overline{|B|} = 50$ G). However we performed a run of the model with typical initial conditions although the initial field density used was random with power-law distributions, index = -1, and B values in the range $1 \leftrightarrow 100$ G with gradient -1. Event-size distributions were produced from the energy release time-series generated, and these distributions are shown in figures 3.28 and 3.29.

Each plot compares a P.D.F. produced by this run with that produced where the initial flux density is in the usual random flat distribution ($\overline{|B|} = 50$ G).

We see that there is little difference between the profiles of the two plots on each figure and conclude that the profiles are fairly independent of the initial flux distribution.

3.4.5 Numerical Instability.

In order to enable the model to run without numerical instability a recurring problem which had to be overcome was numerical instability resulting from cell lengths becoming small and then negative. We have already discussed in section 3.2.2 the necessity of ensuring that $\Delta N << N$. We cannot sustain $\Delta N << N$ when cells become small, and consequently N becomes small. For this reason the mechanism was developed, as already described, which removes cells with size below a critical threshold. We have already seen that this threshold is 100 m.

The radiative cooling mechanism provides a stabilising factor for the temperature, and thus the thermodynamic pressure. Before this sensible component was included the thermodynamic pressure would become unstable within a short period of time.

We wanted to test whether power-law distributions in event-size can be driven by power-law distributions of magnetic field density and cell length.

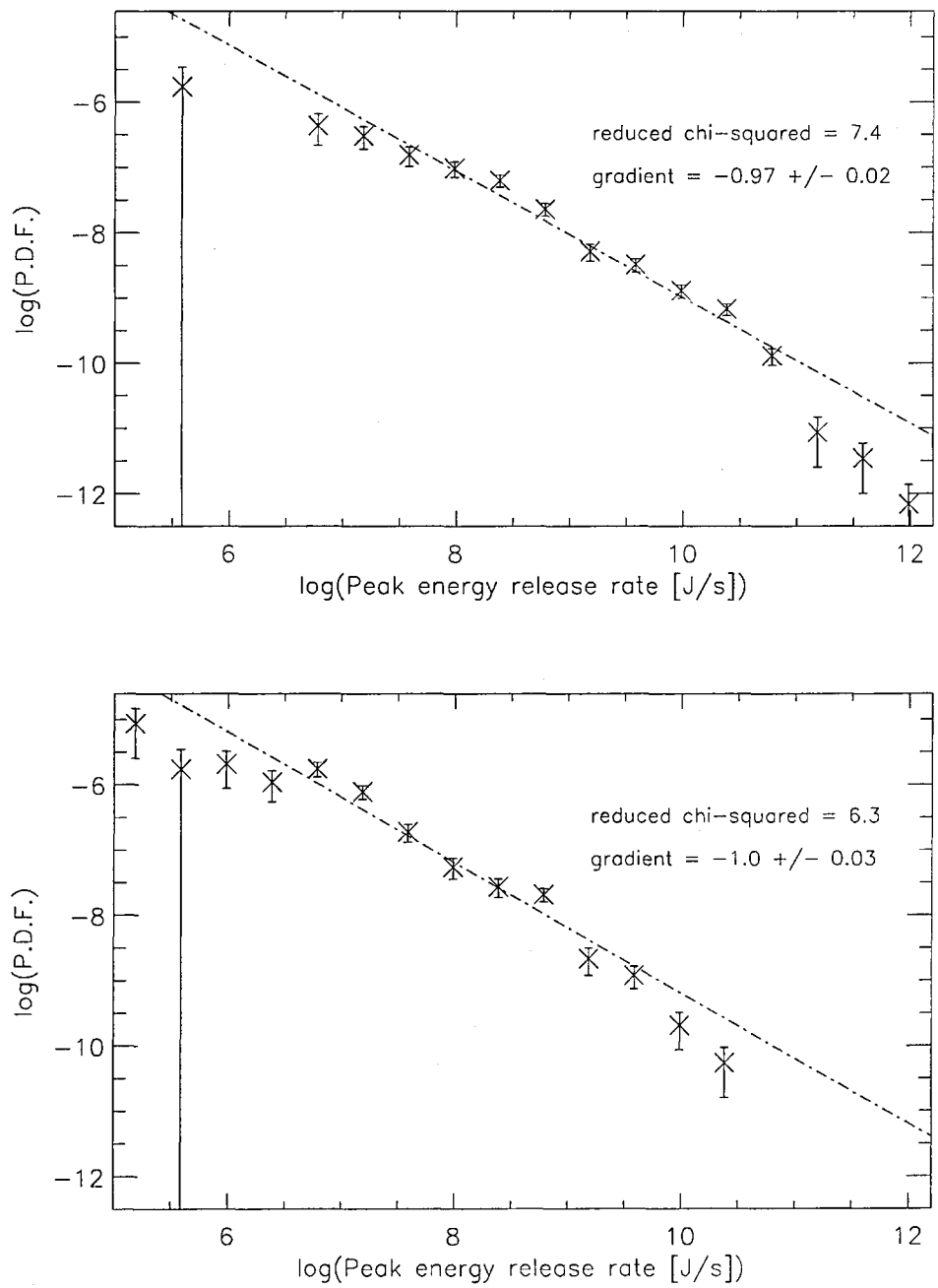

Figure 3.28: Evolved distributions of event-sizes, counted by peak energy release rate. Initial cell length = 10^4 m; log-log axes; bin-size = 0.4; 10^3 cells. First: typical run. Second: power-law (index = -1) distribution of initial magnetic field densities.

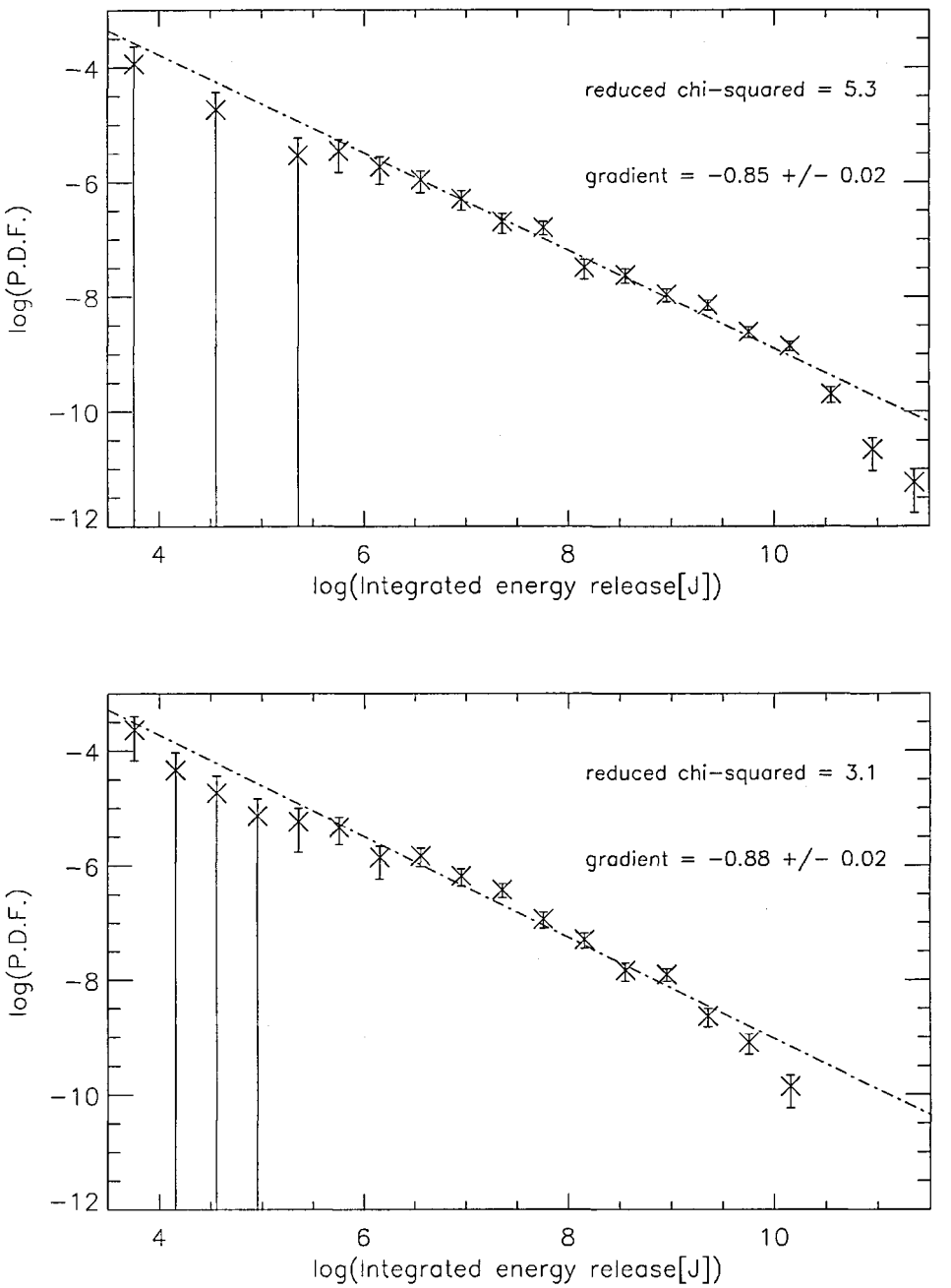

Figure 3.29: Evolved distributions of event-sizes, counted by integrated energy release. Initial cell length = 10^4 m; log-log axes; bin-size = 0.4; 10^3 cells. First: typical run. Second: power-law (index = -1) distribution of initial magnetic field densities.

The model is capable of generating a power-law distribution of length with index = -1 and index = -2 and in the range $10^3 < L < 10^4$ m however it was not possible to run this without numerical instability setting in very quickly, producing cells with unphysical length values.

3.4.6 Edge effects.

There are several sources of errors which manifest themselves at the extremities of distributions and appear as knees or other deviations in the gradients of fit-lines. Some of the causes of these edge effects have been discussed in chapter 3 and will be discussed in section 4.2.

Let's consider some factors which may produce our edge effects :

- Initial cell size.

  The runs all commence with the same initial cell size, typically 10^4 m. Runs where the emergence/submergence of magnetic flux is switched on quickly revert to a state where the distribution of cell length is random with a finite and steady standard deviation. The initial cell size seems however to remain frozen into the model. We will see this later when considering the distribution of sizes of unipolar magnetic field regions.

- Minimum cell size.

  As we learned in chapter 3, in order to obviate certain numerical instability problems it is necessary to have a feature of the model which removes cells from the grid which fall below 100 m. When cells become smaller than this length they produce non-linear behaviour in the recalculation of cell pressures, which then feeds into the equation of motion for each cell, quickly causing instability. Also, the discrete time intervals over which the model runs implies that where a cell is undergoing submergence there will inevitably be an overshoot such that its length becomes negative. Therefore, it is necessary to have a safety measure to catch cells before becoming zero length.

- Maximum cell size.

  It is a feature of the model that when a cell has grown to such a size that it is equal or greater than 1.5 multiplied by mean initial cell length the cell is split into two identical daughter cells. This is described in chapter 3. The purpose is to prevent arbitrarily large cells from forming and extending into the grid (which remains a constant length) thus reducing the number of extant cells and the usefulness of the output data. Clearly, this upper limit to the cell length is fixed throughout a run.

- Initial mean magnetic field density level.

  The typical routine used by the model for allocating initial magnetic field density , as described in chapter 3, generates a value between +100 and −100 G for each cell over a flat random distribution. The magnetic energy stored within each cell, and available for reconnection, is proportional to the square of the magnetic field density within each cell. As we have learned from chapter 3, the routines which carry out the emergence of fresh magnetic flux obey a principle of conservation of the magnetic flux. Therefore, the initial mean magnetic flux density, and also the total magnetic energy stored in the grid are, in effect, frozen into a run at its inception.

There is a systematic effect analysed by Isliker & Benz (2001) and described in more detail in the Introduction whereby sampling of time-series using finite time and frequency resolution samples causes a biasing effect in the P.D.F. In general terms, this effect manifests as an exponential roll-over of the P.D.F. profile at high amplitude and an artificial flat extension of the P.D.F. at low amplitude. Amplitude in our model would be event-size, $|B|$, ϕ or any other parameter we choose.

Our event-size distributions are generated from sampled energy release rate time-series, therefore we would expect that the Isliker effect causes an element of roll-over at the edges of our event-size distributions (peak energy release rate, and integrated energy release). Where this effect is greater than our statistical errors we will see this as a clearly demonstrable effect in our plots. We note that our event-size distributions often show a low-end roll off, and suggest that this is caused at least in part by the 'Isliker effect'. Also, given that our model uses a finite number of spatially finite and discrete cells whose parameter values are considered to summarise continuously varying parameters within the cells, we are justified in considering that the values of these parameters constitute data sampled at finite spatial intervals. Therefore, when considering P.D.F.s of B, ϕ and $L_{unipolar}$ we must remember that these distributions are subject to the Isliker effect.

With regard to the integrated energy release, there are other issues which are responsible for distortions of the distributions. The beginning and end of an event can't be precisely specified. Figure 3.30 illustrates the energy release profile of an event within the model and shows how the integrated energy of an event as calculated differs from the actual. An event is only deemed to begin when the local energy release rate exceeds that taking place between any other pairs of cells in the grid. Therefore, events counted towards the integrated energy release and peak energy release rate distributions occur when energy release between two cells rises above the background level. This background level will also not remain exactly constant but is defined by the energy release level of the events previous to and after any given event. The reconnection between these cells will actually begin earlier and cease later than the temporal extent of the event, and so the total energy release will

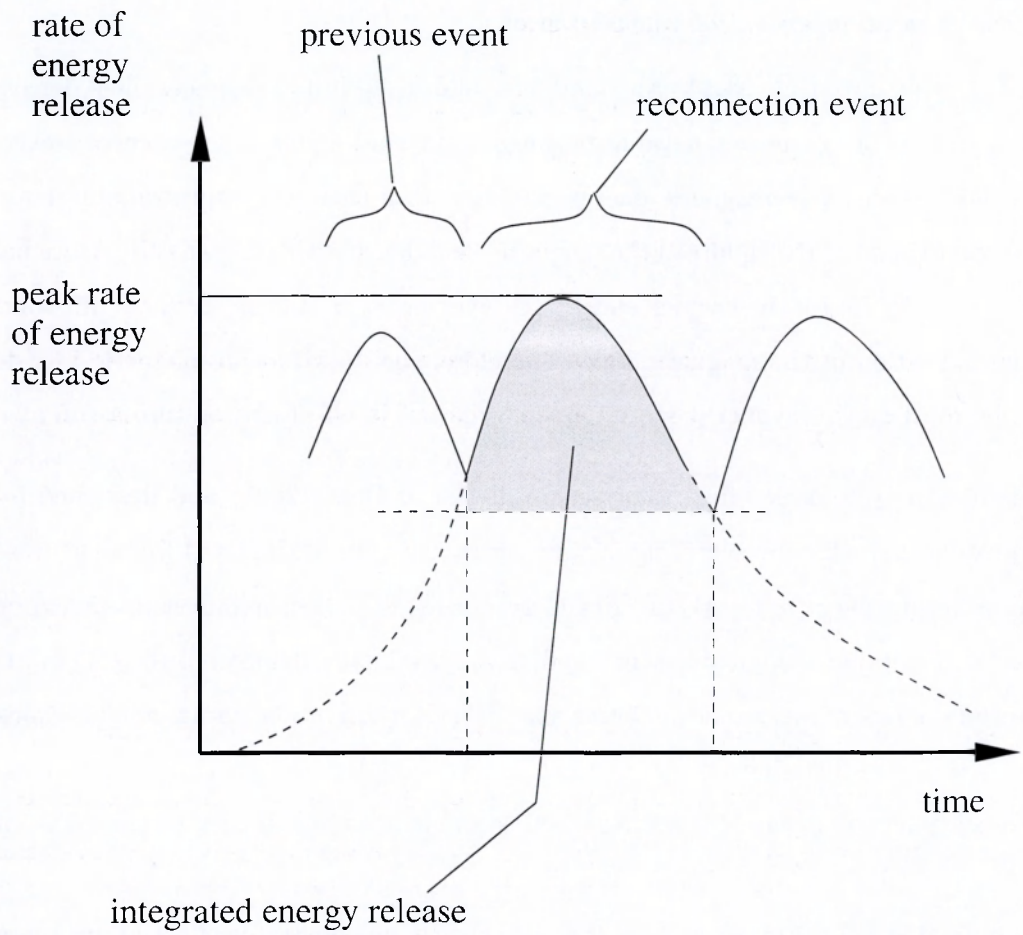

Figure 3.30: Schematic of reconnection event showing energy release as a function of time.

be greater, than the integrated sum used to calculate the distribution. This approach was justified earlier, but nevertheless unavoidably distorts the distributions.

3.5 Magnitude of δt.

Some testing was carried out to determine an appropriate value for the time-step interval. There are two competing factors at play here :

- Smoothness.

  The time interval must be sufficiently small such that changes in cell parameter values are small enough to avoid catastrophic numerical instability.

- Running time.

  The time interval must be large enough to complete a reasonable amount of model-time (hundred to thousands of minutes) during a tolerable amount of real time. If the interval is too small

then the model's runtime will be overlong.

The time-step settled upon was $\delta t = 0.002$ s. A typical run of 3×10^6 time-steps takes four hours to run on the Open University Physics and Astronomy cluster.

3.6 Data Produced by Model.

We need to describe all the forms in which the model produces data. These can be grouped into two main types : cell parameters and magnetic reconnection event-size distributions.

3.6.1 Cell Parameter Data.

Let's consider the cell parameter data. This consists of the following :

- – Magnetic field density values for the entire grid at commencement of run.
  - – Magnetic field density values for the entire grid at completion of run.
  - – Time-series of magnetic field density values for each cell running from 10^6 time-steps to completion of run (typically 3×10^6 time-steps, sampled every 3333 time-steps).
- – Pressure values for the entire grid at commencement of run.
  - – Pressure values for the entire grid at completion of run.
  - – Time-series of P values for each cell running from 10^6 time-steps to completion of run (typically 3×10^6 time-steps, sampled every 3333 time-steps).
- – Cell length values for the entire grid at commencement of run.
  - – Cell length values for the entire grid at completion of run.
- – Total particle number values for the entire grid at commencement of run.
  - – Total particle number values for the entire grid at completion of run.
- – Temperature values for the entire grid at commencement of run.
  - – Temperature values for the entire grid at completion of run.

These data allow us to generate distribution plots for the magnetic field density and the thermodynamic properties, L, P, n and T. Having this data for the end and beginning of the runs allows us to examine the distributions of the settled states of the cell parameters and check that these distributions are not frozen in at the commencement of the model runs.

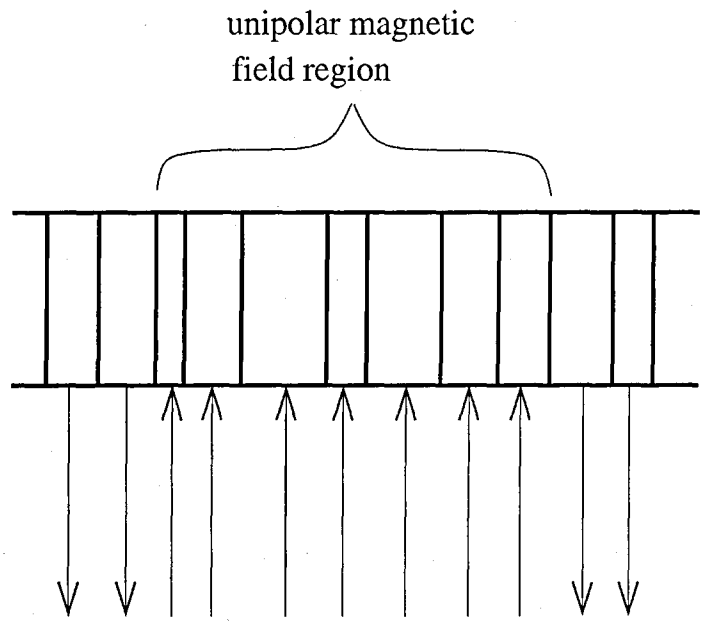

Figure 3.31: A unipolar region.

The complete pressure time-series data allowed us to construct figure 3.16 which demonstrates the authentic fluid dynamics of the fluid in the model, and allows us to compare the sound speed of the model fluid with that calculated according to $C_s = \sqrt{\frac{P\gamma}{\rho}}$.

We have the complete energy release data and magnetic field density data across the grid as a function of time. These allow us to construct analyses of energy release, such as figure 4.3, and magnetic field density, such as figure 4.8, for different runs with distance along the grid on the y-axis and time on the x-axis. We are able to identify the different features of the model in these analyses. We can discern, for instance, emergence of flux, submergence, magnetic reconnection and the fluid behaviour of the gas. Clearly visible is new reconnection taking place between previously separated cells when the cell(s) acting as a barrier submerge and disappear from the grid.

We will find it useful later to consider distributions of sizes of 'unipolar regions'. These are contiguous sections of the grid where the magnetic field of the cells are of the same sign (polarity). There will be no magnetic reconnection between cells in the unipolar region and reconnection will be localised to the ends of the region, or in other words, reconnection may only occur at boundaries between unipolar regions. Figure 3.31 illustrates a unipolar region.

3.6.2 Magnetic Reconnection Event-size Distribution Data.

In section 3.3.4 we explained the form of the time-series reconnection data. Here we will explain how this is processed to produce event-size distributions.

First, the mechanism of counting of event-size distributions should be explained. Let's begin by considering the notion of an 'event' for our purposes.

Within the continuous model reconnection is considered to take place between two adjacent cells which have anti-parallel magnetic flux (the magnetic flux of the two cells is of opposite magnetic polarities). If the two fluxes are parallel (the same magnetic polarity) then no reconnection can occur. Thus, the reconnection region is spatially localised.

When making observations of actual Solar flares, a flare is detected when the local energy release exceeds the background level and the temporal and energy resolution of the instrument. We find that the magnetic reconnection energy release of the continuous model can be characterised as the superposition of a backgound, which, when summed over the entire grid remains fairly constant, plus occasional significant events localised within single cells. The magnitude of these events is such that they are the largest events taking place within the model at any time and thus dominate the magnetic energy release within the grid.

Let us consider a cell where, at a given time, the highest rate of energy release within the grid is taking place. When the energy release rate of that cell drops below that of another cell within the grid and therefore no longer exhibits the highest rate of energy release, we consider the reconnection event to have terminated. However, the caveat here is that if the position of the cell where the new highest energy release rate occurs is one of those cells within a distance of two cells either side of the original cell, then that event is deemed not to have terminated but to continue. Although a reconnection event is considered to occur at only a single reconnection site/cell boundary, it may be the case that high levels of reconnection are occuring in several cells local to this site because this local area has a high magnetic field density and the field polarity is mainly oppositely directed. In this case it is correct that these other very local reconnection regions should be considered part of the same reconnection event. The location (as a consecutive number marking the position of the cell in the grid) of the cell with highest energy release reveals that this site very often migrates along the grid in steps of one cell at a time. It is conjectured that this is a result of a propagating pressure wave. The region of compression would raise the magnetic field density, increase the rate of magnetic reconnection and thus be centred upon the site of highest energy release. We take into account the fact that submergence of cells and division of large cells into two daughter cells changes the consecutive number of a cell.

We deem an event to commence at the point in time when the local rate of energy release produced by one cell reconnecting with one or both of its neighbours exceeds all others in the grid. Thus, throughout a model run, there will always be an event occuring and this will be located where the

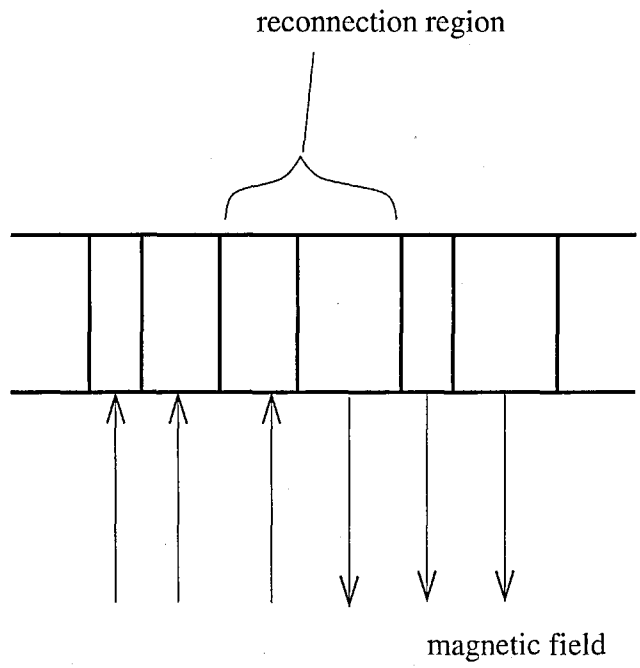

Figure 3.32: Schematic of reconnection region within the grid.

local energy release is greatest. Figure 3.32 illustrates what we mean by a reconnection region in spatial terms and 3.30 shows schematically the notion of an event in temporal terms. As we see in this figure, the event can be characterised either by the peak energy release or the integrated energy release after subtraction of the background energy release. The background level represents the total of many small energy releases occurring in the model and is represented by the horizontal line in figure 3.30. Hence, the shaded region represents the total energy release during the event less the background.

We saw in table 1.2 that in practice flaring events are counted by both peak energy flux and integrated energy flux. Therefore, in order that the results of the model can be compared with real data, such as these, we are using concepts in the model analogous to peak energy flux and total energy. We refer to these as 'peak energy release rate' and 'integrated energy release ', respectively. Figure 3.30 clarifies the meaning of these terms in the context of our model.

The top plot in figure 3.33 shows the time series of the energy release from magnetic reconnection, summed over the whole grid, plotted against time. We can see a number of spikes in this time-series. The middle plot shows the time series of the energy release of only the cell within the grid which has the greatest rate of energy release at any given time during the model run. The lower plot shows the location at any given time of the cell where the greatest level of energy release is occurring. The y-axis represents the consecutive cell number of these cells. These plots cover the entirety of a run,

except the initial settling period. It is clear that the profile of the top plot (total energy release for the entire grid) is sufficiently similar to that of the middle plot that it indicates that the total energy release given by the top plot consists of the middle plot plus a reasonably constant background level.

Figure 3.34 shows these plots expanded by a factor of 20 in the time direction such that a time region of 10^5 time-steps (200 seconds) is covered instead of 2×10^6 time-steps (4000 seconds). In figure 3.33 we can clearly see that each spike corresponds to one location in the grid. It is therefore meaningful to expect events behaving as represented schematically in figure 3.30, and countable by consideration of the time-series of energy release of the entire grid, to correlate to actual energy release events taking place within the model. The opposite of this statement would be that spikes in the total energy release rate correspond to simultaneous superpositions of the energy release at several sites. Figure 3.34 shows that this is not the case.

Thus, given that only one large event occurs at any one time, we can locate that event and sum the energy released from the time that the event exceeds the background level until the time when it sinks below the background level. We can then deduct the background energy released over the duration of the event to obtain the integrated energy released.

We can see that the total energy release rate consists of the sum of the single most significant reconnection event plus the background and therefore, this evidence in conjunction with the fact, clarified above, that each spike relates to an individual cell, allows us to conclude that we are justified in considering only the largest reconnection event to represent the flaring activity within the grid. In other words, the auto-correlation length of events is greater than the total length of the model lattice. This is an interesting result given that it is similar to the behaviour we observe on the Sun insofar as there will only be a single large event at any given time.

So, the energy release time-series is used to generate a list of events each of which has a peak energy release value and an integrated energy released value associated with it. We can then produce distributions of these values on log-log plots (using base 10). The bin sizes used have a width of 0.4 (on log-log axes) and the counts within the bins are normalised according to the bin widths to give us P.D.F.s. Where we are comparing several plots we ensure that the bins are in the same positions to facilitate easy comparison.

Where we have fitted a line to a plot of event-sizes or cell parameter values, we also give a value of X^2 for the fit-line and error estimate for the fit-line gradient. This error on the gradient represents 90%-confidence values.

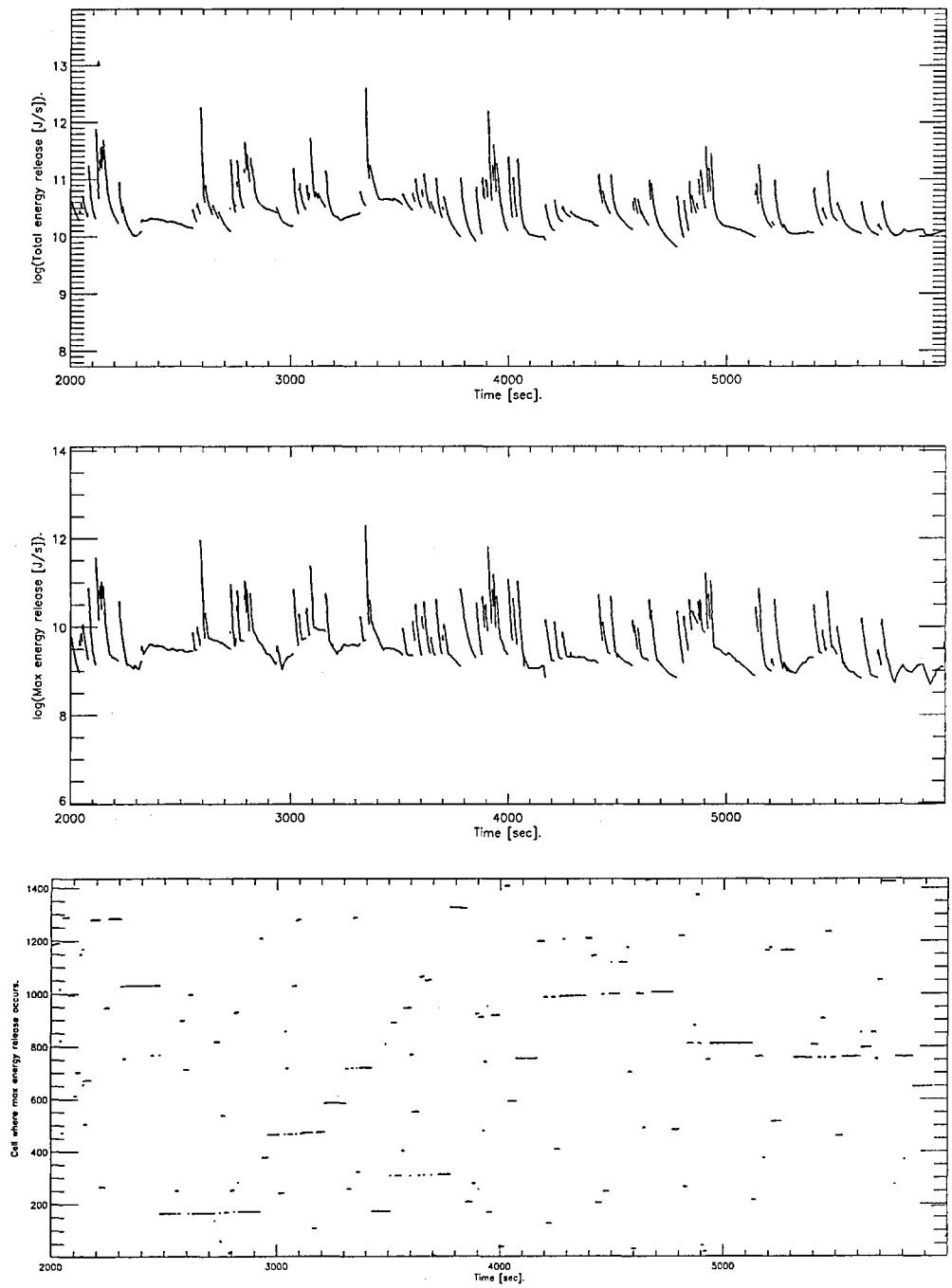

Figure 3.33: Top: total magnetic reconnection energy release time-series for whole grid. Second: magnetic reconnection energy release time-series for cell producing greatest energy release at any given time. Bottom: location of greatest energy release at any given time. (2×10^6 time-steps (4000 seconds)).

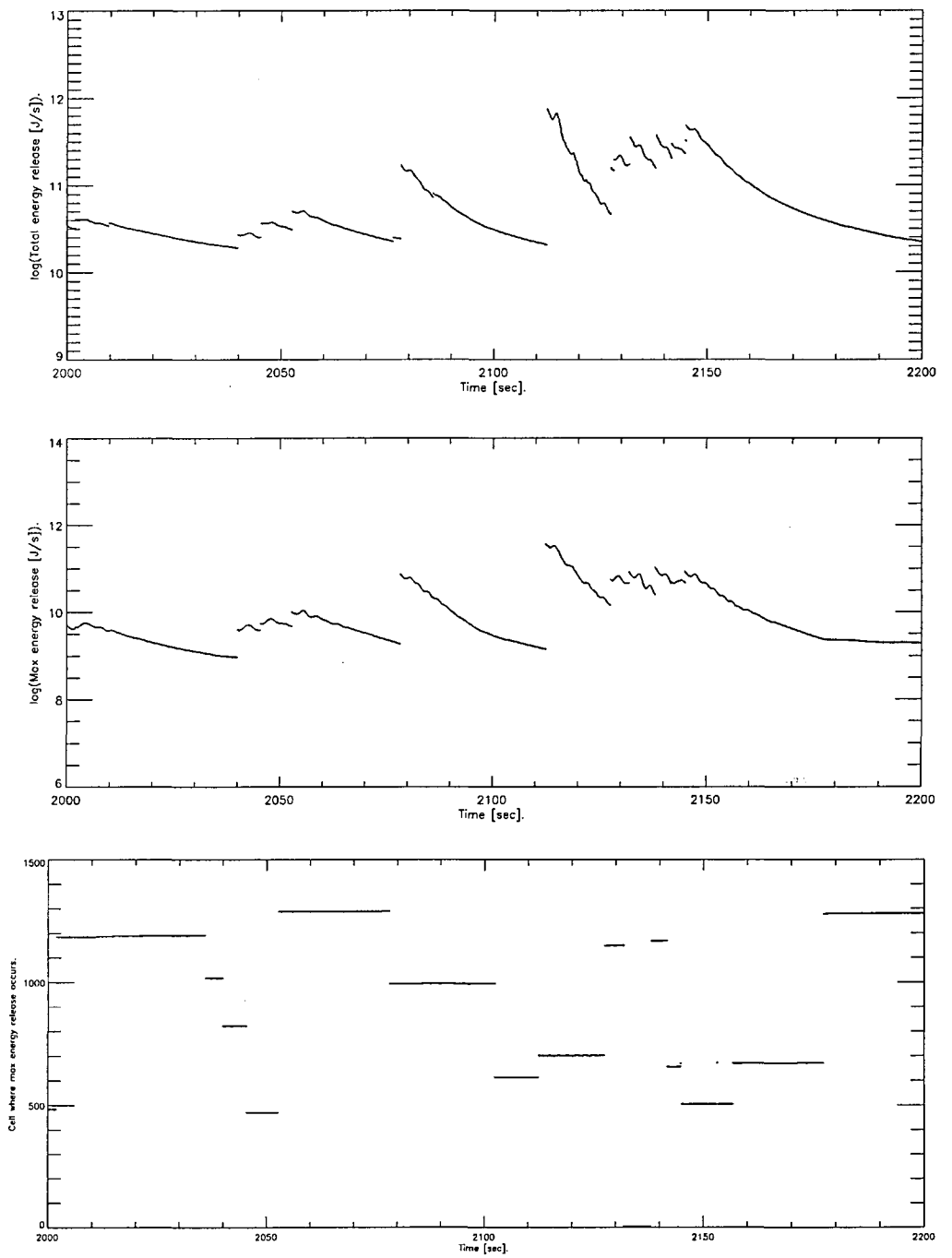

Figure 3.34: Top: total magnetic reconnection energy release time-series for whole grid. Second: magnetic reconnection energy release time-series for cell producing greatest energy release at any given time. Bottom: location of greatest energy release at any given time. (10^5 time-steps (200 seconds)).

Chapter 4

General Results from the Continuous Model.

"Somewhere outside, out under the apple trees, the Nocturnal Goatsucker asked his question again."
Kurt Vonnegut.

"Can't I deduct liquor if I have to get high to talk and talking's my business?"
Andy Warhole.

4.1 Introduction.

As we discussed earlier in the Introduction the Sun exhibits power-laws in the various parameters used to measure flare-sizes and these continue over at least eight orders of magnitude. In the Introduction we also discussed the findings of Meunier (1999), who identified self-similarity of magnetic field regions in the photosphere. We must now ask whether the continuous model is capable of producing similar power-laws. In fact, we have already described in chapter 3 a variety of power-law and power-law-like distributions produced by the model in every variant of the basic conditions used so far.

We start by making a brief comparison between the energy release time-series data produced by the model and the Solar flare X-ray time-series. We will next discuss colour diagrams illustrating magnetic field density and rate of energy release as functions of time and position along the model grid. These diagrams demonstrate some gross behaviours of the model. We examine some distributions of magnetic field density produced by the model using a variety of initial cell lengths ranging from

3×10^3 m to 4×10^4 m and models using 10^3 cells and 5×10^3 cells in the initial state. We discover, for both B and ϕ, that we can divide the distributions into two regions and fit power-laws to the regions of the plots lying above the initial B and ϕ values. We then find that the distributions of unipolar region size are exponential and try to determine if this is an effect frozen into and persisting from the initial state. For five variations of the parameters determining level of emergence/submergence we look at distributions of B, ϕ, L_{unipolar} and event-sizes to ascertain the role of emergence and submergence. Event-size distributions are next obtained for the flux-collision scheme. We look at peak and integrated energy event-size distributions for the typical conditions, although with initial cell lengths of both 10^4 m and 5×10^3 m. The power-law and power-law-like distributions are collected into a table and briefly discussed following which an attempt is made to determine whether either or both reconnection and emergence/submerge of flux are necessary and/or sufficient for production of power-law-like distributions. This is done by comparing B, ϕ and event-size distributions for (1) typical initial conditions, (2) reconnection turned off, and (3) emergence/submergence rate reduced by a factor of 10. These comparisons are made for initial cell lengths of both 10^4 m and 5×10^3 m. Finally we summarise and compare in tabular form the basic properties of the event-size distributions obtained in chapters 4 and 3.

Except where exceptions or variants are specifically mentioned or described, all data plotted in this chapter, and any further results outside this chapter, will be produced by runs using the standard initial parameter values as per the Definition of Commonly Used Terms given at the beginning of the thesis. For convenience of reference we will repeat those here once :

Number of cells	=	10^3
Cell length	=	10^4 m
Reconnection	:	standard mechanism
Emergence/Submergence	:	activated
Cell fraction for emergence/submergence, κ	=	0.1
Flux replacement timescale, $t_{\text{em/sub}}$	=	10^3 s
Noise level, $\frac{\psi}{P}$	=	zero

Each run of the model starts with the cells having a specific length allocated and a random uniform distribution of magnetic field density in the range $-100 \leftrightarrow +100$ G (giving $\overline{|B|} = 50$ G). We can thus easily calculate the mean initial magnetic field density and mean initial cell flux for each run. Where we include in the text plots showing the distributions of unipolar region sizes, magnetic flux density and magnetic flux, we have found it useful to also draw vertical dotted lines showing these

mean initial values ($\overline{L_{\text{unipolar}}}$, $\overline{B}$, $\overline{\phi}$).

4.2 Cell Parameter Distributions.

In this section we address some general features of some of the data and provide comparison with real data.

4.2.1 Time-Series of Energy Release.

Figure 4.1 shows a time-series generated by the model, using the typical initial conditions and parameter values, of the energy release from magnetic reconnection integrated over the whole model grid. Figure 5.3 shows soft X-ray, hard X-ray and gamma ray emission from a single large flare recorded by the SMM ('Solar Maximum Mission') spacecraft at the time of the last Solar maximum.

These plots are included to compare the model results and real data. The timescales are comparable between the two graphs, figure 5.3 covering a span of $\sim$ 1 hour, and figure 4.1 is of 4000 seconds. The first plot of figure 5.3 is soft X-rays, which is thermal emission from material heated by the impulsive hard X-rays. The second plot is of hard X-rays, which will originate from free-free, electron-ion bremsstrahlung. The third plot is for gamma-rays, which originate from nuclear particle and high energy free-free interactions. The hard X-ray and gamma-ray plots may be compared with our results in figure 4.1. In figure 4.1 and hard X-ray and gamma-ray plots of (figure 5.3), we see spikey events with extremely impulsive increases followed by slower (though still fast) decays. The plots are log-linear, therefore since the decays of our model-generated data are concave in shape we recognise them as faster than exponential. In chapter 5 we will determine the form of these decays using an analytical approach. Where we see discontinuity in the line on figure 4.1, this is a result of the suddenness of the increases. The time-series on both of these figures ranges over a little less than two orders of magnitude, with a few exceptions. What we are looking at in figure 4.1 is a superposition of a few large events at any one time superposed upon a much lower background of many small reconnection events.

4.2.2 Energy Release Analysis.

Let's have a look now at a diagram showing the energy release from cells in the model : figure 4.3. This diagram demonstrates the rate of energy release by magnetic reconnection as a function of both distance along the grid and time. Thus we have time along the x-axis, running from zero to 2×10^6 time-steps (4000 seconds) and the y-axis represents position within the grid of the model. The total length of the grid (i.e. total length of cells) remains constant. This diagram only shows 1/10 the full

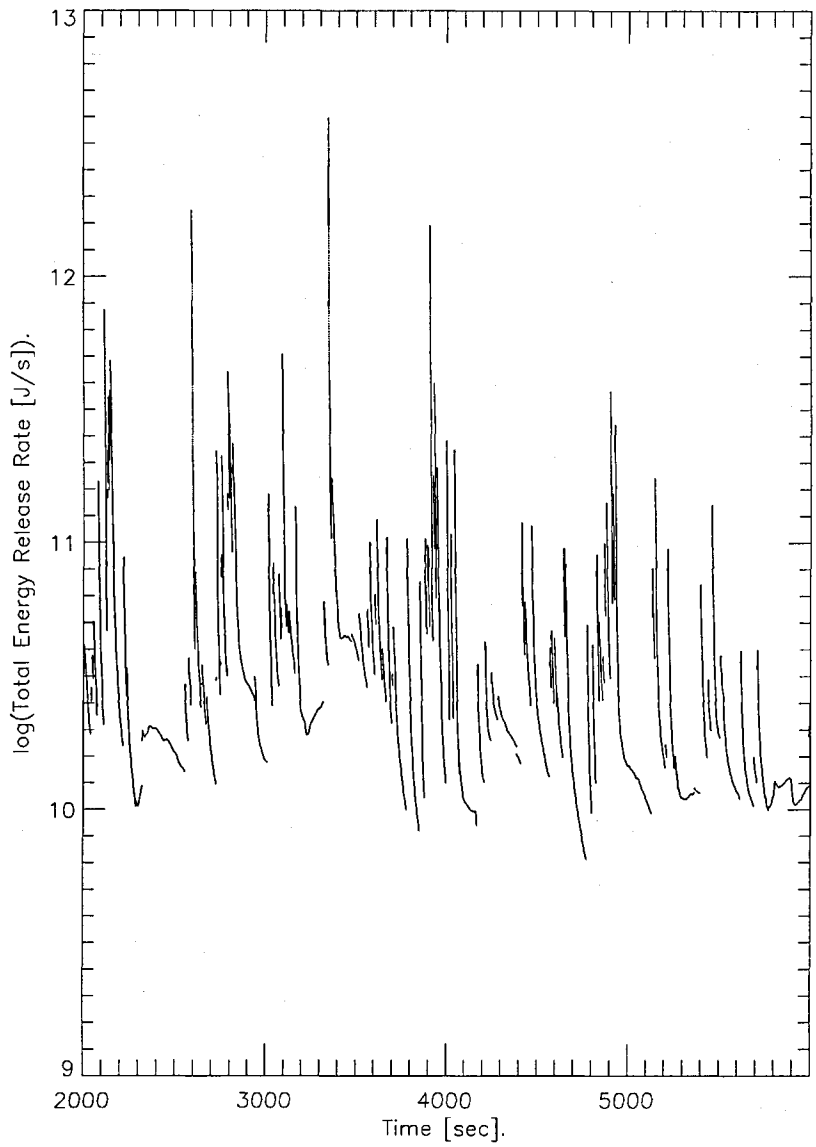

Figure 4.1: Total magnetic reconnection energy release time-series for whole grid. (2×10^6 time-steps (4000 seconds)).

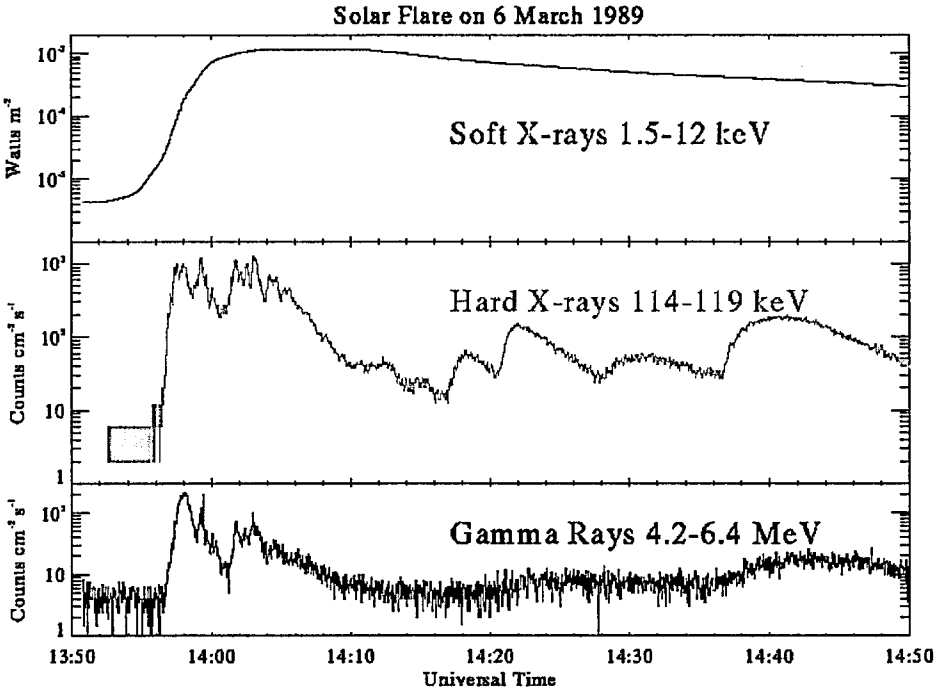

Figure 4.2: Solar X-ray flux measured by SMM.

length of the grid (i.e. approximately 100 cells, or 10^6 m). The grey regions represent cells where no energy release is taking place. This occurs when the cell is not undergoing reconnection with either of its immediate neighbours, i.e. its magnetic flux is parallel with that of both neighbours. Red and blue regions represent energy release, where red equates to low energy release rate, and blue equates to high energy release rate. Thus, the more blue and the less red a pixel is, the higher the energy release rate. Uniformly coloured bands are recognisable as individual cells. Oscillations of the cells due to the fluid dynamical behaviour are clearly evidenced by the waves we can see in the cell positions. Cells lower in the diagram appear to undergo smaller amplitude oscillations, tending to zero at the very bottom of the diagram. This is an artefact caused by the fact that the diagram shows the position of cells relative to the lower-most cell.

Thus, the figure shows us a range of energy release rates occuring simultaneously. We see sites (circles A, B and D for example) where energy release suddenly switches on within a cell. Commencement of energy release is visible within several adjacent cells, up to five in the energy release analysis.

There are examples where energy release suddenly switches off (circle C). Additional to the wave behaviour, we see the spacing between groups of cells increase and decrease. These behaviours are

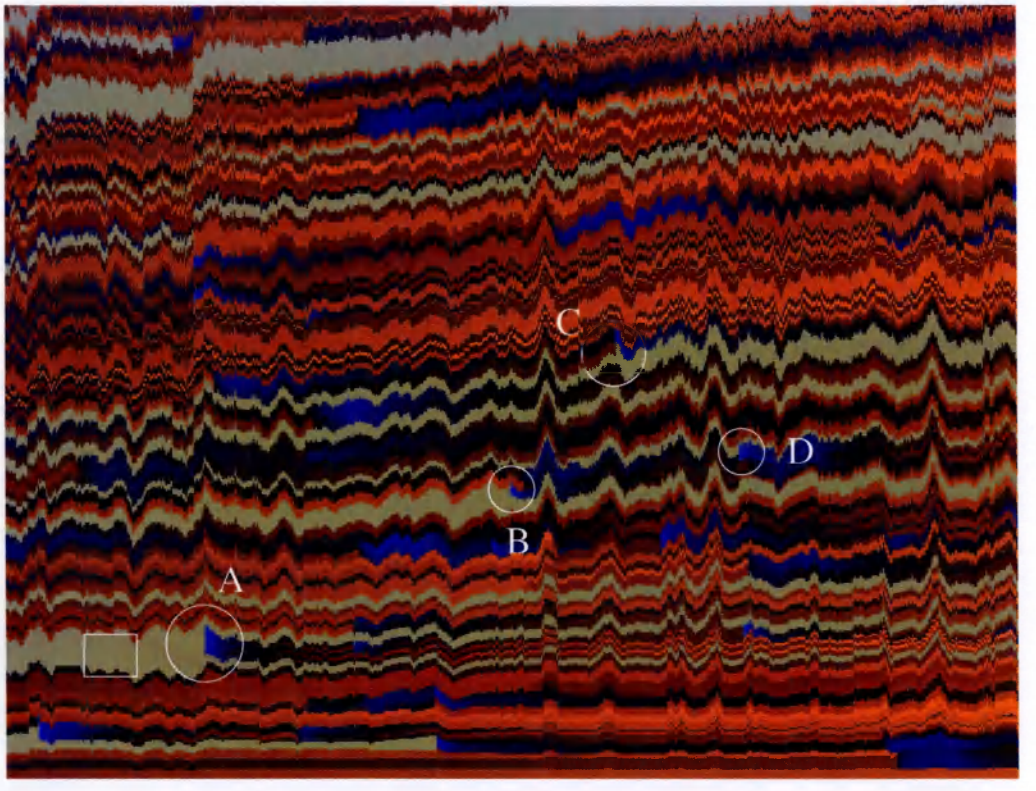

Figure 4.3: Magnetic energy release analysis. Energy release is given as a function of time and grid position. The x-axis shows time, the positive direction being to the right. The y-axis shows cell position within the model grid and is directly proportional to physical distance. Covers a complete run (4000 seconds) and 10^6 metres. Grey regions correspond to zero energy release. Red and blue regions correspond to non-zero energy release (blue : high energy release rate; red : low energy release rate).

explained by the emergence and submergence of magnetic flux.

Where energy release is not occurring within a cell, the emergence of a new cell beside it which has anti-parallel flux will allow reconnection and therefore energy release to commence. See figure 4.4. Similarly, the submergence of a cell which is preventing anti-parallel flux from meeting and reconnecting, will allow reconnection to commence. See figure 4.5. The corollary of this is that energy release can be arrested by emergence and submergence of cells. Occasionally there will be a cell with anti-parallel flux compared with its neighbours (see figure 4.6) and therefore undergoing magnetic reconnection with both neighbours. If the cell is submerging then when the submergence is complete one of its neighbours may become surrounded by cells with parallel flux, and therefore stop undergoing energy release. Also, as we can see in figure 4.7, the emergence of a new cell can act to prevent reconnection.

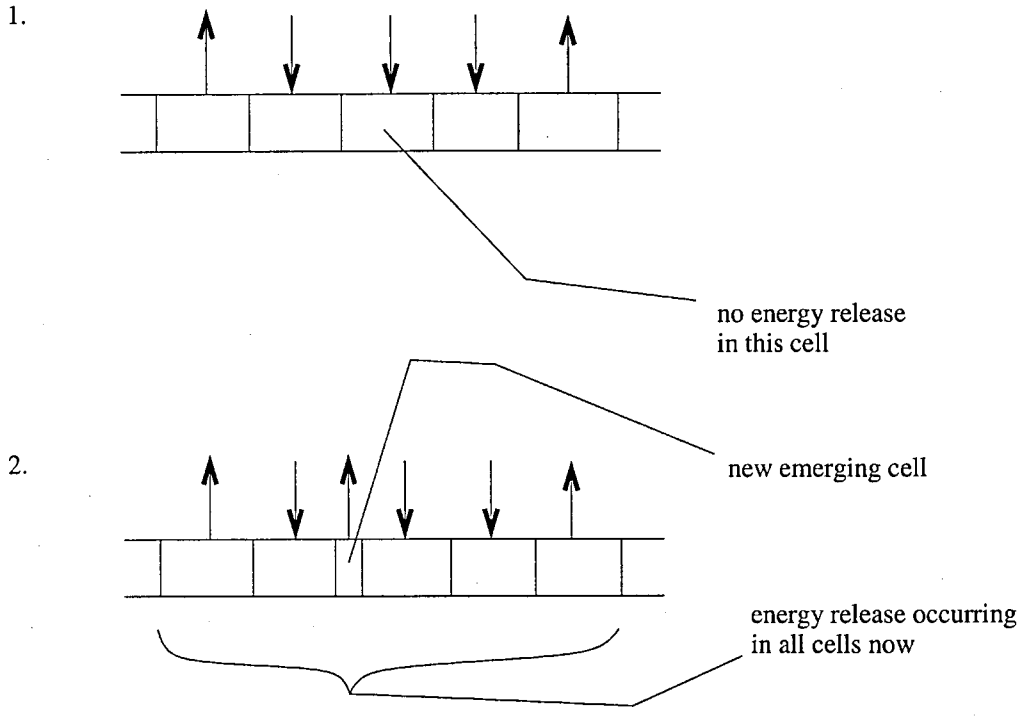

Figure 4.4: Emergence facilitating commencement of energy release.

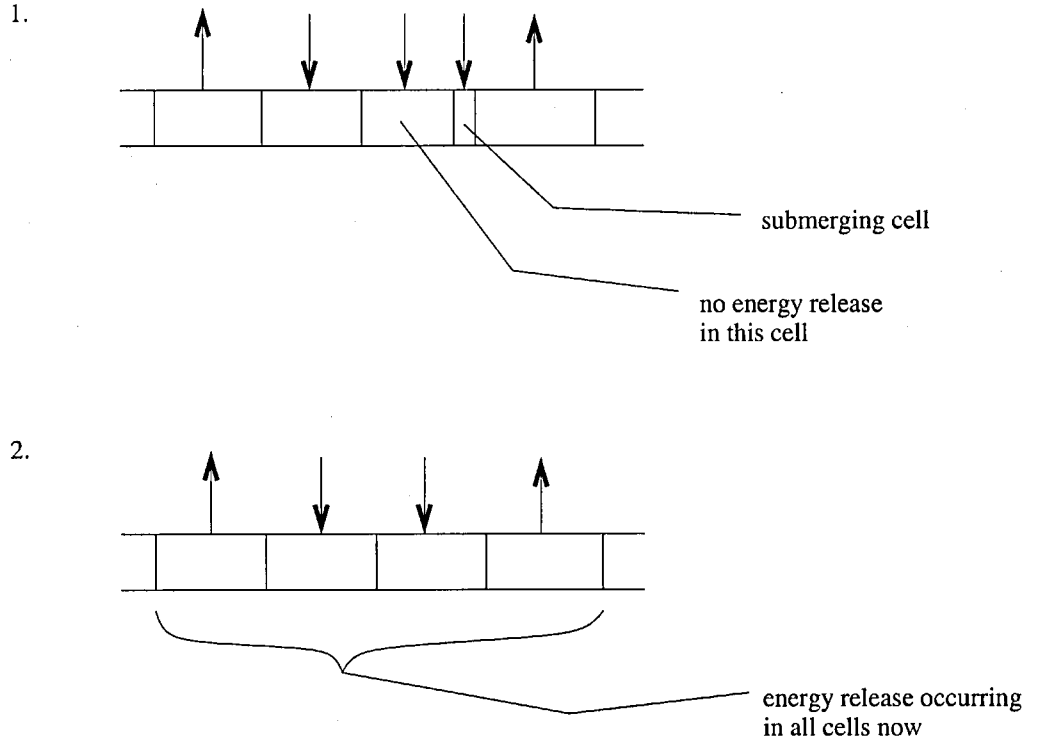

Figure 4.5: Submergence facilitating commencement of energy release.

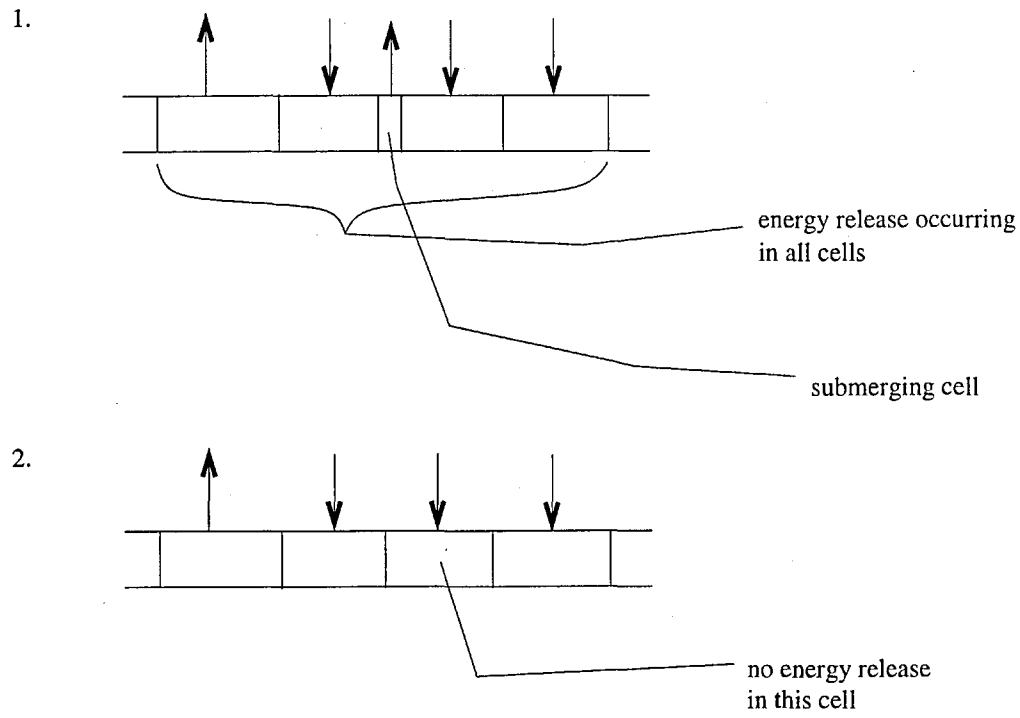

Figure 4.6: Submergence causing energy release to cease.

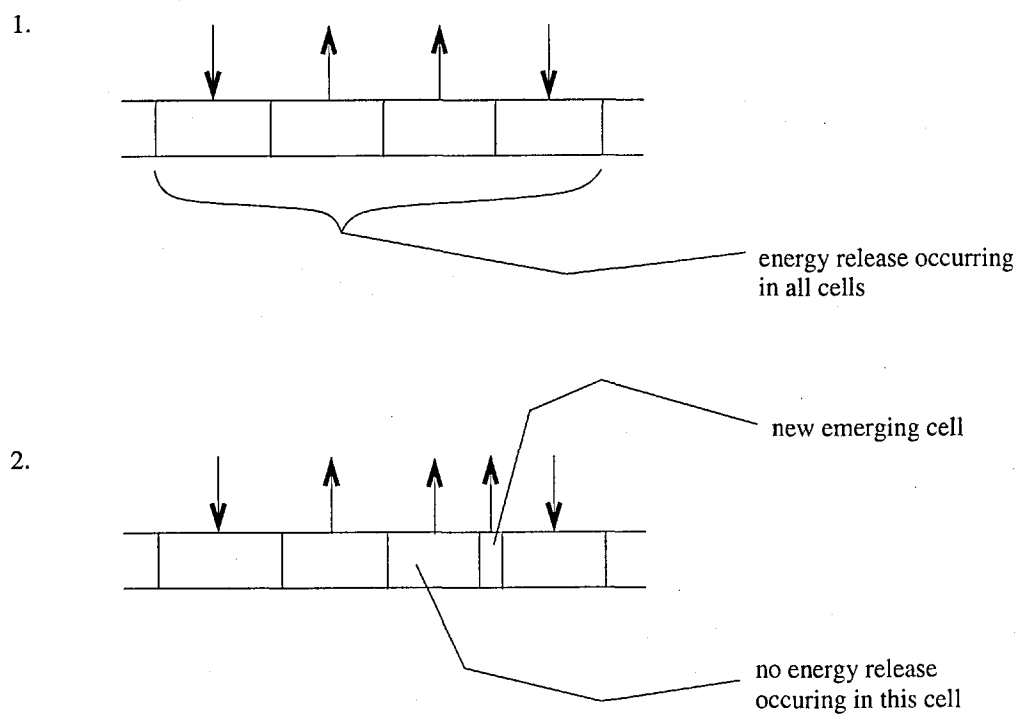

Figure 4.7: Emergence causing energy release to cease.

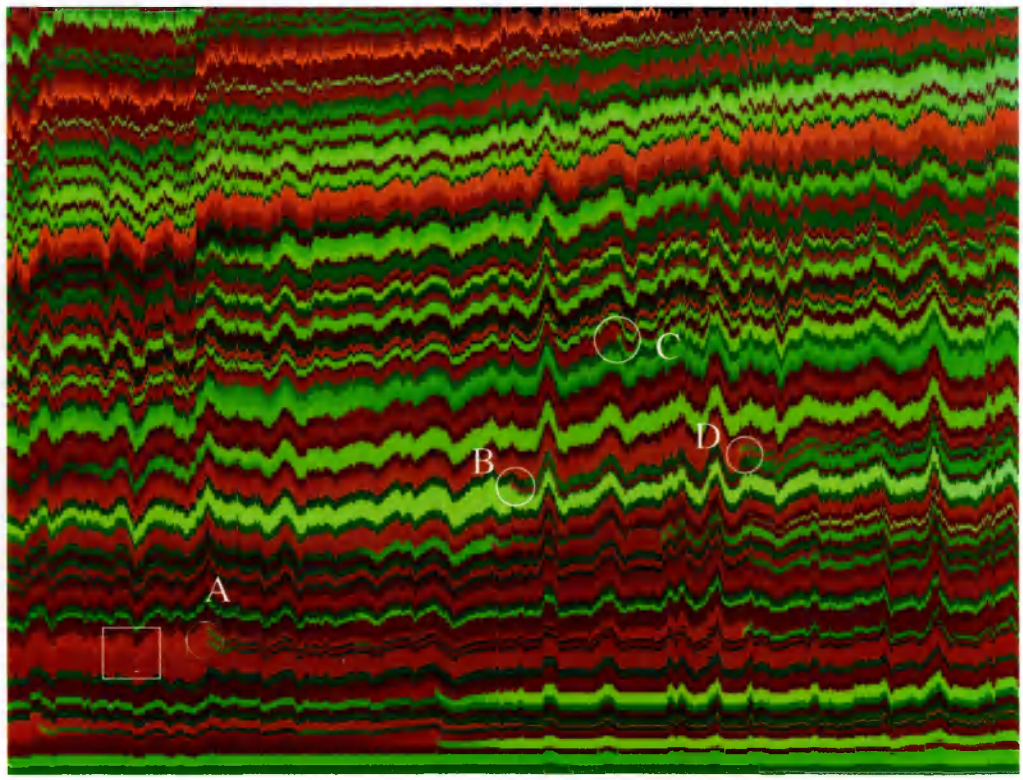

Figure 4.8: Magnetic field density analysis. Field density is given as a function of time and grid position. The x-axis shows time, the positive direction being to the right. The y-axis shows cell position within the model grid and is directly proportional to physical distance. Covers a complete run (4000 seconds) and 10^6 metres. Red pixels correspond to positive magnetic field, and green corresponds to negative magnetic field. The colour intensity corresponds directly to the magnetic field density.

Wherever we see events starting, if we follow the cell through increasing time the colour on the diagram changes from blue through to red. This is due to the progressive depletion of magnetic energy stored in that cell and the neighbour(s) with which reconnection is occuring. We can see some areas where a cell becomes very narrow and the colour moves towards blue. The cause of this is the increase in magnetic field density resulting from compression of the cell. We expect such enhanced field density to cause more rapid energy release.

4.2.3 Magnetic Field Analysis.

Now, figure 4.8 shows a plot for the same run of the model and covering the same part of the grid. However, the colours of this diagram express magnetic field densities. Positive field density is shown in red, and negative in green. The greater the magnitude of the field the greater the red, or green,

value at that pixel. Thus, we expect grey regions of the energy release analysis to correlate to cells where the magnetic field polarity on either side is the same as that adjacent to the cell, and therefore where no reconnection can occur. These grey regions will therefore correlate to regions of figure 4.8 where there are blocks of uniform colour (in the y-direction).

The squares and circles in figures 4.8 and 4.3 are located in the same positions and show some features worthy of note. The cells marked by a square in figure 4.3 show a region where there is no energy release, and this correlates to the region marked by a square in figure 4.8, where we can see that the magnetic field is unipolar. Circle A shows a region where fresh magnetic flux emerges in the middle of a previously unipolar region, suddenly providing opportunity for magnetic reconnection and energy release. Similarly, circles B and D both show areas where emergence occurs, facilitating the commencement of energy release. Circle C shows the submergence of magnetic flux causing the energy release to stop. If we look carefully, we can see the magnetic field density of cells reduce owing to the reduction of their magnetic flux by the process of reconnection. Although it is difficult to see, we would expect the colour intensities of red and green in figure 4.8 to fluctuate according to the compression and expansion of cells.

Thus, although these two figures show only approximately one tenth of the cells in the full grid. We can observe a range of fluid behaviour and its effect upon magnetic reconnection between the cells.

4.2.4 Distribution of Magnetic Flux Density.

For a given run, if we look at the state of the grid at the completion of the run there will be a distribution of magnetic field density values from which we can produce a P.D.F.

Let's first look at the initial distribution of magnetic field density so that we can establish that the distribution in the settled state isn't simply the initial state frozen into the model. Now, figure 4.9 shows us the initial distribution of magnetic field densities for this run. The upper plot uses linear axes and the lower uses log axes. With regard only to the lower plot, the upper end of the highest bin is not coincident with the upper end of the range of data, therefore this bin is only partially filled and we expect the bin-count to be anomalously low after normalisation of the bin. Therefore we shall discard this point when considering the profile of the distribution as shown in this lower plot. We expect these distributions to be flat since they are random and uniformly distributed. We can see that this is the case.

Now let's look at the magnetic field density distribution for runs at a point after the run has settled into a steady state. The top plot of figure 4.10 uses data from the same run as figure 4.9.

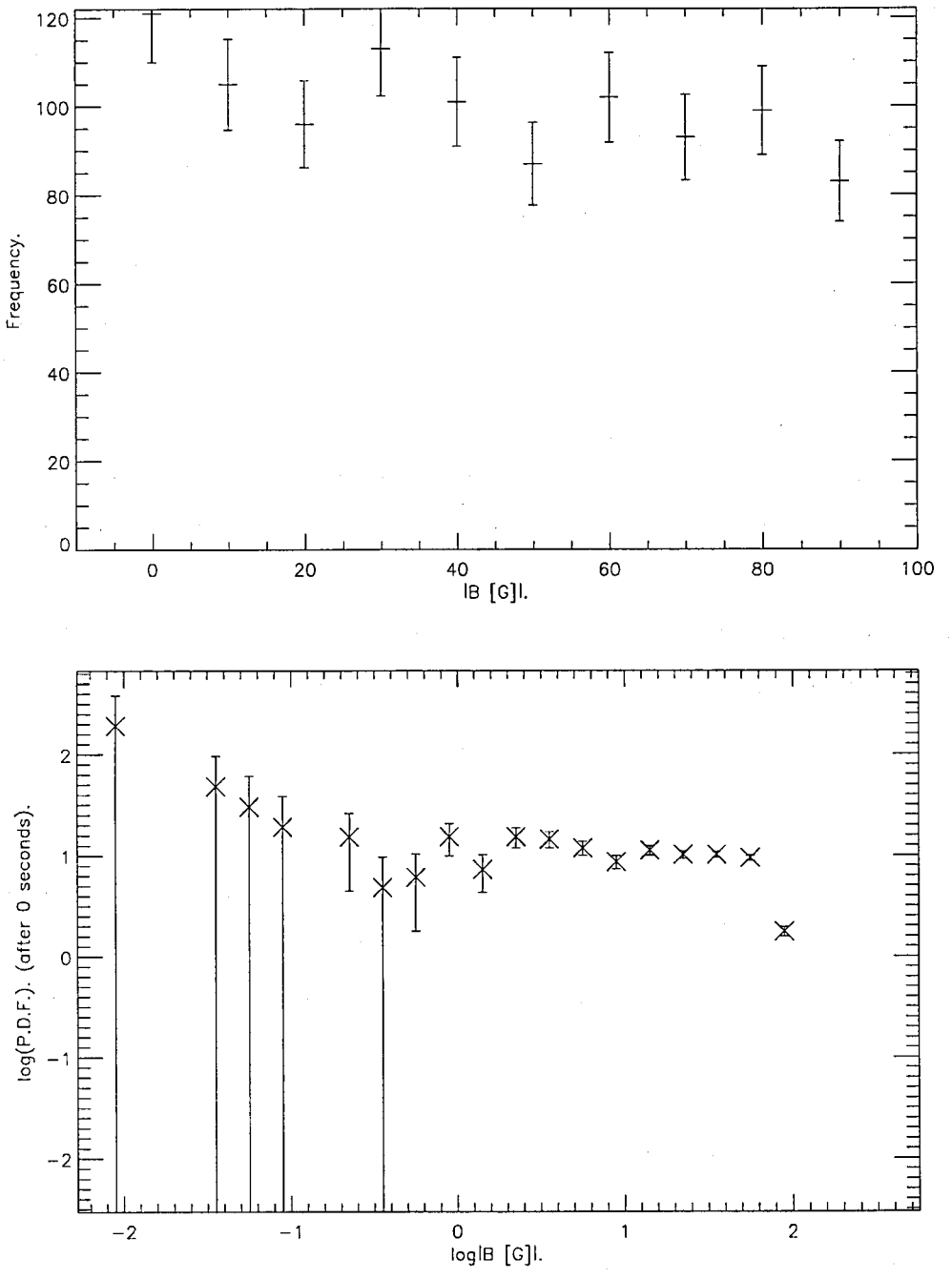

Figure 4.9: Initial distribution of magnetic field density. 10^3 cells. Top: linear axes; normalised; bin-size = 10 G. Bottom: log axes; bin-size = 0.2.

Regarding P.D.F. plots for magnetic field density distribution and magnetic flux distribution, the magnetic field density data only pertains to cells with length (at the completion of the run) greater or equal to the initial cell length. We discussed earlier that smaller cells are considered to lie below the resolution of the model therefore we must discard these prior to calculating any statistics.

Figure 4.10 shows the magnetic field density distributions for two runs with different numbers of cells (10^3 and 5×10^3 cells, all other conditions the same). We can see that the process of running the model has had the effect of moving the distribution of magnetic field density from a flat one to a more complicated profile. The range of field densities has increased, reaching more than $\sim$ log(400 G)=2.6. Dips have appeared at $\sim$ log(6.3 G)=0.8. Above $\sim$ log(40 G)=1.7 we see a power-law profile. The initial magnetic field density is uniformly distributed in the range $-100 \leftrightarrow +100$ G and the mean absolute value, in common with every run of the model is therefore $\sim$ log(50 G)=1.7 at the commencement of the run. Vertical lines have been drawn at these points on the plots of figure 4.10 to show this flux density. We can see that above this flux density there are power-law distributions in both plots. Thus it appears that some of the magnetic flux has been redistributed by the processing of the model into small numbers of cells with higher flux densities, and with power-law distributions. Both plots on figure 4.10 have the same general form, as we would expect. The bottom plot is different in origin only in that the data produced is higher quality since we have more points - the run commencing with 5×10^3 cells compared with 10^3. We see the same gradient for both plots of figure 4.10 which is not surprising since the only difference is the initial number of cells. Of particular interest to us is the power-law-like range on the right-hand side of these plots. On both top and bottom plots $\log|B| = 1.7$ is the point where the power-law distribution ends. This is clearer on the bottom plot, for which the data are more reliable.

Figure 4.11 shows the same type of results plotted where we have varied the initial cell length to 3×10^3 m, 5×10^3 m and 8×10^3 m, all other conditions remaining the same. We see similar profiles again. There is the same dip and redistribution of magnetic flux from the mid-range to above $\sim$ log(50 G) = 1.7. Also there is the power-law distribution produced from $\sim$ log(50 G) = 1.7 upwards and where the initial length is 8×10^3 m we again find the phenomenon of the power-law commencing at an x-value of $\sim$ log(50 G)=1.7.

Figure 4.12 shows three plots giving P.D.F.s of magnetic field density for cell lengths 10^4 m, 2×10^4 m and 4×10^4 m, running from top to bottom. Again, we see a power-law-like distribution above the mean initial flux density.

Thus, over a range of initial cell lengths, from 3×10^3 m to 4×10^4 m we see production of power-law-like distributions in the region immediately upwards from the initial mean flux density.

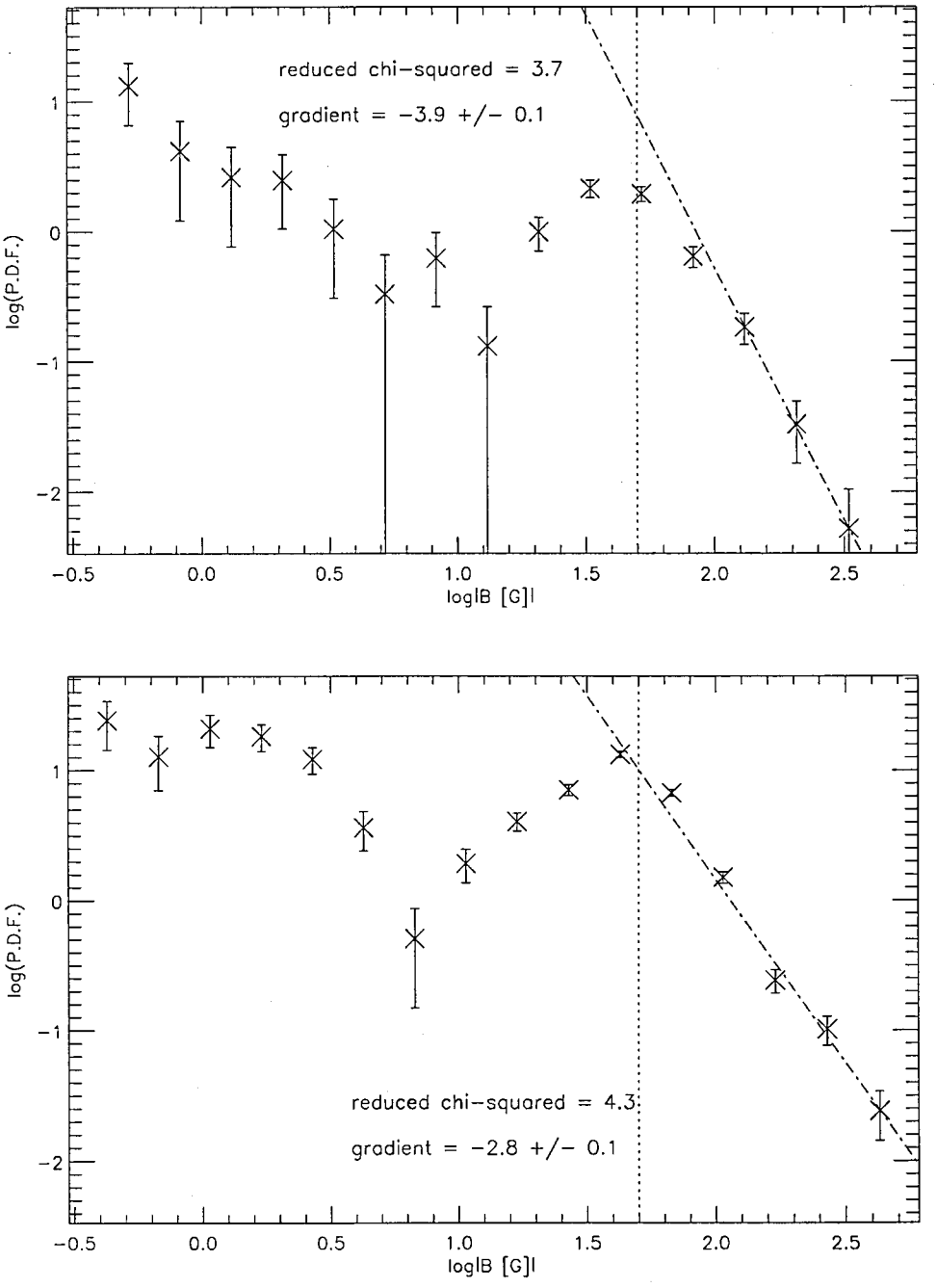

Figure 4.10: Evolved distributions of magnetic field density. Initial cell lengths are 10^4 m; bin-size = 0.2. Dotted lines mark mean initial magnetic field density. Top: 10^3 cells. Bottom: 5×10^3 cells.

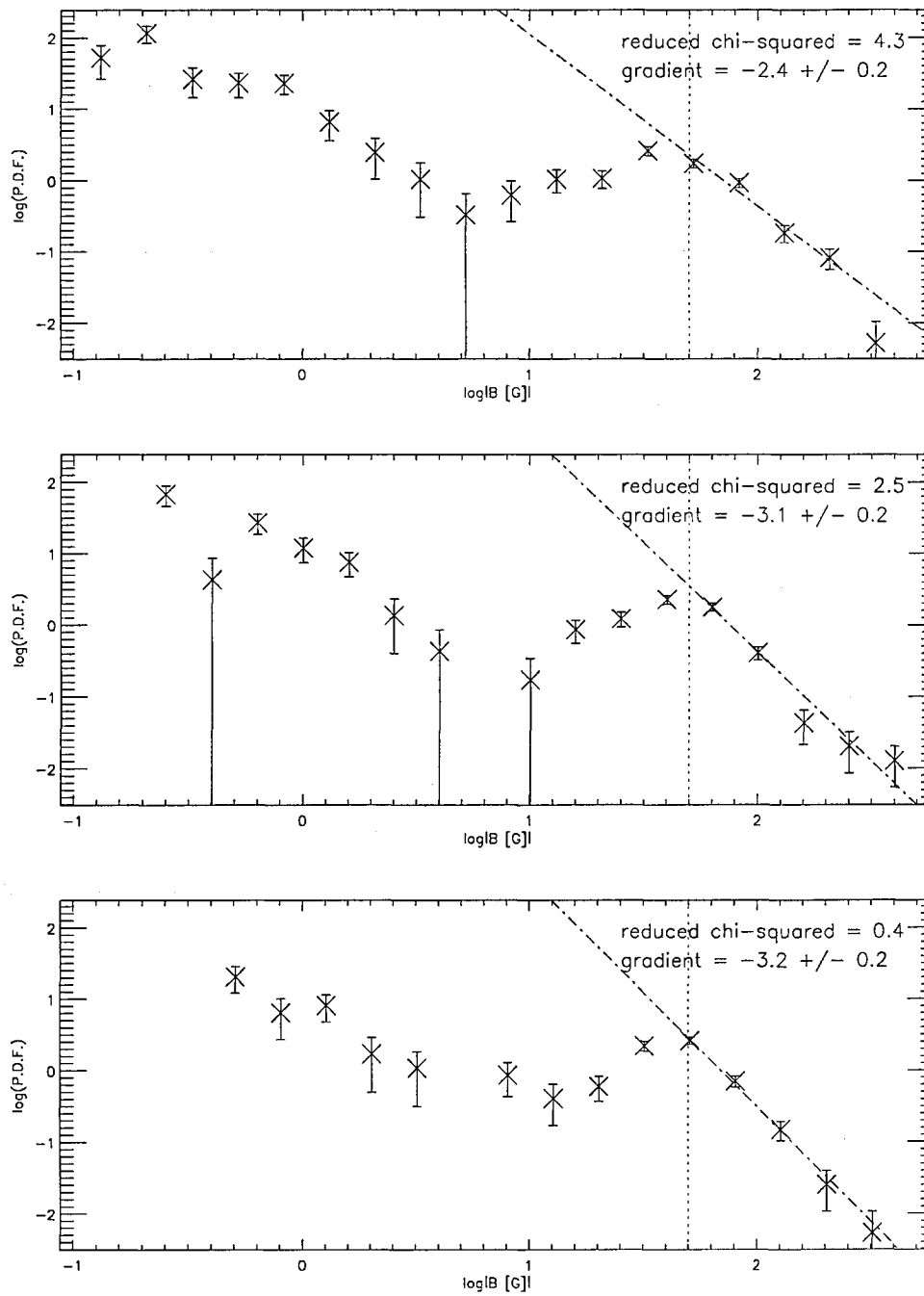

Figure 4.11: Evolved distributions of magnetic field density. Bin-size = 0.2; 10^3 cells. Dotted lines mark mean initial magnetic field density. initial cell lengths are : Top: 3×10^3 m. Second: 5×10^3 m. Third: 8×10^3 m.

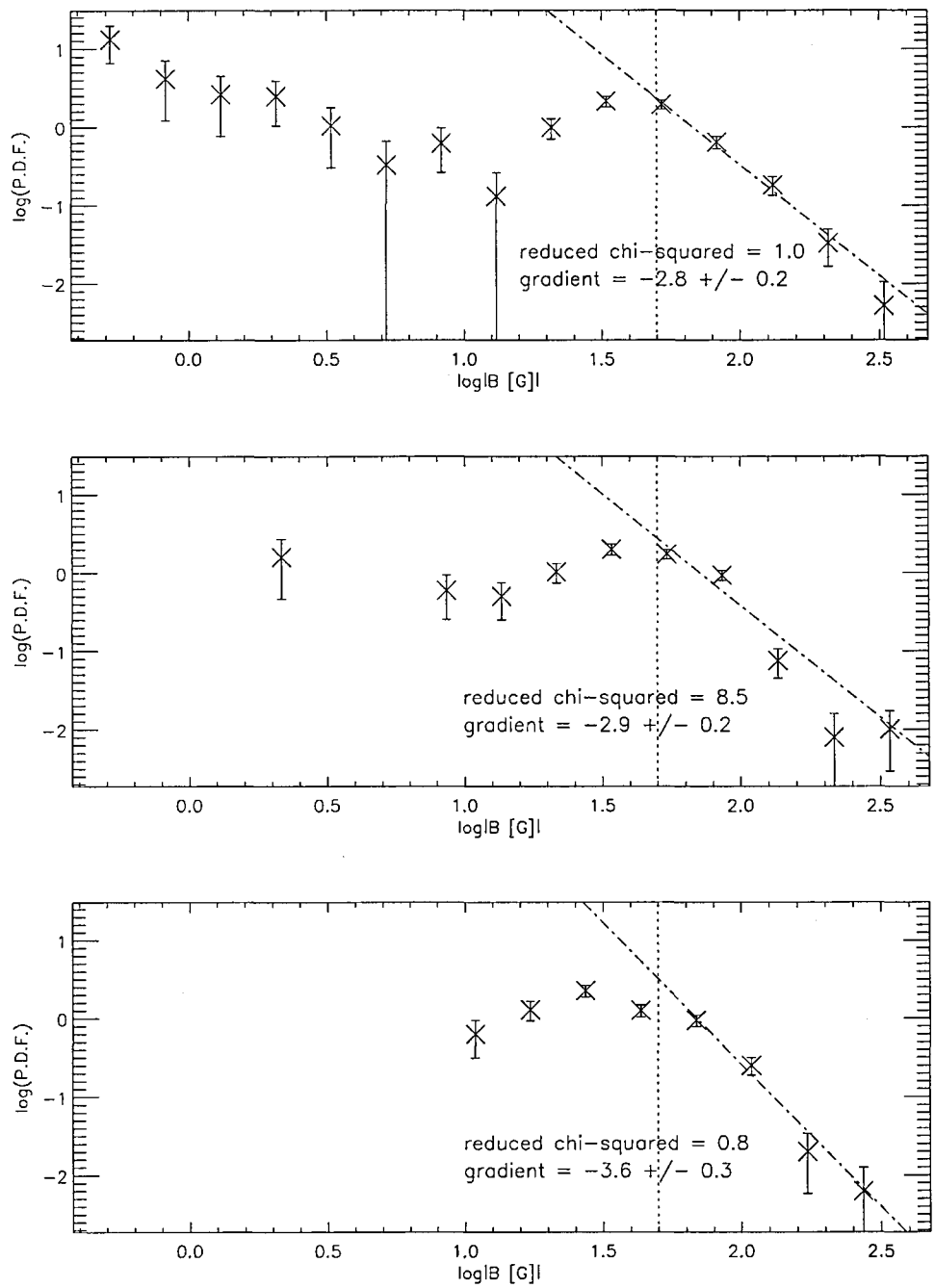

Figure 4.12: Evolved distributions of magnetic field density. Bin-size = 0.2; 10^3 cells. Dotted lines mark mean initial magnetic field density. initial cell lengths are : Top: 10^4 m. Second: 2×10^4 m. Third: 4×10^4 m.

Because we see these power-laws above the mean initial flux density in a region of the plots where the bin count would be zero in the initial conditions of the model, we shall fit a line to the data points lying above the mean initial flux density whenever we have a plot showing distributions of magnetic flux density and exhibiting these power-law features. Unless there is a good reason (such as a point relates to a bin straddling the end of the distribution and therefore produces an artifically low count) we will not discard any point within this range in making the fit. Therefore we will have the same basis for comparison across all the plots.

In all three figures 4.10, 4.11 and 4.12 we see a peculiar distribution in the x-range lying below the initial mean flux density. In fact, the shape of this part of the plots is similar between all our plots which show distributions of magnetic flux and magnetic flux density. The running of the model has produced a re-distribution of magnetic flux where flux around the $\log|B| = 0.6 \leftrightarrow 1.0$ range has become depleted. We expect this flux has been moved, by the emergence/submergence and reconnection processes, to above $\log|B| = 1.7$ and to below $\log|B| = 0$. It is not clear how this may be analysed. We see the same phenomenon in every plot showing a P.D.F. of flux density in the thesis including figures 3.17 and 3.18 shown in chapter 3. From now on we will therefore restrict our x-axis to show only the range of interest.

In figures 4.10 and 4.11 the magnetic field density reaches values of several hundred Gauss, far in excess of the initial values (between -100 G $\leftrightarrow +100$ G).

We can conclude that the model produces power-laws in the distribution of magnetic flux density above a threshold of approximately $|B| = 50$ G.

4.2.5 Distribution of Magnetic Flux.

Let us now consider the distribution of cell magnetic fluxes produced by the model. The initial distributions will be flat since $\phi_i = B_i L_i W$ and initially, all L_i will take a single identical value, the width of the grid, W, does not alter from 10^3 m and B_i takes a uniform random distribution. We can see this clearly in the top plot of figure 4.13 confirming the initial distribution is flat. We should note that the same effect occurs here as in figure 4.9 : the upper end of the highest bin is not coincident with the upper end of the range of data, therefore this bin is only partially filled and we expect the bin-count to be anomalously low after normalisation of the bin. Therefore we can ignore this point. The second and third plots in figure 4.13 are equivalent to the two plots in figure 4.10 insofar as both show results for 10^3 cells and 5×10^3 cells. Figure 4.13 shows magnetic flux whereas figure 4.10 shows magnetic flux density. Again we see similar profiles in the evolved distributions, with power-laws at the high end of the plot. There is data missing from the lower ends of the plots

owing to the fact that we ignore cells which are shorter in length than the initial 10^4 m. Such cells are considered to fall below the resolution of the model.

Now, let's consider the mean initial flux in the cells of the model. The initial magnetic field density is uniformly distributed in the range -100 G $\leftrightarrow$ $+100$ G and the mean absolute value is therefore 50 G. Figure 4.14 shows the typical cell we are considering here, and for a cell of length 10^4 m a flux density value of 50 G gives a total magnetic flux for the cell of $5 \times 10^{11} = 10^{12.70}$ Mx. Vertical dotted lines have been drawn on the plots of figure 4.13 to show this level of flux density. This point appears suprisingly far to the right of these plots, however this is an effect of the log x-axis. We can see that above this level there is a power-law distribution in both the second and third plots. This indicates that the processing of the model produces a power-law distribution in the magnetic flux distributions. The run which produced the second plot of figure 4.13 used cells with initial length of 10^4 m. Figure 4.15 shows comparable plots, initial lengths 3×10^3 m, 5×10^3 m and 8×10^3 m.

Thus, figure 4.15 shows us plots of magnetic flux distribution over a range of initial cell lengths from 3×10^3 m to 8×10^3 m and in all of these we see similar power-law-like distributions upwards of the mean initial flux.

Therefore we conclude that the model produces power-laws in the distribution of magnetic flux above the mean initial levels.

Because we see these power-laws above the mean initial flux in a region of the plots where the bin count would be zero in the initial conditions of the model, we shall fit a line to the data points lying above the mean initial flux whenever we have a plot showing distributions of magnetic flux and exhibiting these power-law features. Unless there is a good reason (such as a point relates to a bin straddling the end of the distribution and therefore produces an artifically low count) we will not discard any point in making the fit. Therefore we will have the same basis for comparison across all the plots.

The profiles of figures 4.11 (flux density) and 4.15 (flux) are almost identical. These plots were produced from the same runs. Again, these plots were produced from the same runs. We conclude that there is very little correlation between B and L.

In both figures 4.13 and 4.15 we see that below the initial mean flux the distribution has changed from the initial flat distribution as a result of running the model. We have commented up this in section 4.2.4. From now on we will restrict our x-axis to show only the range upwards from the value of the initial mean flux.

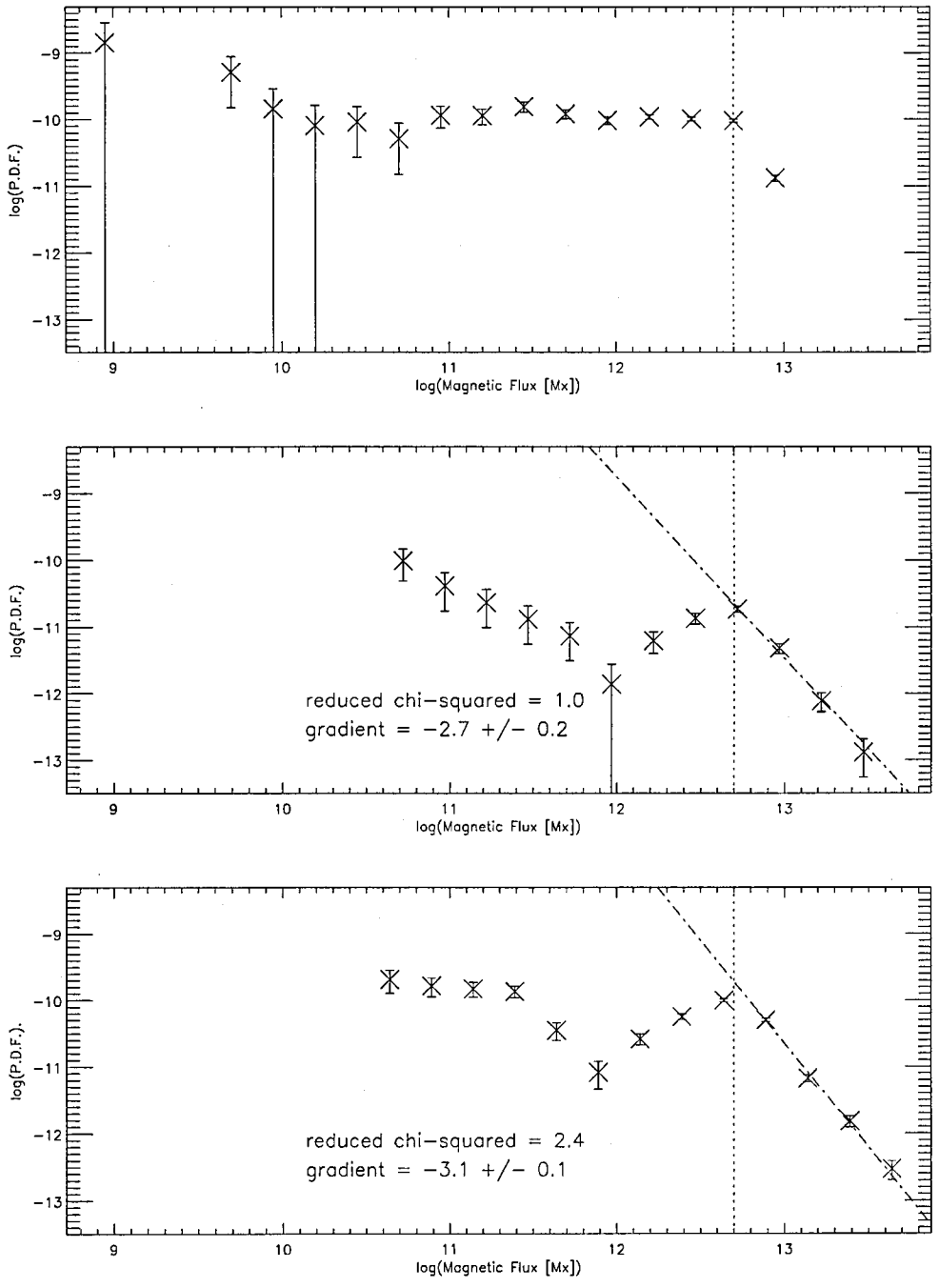

Figure 4.13: Distributions of magnetic flux; initial cell length = 10^4 m; bin-size = 0.25. Dotted lines mark mean initial magnetic flux. Top: initial distribution; 10^3 cells. Second: evolved distribution; 10^3 cells. Third: evolved distribution; 5×10^3 cells.

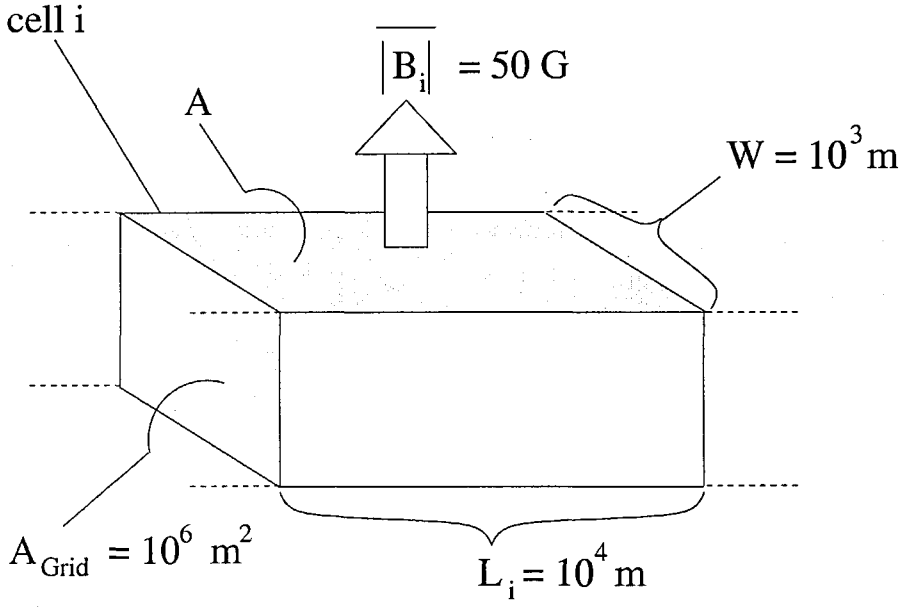

Figure 4.14: Typical cell in inital state where cell length = 10^4 m.

4.2.6 Distribution of Unipolar Region Sizes.

In addition to looking at magnetic field density and total magnetic flux we should also consider the sizes of the islands of same-polarity ('unipolar') magnetic flux. The notion of a unipolar region was explained in section 3.6.1. We can produce distributions of the sizes of these regions and so have a measure of the way they scale.

The plots in figure 4.16 which use a linear scale on the x-axis, are produced by counting and binning the sizes of the regions of unipolar field. The bin-size is 10^4 m, the same as the initial cell length. The top plot shows the initial distribution for a run with 10^3 cells, the second shows the evolved distribution for this same run. The third plot shows the evolved distribution for a run starting with 5×10^3 cells. Typically, these runs will commence with the magnetic field density of each cell being determined by a uniformly random distribution in the range $-100 \leftrightarrow +100$ G. Given this random distribution the unipolar region sizes will initially be exponentially distributed. The argument for this is explained fully in chapter 5. The second and third plots show us that the processing of the model has not destroyed the profile, although the gradient has changed in both cases to ~ -0.38. We must ask ourselves whether the exponential profile is frozen into the initial conditions of the run and remains thereafter.

To ascertain the answer to this question we will consider a run where the initial distribution is not exponential but is instead a delta function. In the initial state the polarity of the magnetic field is made to alternate every three cells. Since the initial cell length is constant at 10^4 m we are

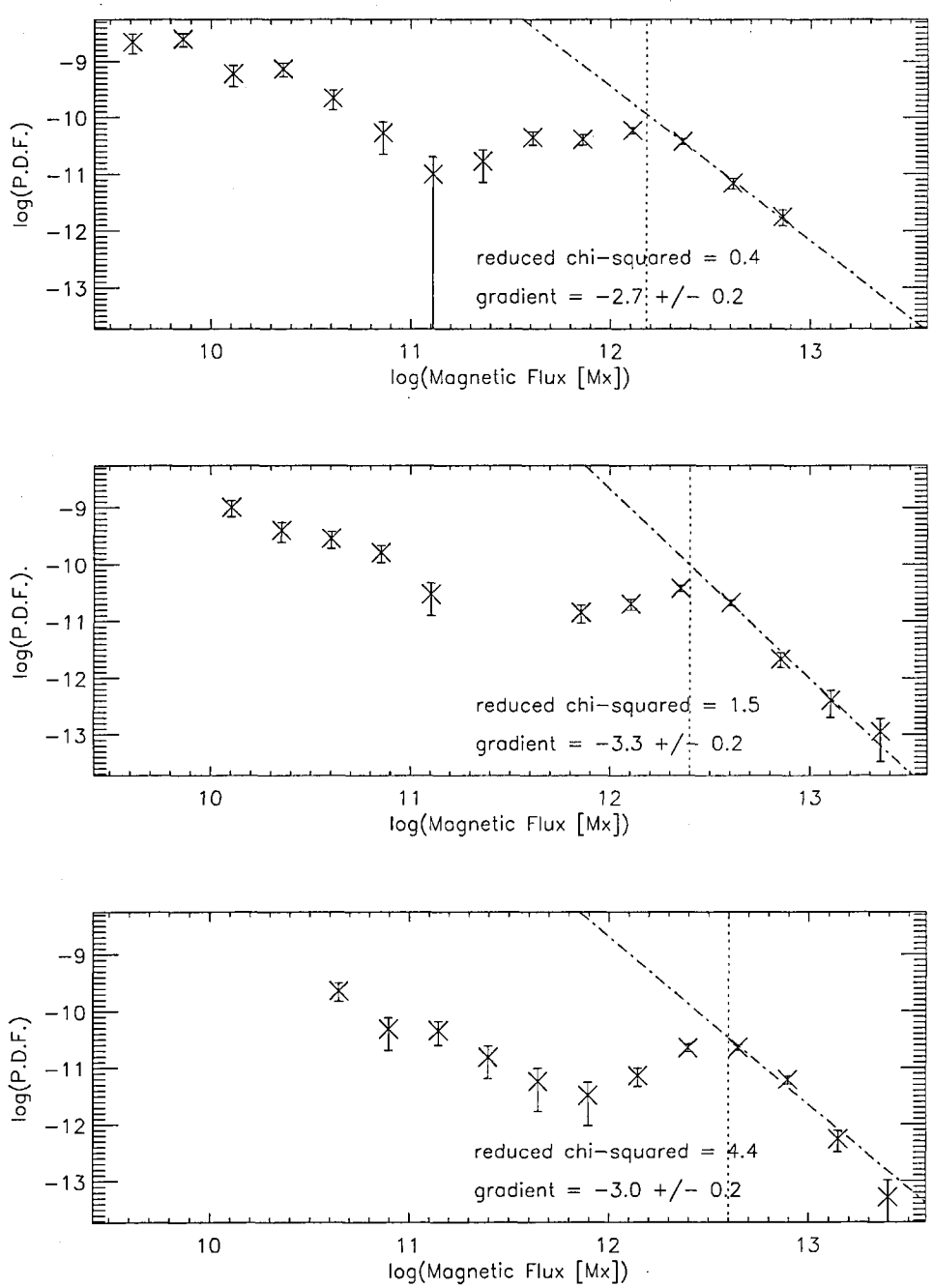

Figure 4.15: Distributions of magnetic flux; 10^3 cells; bin-size = 0.25. Dotted lines mark mean initial magnetic flux. Top: evolved distribution; initial cell length = 3×10^3 m. Second: evolved distribution; initial cell length = 5×10^3 m. Third: evolved distribution; initial cell length = 8×10^3 m.

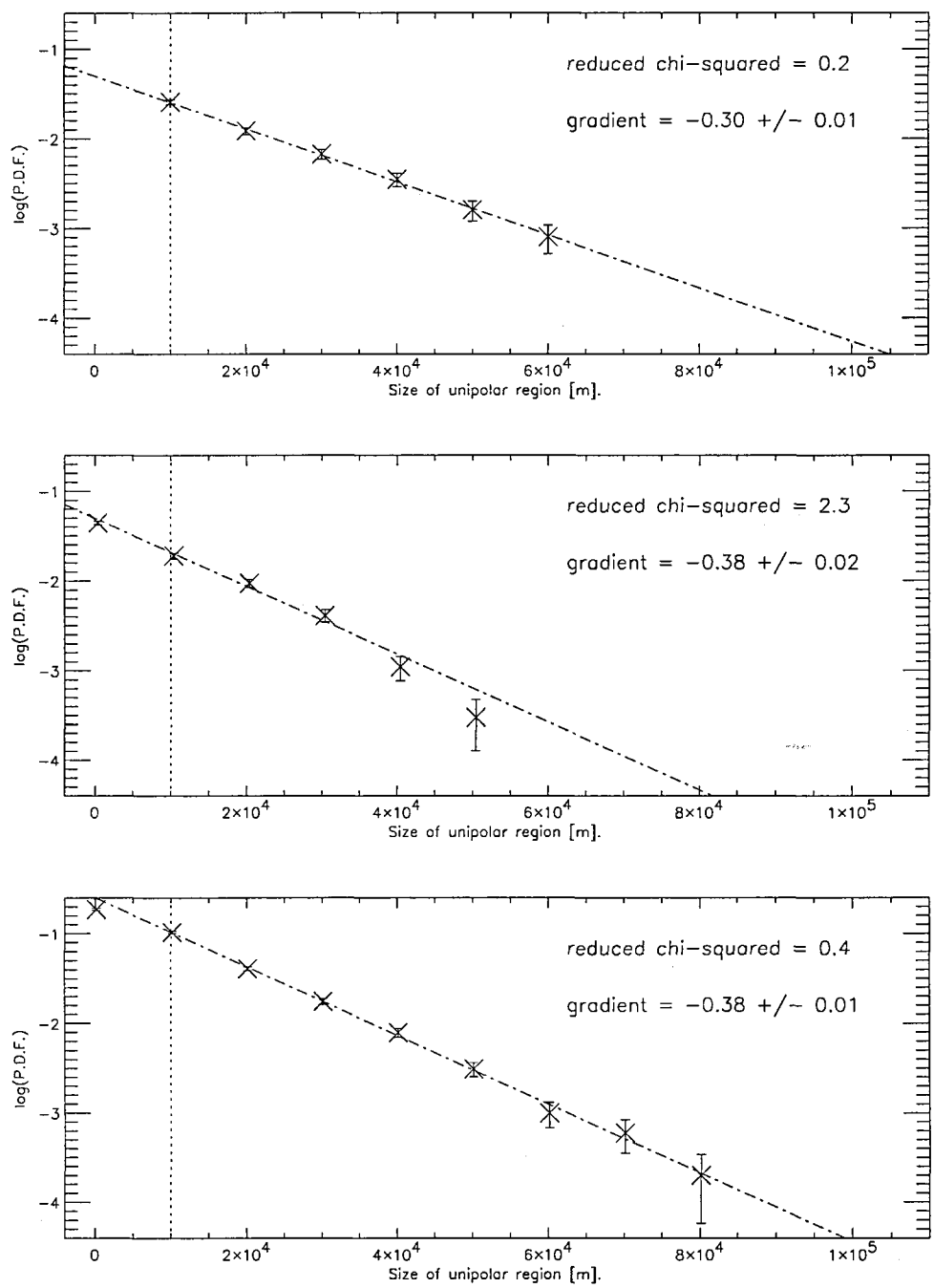

Figure 4.16: Distributions of sizes of regions of unipolar magnetic flux, using log-linear axes; initial cell length = 10^4 m; bin-size = 10^4 m. Dotted lines mark initial cell length. Top: initial distribution; 10^3 cells. Second: evolved distribution; 10^3 cells. Third: evolved distribution; 5×10^3 cells.

therefore ensuring that the unipolar regions are uniformly of length 3×10^4 m. We can then see where the distribution settles to after this initial state. Figure 4.17 shows this data for initial cell lengths of 10^4 m and and 5×10^3 m. The top plot of this figure shows (this is the same data as the top plot of figure 4.16) that the model has produced a fairly smooth exponential distribution, however the second plot of figure 4.17 shows us that the distribution has also evolved to an exponential-like distribution, although from a delta function, yet it retains after running for 3×10^6 time-steps a memory of the initial unipolar region size. The same can be said more obviously of the third plot. In fact, we realise that the third plot is of the same profile as the second plot when we consider that the only difference is the halving of the initial cell length. This is why the third plot looks like the second although compressed in the x-direction by a factor of two. Either (1) these two distributions are tending towards the exponential but 3×10^6 time-steps is insufficient to reach that point, or (2) the distributions have reached steady states and there are two regimes frozen into the distributions : below and above the initial unipolar region sizes (dotted lines).

Figure 4.18 clarifies what happens for three different cell lengths shorter than 10^4 m. These three plots show straight lines on log-linear axes for three different initial cell lengths, 3×10^3 m, 5×10^3 and 8×10^3 m. The initial lengths (below which we should disregard the data) are shown by vertical dotted lines.

4.2.7 Effect of Varying Emergence/Submergence rate.

We saw in section 3.3.2 that the continuous model emerges flux such that the magnetic flux density increases at a mean rate of ~ 3.9 G s^{-1}. A typical run of the model uses the parameter value $\kappa = 0.1$. We recall that this means that 1 in 10 cells are involved in emergence and submergence. There are equal numbers of cells emerging flux and submerging flux, therefore 1 in 20 cells are undergoing emergence, and likewise submergence. Also, $t_{\mathrm{em/sub}} = 10^3$ s. We recall that this (the 'replacement timescale') means that the rate of change of cell material is such that it would take 10^3 s for N_{init} particles to emerge or submerge.

We are interested to see if variations of κ and $t_{\mathrm{em/sub}}$ produce effects, expected or otherwise in the distributions of unipolar region size, magnetic field density, magnetic flux and event-sizes. Table 4.1 shows the range of parameters investigated.

We will see below that we can't obtain sufficient data to produce useful distributions of flux density for runs 2, 3 and 4, and therefore can't obtain a useful idea of the effect upon B of varying the level of reconnection. We therefore performed runs 6 and 7 in order to give two further levels of reduced emergence/submergence activity.

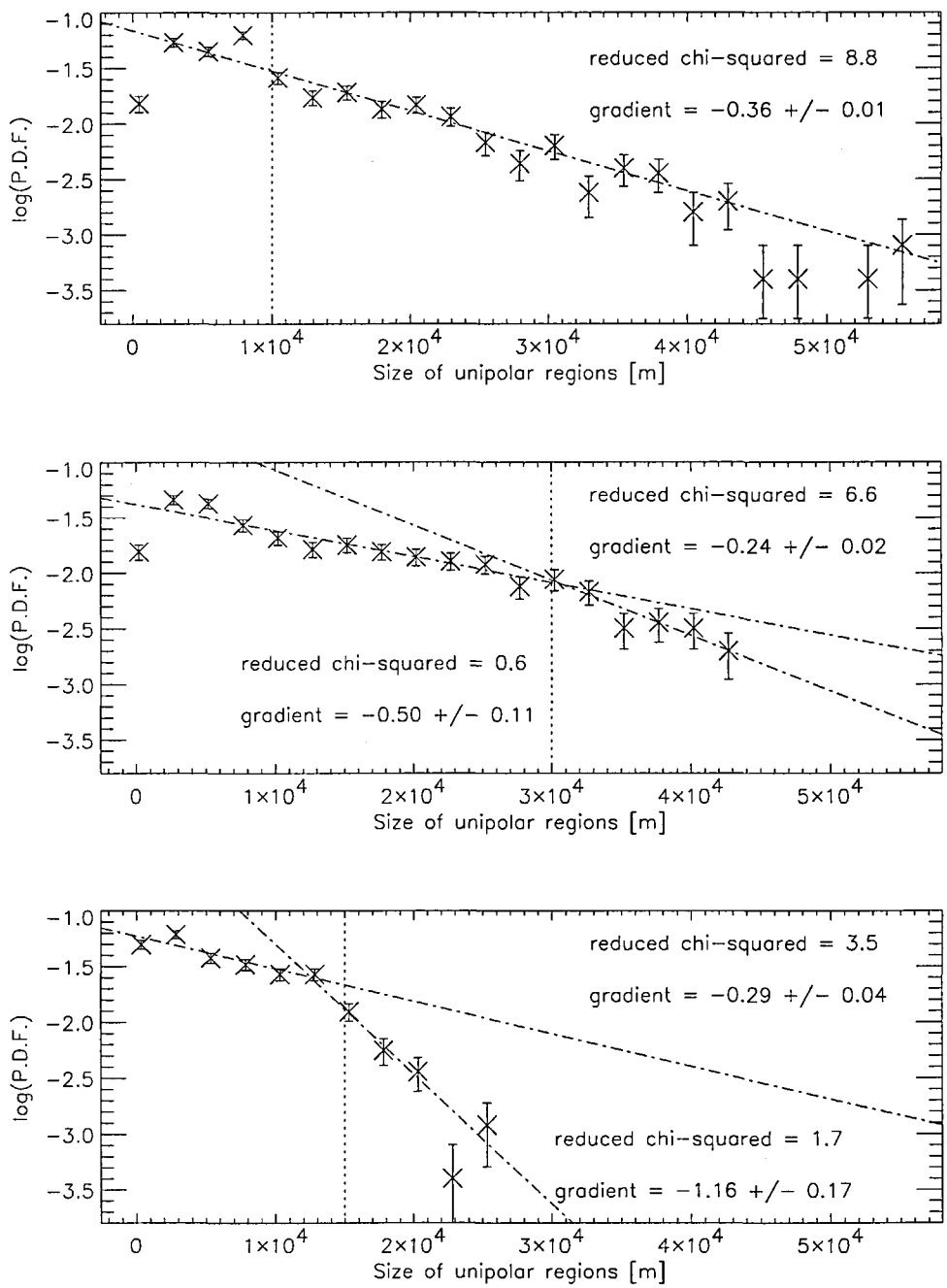

Figure 4.17: Evolved distributions of sizes of regions of unipolar magnetic flux, using log-linear axes; initially 10^3 cells; bin-size = 2.5×10^3 m. For first plot, dotted line shows initial cell length. For second and third plots, dotted lines mark initial unipolar region size. Top: run commenced with (usual) random initial flux density; initial cell length = 10^4 m. Second: run commenced with a uniform single value of size of unipolar region : $L_{\text{unipolar}} = 3 \times L_{\text{init,cell}}$; initial cell length = 10^4 m. Third: run commenced with a uniform single value of size of unipolar region : $L_{\text{unipolar}} = 3 \times L_{\text{init,cell}}$; initial cell length = 5×10^3 m.

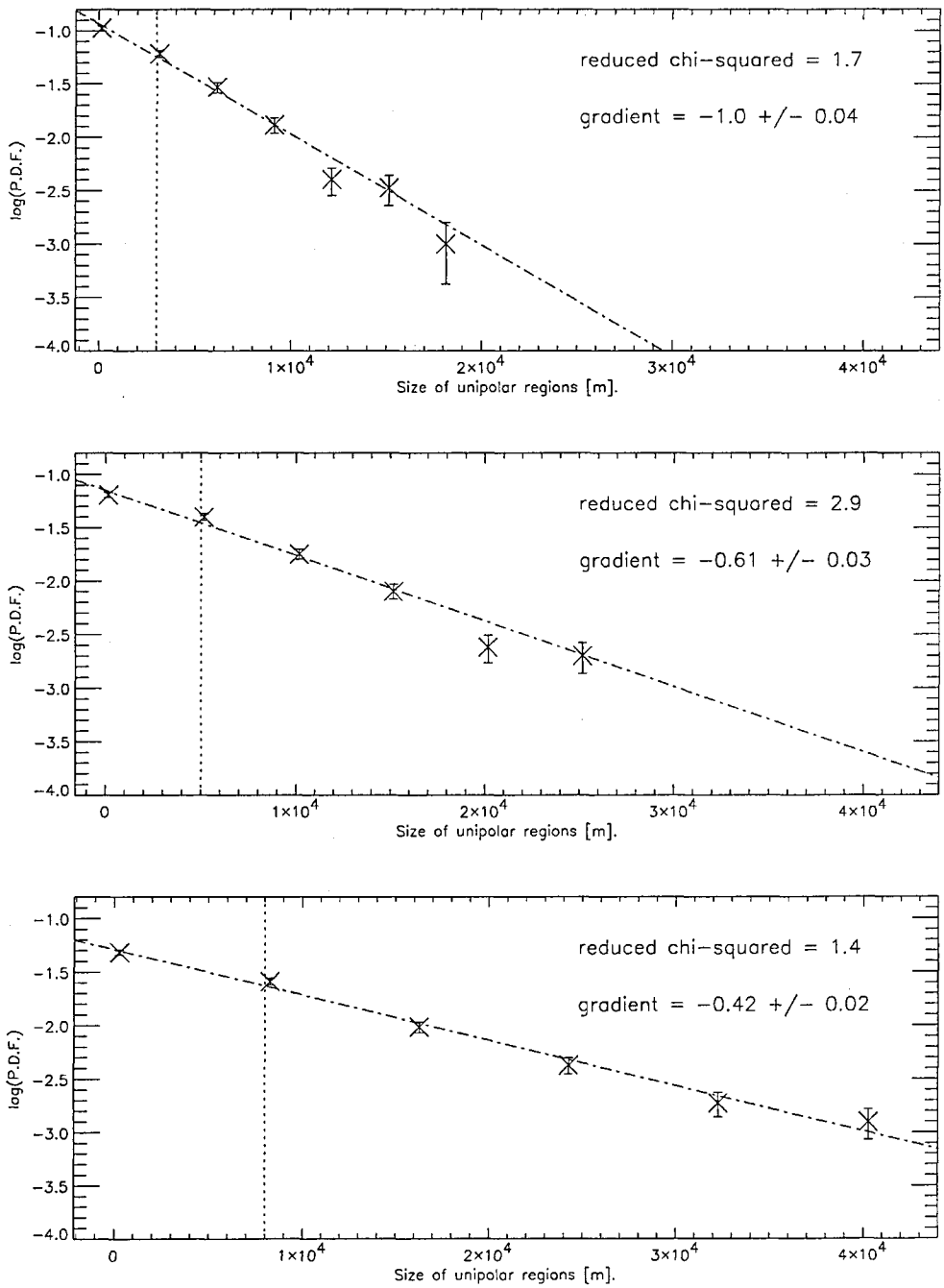

Figure 4.18: Evolved distributions of size of regions of unipolar magnetic flux, using log-linear axes; bin-size = 10^4 m; 10^3 cells. Dotted lines mark mean initial magnetic flux. Top: initial cell length = 3×10^3 m. Second: initial cell length = 5×10^3 m. Third: initial cell length = 8×10^3 m.

4.2.7.1 Distribution of Unipolar Region Sizes.

A reduction of $t_{em/sub}$ and/or an increase in κ will produce greater emergence/submergence turnover of cell material and therefore breaking up of cells to smaller sizes and greater numbers of cells. Therefore there will be fewer large unipolar regions and more smaller regions. Figure 4.19 compares distributions of unipolar region sizes of these five runs. The initial cell length is marked by vertical dotted lines.

It is clear from the second, third and fourth plots that raising the level of emergence and submergence by increasing κ and reducing $t_{em/sub}$ produces gradients steeper than -0.36 which implies enhanced proportions of smaller unipolar regions compared with the larger regions caused by the increased emergence/submergence. We see the opposite effect in the fifth plot.

4.2.7.2 Distribution of Magnetic Field Density.

We have already seen in figures 4.12 and 4.11 that for the length range we have considered (3×10^3 m to 4×10^4 m) power-law-like distributions in magnetic field density are produced for flux densities upwards from the initial mean flux density. The second to fourth plots of figure 4.20 shows us that increasing the rate of emergence and submergence by increasing κ to 0.2 or 0.4 or decreasing $t_{em/sub}$ to 500 s disturbs the form of this power-law. The increased rate submerges cells at a higher rate and thus brings together opposite polarity cells with greater frequency. These cells will suffer depleted magnetic flux and so we would expect significant numbers of cells with low magnetic flux density. This might explain the slight lowering we see of the minimum x-axis value from $\log(0.5\ \text{G}) = -0.3$ to $\log(0.28\ \text{G}) = -0.55$.

Run No.	$t_{em/sub}$ [s]	κ	effect
1.	1000	0.1	typical
2.	1000	0.2	increased emergence/submergence
3.	1000	0.4	increased emergence/submergence
4.	500	0.1	increased emergence/submergence
5.	2000	0.1	decreased emergence/submergence
6.	4000	0.1	decreased emergence/submergence
7.	8000	0.1	decreased emergence/submergence

Table 4.1: Runs performed to test variation in parameters controlling rates of emergence and submergence.

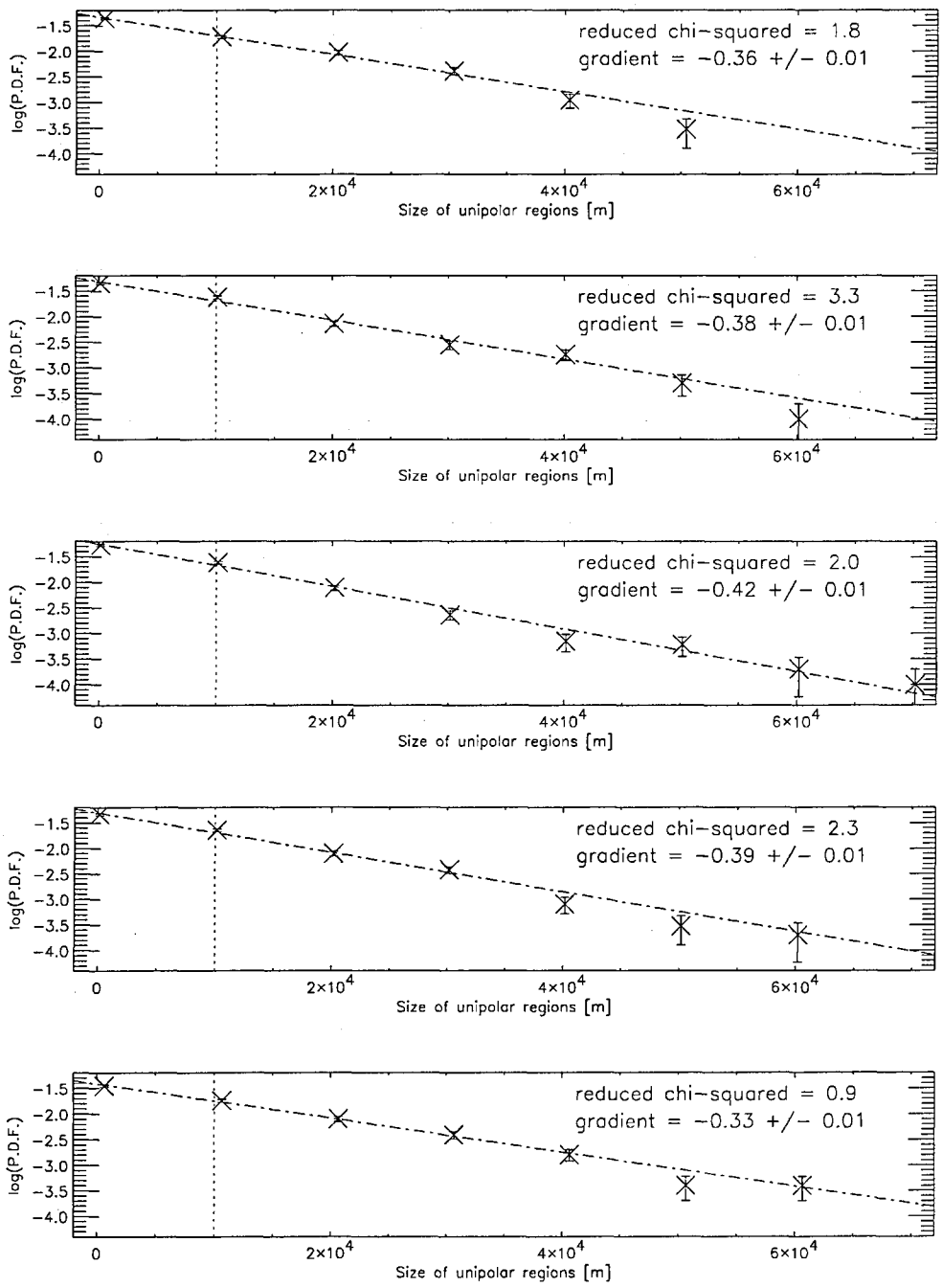

Figure 4.19: Evolved distributions of size of regions of unipolar magnetic flux, using log-linear axes; bin-size = 10^4 m. Dotted lines mark the initial unipolar region size. First: typical initial conditions. Second: $\kappa = 0.2$. Third: $\kappa = 0.4$. Fourth: $t_{\mathrm{em/sub}} = 500$ s. Fifth: $t_{\mathrm{em/sub}} = 2000$ s.

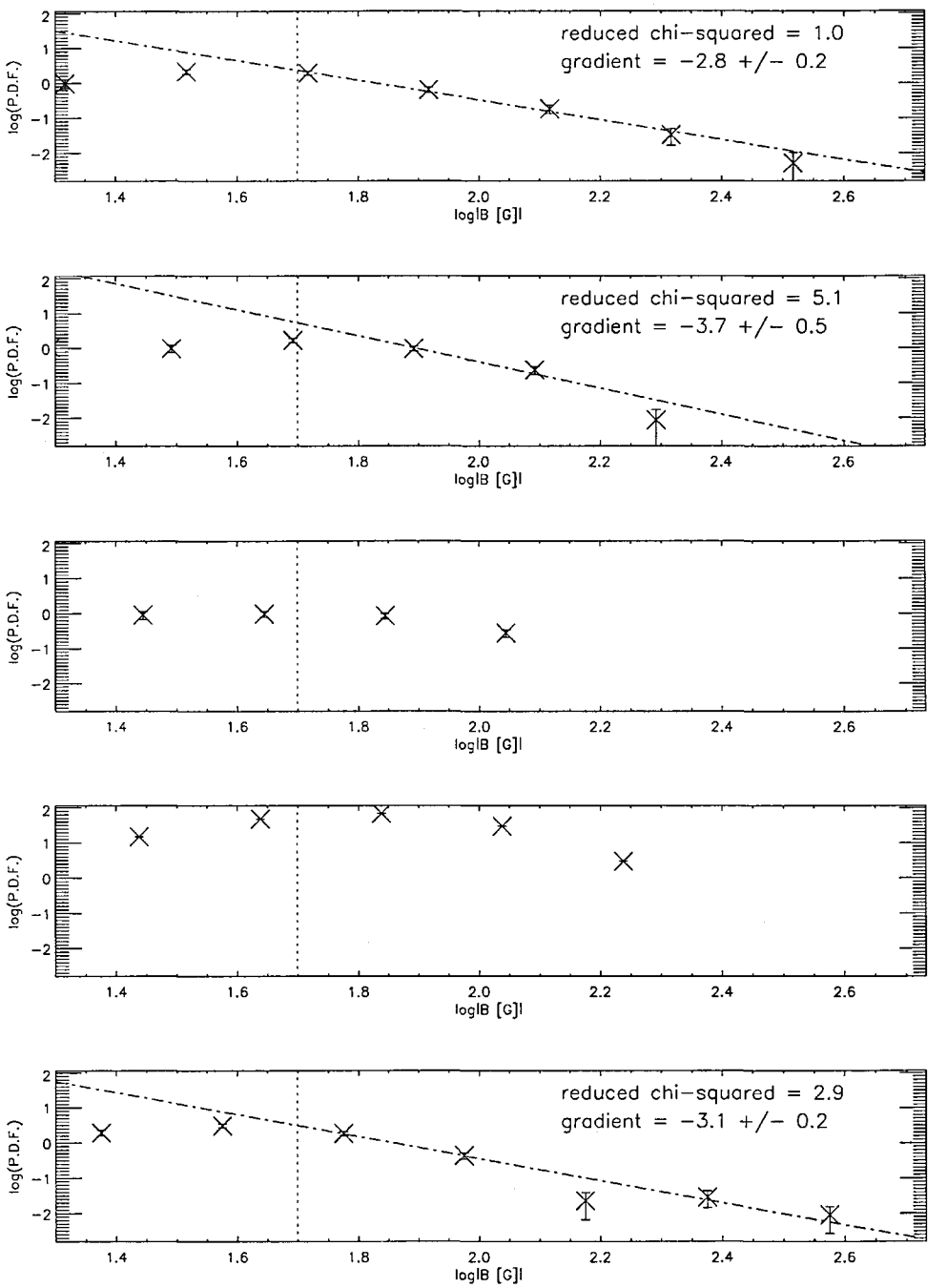

Figure 4.20: Evolved distributions of magnetic flux density, using log-log axes; bin-size = 0.2. Dotted lines mark mean initial magnetic field density. First: typical initial conditions. Second: $\kappa = 0.2$. Third: $\kappa = 0.4$. Fourth: $t_{\mathrm{em/sub}} = 500$ s. Fifth: $t_{\mathrm{em/sub}} = 2000$ s.

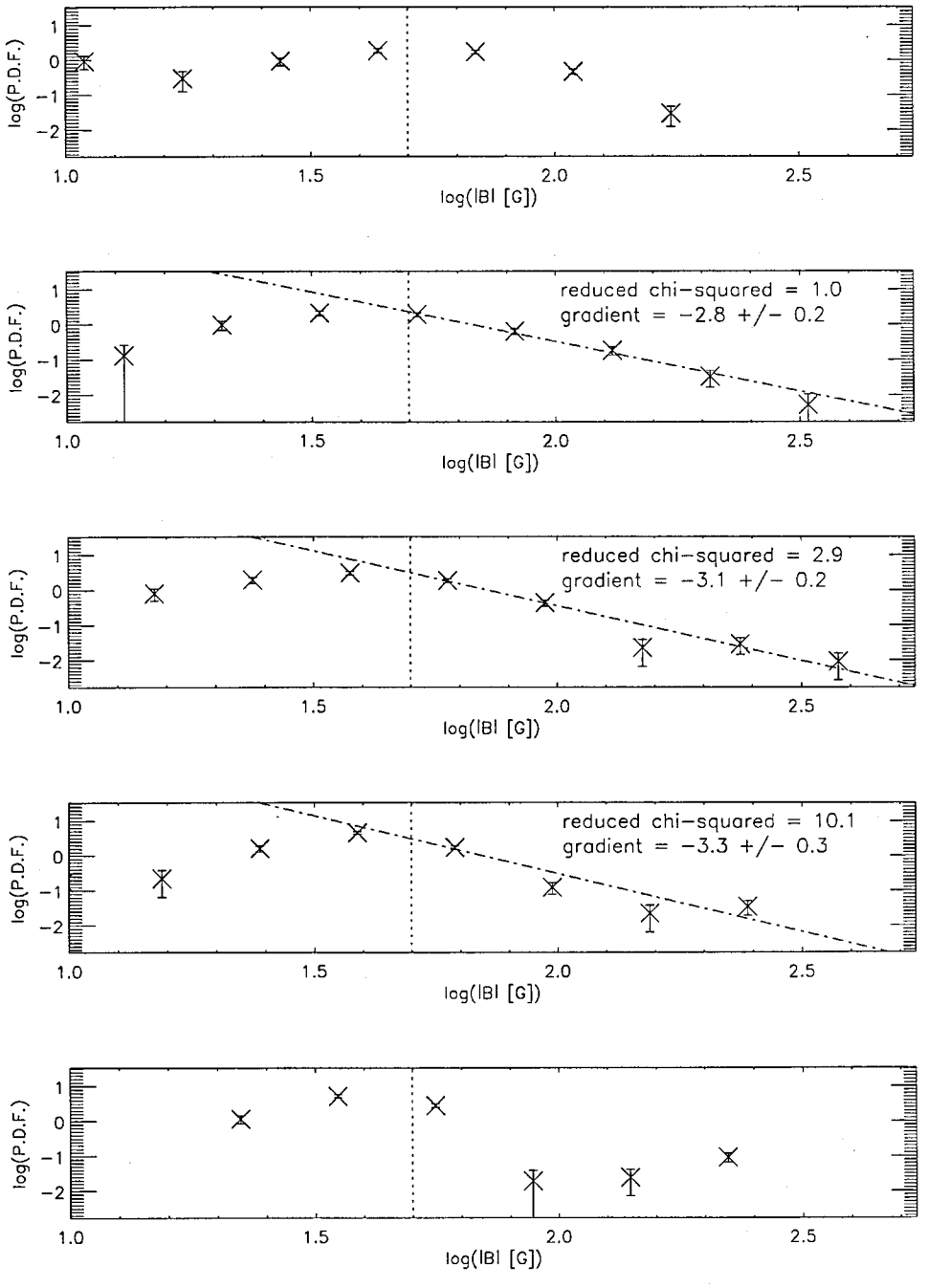

Figure 4.21: Evolved distributions of magnetic flux density, using log-log axes; bin-size = 0.2. Dotted lines mark mean initial magnetic field density. First: $t_{\mathrm{em/sub}} = 500$ s. Second: typical rate. Third: $t_{\mathrm{em/sub}} = 2000$ s. Fourth: $t_{\mathrm{em/sub}} = 4000$ s. Fifth: $t_{\mathrm{em/sub}} = 8000$ s.

Figure 4.21 shows us plots of P.D.F.s for $|B|$ for the following runs, from the upper-most plot downwards : $t_{\mathrm{em/sub}} = 500$ s, $t_{\mathrm{em/sub}} = 1000$ s, $t_{\mathrm{em/sub}} = 2000$ s, $t_{\mathrm{em/sub}} = 4000$ s, $t_{\mathrm{em/sub}} = 8000$ s.

There is insufficient data on the first plot to give a useful distribution in the region of interest, above the mean initial flux density of log(50 G)=1.70. The second plot shows the data produced by our run using typical initial conditions and is consistent with a power-law, although only five points. The fifth plot shows a complete breakdown in the data. The emergence/submergence rate is at its lowest in this run. Our third and fourth plots also show a more complicated distribution than the power-law of the second plot. We have fitted straight lines to these data however and found that the gradient increases with decreasing emergence/submergence. We will refer to this later in chapter 5.

4.2.7.3 Distribution of Magnetic Flux.

We would expect that reducing $t_{\mathrm{em/sub}}$ or increasing κ would tend to produce smaller cells with consequently less flux contained within them. In the same way, increased convection in a fluid results in disruption of convection cells from quasi-steady state into smaller length-scales and chaotic behaviour.

The typical run gives us a power-law-like distribution in the distribution of magnetic flux, more specifically in the range extending upwards from the mean initial flux value and covering 0.8 of an order of magnitude (figure 4.22). The figure shows that like the magnetic flux density distributions (figure 4.20) increasing the rate of emergence and submergence by increasing κ to 0.2 or 0.4 or decreasing $t_{\mathrm{em/sub}}$ to 500 s destroys power-law-like distribution.

The profiles of figures 4.20 (flux density) and 4.22 (flux) are almost identical. These plots were produced from the same runs. We conclude that there is very little correlation between B and L.

4.2.7.4 Distribution of Magnetic Reconnection Event-sizes.

We would expect the increased emergence/submergence to reduce cell lengths, and therefore increase the number of cells. There would thus be a greater number of boundaries between cells. The background level of total energy release would be enhanced. Conversely therefore, the fifth run of figure 4.23 (reduced replacement timescale $t_{\mathrm{em/sub}} = 2000$ s) should therefore have a reduced background level. This reduced background level will be reflected in the lowest value of the peak energy release rate. The background rate of energy release effectively draws a lower limit across our plots on figure 4.23 and prevents events from occurring below the background level. See figure 3.30 for clarification of this point. We see this occurring in the x-range of the fifth plot of figure 4.23 insofar as the x-range reaches down to 1.5 orders of magnitude below the other plots. This run has

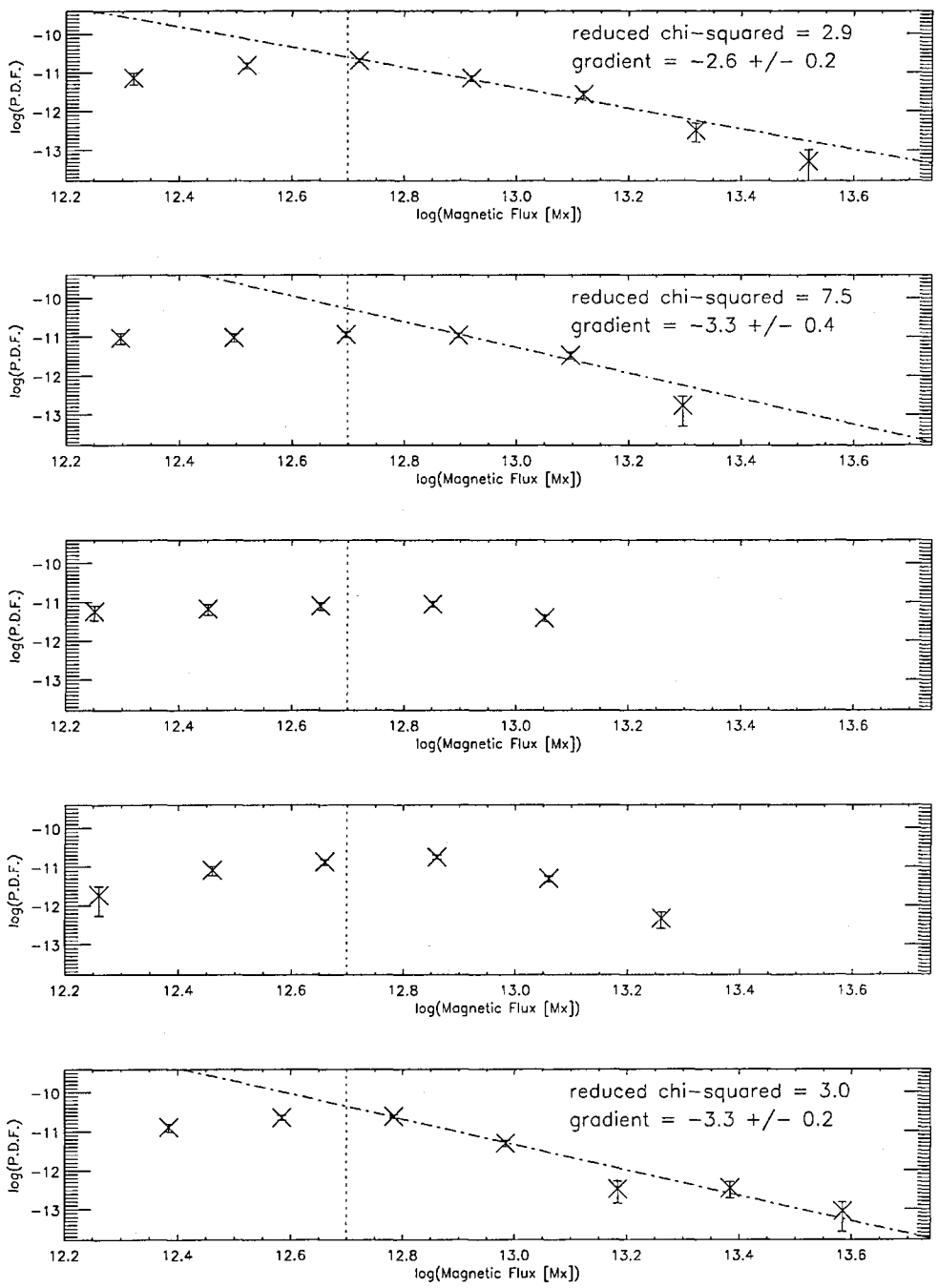

Figure 4.22: Evolved distributions of magnetic flux, using log-log axes; bin-size = 0.2. Dotted lines mark mean initial magnetic field density. First: typical initial conditions. Second: $\kappa = 0.2$. Third: $\kappa = 0.4$. Fourth: $t_{\mathrm{em/sub}} = 500$ s. Fifth: $t_{\mathrm{em/sub}} = 2000$ s.

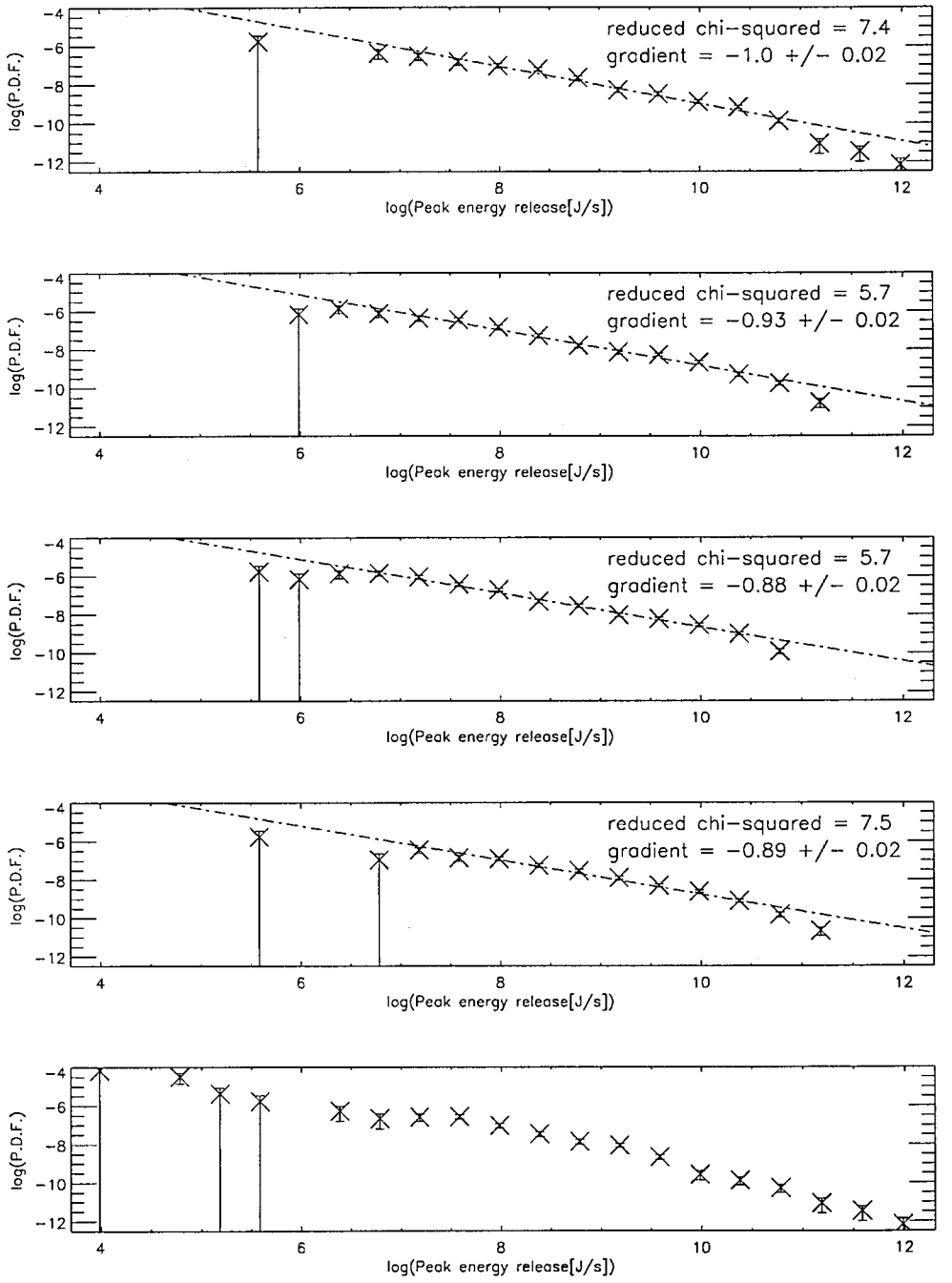

Figure 4.23: Evolved distributions of sizes of events, counted by peak energy release rate. Log-log axes; bin-size = 0.4. First: typical initial conditions. Second: $\kappa = 0.2$. Third: $\kappa = 0.4$. Fourth: $t_{\mathrm{em/sub}} = 500$ s. Fifth: $t_{\mathrm{em/sub}} = 2000$ s.

an increased replacement timescale ($t_{\text{em/sub}} = 2000$ s) therefore the rate of flow of cell material into and out of the emerging and submerging cells is reduced by half compared with the typical run. We expect a lower background level for the fifth run ($t_{\text{em/sub}} = 2000$ s) and a correspondingly lower lower-limit, which we in fact see here.

It is unclear whether the energy release rate in the individual reconnection events would be enhanced or not. If not, then the counts of integrated energy release would be reduced (given that the background level of energy release rate integrated over the duration of an event is subtracted from the total integrated energy release during an event to give the integrated energy release, which is then binned etc. See figure 3.30). Also it is unclear whether the peak rate of energy release of individual reconnection events would be enhanced.

Figures 4.23 and 4.24 demonstrate no changes to the positions nor profiles of the (peak energy release rate and integrated energy release) event-size distributions caused by changing the emergence/submergence rates. Neither plots two, three or four show the expected enhanced background level.

We discuss in section 4.2.9 an analytical approach to deriving mean and maximum event-sizes.

4.2.8 Flux-Collision Model.

The figures in section 4.2.8 show comparisons between results generated by a run commencing with the typical initial parameter values (as per the Definition of Commonly Used Terms given at the beginning of the thesis) and results generated by the model as described in section 3.3.2.1, where a regular pattern of submergence and emergence is imposed upon the model. Our purpose is to ascertain whether this 'flux-collision' approach, a variant of the continuous model, gives different results from the typical run.

Within each figure the upper plot shows data for the typical run and the lower shows that for the flux-collision scheme.

The dotted vertical line on figure 4.25 marks the initial cell length. Use of the flux-collision scheme doesn't produce a power-law profile. The flux emergence in this flux-collision scheme is different only in the location of the emergence, not in the level or distribution.

Regarding figure 4.27, the flux collision scheme appears to complicate the exponential profile in the region to the right of the initial flux. However the gradients of the fit lines of the upper and lower plots of figure 4.27 are very similar. This has little statistical significance however, given how few points there are in these plots. We note that the plots of figures 4.26 and 4.27 corresponding to the same runs are almost identical. Given that $\phi_i \propto B_i \, L_i$, we know that B and L are not well

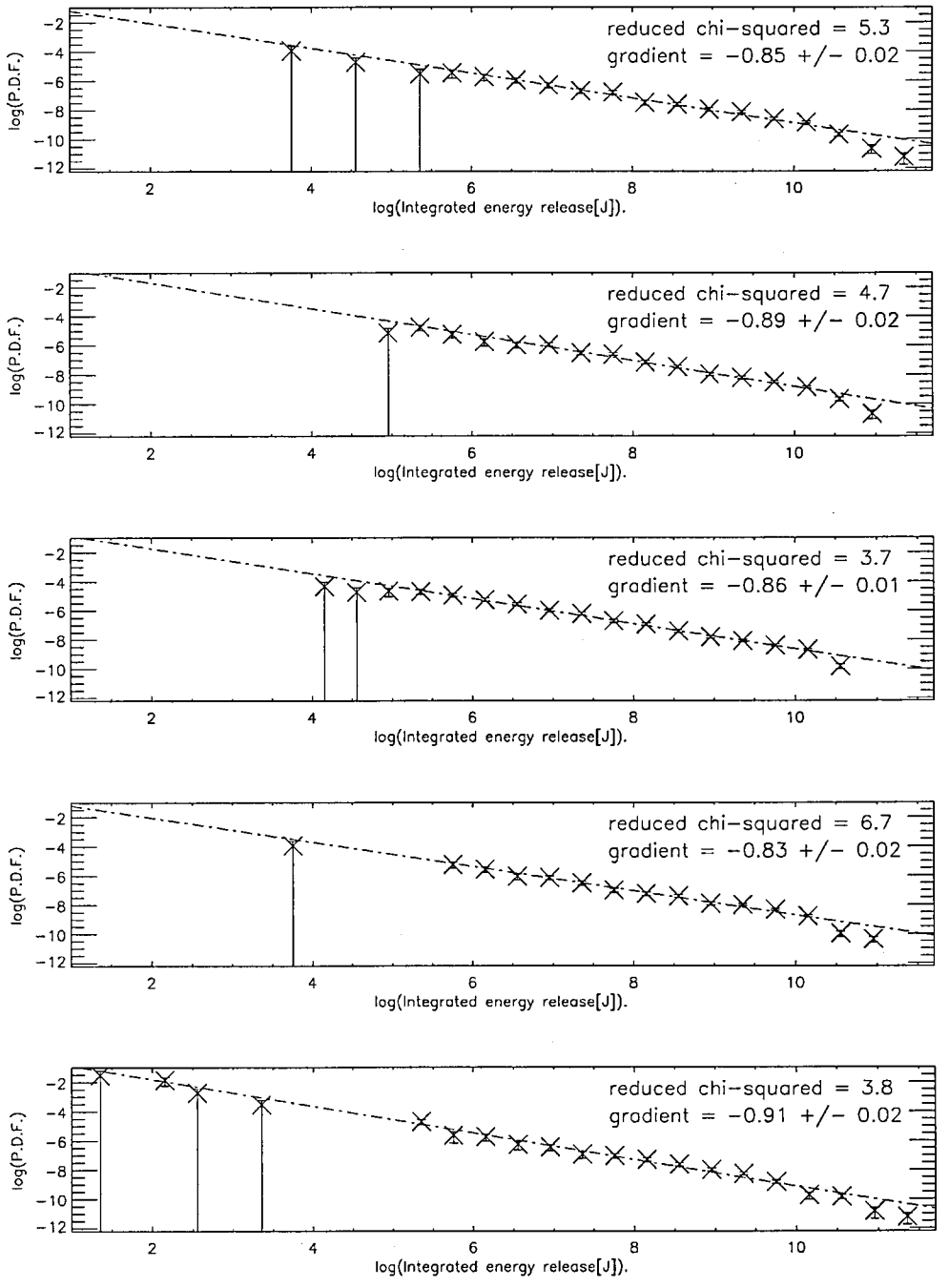

Figure 4.24: Evolved distributions of sizes of events, counted by integrated energy release. Log-log axes; bin-size = 0.4. First: typical initial conditions. Second: $\kappa = 0.2$. Third: $\kappa = 0.4$. Fourth: $t_{\mathrm{em/sub}} = 500$ s. Fifth: $t_{\mathrm{em/sub}} = 2000$ s.

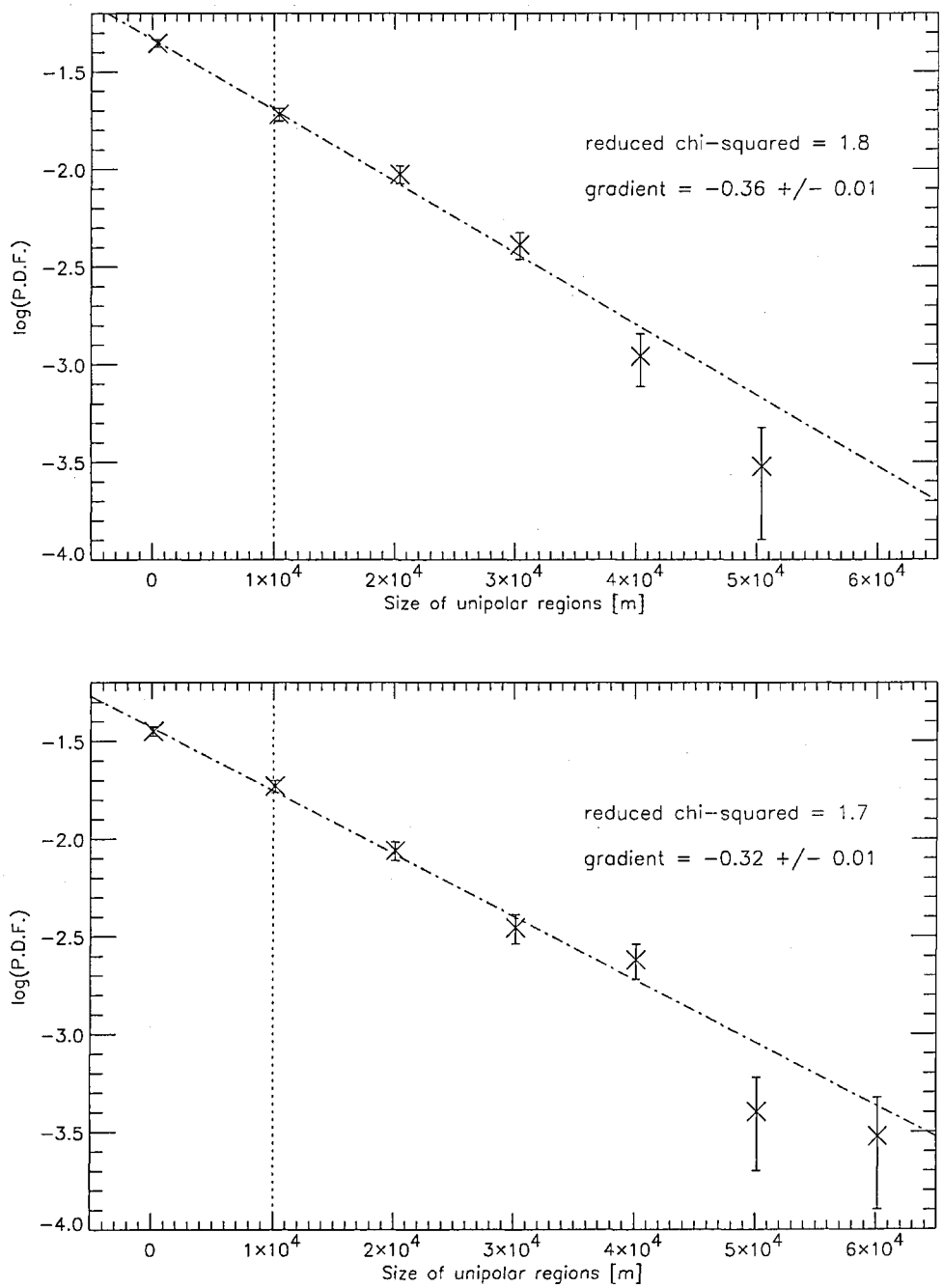

Figure 4.25: Evolved distributions of size of regions of unipolar magnetic flux, using log-log axes; bin-size = 0.1. Dotted lines mark initial unipolar region size. Top: run using typical initial conditions. Bottom: run using flux-collision initial conditions.

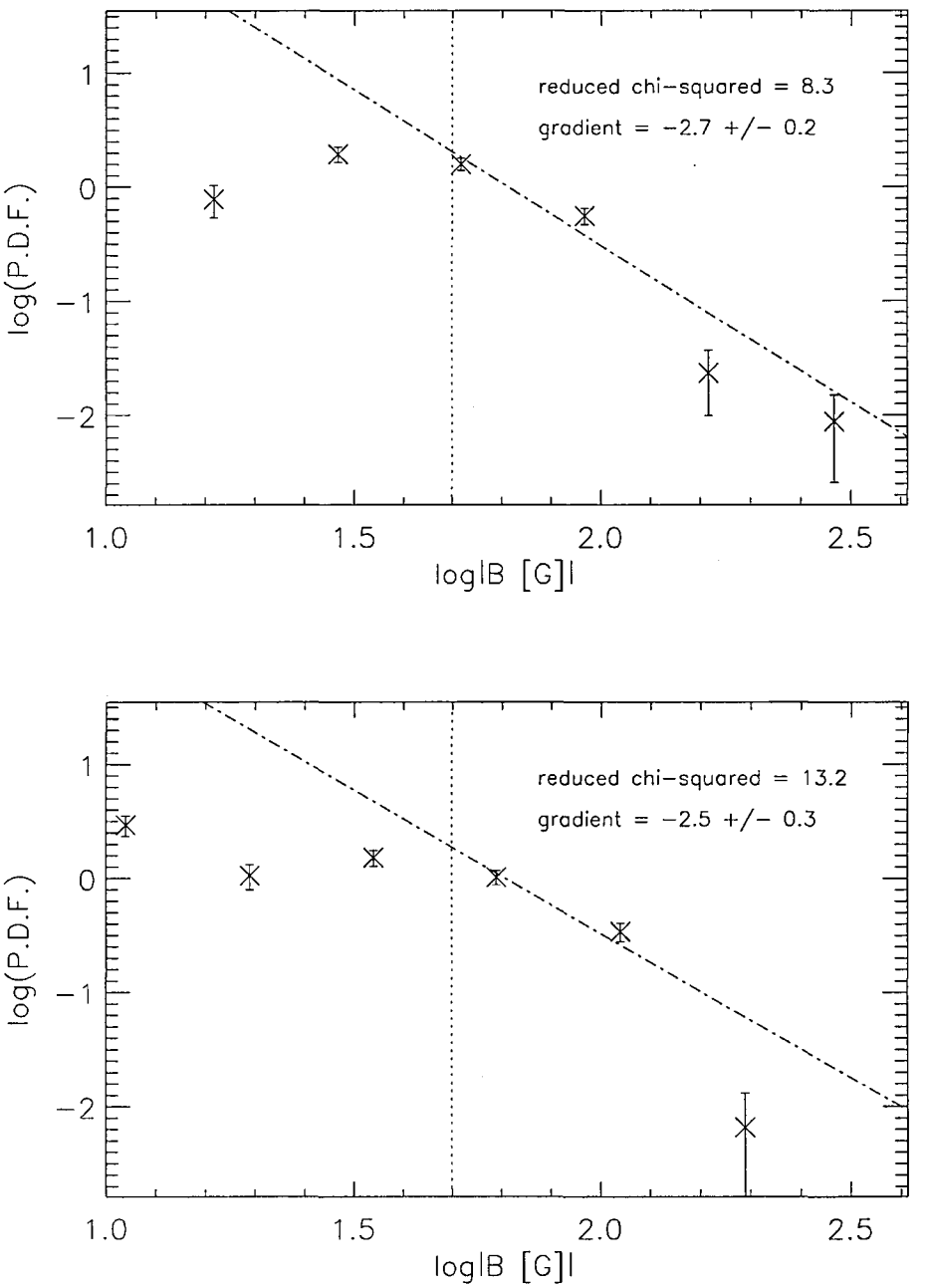

Figure 4.26: Evolved distributions of magnetic flux density, using log-log axes; bin-size = 0.25. Dotted lines mark mean initial magnetic field density. Top: run using typical initial conditions. Bottom: run using flux-collision initial conditions.

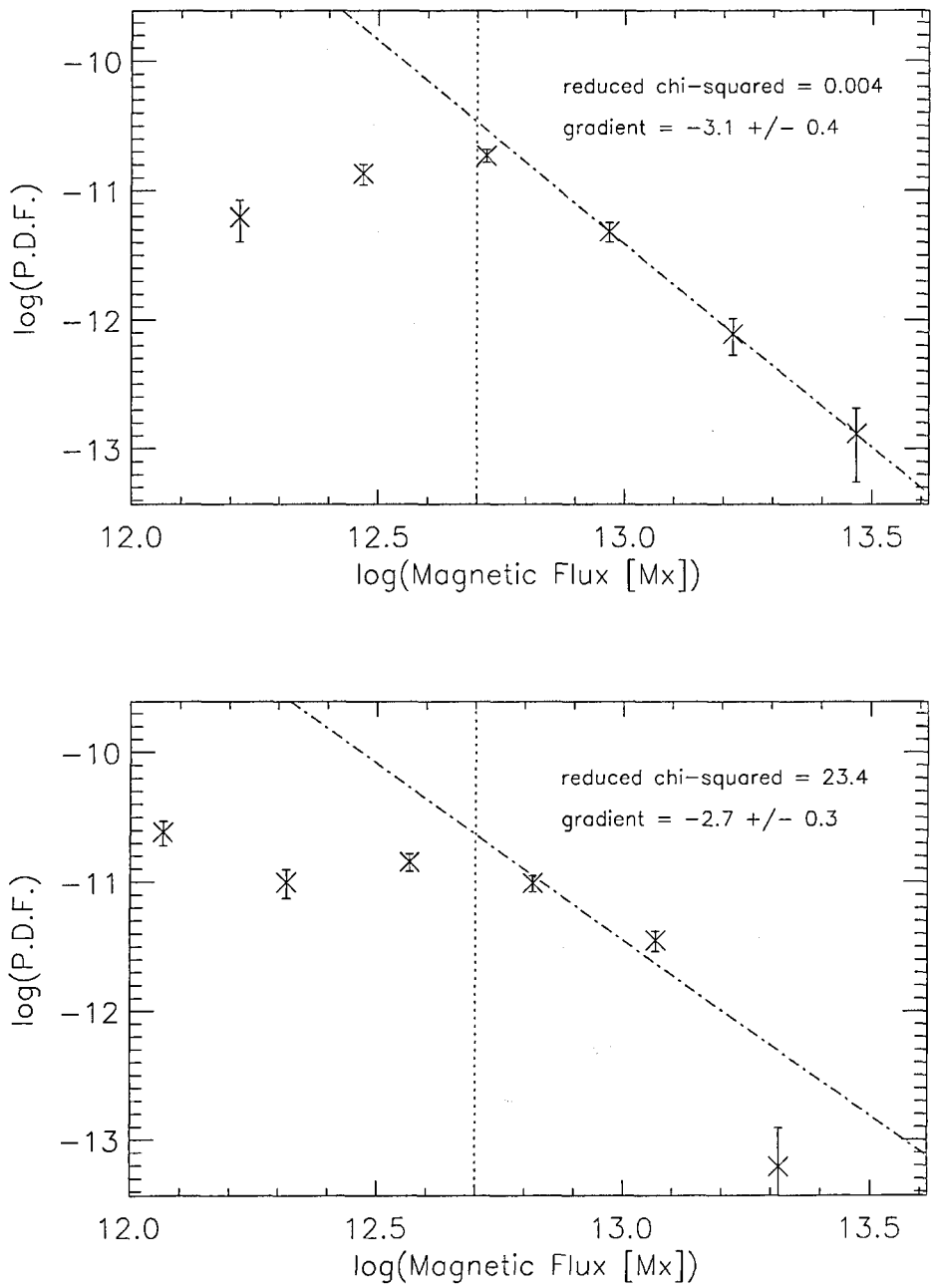

Figure 4.27: Evolved distributions of magnetic flux, using log-log axes; bin-size = 0.25. Dotted lines mark mean initial magnetic flux. Top: run using typical initial conditions. Bottom: run using flux-collision initial conditions.

correlated.

We have fitted a line to the second plot of figure 4.28, taking into account every data point. We have also fitted a line to the first plot, however, we discarded the last three points on this plot. Given that the second plot looks like the first plot up to 10.5 on the x-axis, we fitted to these points in order to only consider the data which lie in the x-range common to both plots. We have applied the same approach to figure 4.29 and discounted the last three data points of the upper plot in performing the line fitting.

On figures 4.28 and 4.29 we can see that the flux collision scheme leaves the positions and gradients of the peak energy release rate and integrated energy release profiles unchanged apart from introducing small dips in the bin counts in the middle of the respective x-ranges and reducing the dynamic ranges by eliminating some of the larger events. The changes in these event-size distributions are small.

Thus, we find only small changes caused by the flux-collision scheme, probably due to the way in which it forces the emergence/submergence pattern into artificial regular alternating bands of colliding and spreading magnetic flux.

4.2.9 Distributions of Event-sizes.

As explained by Crosby et al. (1998), the largest Solar flaring events are approximately 10^{25} J and the magnitude of flares recorded extends down to the limits of the instruments, and certainly down to 10^{17} J. Also, they show the HXRB/SMM and ICE data which gives the distribution of this parameter as a power-law with an index of -1.53±0.02 and -1.67±0.02, respectively. The run from which we have generated figure 4.1 produced events ranging in size from 3.8×10^5 to 1.9×10^{12} J s^{-1} regarding peak energy release rate, and from 5.7×10^4 to 3.1×10^{12} J regarding integrated energy release. Thus the model produces events ranging over eight orders of magnitude. However, our model has a finite number of cells (initially 10^3 cells) and a uniform initial cell length of 10^4 metres. As discussed in section 3.2.2, there will be no cells in the model with length less than 100 metres, and no cells with length greater than $1.5 \times L_{\text{init}}$ thus we expect these to limit the maximum and minimum events occuring within the model.

Figures 4.30 and 4.31 show profiles of the peak energy release (figure 4.30) rate and integrated energy release (figure 4.31) for a run (typical initial parameters) with initial cell length of 10^4 m (top plot) and 5×10^3 m (bottom plot). Distributions for 10^4 m and for 5×10^3 m are almost identical in both cases. These distributions are not strictly power-law though have a power-law-like profile. Both show regions of approximate power-law form lying between edge effects. The region between

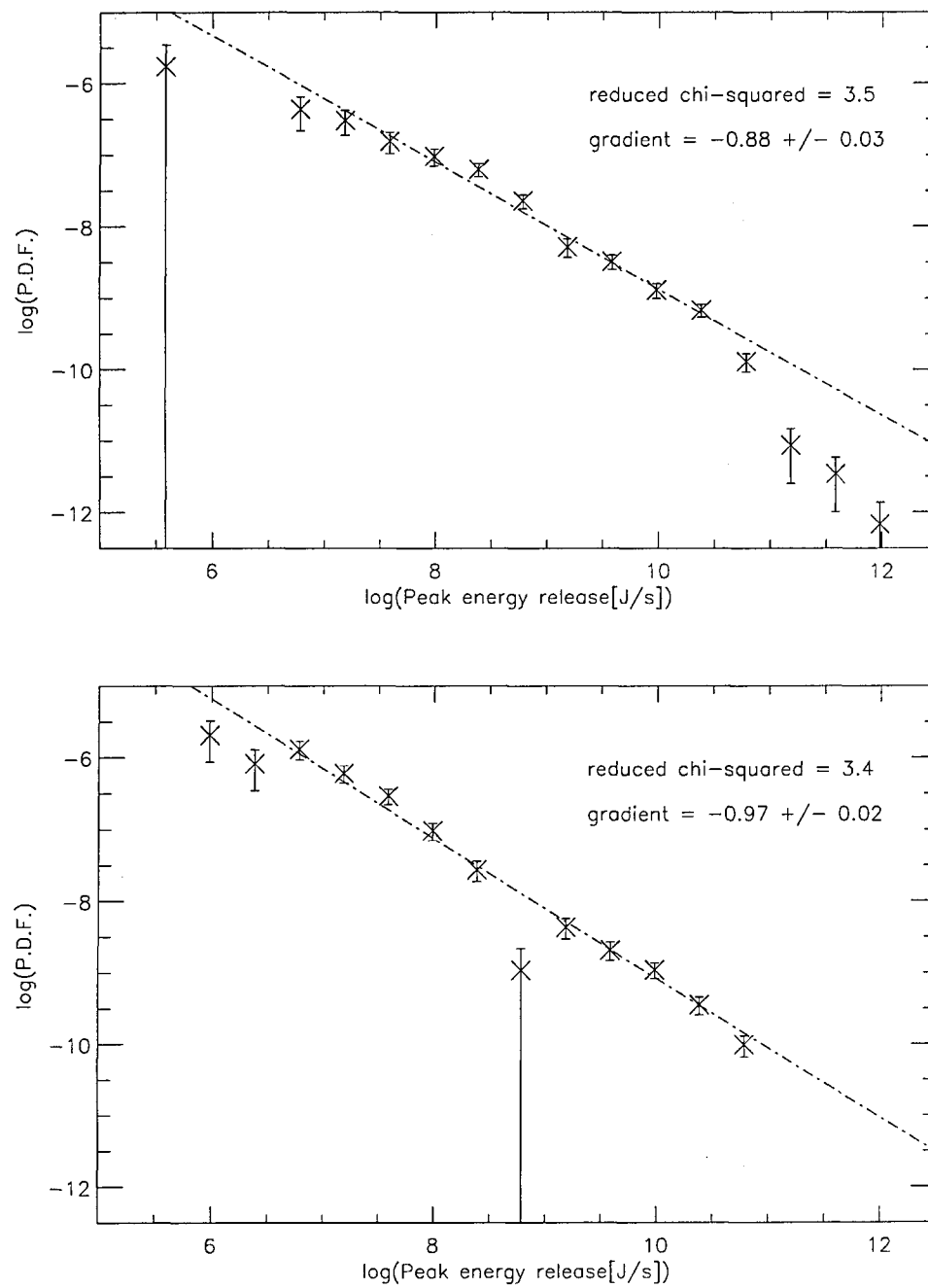

Figure 4.28: Evolved distributions of sizes of events, counted by peak energy release rate. Log-log axes; bin-size = 0.4. Top: run using typical initial conditions. Bottom: run using flux-collision initial conditions.

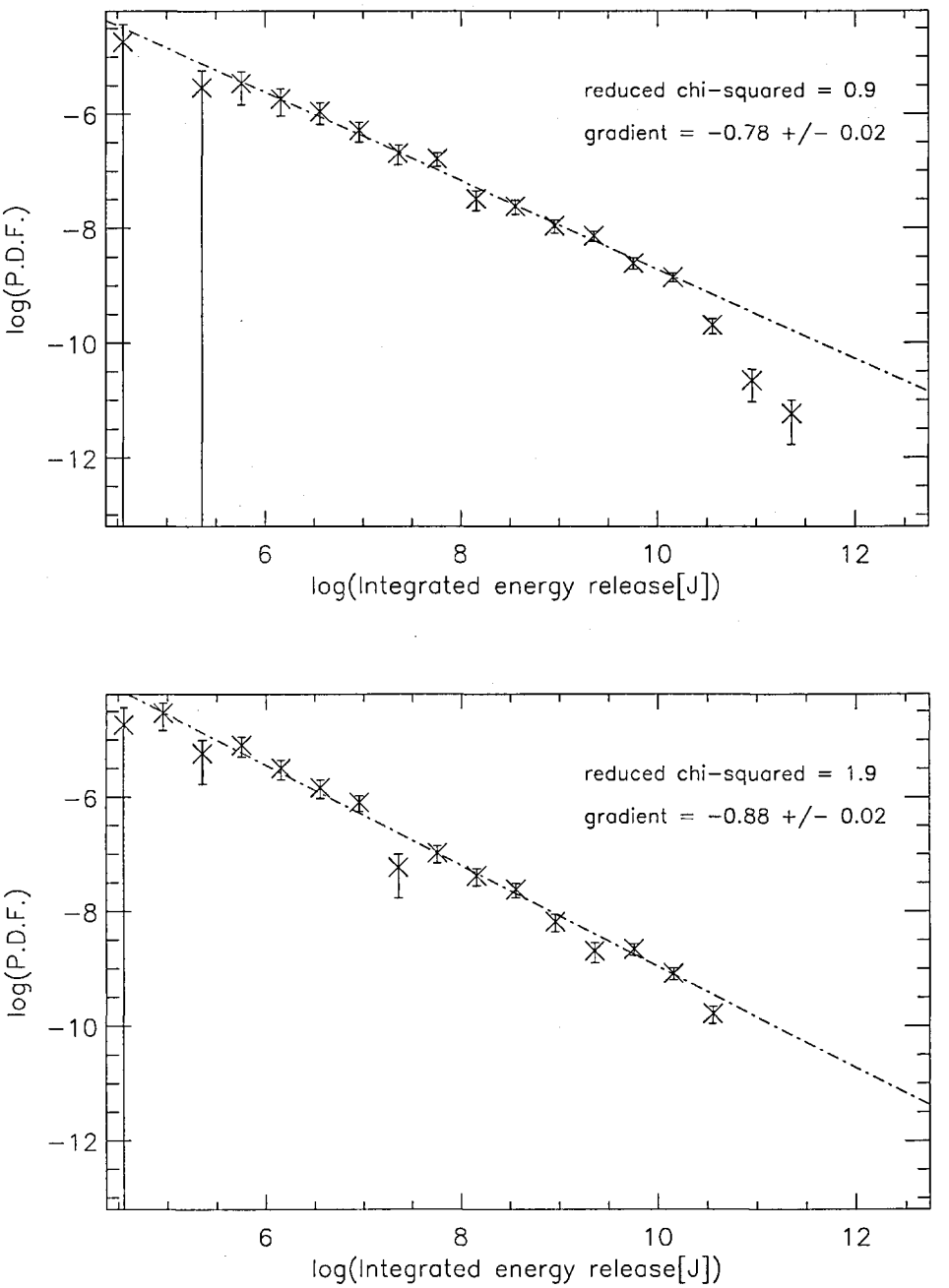

Figure 4.29: Evolved distributions of sizes of events, counted by integrated energy release. Log-log axes; bin-size = 0.4. Top: run using typical initial conditions. Bottom: run using flux-collision initial conditions.

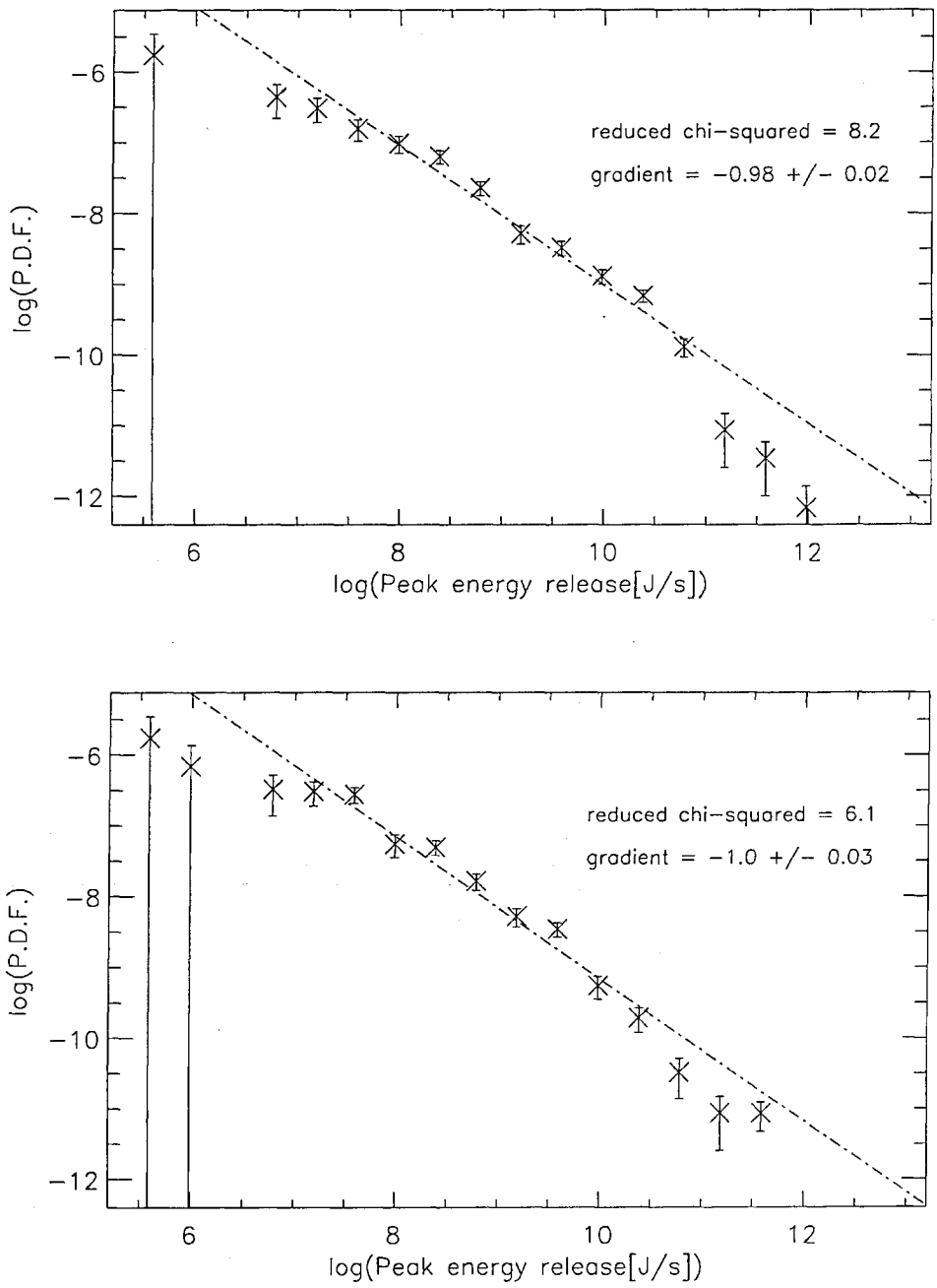

Figure 4.30: Evolved distributions of sizes of events, counted by peak energy release rate. Log-log axes; 10^3 cells; bin-size = 0.4. Top: initial cell length = 10^4 m, second: initial cell length = 5×10^3 m.

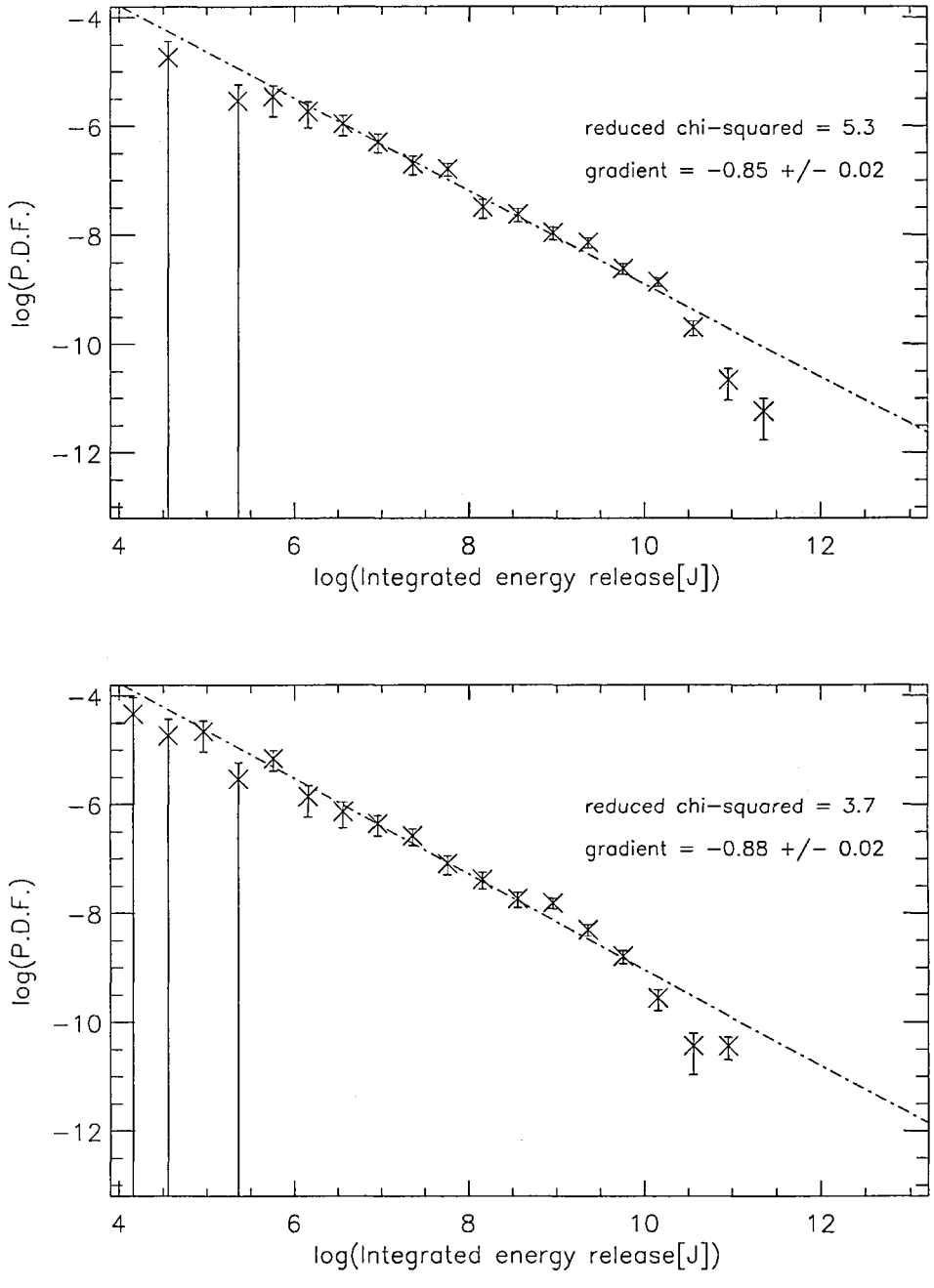

Figure 4.31: Evolved distributions of sizes of events, counted by integrated energy release. Log-log axes; 10^3 cells; bin-size = 0.4. Top: initial cell length = 10^4 m, second: initial cell length = 5×10^3 m.

edge effects on figure 4.30 shows a range of 10^7 J s^{-1} to 10^{11} J s^{-1} : four orders of magnitude. Similarly, figure 4.31 shows a range of 10^7 J to 10^{11} J. Again, the model has produced data ranging over four orders of magnitude. As we have already elaborated, satellite data in terms of integrated flux presently covers at least eight orders of magnitude, ranging from 10^{24} J to 10^{32} J.

In chapter 5 we will consider some simple analytical approaches to the event-sizes our model-generates.

4.3 Power-Laws Obtained from the Model.

4.3.1 Power-Laws Produced.

Table 4.2 lists the runs and parameters where we have found power-law and power-law-like distributions produced by the model. The table notes the power-law index and the relevant figure. We have included the various power-law and power-law-like distributions generated by the different runs explored in chapter 3.

We saw in section 4.2 a few examples of power-laws generated by the model, although we find exponential distributions for the size of unipolar regions.

Of note was the production of power-laws in the magnetic field density and magnetic flux distributions. In particular, the distributions of event-size counted by integrated energy are close to power-law in profile.

Figure 4.10 shows that the new part of the magnetic field density distribution above the initial magnetic field density is in a power-law form. The upper plot shows data for 10^3 cells whereas the lower plot shows data for 5×10^3 cells. Other parameters were as per the typical initial parameter values detailed in the Definition of Commonly Used Terms given at the beginning of the thesis.

Figure 4.11 shows us similar plots to figure 4.10 although with 10^3 cells and three different cell lengths : running from the top plot to the bottom plots, 3×10^3, 5×10^3 and 8×10^3 m. Again we see approximately a power-law distribution in the new part of the x-range, generated by the model. The distribution is most clearly manifest as a power-law in the third, 8×10^3 m, plot.

Considering figures 4.20 and 4.22 in section 4.2.7, it appears that increasing the emergence/submergence rate destroys power-law distributions in B and ϕ. Power-laws are evident in the magnetic field density and magnetic flux distributions generated by the run using typical conditions, as shown in the first plots on figures 4.20 and 4.22.

We should ask whether these power-law-like distributions in B, ϕ and event-size are transient distributions reached before the distributions have reached any quasi-steady state, in which case we

Details of run	Figure No.	Cell parameter	Power-law index	Error Estimate on Index	Reduced X^2
typical	4.10	B	-3.9	0.1	3.7
5×10^3 cells	4.10	B	-2.8	0.1	4.3
$L_{\text{init}} = 3 \times 10^3$ m	4.11	B	-2.4	0.2	4.3
$L_{\text{init}} = 5 \times 10^3$ m	4.11	B	-3.1	0.2	2.5
$L_{\text{init}} = 8 \times 10^3$ m	4.11	B	-3.2	0.2	0.4
$L_{\text{init}} = 2 \times 10^4$ m	4.12	B	-2.9	0.2	8.5
$L_{\text{init}} = 4 \times 10^4$ m	4.12	B	-3.6	0.3	0.8
typical	4.13	ϕ	-2.7	0.2	1.0
$N_{\text{cells}} = 5 \times 10^3$	4.13	ϕ	-3.1	0.1	2.4
$L_{\text{init}} = 3 \times 10^3$ m	4.15	ϕ	-2.7	0.2	0.4
$L_{\text{init}} = 5 \times 10^3$ m	4.15	ϕ	-3.3	0.2	1.5
$L_{\text{init}} = 8 \times 10^3$ m	4.15	ϕ	-3.0	0.2	4.4
κ=0.2	4.20	B	-3.7	0.5	5.1
$t_{\text{em/sub}}$=2000 s	4.20	B	-3.1	0.2	2.9
κ=0.2	4.22	ϕ	-3.3	0.4	7.5
$t_{\text{em/sub}}$=2000 s	4.22	ϕ	-3.3	0.2	3.0
typical	4.23	$\dot{E}_{\text{peak}}$	-1.0	0.02	7.4
κ=0.2	4.23	$\dot{E}_{\text{peak}}$	-0.93	0.02	5.7

Table 4.2: Power-law distributions generated by the continuous model.

Details of run	Figure No.	Cell parameter	Power-law index	Error Estimate on Index	Reduced X^2
κ=0.4	4.23	$\dot{E}_{\rm peak}$	-0.88	0.02	5.7
$t_{\rm em/sub}$=500 s	4.23	$\dot{E}_{\rm peak}$	-0.89	0.02	7.5
κ=0.4	4.23	$\dot{E}_{\rm peak}$	-0.88	0.02	5.7
$t_{\rm em/sub}$=500 s	4.23	$\dot{E}_{\rm peak}$	-0.89	0.02	7.5
typical	4.24	$E_{\rm int}$	-0.85	0.02	5.3
κ=0.2	4.24	$E_{\rm int}$	-0.89	0.02	4.7
κ=0.4	4.24	$E_{\rm int}$	-0.86	0.01	3.7
$t_{\rm em/sub}$=500 s	4.24	$E_{\rm int}$	-0.83	0.02	6.7
$t_{\rm em/sub}$=2000 s	4.24	$E_{\rm int}$	-0.91	0.02	3.8
flux-collision	4.28	$\dot{E}_{\rm peak}$	-0.97	0.02	3.4
flux-collision	4.29	$E_{\rm int}$	-0.88	0.02	1.9
$L_{\rm init} = 5 \times 10^3$ m	4.30	$\dot{E}_{\rm peak}$	-1.0	0.03	6.1
$L_{\rm init} = 5 \times 10^3$ m	4.31	$E_{\rm int}$	-0.88	0.02	3.7
$L_{\rm init} = 5 \times 10^3$ m	4.37	B	-3.0	0.2	1.6
$L_{\rm init} = 5 \times 10^3$ m and $t_{\rm em/sub} = 10^4$ s	4.38	B	-2.6	0.1	37.5
$t_{\rm em/sub} = 10^4$ s	4.39	ϕ	-2.9	0.2	1.6
$t_{\rm em/sub} = 10^4$ s	4.40	ϕ	-2.5	0.1	6.1
$L_{\rm init} = 5 \times 10^3$ m and $t_{\rm em/sub} = 10^4$ s	4.41	$\dot{E}_{\rm peak}$	-0.90	0.06	4.4

Table 4.3: Power-law distributions generated by the continuous model (continuation 1).

Details of run	Figure No.	Cell parameter	Power-law index	Error Estimate on Index	Reduced X^2
$L_{\rm init} = 5 \times 10^3$ m and $t_{\rm em/sub} = 10^4$ s	4.42	$\dot{E}_{\rm peak}$	-0.97	0.03	4.2
$L_{\rm init} = 5 \times 10^3$ m and $t_{\rm em/sub} = 10^4$ s	4.44	$E_{\rm int}$	-0.89	0.03	1.1
$t_{\rm em/sub} = 10^4$ s	4.43	$E_{\rm int}$	-0.90	0.03	1.6
$\frac{\psi}{P}$=0.001	3.17	B	-3.3	0.3	0.3
$\frac{\psi}{P}$=0.005	3.17	B	-3.3	0.2	2.0
$\frac{\psi}{P}$=0.01	3.17	B	-2.9	0.2	3.6
$\frac{\psi}{P}$=0.001	3.18	ϕ	-3.2	0.2	2.8
$\frac{\psi}{P}$=0.005	3.18	ϕ	-3.2	0.2	2.1
$\frac{\psi}{P}$=0.01	3.18	ϕ	-2.5	0.2	4.6
$\frac{\psi}{P}$=0.001	3.20	$\dot{E}_{\rm peak}$	-0.93	0.02	14.8
$\frac{\psi}{P}$=0.005	3.20	$\dot{E}_{\rm peak}$	-1.1	0.04	2.9
$\frac{\psi}{P}$=0.01	3.20	$\dot{E}_{\rm peak}$	-1.0	0.03	6.3
$\frac{\psi}{P}$=0.001	3.21	$E_{\rm int}$	-0.99	0.01	23.4
$\frac{\psi}{P}$=0.005	3.21	$E_{\rm int}$	-0.85	0.04	3.0
$\frac{\psi}{P}$=0.01	3.21	$E_{\rm int}$	-0.91	0.03	4.3
$L_{\rm min}$=200 m	3.22	$\dot{E}_{\rm peak}$	-1.0	0.03	8.1
$L_{\rm min}$=500 m	3.22	$\dot{E}_{\rm peak}$	-0.97	0.03	7.7
$L_{\rm min}$=200 m	3.23	$E_{\rm int}$	-0.90	0.02	5.5
$L_{\rm min}$=500 m	3.23	$E_{\rm int}$	-0.87	0.02	5.2

Table 4.4: Power-law distributions generated by the continuous model (continuation 2).

Details of run	Figure No.	Cell parameter	Power-law index	Error Estimate on Index	Reduced X^2
$L_{max} = 1.2 \times L_{init}$	3.24	$\dot{E}_{peak}$	-1.0	0.03	8.3
$L_{max} = 2.0 \times L_{init}$	3.24	$\dot{E}_{peak}$	-1.1	0.03	8.2
$L_{max} = 1.2 \times L_{init}$	3.25	E_{int}	-0.86	0.02	4.0
$L_{max} = 2.0 \times L_{init}$	3.25	E_{int}	-0.91	0.02	5.8
half-heating	3.26	$\dot{E}_{peak}$	-0.96	0.03	6.1
full-heating	3.26	$\dot{E}_{peak}$	-0.99	0.03	9.6
random heating	3.26	$\dot{E}_{peak}$	-0.91	0.02	3.9
half-heating	3.27	E_{int}	-0.86	0.03	5.4
full-heating	3.27	E_{int}	-0.90	0.02	7.5
random heating	3.27	E_{int}	-0.84	0.02	3.0
energy release rate multiplied by realisation of a random variable, η $(0.9 < \eta < 1.1)$	5.12	B	-2.8	0.2	1.8
energy release rate multiplied by realisation of a random variable, η $(0 < \eta < 1)$	5.12	B	-2.9	0.2	1.3
threshold in B of 20 G	5.12	B	-2.7	0.2	3.7
threshold in B of 50 G	5.12	B	-3.1	0.3	0.2
energy release rate multiplied by realisation of a random variable, η $(0.9 < \eta < 1.1)$	5.13	ϕ	-2.9	0.2	1.9

Table 4.5: Power-law distributions generated by the continuous model (continuation 3).

Details of run	Figure No.	Cell parameter	Power-law index	Error Estimate on Index	Reduced X^2
energy release rate multiplied by realisation					
of a random variable, η $(0 < \eta < 1)$	5.13	ϕ	-2.6	0.2	2.9
threshold in B of 20 G	5.13	ϕ	-2.6	0.2	3.8
threshold in B of 50 G	5.13	ϕ	-3.1	0.3	0.4
energy release rate multiplied by realisation					
of a random variable, η $(0 < \eta < 1)$	5.14	$\dot{E}_{\rm peak}$	-0.97	0.02	7.4
threshold in B of 20 G	5.14	$\dot{E}_{\rm peak}$	-1.0	0.03	7.4
threshold in B of 50 G	5.14	$\dot{E}_{\rm peak}$	-1.1	0.01	11.9
energy release rate multiplied by realisation					
of a random variable, η $(0 < \eta < 1)$	5.15	$E_{\rm int}$	-0.85	0.02	5.3
threshold in B of 20 G	5.15	$E_{\rm int}$	-0.90	0.02	6.5
threshold in B of 50 G	5.15	$E_{\rm int}$	-1.0	0.01	10.2
extended run of 10^7 time-steps (2×10^4 s)	4.34	$\dot{E}_{\rm peak}$	-0.88	0.01	43.1
extended run of 10^7 time-steps (2×10^4 s)	4.35	$E_{\rm int}$	-0.84	0.01	24.4
power-law (index = -1) distribution of initial					
magnetic field densities	3.28	$\dot{E}_{\rm peak}$	-1.0	0.03	6.3
power-law (index = -1) distribution of initial					
magnetic field densities	3.29	$E_{\rm int}$	-0.88	0.02	3.1

Table 4.6: Power-law distributions generated by the continuous model (continuation 4).

would expect longer runs to produce different, more evolved distributions. We performed a run using the typical initial conditions and parameter values but running the model for 10^7 time-steps (2×10^4 s) with 5×10^3 cells instead of the usual 3×10^6 time-steps (6×10^3 s) and 10^3 cells.

Figures 4.32, 4.33, 4.34, 4.35 and 4.36 show distributions of flux density, magnetic flux, event-size distribution counted by peak energy release rate and counted by integrated energy release. The lower plots show the distributions obtained for the extended run (10^7 time-steps), and the upper plots show distributions for the usual run of 3×10^6 time-steps. We recall that vertical dotted lines reflect the initial values of mean flux density (figure 4.32), mean flux (figure 4.33) and initial cell size (figure 4.36).

Magnetic flux density in Extended Run.

Considering figure 4.32, for the extended run there remains two regimes in the flux distribution : a region generally below the initial mean flux and one above that level. the flat distribution in the lower part of the x-range extends approximately 0.2 into the upper regime. After running for 10^7 time-steps it appears that this distribution is in a settled state. The region between $\log|B| = 1.9$ and $\log|B| = 2.3$ is power-law-like.

Magnetic flux in Extended Run.

Considering figure 4.33, the distribution of flux is very similar in form to that of the flux density. Since we know that $\phi = B\ L$, this indicates that there is very little correlation between cell length and flux density. The region below $\log\phi = 12.9$ is a flat distribution.

Event-sizes in Extended Run.

Regarding the peak energy release rate event-size distribution (figure 4.34) the extended model has generated events down to $\dot{E}_{\text{peak}} = 4$ compared with 5.5 for the typical run. The total dynamic range for the extended run is eight orders of magnitude. The distribution for the extended run is broken into 3 regimes as we can see in figure 4.34. The gradient of the central part of the distribution is -0.88 compared with -0.97 for the typical run.

Regarding the integrated energy release event-size distribution (figure 4.35) we find a very similar profile (for the extended run) to that of the figure 4.34, with the smallest events being around $E_{\text{int}} = 1$ compared with 4 for the typical run. The total dynamic range for the extended run is ten orders of magnitude. The gradient of the central part of the plot is almost identical, at -0.84, with that of the typical run.

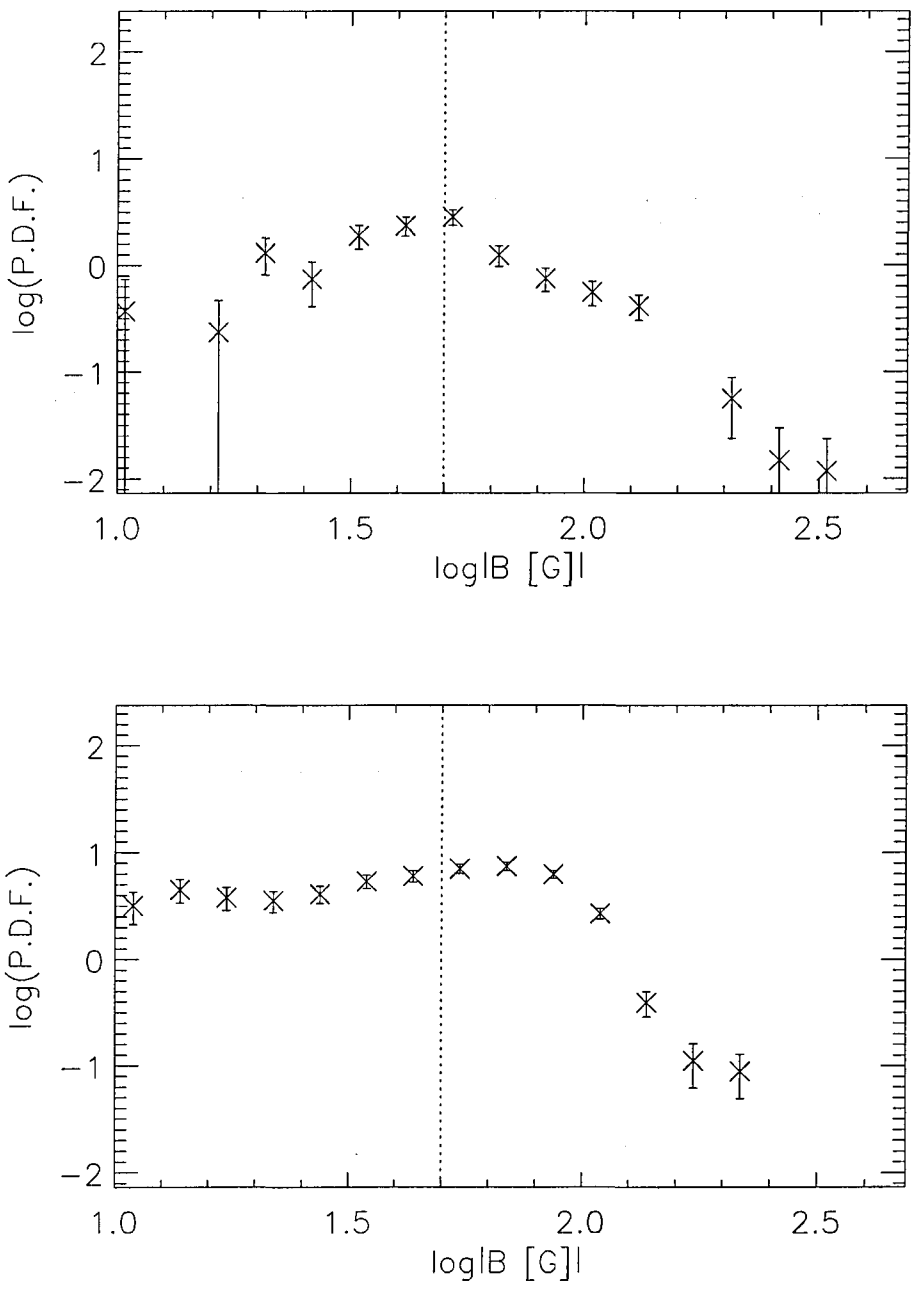

Figure 4.32: Evolved distributions of magnetic flux density. Bin-size = 0.1; initial cell length = 10^4 m. Dotted lines mark mean initial magnetic flux density. Upper: typical run (3×10^6 time-steps and 10^3 cells). Lower: extended run (10^7 time-steps and 5×10^3) cells

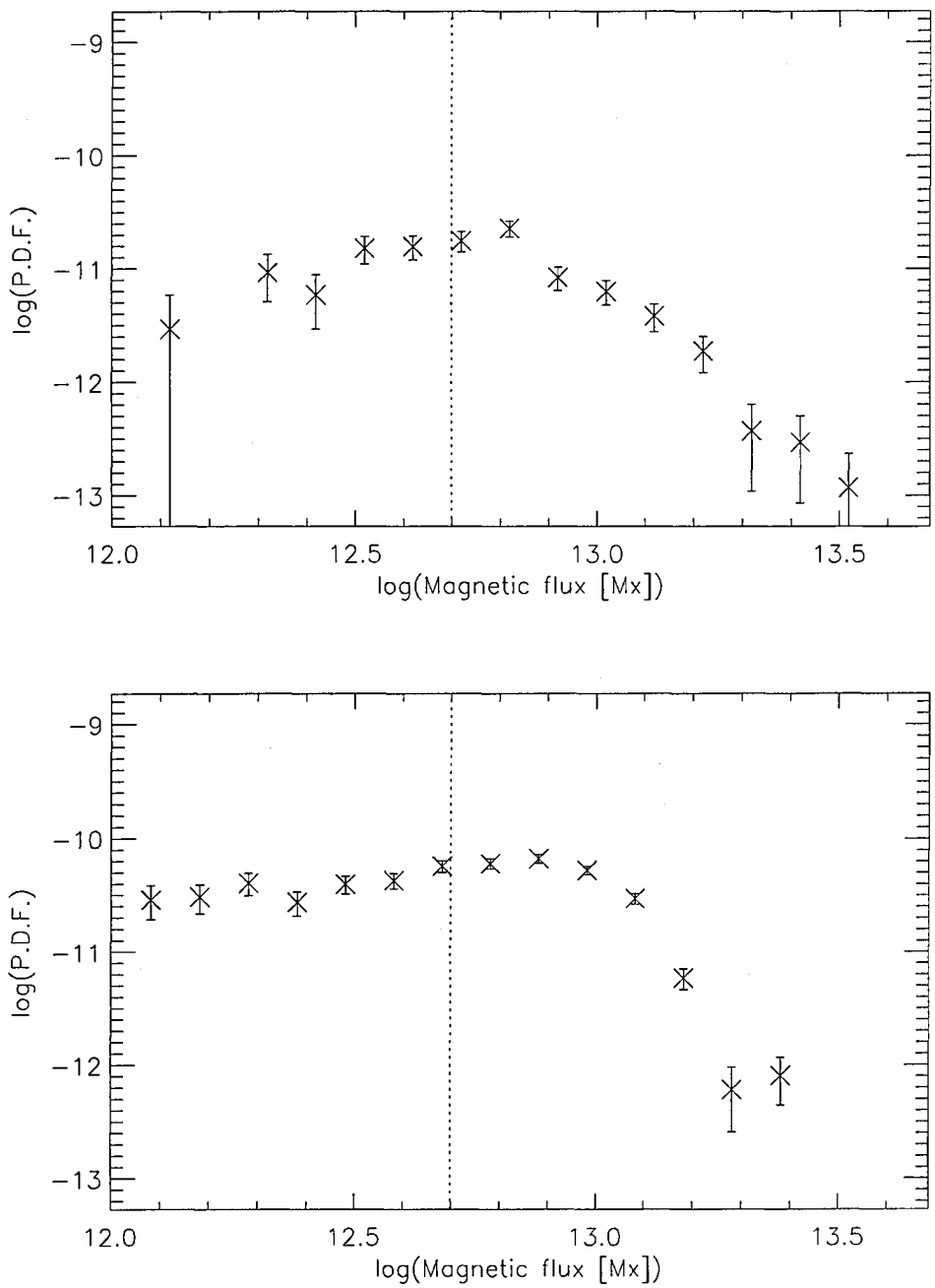

Figure 4.33: Evolved distributions of magnetic flux. Bin-size = 0.1; initial cell length = 10^4 m. Dotted lines mark mean initial magnetic flux. Upper: typical run (3×10^6 time-steps and 10^3 cells). Lower: extended run (10^7 time-steps and 5×10^3) cells

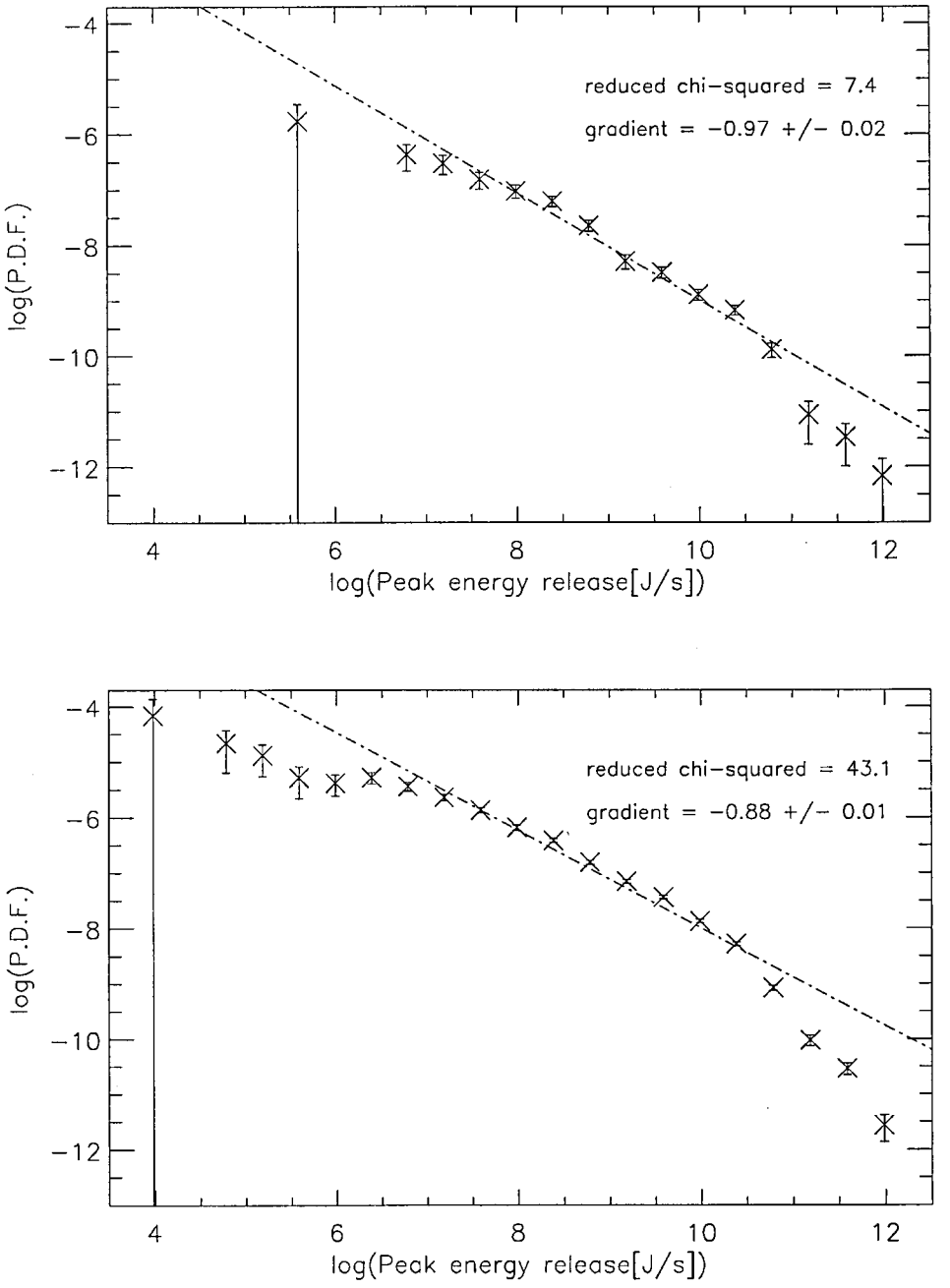

Figure 4.34: Evolved distributions of event-sizes counted by peak energy release rate comparing typical run with extended run. Bin-size = 0.4; initial cell length = 10^4 m. Upper: typical run (3×10^6 time-steps and 10^3 cells). Lower: extended run (10^7 time-steps and 5×10^3) cells

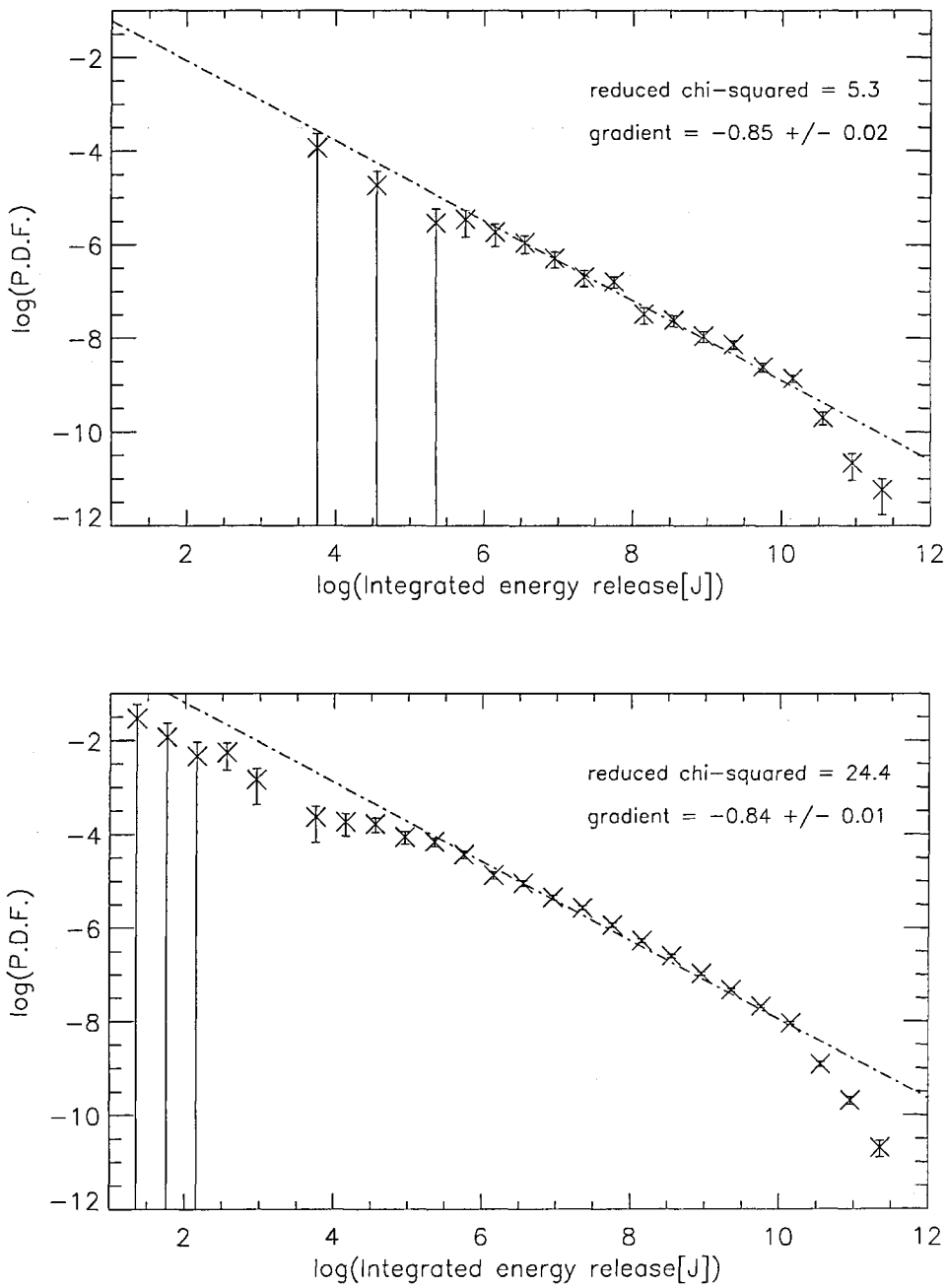

Figure 4.35: Evolved distributions of event-sizes counted by integrated energy release comparing typical run with extended run. Bin-size = 0.4; initial cell length = 10^4 m. Upper: typical run (3×10^6 time-steps and 10^3 cells). Lower: extended run (10^7 time-steps and 5×10^3) cells.

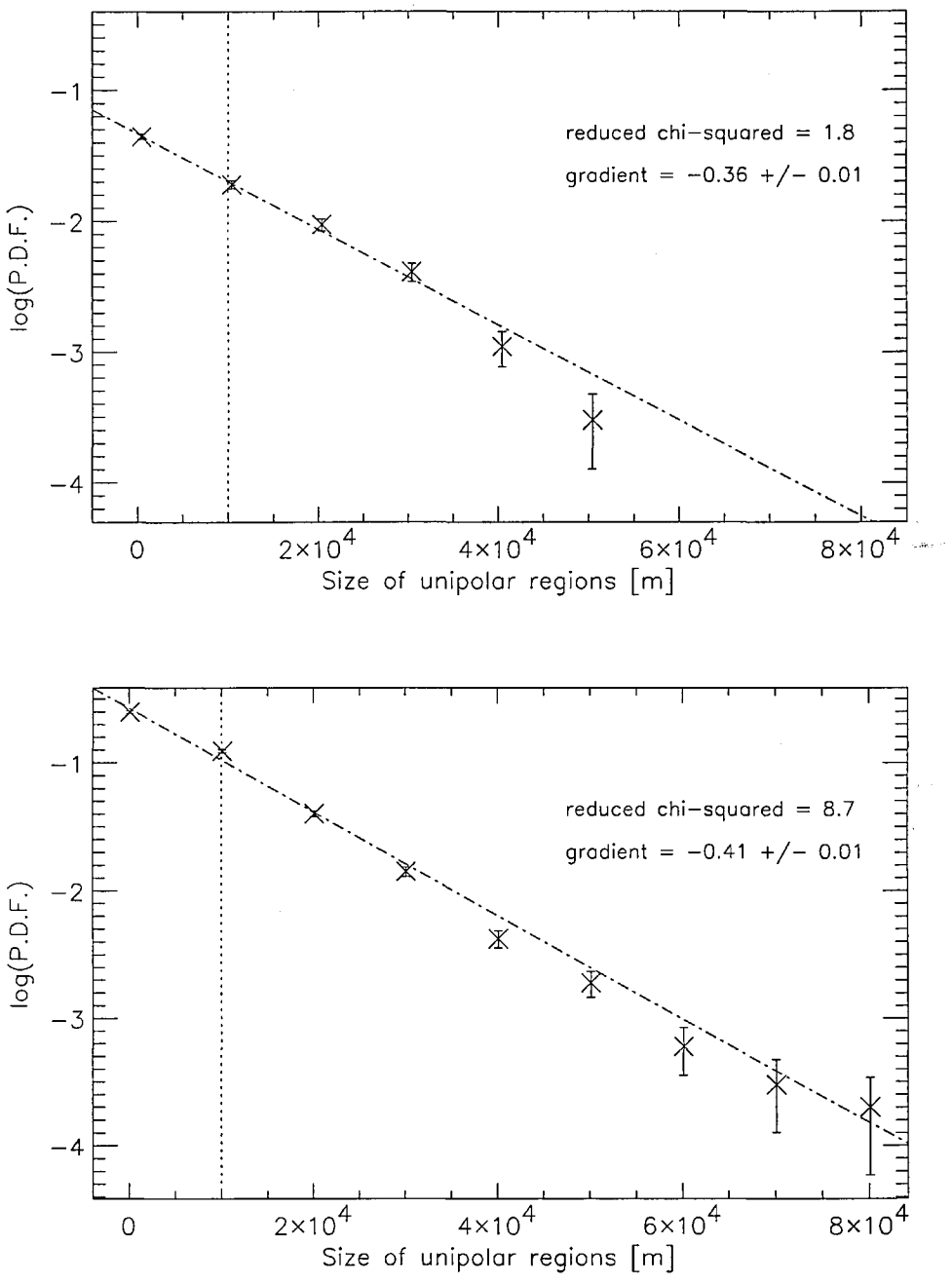

Figure 4.36: Evolved distributions of unipolar region size. Bin-size = 10^4 m; initial cell length = 10^4 m. Upper: typical run (3×10^6 time-steps and 10^3 cells). Lower: extended run (10^7 time-steps and 5×10^3) cells

Thus, it appears that we can generate larger dynamic ranges when the model is run for 10^7 rather than 3×10^6 time-steps, although the ranges for the typical run are anyway around six and eight orders of magnitude, respectively, for the peak and integrated energy release.

Unipolar Region Sizes in Extended Run.

The distribution of unipolar region sizes remains exponential with approximately the same gradient (-0.41 compared with -0.36) although the dynamic range has increased from 5×10^4 m (largest regions are five times the initial cell size) to 8×10^4 m (largest regions are eight times the initial cell size).

Conclusion.

Thus, we have determined that the profiles of the distributions remain generally unchanged although with enlarged dynamic ranges. We expect this enlargement of dynamic range given that the run uses an initial state with 5×10^3 cells compared with the usual 10^3 cells.

4.3.2 Power-Laws Caused by Reconnection or Emergence/Submergence.

Where there are power-laws in the data, we should seek to establish whether :

1. these are a result of power-laws frozen into the model at the beginning of a run, or
2. the power-laws are caused by the reconnection process, or
3. the power-laws are caused by the emergence/submergence process.
4. the power-laws are caused by a combination of reconnection and the emergence/submergence process.

We will examine the power-laws we have obtained from the model with a view to answering this question.

We will compare magnetic field density, magnetic flux and event-size distributions for the following runs :

1. 'typical' initial conditions, as per the Definition of Commonly Used Terms given at the beginning of the thesis.
2. same as above, but reconnection turned off.
3. same as 'typical', but emergence/submergence reduced by setting flux replacement timescale, $t_{\mathrm{em/sub}} = 10^4$ s instead of $t_{\mathrm{em/sub}} = 10^3$ s.

The three plots on each figure will relate to these three runs in the same order. Thus, the second plot allows us to compare the typical behaviour with a run where there is no effect from the depletion of magnetic field density caused by reconnection. The third plot allows us to compare the typical run with one where the effect of the emergence/submergence is reduced. We cannot obtain event-size distributions when the reconnection process is turned off, so figures showing the peak and integrated energy release will only compare two plots (1. and 3. above).

In order to check the dependency upon initial cell length we also produced these distributions for the same conditions but initial cell length of 5×10^3 m.

With regard to distributions of magnetic field density let us look again at figure 4.20.

Now, the second, third and fourth plots show us that increasing the emergence/submergence rate by decreasing the flux replacement timescale ($t_{\mathrm{em/sub}}$) or increasing the fraction of cells undergoing emergence/submergence (κ) has the effect of destroying the model-produced power law in the upper part of the x-range.

Similarly, with regard to distributions of magnetic flux, figure 4.22, second, third and fourth plots, shows us that increasing the emergence/submergence rate again has the effect of destroying the model-produced power law in the upper part of the x-range.

Figures 4.37 and 4.38 show us magnetic field density data from the three runs described above, but for initial cell lengths 10^4 m and 5×10^3 m respectively. The first plots in each of these two figures shows data from the typical run, as described above, with (1) reconnection turned on, and (2) $t_{\mathrm{em/sub}} = 1000$ s, $\kappa = 0.1$. We can see power-law distributions on the far right-hand sides, above the mean initial magnetic flux densities. The second plots on these figures show data from a run where the reconnection has been turned off. We can see that the power-laws have been destroyed and there is evidence of no discernable distribution. The third plots on these figures show data from a run where the emergence/submergence rate has been reduced by a factor of 10 by setting the flux replacement timescale, $t_{\mathrm{em/sub}} = 10^4$ s. Again, the power-laws have been destroyed and there are no noteworthy distributions. Thus, whether cell length is 10^4 m or 5×10^3 m, the effect upon the magnetic field density of removing the reconnection process, or reducing the emergence/submergence is the same : obliteration of the power-law distributions.

Figures 4.39 and 4.40 show us magnetic flux data from the three runs described above, but for initial cell lengths 10^4 m and 5×10^3 m respectively. The first plots in each of these two figures shows data from the typical run, as described above, with reconnection turned on, $t_{\mathrm{em/sub}} = 1000$ s and $\kappa = 0.1$. We can see power-law-like distributions on the far right-hand sides, above the initial magnetic flux levels. The second plots on these figures show data from a run where the reconnection has been

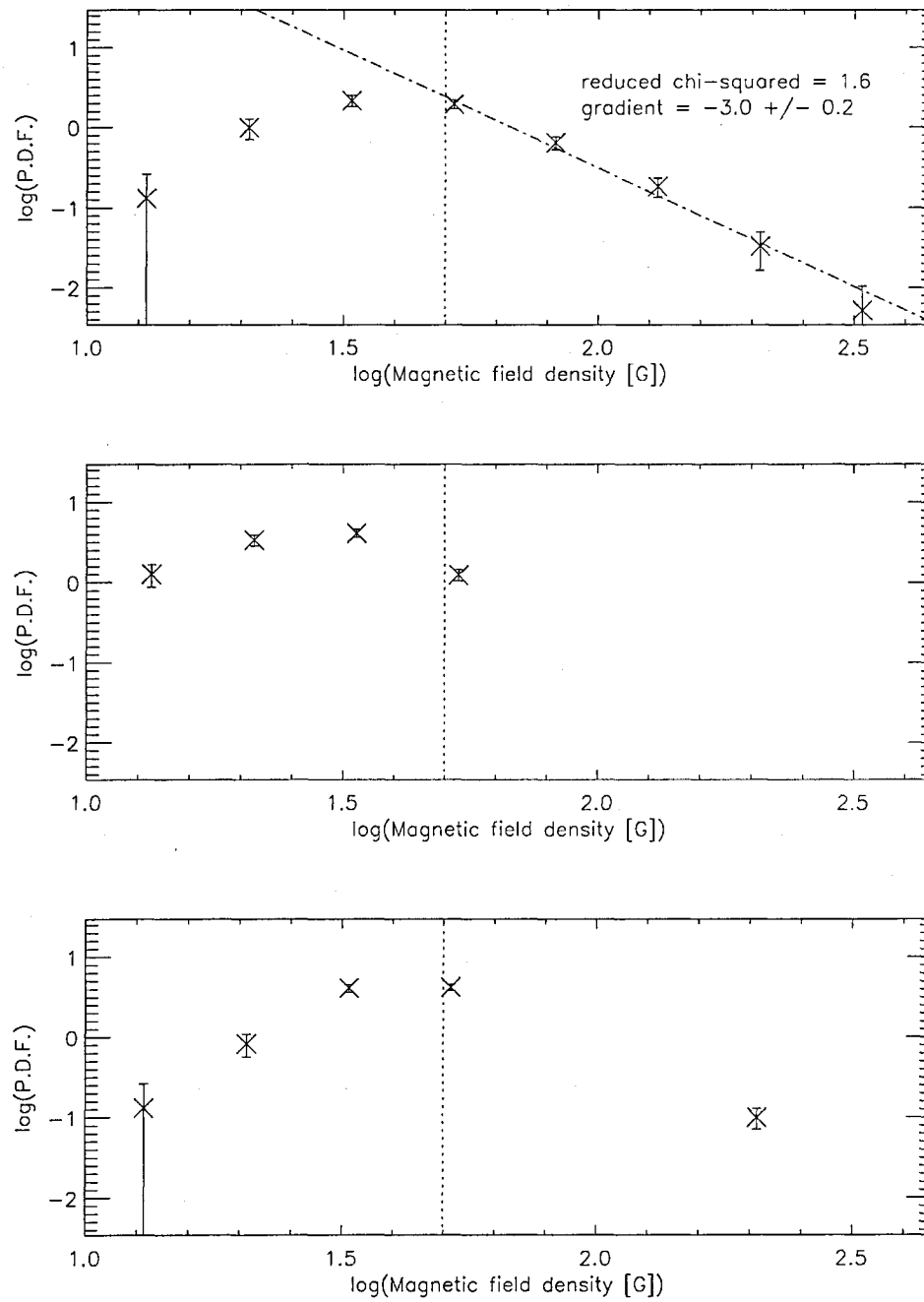

Figure 4.37: Evolved distributions of magnetic field density. Bin-size = 0.2; 10^3 cells; initial cell length = 10^4 m. Dotted lines mark mean initial magnetic field density. Top: typical run. Second: reconnection turned off. Third: emergence/submergence activity reduced, flux replacement timescale, $t_{\mathrm{em/sub}} = 10^4$ s.

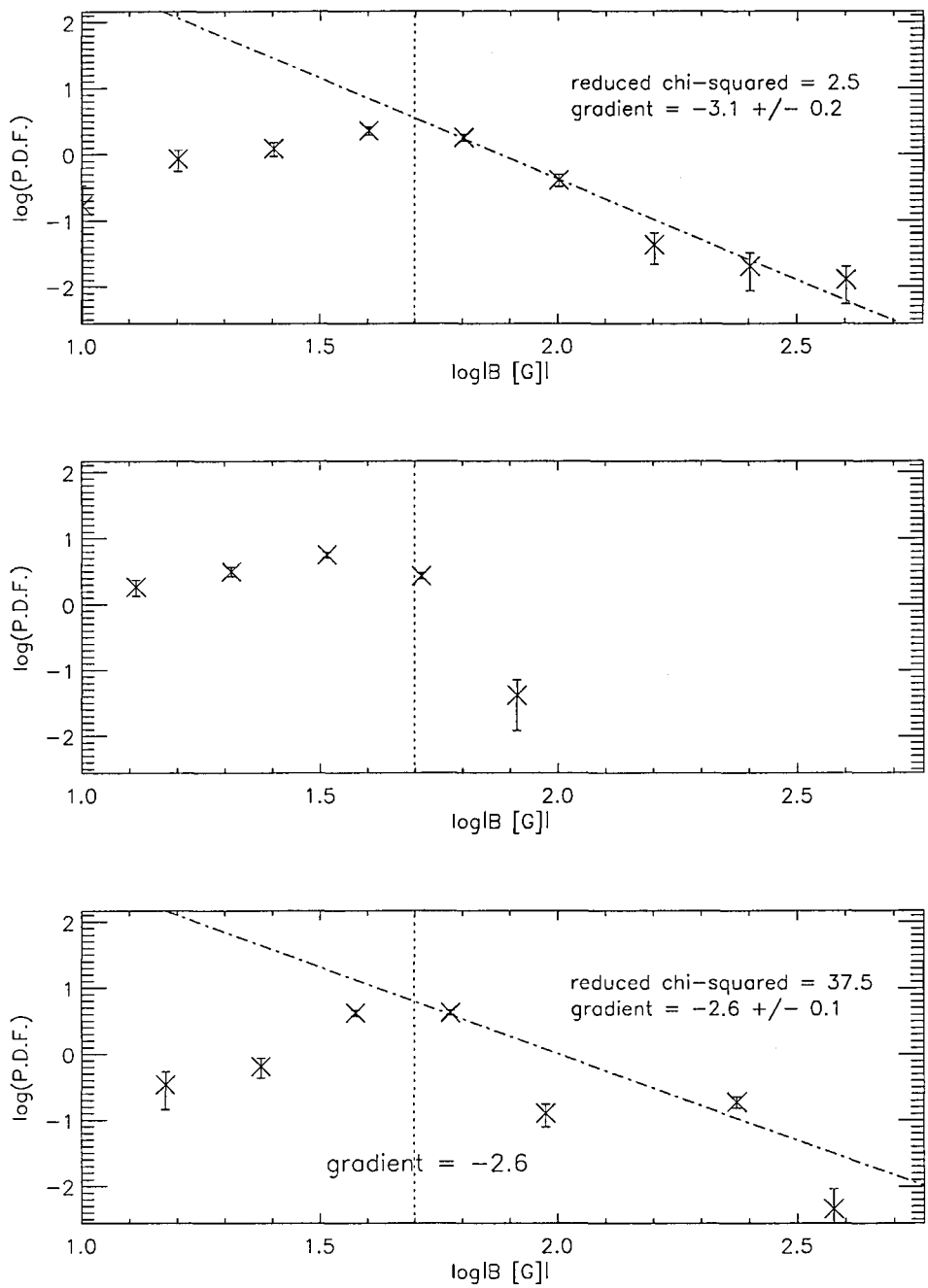

Figure 4.38: Evolved distributions of magnetic field density. Bin-size = 0.2; 10^3 cells; initial cell length = 5×10^3 m. Dotted lines mark mean initial magnetic field density. Top: typical run. Second: reconnection turned off. Third: emergence/submergence activity reduced, flux replacement timescale, $t_{\mathrm{em/sub}} = 10^4$ s.

turned off. We can see that turning off the reconnection results in obliteration of the power-law-like distributions. The third plots show data from a run where the emergence/submergence rate has been reduced by a factor of 10 by setting the flux replacement timescale, $t_{em/sub} = 10^4$ s. While reducing the emergence/submergence seems to produce a different distrubution at levels of magnetic flux below the mean initial level (marked by a dotted line), the power-law-like distribution at a level above the dotted line has been complicated although it appears to preserve the skeleton of a power-law. Thus, we find again that whether cell length is 10^4 m or 5×10^3 m, the effect upon the total magnetic flux of removing the reconnection process is to destroy power-laws. Reducing the emergence/submergence rate however does not destroy the power-laws.

Figures 4.23 and 4.24 show five plots each relating to the five runs referred to in table 4.1. These two figures show that increasing the emergence/submergence rate by increasing κ or decreasing $t_{em/sub}$ has no effect upon the profiles of event-sizes, although the dynamic range may be slightly reduced. The last plot on both of these figures shows data for reduced emergence/submergence rate ($t_{em/sub} = 2000$ s, instead of 1000 s) and again we see no substantial difference in the distribution.

Let's look at figures 4.41 (initial cell length of 10^4 m) and 4.42 (initial cell length of 5×10^3 m) which show peak energy release rate event-size distributions. On each figure, the first plot shows event-size data for the typical run. The second plot shows event-size data for the reduced-emergence/submergence run. The first plots on these figures are not power-law but exhibit power-law-like behaviour for at least part of the x-range.

In figure 4.41, where the initial cell length is 10^4 m, the second plot shows us that reduced emergence/submergence complicates further the distribution in the peak energy release rate distribution. Likewise for figure 4.42, where the initial cell length is 5×10^3 m, in respect of the power-law-like distribution in the peak energy release rate event-sizes of this figure. In the upper plot of figure 4.41 we have reduced $X^2 = 7.4$ whereas in the lower plot, where emergence/submergence is reduced, we have reduced $X^2 = 4.4$. Similarly, in the upper plot of figure 4.42 we have $X^2 = 4.2$ whereas in the lower plot, where emergence/submergence is reduced, we have $X^2 = 2.1$. These values of X^2 are misleading because the lines are fits to all of the points on each plot.

It appears thus that without emergence/submergence the distribution of event-sizes becomes more scattered.

Figures 4.43 (initial cell length of 10^4 m) and 4.44 (initial cell length of 5×10^3 m) show event-size data for these two runs again, although we are now looking at event-size distributions counted by integrated energy release. The first plot on each of these two figures shows power-law-like distributions stretching over at least six orders of magnitude. In fact, if we compare the first plots on these two

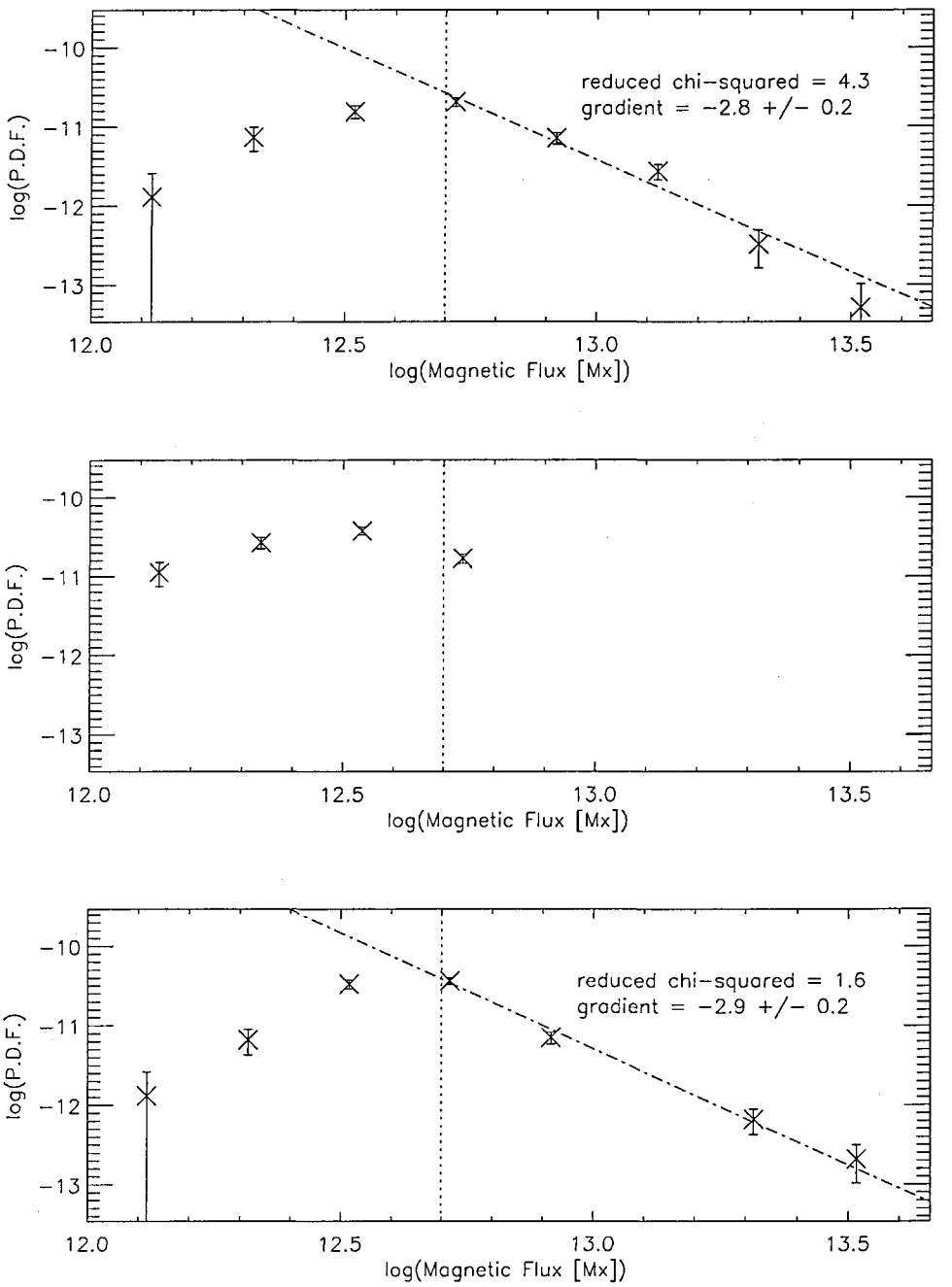

Figure 4.39: Evolved distributions of magnetic flux. Bin-size = 0.2; 10^3 cells; initial cell length = 10^4 m. Dotted lines mark mean initial magnetic flux. Top: typical run. Second: reconnection turned off. Third: emergence/submergence activity reduced, flux replacement timescale, $t_{\mathrm{em/sub}} = 10^4$ s.

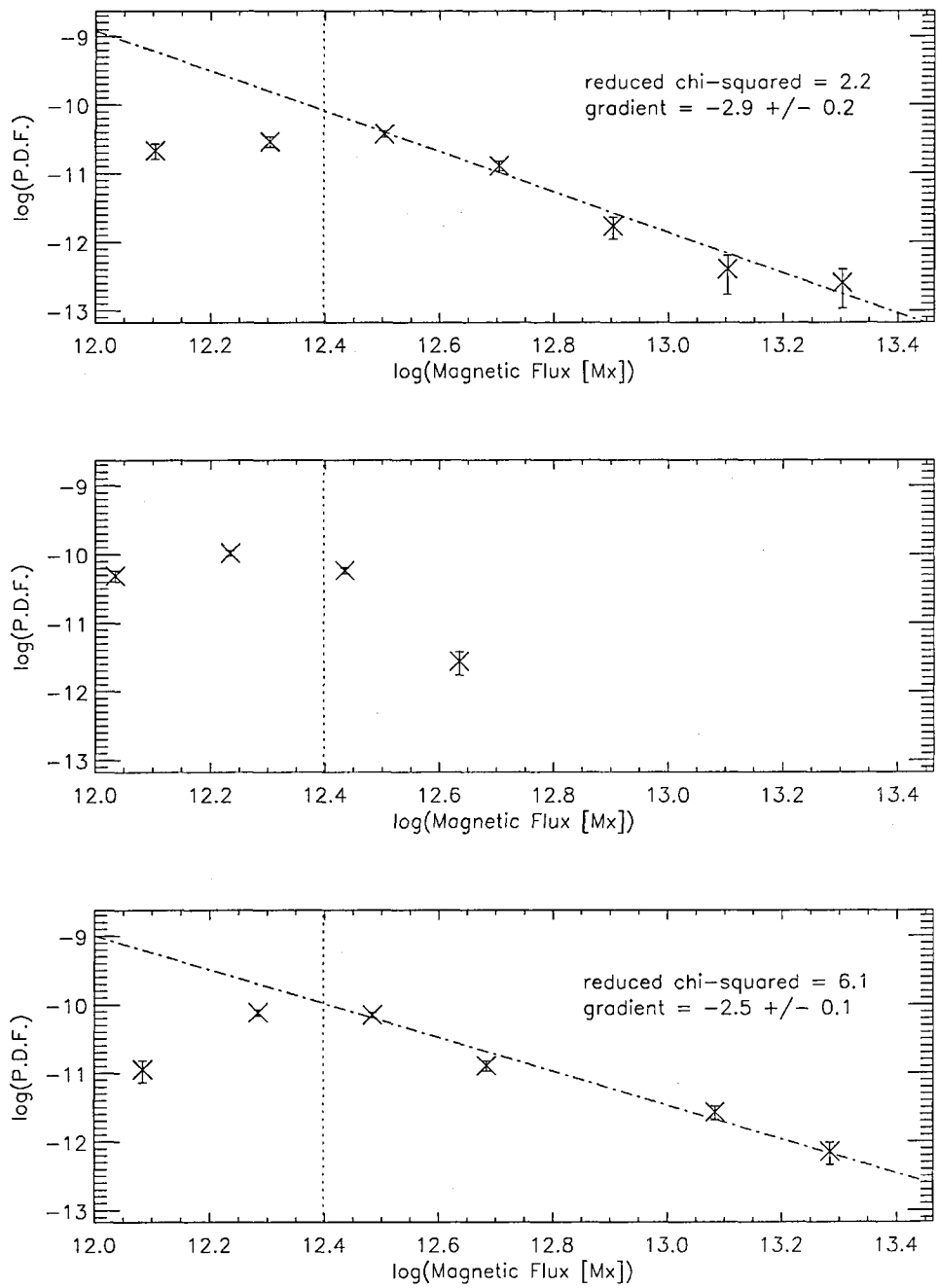

Figure 4.40: Evolved distributions of magnetic flux. Bin-size = 0.2; 10^3 cells; initial cell length = 5×10^3 m. Dotted lines mark mean initial magnetic flux. Top: typical run. Second: reconnection turned off. Third: emergence/submergence activity reduced, flux replacement timescale, $t_{\mathrm{em/sub}} = 10^4$ s.

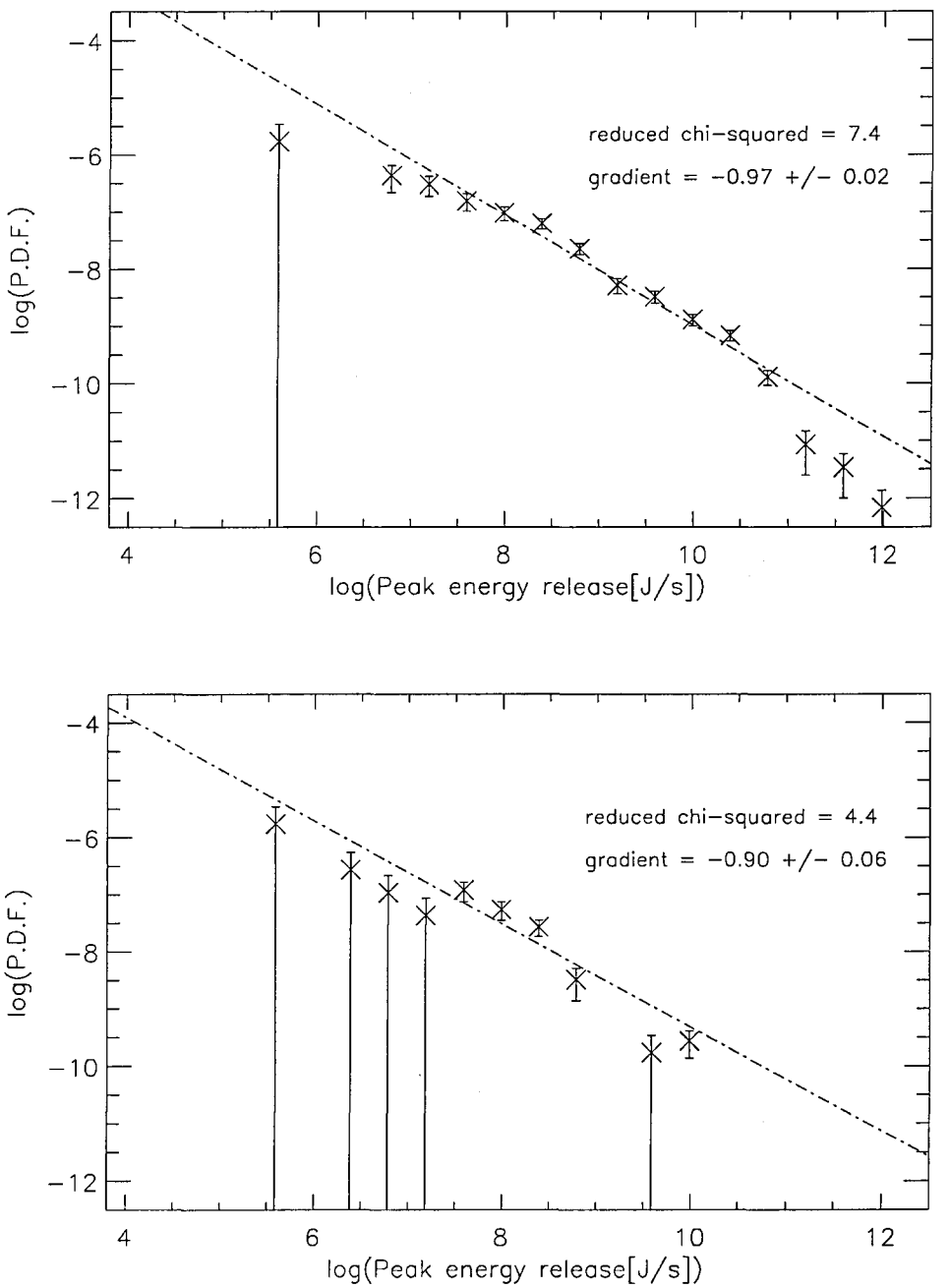

Figure 4.41: Evolved distributions of sizes of events, counted by peak energy release rate. Initial cell length = 10^4 m; log-log axes; bin-size = 0.4; 10^3 cells. First: typical run. Second: emergence/submergence activity reduced, flux replacement timescale, $t_{em/sub} = 10^4$ s.

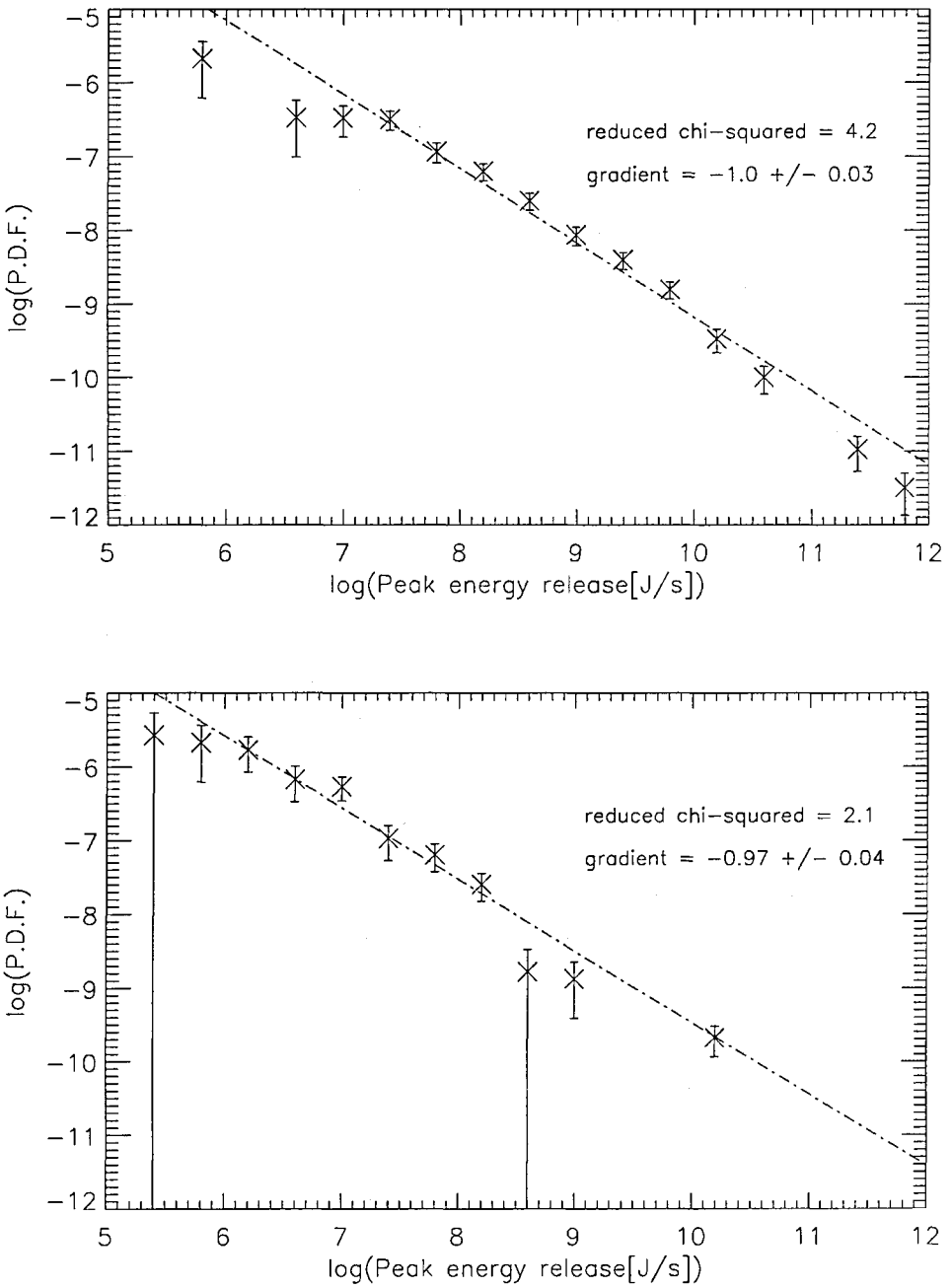

Figure 4.42: Evolved distributions of sizes of events, counted by peak energy release rate. Initial cell length = 5×10^3 m; log-log axes; bin-size = 0.4; 10^3 cells. First: typical run. Second: emergence/submergence activity reduced, flux replacement timescale, $t_{\mathrm{em/sub}} = 10^4$ s.

figures we can see that despite the factor of two difference in the mean initial cell length the two profiles are in almost the same position with the same slope. Figure 4.43 shows us that the power-law-like distributions and their dynamic ranges are maintained for reduced emergence/submergence although the profile has become more complicated. Looking at figure 4.44 however, we see that the dynamic range is slightly shortened in the second plot although the profile remains the same.

Thus, it seems that the power-law-like profiles of event-size distributions are highly robust although the presence of reconnection, and to a lesser extent emergence/submergence is necessary to maintain the power-law-like distributions in $|B|$ and ϕ.

4.4 Summary.

4.4.1 Magnetic Field Density.

Regarding the magnetic field density, it thus appears that in order to obtain at least a power-law distribution both reconnection and a certain level of emergence/submergence is required. If there is too much emergence then power-laws will be destroyed, i.e. $t_{\text{em/sub}} = 500$ s, or $\kappa = 0.4$ (see figure 4.20). If there is too little emergence/submergence, i.e. $t_{\text{em/sub}} = 2000$ s then the power-law distribution will also break down. It is clear from figures 4.38 and 4.37 that both energy release from reconnection and at least the standard level of emergence/submergence ($t_{\text{em/sub}} = 10^3$ s and $\kappa = 0.1$) are necessary for power-laws in magnetic field density. The distributions are not robust in respect of the values of κ and $t_{\text{em/sub}}$. Figures 4.39 and 4.40 indicate that reconnection is essential for the generation of power-law distributions in B.

4.4.2 Magnetic Flux.

Figure 4.22 shows us that more than or less than the standard level of emergence/submergence will cause the power-law in the magnetic flux to break down. The distributions are not robust in respect of the values of κ and $t_{\text{em/sub}}$. Also figures 4.40 and 4.39 show that destruction of magnetic flux and/or heating by reconnection is necessary to maintain the power-law-like distribution in ϕ shown on the first plot of figure 4.22. Thus, again we find that both energy release from reconnection and the standard level of emergence/submergence ($t_{\text{em/sub}} = 10^3$ s and $\kappa = 0.1$) are necessary for power-laws in magnetic field density and neither specifically drive the power-law distribution.

It is interesting that in many parts of the parameter space which we have explored we obtain power-law-like distributions in B and ϕ yet these run from and above the initial mean levels on the plots. Without exception the distributions below these levels, marked by vertical dotted lines, are

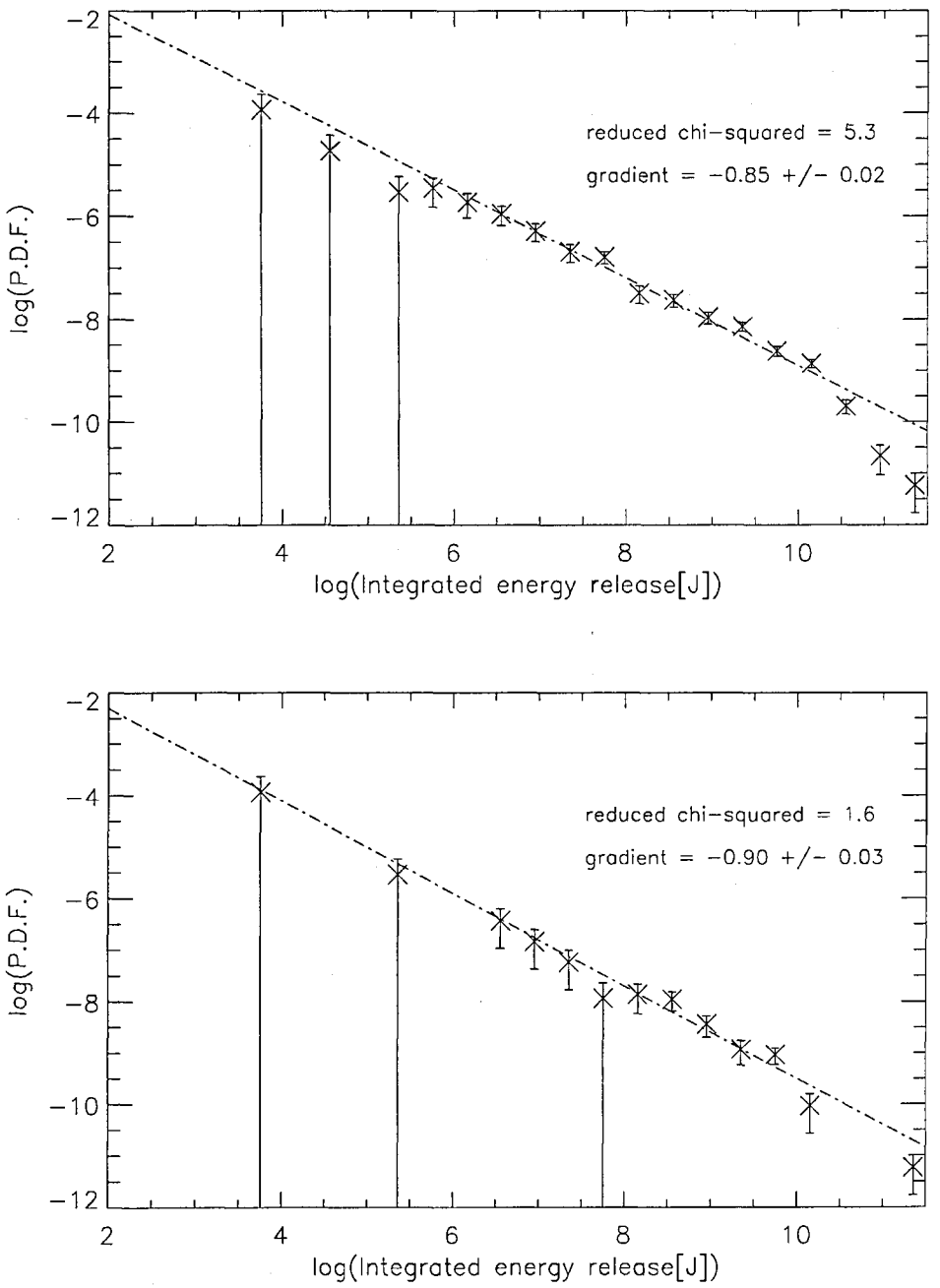

Figure 4.43: Evolved distributions of sizes of events, counted by integrated energy release. Initial cell length = 10^4 m; log-log axes; bin-size = 0.4; 10^3 cells. First: typical run. Second: emergence/submergence activity reduced, flux replacement timescale, $t_{\mathrm{em/sub}} = 10^4$ s.

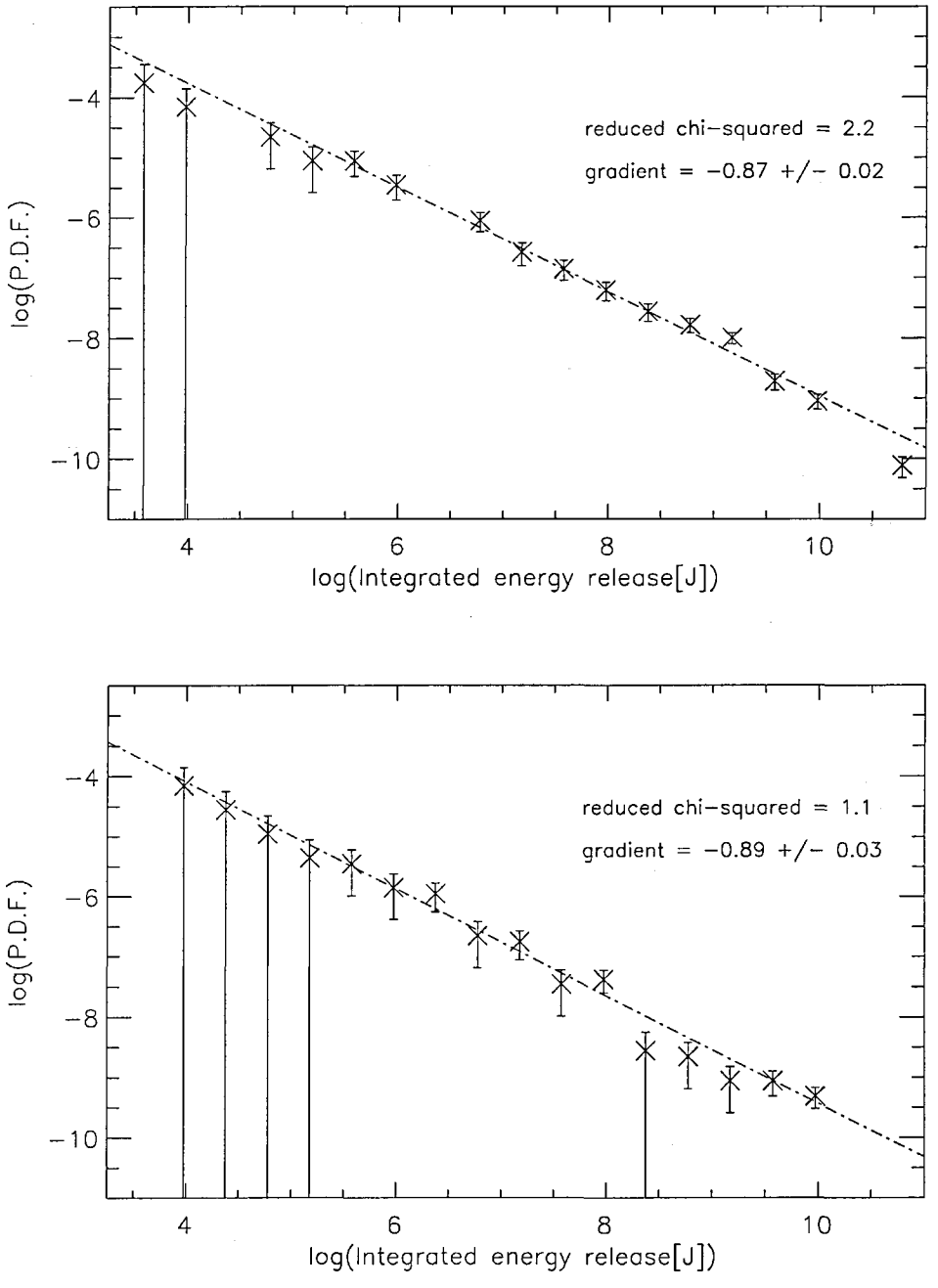

Figure 4.44: Evolved distributions of sizes of events, counted by integrated energy release. Initial cell length = 5×10^3 m; log-log axes; bin-size = 0.4; 10^3 cells. First: typical run. Second : emergence/submergence activity reduced, flux replacement timescale, $t_{\mathrm{em/sub}} = 10^4$ s.

	Peak energy release rate [J s^{-1}]	Integrated energy released [J]
Dynamic range	$10^5 \leftrightarrow 10^{12}$	$10^4 \leftrightarrow 10^{11}$
Gradient	-0.88 $\leftrightarrow$ -1.09	-0.83 $\leftrightarrow$ -0.91

Table 4.7: Dynamic ranges and power-laws in peak and integrated energy release.

not power-law-like and have no noteworthy profile.

4.4.3 Event-sizes.

The second plots of figures 4.41, 4.42, 4.43 and 4.44 show profiles similar to the typical run (uppermost plots), although the distributions are more complicated. This might indicate that the reconnection is largely responsible for the nice profiles of the uppermost plots, but that there is a contribution from the emergence/submergence. Reducing the emergence/submergence changes neither the position nor slope of the distributions. Perhaps a requirement of the peak and integrated energy release event-size distributions is a small level of emergence/submergence, and $t_{\mathrm{em/sub}} = 10^4$ s and $\kappa = 0.1$ is sufficient.

Table 4.7 shows the event-size dynamic ranges and power-law indexes obtained from the model. We find that power-law-like peak and integrated energy event-size distributions are invariably produced. We also find that between the many parts of the parameter space we have explored, not only in this chapter but also in chapter 3 the profiles of these distributions are extremely similar and robust, with dynamic ranges and gradients in general terms as given in table 4.7.

Chapter 5

Discussion and Future Work.

"This really happened."
Kurt Vonnegut.

"Come off it!"
Jeremy Paxman.

We will first discuss a number of specific matters before returning to the specific questions we posed in the Introduction. These matters are :

1. An explanation of the initial distribution of unipolar region sizes.
2. An analytical approach explaining aspects of the event-size distributions generated by the model and energy release time-series.
3. A comment upon the robustness of B, ϕ, L_{unipolar} and event-size distribution profiles-.
4. The variation of $|B|$ with the Solar cycle.

The questions we posed in the Introduction were as follows :

1. How does the power-law flux density distribution arise?
2. How does the power-law event-size distribution arise?
3. Do we see sufficient dynamic range and appropriate power-law indexes in the data?

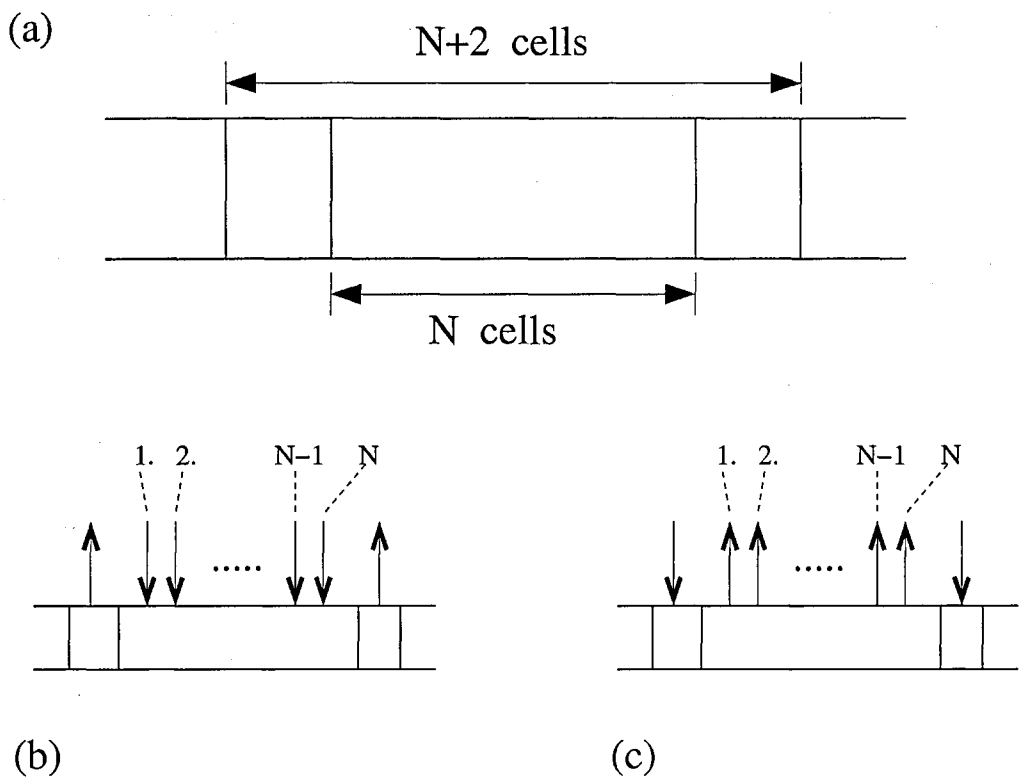

Figure 5.1: (a) Schematic of unipolar region of length N cells. (b) and (b) Two possibilities of unipolar region flux polarities.

4. Can features of flaring events be obtained with this model?

5. How do the results depend on the details of the reconnection mechanism?

6. What is the relevance of Self-Organised Criticality?

Finally, we will briefly discuss possible future work.

5.1 Unipolar Region Sizes.

We recall that we saw plots in section 4.2 demonstrating that the initial distribution of unipolar region sizes is exponential. Specifically, the top plot of figure 4.16 gives the initial distribution, the gradient being -0.30. We will now derive analytically the profile and gradient of this distribution.

If we consider a long series of cells and choose any consecutive group of N cells from these at random, we can find the probability of these N cells being a unipolar region.

Assuming every cell has magnetic flux attached to it, the polarity of the flux is a random variable with probability $p = 0.5$ of the flux in each cell being positive. Therefore, $(1 - p)$ is the probability of negative flux.

To find the probability $P(N)$ of obtaining a unipolar region with negative flux (diagram (a) in figure 5.1), we have :

$$P(N) = p^2\ (1-p)^N$$

Diagram (b) is the same as (a) except with reversed polarity. There are therefore two ways of obtaining a unipolar region of size N.

Thus, we have :

$$\begin{aligned} P(N) &= 2\,p^2\ (1-p)^N \\ &= (0.5)\ (0.5)^N \end{aligned} \tag{5.1}$$

If our grid is long enough to ignore edge effects we can take this to be the P.D.F. of unipolar region size. Therefore,

$$\begin{aligned} \log_{10} P(N) &= \log_{10} 0.5\ +\ N\ \log_{10} 0.5 \\ &= -0.30\ -\ 0.30\ N \end{aligned} \tag{5.2}$$

Thus, equation 5.1 implies an exponential P.D.F. for N and equation 5.2 tells us that if we plot $\log_{10} P(N)$ -v- N we would expect the distribution to be a straight line of gradient ≈ -0.3. Both of these results are found in the results of the model as shown in figure 4.16. Thus, we are clear that unipolar regions will initially be exponentially distributed with a gradient of -0.3.

5.2 An Analytical Approach to Peak Energy Release Rate and Integrated Energy Release Event-size Distributions.

Using a simplified approach we can attempt to generate order-of-magnitude approximations to the features of the model-generated distributions and compare these to the results generated. We will do this for the run using the typical initial parameter values. We will calculate estimated values of peak energy release rate and integrated energy release. We will also obtain an estimate of event duration and algebraic expressions for rate of energy release and field density during reconnection. These will allow us to produce decay curves for the energy release rate.

Let us first establish the values of some supporting parameters. Now, the first plot of figure 4.20 indicates that magnetic field density reaches a maximum of $|B_{\max}| \approx 10^{2.5}$ G. Also, given the initial

distribution of magnetic field density in the range $-100 \leftrightarrow +100$ G, we can take a mean value of $\overline{|B|} \approx 50$ G. Where $\overline{n} \approx 10^{23}$ m^{-3} and $m = m_{\rm p} = 1.673 \times 10^{-27}$ kg we have $\overline{\rho} \approx 1.7 \times 10^{-4}$ kg m^{-3} typically. Also, $\mu_0 = 1.256 \times 10^{-6}$ H m^{-1}.

We know that :

$$C_{\rm A} = \frac{|B|}{\sqrt{\mu_0 \rho}}$$

Thus, where magnetic field density is a mean we have $C_{\rm A} \approx 345$ m s^{-1} and when magnetic field density is a maximum we have $C_{\rm A} \approx 2.18 \times 10^3$ m s^{-1}

For the calculations made in this section we will use the following values :

$$\begin{aligned}
\overline{L} &= 10^4 \text{ m} \\
\overline{|B|} &= 50 \text{ G} \\
|B_{\rm max}| &= 10^{2.5} \text{ G} = 316 \text{ G} \\
A_{\rm grid} &= 10^6 \text{ m}^2 \\
\overline{\rho} &= 1.7 \times 10^{-4} \text{ kg m}^{-3} \\
\mu_0 &= 1.256 \times 10^{-6} \text{ H m}^{-1} \\
\delta t &= 0.002 \text{ s} \\
\overline{C_{\rm A}} &= 345 \text{ m s}^{-1} \\
C_{\rm A,max} &= 2.18 \times 10^3 \text{ m s}^{-1}
\end{aligned}$$

We will now obtain an estimate of the typical duration, D, of events. For reasons which will become clear below, this duration has the sense of a half-life because it represents the timescale of the decaying energy release rate, or equivalently, the decaying flux density.

Generally through these analytical investigations of section 5.2 we assume the following :

1. during an event the entire magnetic energy within a cell is destroyed in the reconnection process. Thus, B will drop to zero during the progress of the event.
2. during an event magnetic energy is released at a constant rate.
3. as mentioned earlier, we are treating each cell as being of constant length 10^4 m.

The two assumptions mean that events would have square profiles if represented on a plot of $\dot{E}$ -v- t, i.e. that when the event overtakes the background level it will instantaneously increase to a level above the background, then persists for a while at that level before instantaneously dropping

below the background. In fact B will never reach zero before the culmination of an event because prior to that point it will be overtaken by another reconnection site. The rate of energy release, $\dot{E}$, is dependent upon B and as B reduces we would expect $\dot{E}$ to attenuate accordingly, nevertheless for simplicity we assume constant $\dot{E}$.

We know that :

$$E_B \approx \overline{L}\, A_{\text{grid}} \frac{\overline{|B|}^2}{2\mu_0} \tag{5.3}$$

$$\dot{E} \approx -\overline{C_{\text{A}}}\, A_{\text{grid}} \frac{\overline{|B|}^2}{2\mu_0} \tag{5.4}$$

Typically, where a run commences with 10^3 cells and the cell length is uniformly 10^4 m we find that the model settles into a state where there are $\sim 1.4 \times 10^3$ cells. Therefore we have :

$$\begin{aligned} D &\approx \frac{E_B}{-\dot{E}} \\ &\approx \frac{\overline{L}}{\overline{C_{\text{A}}}} \\ &\approx \frac{10^7/(1.4 \times 10^3)}{345} \text{ s} \\ &\approx 20.70 \text{ s} \end{aligned}$$

Over a model run of 4000 s we might therefore expect the number of events :

$$\sim \frac{4000}{20.70} \approx 193 \quad \text{events}$$

In fact, during the run (typical parameter values) which generated figure 3.9 there were 171 events. Our estimate is remarkably close to this value.

We recall in table 1.2 that the threshold duration of the instruments SMM and ICE were 200 s and 100 s respectively and we might therefore consider these figures to be upper limits upon event duration. These figures tie in with our estimated mean duration of 20.70 s.

Estimate of Integrated Energy Release.

We will calculate a typical value for integrated energy release, E_{int}. Let us assume that the whole of the magnetic energy of a cell is consumed by a perfect reconnection event with zero background energy release : irrespective of whether the cell reconnects with one or both neighbours, it completely exhausts the magnetic energy it contains.

When we say 'typical cell', we must remember that only cells with very high rate of energy release are counted towards the event-size distribution, therefore we should consider our result here to be highly tentative.

We know that the magnetic energy contained by a cell is :

$$E_B \approx L\, A_{\text{grid}}\, \frac{|B|^2}{2\mu_0}$$

Thus, for our typical cell we have instead :

$$\begin{aligned} E_{\text{int}} &\approx \overline{L}\, A_{\text{grid}}\, \frac{\overline{|B|}^2}{2\mu_0} \\ &\approx \frac{10^4 \times 10^6 \times (5 \times 10^{-3})^2}{2 \times 1.256 \times 10^{-6}} \\ &\approx 10^{11}\ \text{J} \end{aligned}$$

Considering figure 4.24 we can see that we have a result reasonably in line with the largest events produced by the typical run of the model.

Estimate of Peak Energy Release Rate.

We will now obtain an estimate for the maximum value of the peak flux occurring in an individual reconnection event. In other words, the likely highest value obtained for energy release where reconnection is occurring between two adjacent cells. This will occur where C_{A} and B are both high. Similarly to equation 5.4 we have :

$$\begin{aligned} |\dot{E}| &\approx C_{\text{A,max}}\, A_{\text{grid}}\, \frac{|B_{\text{max}}|^2}{2\ \mu_0} \\ &\approx \frac{|B_{\text{max}}|}{\sqrt{\mu_0 \overline{\rho}}}\, A_{\text{grid}}\, \frac{|B_{\text{max}}|^2}{2\mu_0} \end{aligned}$$

$$\approx \; 10^{11.94} \text{ J s}^{-1}$$

The lower plot of figure 3.9 shows us that this is a good estimate for the upper limit of peak energy release rate.

In a sense, the lower limit for peak energy release rate is the background rate since it is at the point that an event significantly exceeds the background energy release that a cell undergoing reconnection becomes a reconnection event. However, it is unlikely that any events will be as small as this minimal size because the event occurring at any particular time during the run will by definition be the site of greatest energy release at that time in the model.

We can attempt to calculate a likely mean value for peak energy release. Taking mean values for alfven speed and magnetic field density we know :

$$\begin{aligned} |\overline{\dot{E}}| &\approx \overline{C_{\text{A}}}\, A_{\text{grid}}\, \frac{\overline{|B|}^2}{2\mu_0} \\ &\approx 10^{9.54} \text{ J s}^{-1} \end{aligned}$$

This value lies in the middle of the data on the top plot of figure 4.30, and as we would expect, also sits at the mean level of the lower plot on figure 3.9.

Decay of Rate of Energy Release, $\dot{E}$.

We have already mentioned that $\dot{E}$ will diminish during an event. Let's now consider this in more detail and obtain expressions showing how $\dot{E}$ and B vary with time, t.

Figure 5.5 shows that the energy available for release by reconnection is the volume $C_{\text{A}} A_{\text{grid}}$ multiplied by the magnetic energy density, given by $\frac{B^2}{2\mu_0}$.

Thus,

$$\begin{aligned} \dot{E} &= -\, C_{\text{A}}\, A_{\text{grid}}\, \frac{B^2}{2\,\mu_0} \\ &= -\, \frac{|B|}{\sqrt{\mu_0\,\rho}}\, A_{\text{grid}}\, \frac{B^2}{2\,\mu_0} \\ &= -\, \frac{A_{\text{grid}}\, |B|^3}{2\,\sqrt{\rho}\,\mu_0^{\frac{3}{2}}} \end{aligned} \tag{5.5}$$

Also,

$$\frac{\mathrm{d}\phi}{\mathrm{d}t} = -C_{\mathrm{A}}\, W\, |B|$$

However, we know : $\phi = |B|\, L\, W$

Therefore :

$$\begin{aligned} \frac{\mathrm{d}B}{\mathrm{d}t} &= -\frac{C_{\mathrm{A}}\, |B|}{L} \\ &= -\frac{B^2}{L\sqrt{\mu_0\, \rho}} \end{aligned}$$

Let C be a constant, where :

$$C = \frac{1}{L\sqrt{\mu_0\, \rho}}$$

We recall that L is the cell length. So, we have :

$$\begin{aligned} \frac{\mathrm{d}B}{\mathrm{d}t} &= -C\, B^2 \\ \int \frac{\mathrm{d}B}{B^2} &= -C \int \mathrm{d}t \\ -\frac{1}{B} &= -C\,(t + t_0) \end{aligned}$$

where t_0 is a constant of integration.

When $t = 0$, let $B = B_0$, hence :

$$\begin{aligned} -\frac{1}{B_0} &= -C\, t_0 \\ t_0 &= \frac{1}{C\, B_0} \end{aligned}$$

So,

$$-\frac{1}{B} = -C\, t - \frac{1}{B_0}$$

Thus, rearranging :

$$B = \frac{B_0}{1 + B_0\, C\, t} \tag{5.6}$$

Therefore, B decreases as t^{-1}, where the half-life of the magnetic field density, $\tau_B = \frac{1}{B_0\, C}$

Substituting equation 5.6 for B in equation 5.5 gives :

$$\dot{E} = -\left(\frac{A_{\text{grid}}}{2\,\sqrt{\rho}\,\mu_0^{\frac{3}{2}}}\right)\left(\frac{B_0}{1+\frac{t}{\tau}}\right)^3$$

Therefore we find that :

$$|\dot{E}| \propto \frac{1}{(1+\frac{t}{\tau})^3} \tag{5.7}$$

This represents a rapid decay. Where $t >> \tau$, $|\dot{E}| \propto t^{-3}$

Now, let's consider the half-life of the magnetic field density, τ_B, where $B_0 = 50$ G.

$$\begin{aligned} \tau_B &= \frac{1}{B_0\, C} \\ &= \frac{1}{B_0\,\left(\frac{1}{L\,\sqrt{\mu_0\,\rho}}\right)} \\ &= \frac{L\,\sqrt{\mu_0\,\rho}}{B_0} \end{aligned} \tag{5.8}$$

Thus :

$$\tau_B|_{B_0=50\text{ G}} = 29\text{ s}$$

and, where $B = B_{\max}$:

$$\tau_B|_{B_0=316\text{ G}} = 4.6\text{ s}$$

An examination of figure 3.34 shows that these values for τ_B are realistic for the model. So, we find that the rate of energy release and flux density will decay quickly. Figure 5.2 shows us the time-series of rate of energy release by reconnection for a run using the typical conditions and parameter values. The half-life values we have calculated explain the steep decay curves we see in figure 5.2. By way of comparison figure 5.3, already referred to in section 4.2.1, shows us soft and hard X-ray and gamma-ray photon count time-series for a typical Solar flare during Solar maximum.

We can see some similarities between the profiles of figures 5.2 and 5.3 : both have a continuum background on to which are superimposed individual large events. These events each peak very rapidly then decay rapidly. The time-scales are very similar : the model-generated data covers 4000

seconds and the events have half-lives of a few seconds where the Solar flare data covers 3600 seconds. Our model is bound to produce many small events and no large events for the following reasons. The notion of an event means the interaction (reconnection) between a cell and both, or either, or its neighbours. An event cannot extend into a larger region. Therefore we cannot simulate an active region, for instance, without changing the definition of an event to mean perhaps something like the sum of all the reconnections occuring within a specified local region. We also can't simply use very large cells because there will then be fewer boundaries, or interactions, between the cells and reconnection cannot by definition occur within cells. In both synthetic and real data (figures 5.2 and 5.3) we find that the events typically raise above the background by up to two orders of magnitude.

We will now plot some example synthetic decay curves, for $\dot{E}$, generated according to our derived expression :

$$|\dot{E}| \propto \frac{1}{(1+\frac{t}{\tau})^3}$$

This will allow us to compare these synthetic curves with the decay curves of the real Solar X-ray photon flux. We must remember though that whereas figure 5.3 shows photon counts our expression for $\dot{E}$ is in terms of J s^{-1}.

Figure 5.4 shows plots of energy release rate. We have the first 200 seconds of figure 5.2 (top-left plot), which shows the total energy release rate for the entire grid; the first 200 seconds of the energy release rate for the largest events in the same run (top-right plot); the calculated decay profile for the energy release rate of a cell with length, $L = 10^4$ m, $\rho = \overline{\rho} = 1.7 \times 10^{-4}$ kg m^{-3} and initial $B_0 = 10^3$ G (bottom-left plot); same as previous but with $B_0 = 10^2$ G (bottom-right plot).

The top-left and top-right plots match, indicating that the total grid energy release is dominated by at most one individual large event occurring at any time. Looking at the lower plots we see that the greater the value of B_0 the smaller the half-life, as we would expect from equation 5.8. A drop of 0.3 on the logarithmic y-axis represents a halving of the energy release rate. These plots all have the same axes therefore we can compare these easily. It seems that many, if not all, of the decaying line-segments on the upper two plots could be represented by sections of the profiles given on the lower plots. Certainly, by visually matching these plots, it appears plausible that the energy release profiles generated by our model undergo decay in accordance with equation 5.7 :

$$|\dot{E}| \propto \frac{1}{(1+\frac{t}{\tau})^3}$$

Now, these upper plots of figure 5.4 appear similar to the profiles in the SMM data (figure 5.3). We conjecture that the Solar X-ray photon flux also undergoes decay according to something similar in form to equation 5.7 and this might indicate a similar underlying process, i.e. release of magnetic

energy from the plasma following the rule that : $|\dot{E}| \propto C_{\rm A} B^2$, which underpins the reconnection mechanism of the model.

The smallest events counted by the integrated energy method would in principal be marginally more than zero (after subtraction of the background level). Given an extremely long run time we might expect to see such events, however, we are unlikely to see such events over shorter periods because where there are many cells (certainly $\geq 10^3$) there will always be events whose energy release rate lies significantly above the background level and it is, by definition, only the largest of these events which will be counted towards the event-size distribution.

Now, we will make further order-of-magnitude calculations regarding the energy release rate of the model. Let us assume that each cell is identically 10^4 m in length, and that the evolved steady state has $\sim 1.4 \times 10^3$ cells present in the grid at any time (section 5.2).

As we have seen, reconnection in the model requires calculating the volume of a cell swept out at the Alfven speed during a single time-step and determining the energy stored within the magnetic field of that volume. This energy is assumed to be available for reconnection. This is the method we will use here in our estimate. Figure 5.5 illustrates the volume we are considering within the cell. Where $\xi_{\rm mag}$ is the magnetic energy density, the average energy release within a typical cell is given by :

$$\begin{aligned}
\dot{E} &\approx -\overline{C_{\rm A}}\, A_{\rm grid}\, \xi_{\rm mag} \\
&\approx -\overline{C_{\rm A}}\, A_{\rm grid}\, \frac{\overline{|B|}^2}{2\mu_0} \\
&\approx -345 \times 10^6 \times \frac{(5 \times 10^{-3})^2}{2 \times 1.257 \times 10^{-6}} \\
&\approx -3.43 \times 10^9 \text{ J s}^{-1}
\end{aligned}$$

We are considering a typical run where there are $\sim 1.4 \times 10^3$ cells present in the steady state (section 5.2), thus the total background level of energy release :

$$\begin{aligned}
\dot{E}_{\rm background} &\approx 1.4 \times 10^3 \times 3.43 \times 10^9 \text{ J s}^{-1} \\
&\approx 4.80 \times 10^{12} \text{ J s}^{-1}
\end{aligned}$$

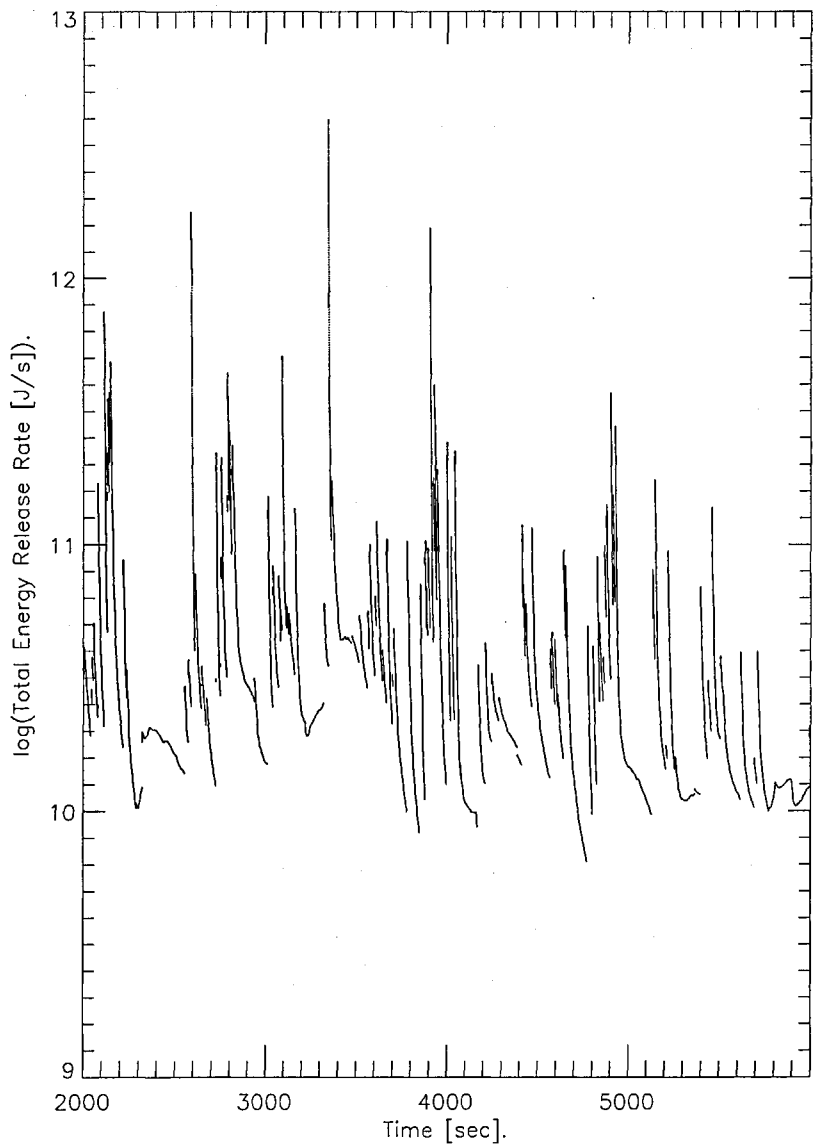

Figure 5.2: Total magnetic reconnection energy release time-series for whole grid. (2×10^6 time-steps (4000 seconds)).

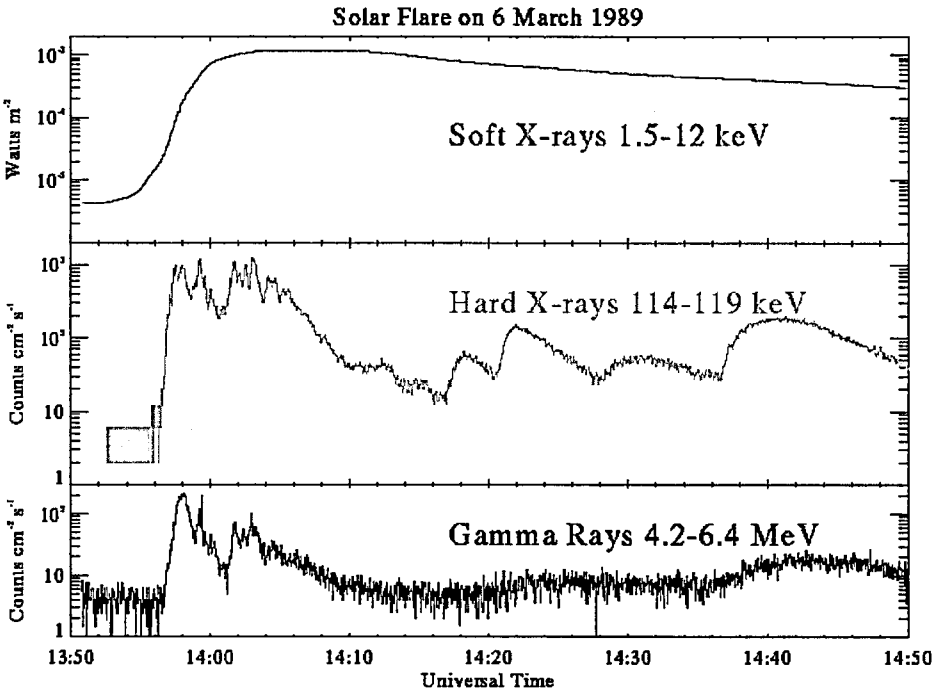

Figure 5.3: Solar X-ray flux measured by SMM.

$$\approx \ 10^{12.68} \text{ J s}^{-1}$$

Now, figure 5.2 shows a background level of $\approx 10^{10.0}$ J s^{-1}, which is much smaller than our derived value. Our derivation however rests on assuming a constant level of energy release per cell. We saw earlier however that for any given reconnection event the energy release rate decays approximately as per :

$$|\dot{E}| \ \propto \ \frac{1}{(1+\frac{t}{\tau})^3}$$

Figure 5.6 shows a pictorial representation of our problem here. Area ABCD (shaded region) represents the actual integrated energy flux of an event, whereas area ABCE represents the integrated flux assumed by our calculation. Area ABCD divided by Δt gives the true mean energy flux. Given the decay profiles which we see in figures 5.4 and 5.2 we can appreciate that figure 5.6 considerably understates the problem. Equation 5.7 indicates that $|\dot{E}|$ falls as $\frac{1}{(1+\frac{t}{\tau})^3}$ and we have already determined that $\tau_B|_{B_0=50\text{ G}} = 29$ s. The largest events in the grid will have flux density values larger than 50 G and will therefore have shorter half-lives, thus we expect $|\dot{E}|$ will decay on a timescale of

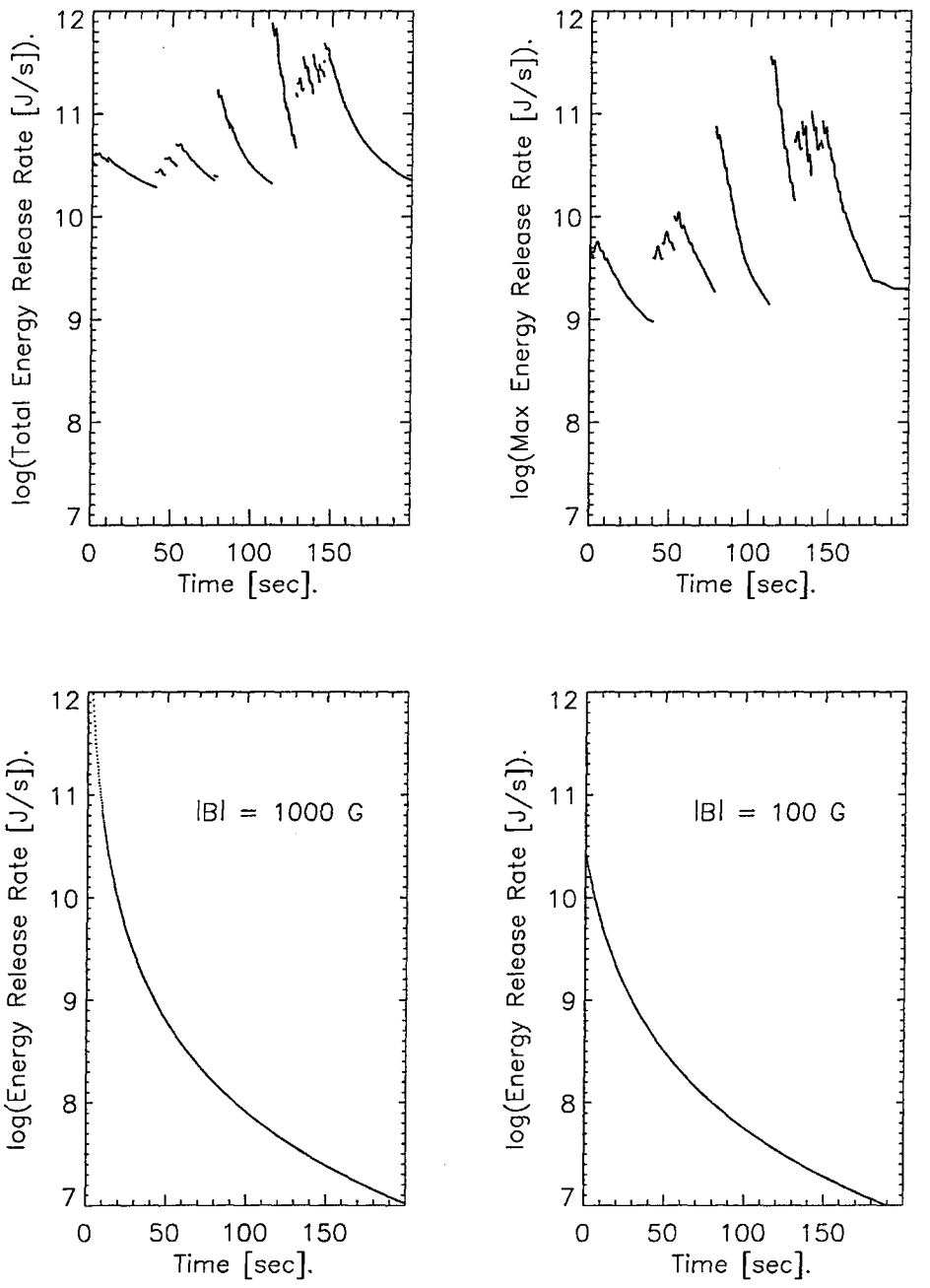

Figure 5.4: Comparisons of energy release rate profiles. Top-left: total energy release for typical conditions, first 200 s only of run. Top-right: energy release of largest event in grid, for typical conditions, first 200 s only of run. Lower-left: calculated approximate decay of energy release rate for a cell of length 10^4 m, density 1.7×10^{-4} kg m^{-3} and initial flux density, $B_0 = 10^3$ G. Lower-right: calculated approximate decay of energy release rate for a cell of length 10^4 m, density 1.7×10^{-4} kg m^{-3} and initial flux density, $B_0 = 10^2$ G.

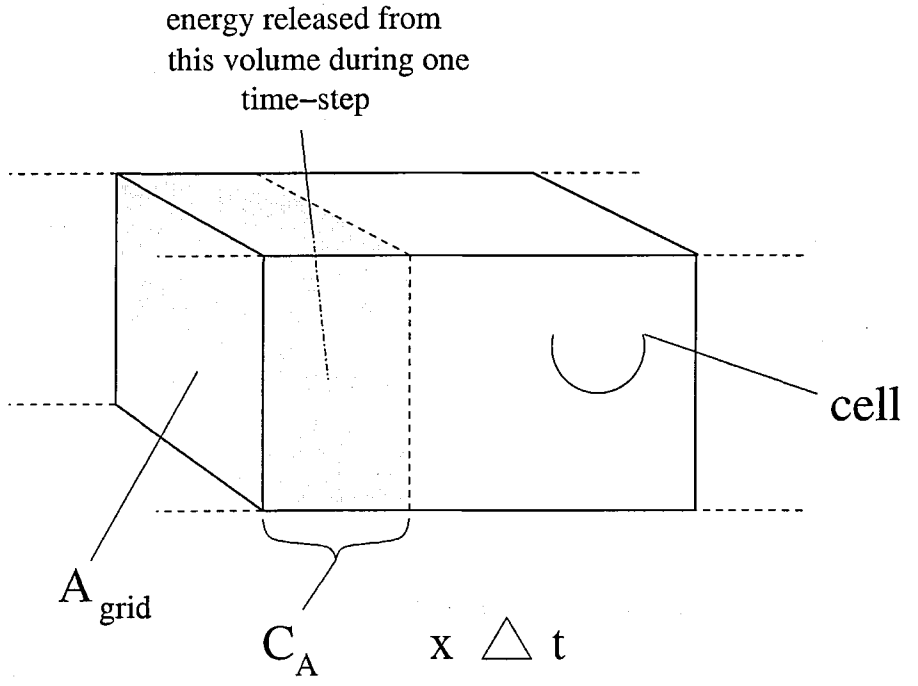

Figure 5.5: Schematic of approach to calculating magnetic energy release rate.

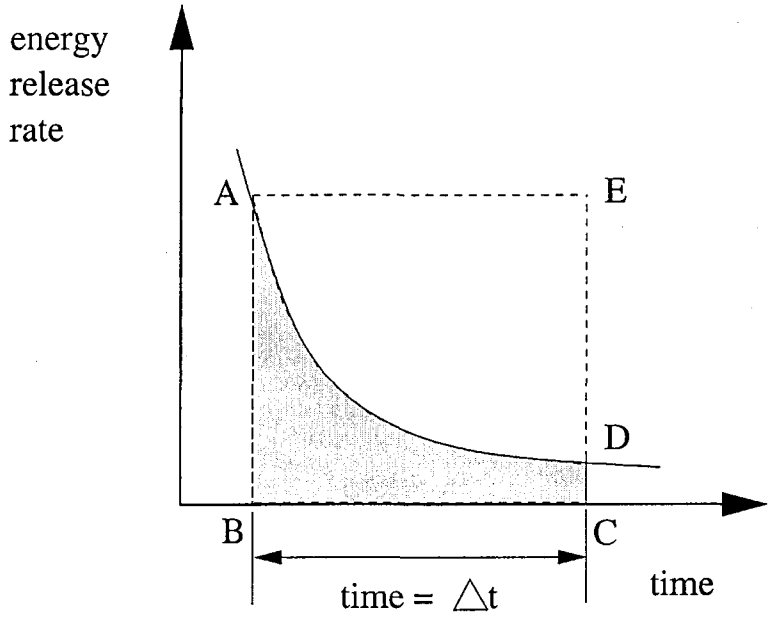

Figure 5.6: Representation of the difficulty of assuming constant energy release rate when calculating background flux.

seconds.

Therefore in this case assumption of constant $|\dot{E}|$ will give a greatly over-estimated value of the typical energy release rate for a single cell, and hence the whole grid.

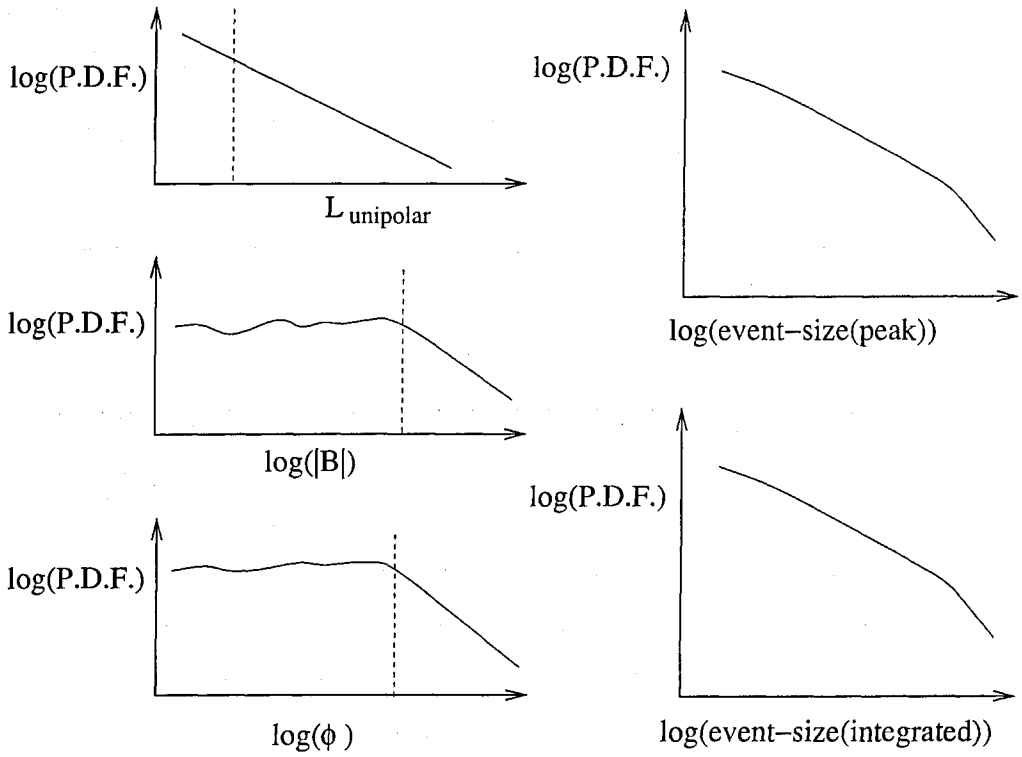

Figure 5.7: Schematic of results distributions. L_{unipolar}, B, ϕ, event-sizes counted by peak and integrated energy release. Vertical dotted lines represent initial mean values.

5.3 A Comment upon the Robustness of B, ϕ, L_{unipolar} and Event-size Distribution Profiles.

Throughout the examination of runs utilising a variety of variations of initial conditions and parameters, we have seen that the recurring form of these distributions are as shown schematically in figure 5.7. The only exceptions are the event-size distributions for the run using a random multiplier on the energy release rate of $0.9 < \zeta < 1.1$. These two distributions are S-shaped. The weight of evidence suggests nevertheless that in the face of the numerous variations in the initial conditions which we have explored, the underlying structure of the model produces these distributions : power-law in B, ϕ and event-sizes, exponential in unipolar region size.

5.4 Variation of $|B|$ with the Solar Cycle.

We mentioned in the Introduction that Schrijver & Harvey (1989) produced distributions of flux density for six different points in the Solar cycle with maximum around the year 1980. These are shown again in figure 5.8. The x-axis represents magnetic field density in Gauss. We can see that

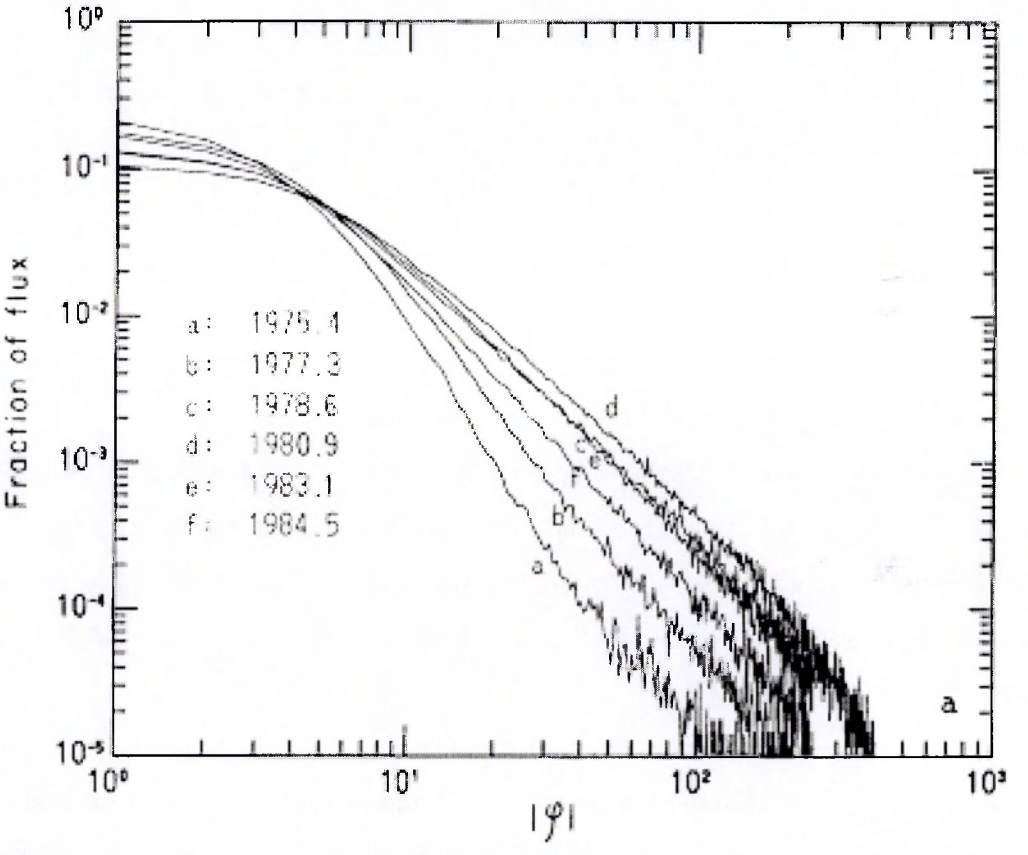

Figure 5.8: P.D.F. of $|B|$ (despite the use of ϕ in the figure) at different times in the Solar cycle. Bin-size = 1 G. Time interval 'd' represents Solar maximum. (Schrijver & Harvey 1989).

the distributions become decreased in steepness approaching Solar maximum and steeper afterwards. This is possibly caused by the increased flux emergence during Solar maximum bringing flux to the photosphere at a higher rate than usual. Thus by varying κ and $t_{\mathrm{em/sub}}$ we might expect our model to produce data showing this same pattern.

Referring back to figure 4.20 in section 4.2.7, the first plot has a gradient of -2.8 in the typical initial conditions. The second plot shows us that raising the rate of emergence and submergence by increasing the proportion of cells undergoing these processes, κ, from 0.1 to 0.2 has the effect of increasing the gradient to -3.7. The flux distribution has broken down in the third plot, where $\kappa = 0.4$. In the fourth plot we have increased the emergence/submergence activity by reducing the replacement time-scale, $t_{\mathrm{em/sub}}$, to 500 s from 1000 s. The gradient of the flux distribution has broken down. In the fifth plot we have reduced the emergence/submergence activity by increasing $t_{\mathrm{em/sub}}$ to 2000 s from 1000 s. This has also increased the gradient, to -3.1. Thus, our flux density data on changing the emergence/submergence rate is limited to increasing κ from 0.1 to 0.2 (second plot, increasing emergence/submergence rate) and increasing $t_{\mathrm{em/sub}}$ from 1000 s to 2000 s (fifth plot, decreasing emergence/submergence rate). The second plot is contrary to our expectation that increasing the level of flux emergence/submergence reduces the gradient.

We can supplement this data with figure 4.21. The third and fourth plots show successively lower rates of flux emergence/submergence and increasing gradients, in agreement qualitatively with figure 5.8. We must however qualify this evidence : firstly these plots do not show smooth distributions, and secondly there are only four or five bins within the region of the plot which is of interest (region above mean initial flux density).

Thus, we can see that it is difficult to produce a useful distribution of flux density by varying κ or $t_{\mathrm{em/sub}}$. The model emerges flux with a uniform spatial distribution each time-step, since each emerging cell receives the same dose of flux. The flux density emerged therefore depends inversely upon the length of each cell. Increased emergence will result in increased reconnection, but it is unclear given the data, what effect reconnection will have upon the flux density distribution. Simply increasing κ or decreasing $t_{\mathrm{em/sub}}$ will not represent the increase of flux emergence moving towards Solar maximum if it is the case that Solar flux emergence occurs with a power-law, or other, distribution. Our model would need to emulate this distribution in order to test if increased emergence directly results in the model in a flattening of the flux density distribution gradient (and therefore gives confirmation that the model is a useful representation of the relevant Solar processes).

Looking generally at the shape of the curves of figure 5.8 we can see a likeness with the general shapes of the distributions of flux density given in figure 4.21 and other figures showing distributions

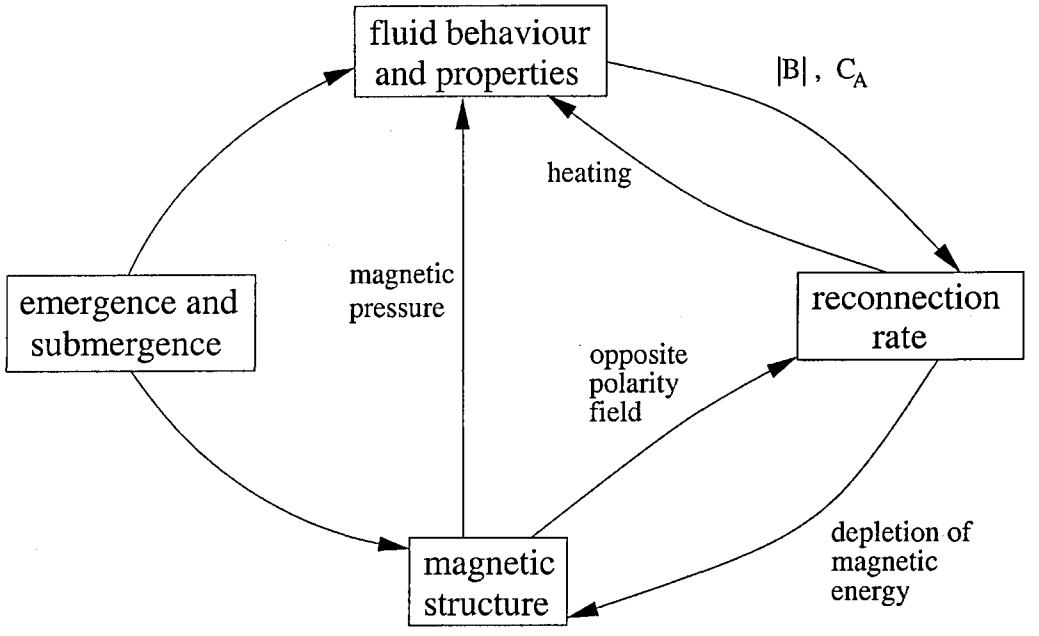

Figure 5.9: Schematic of self-interaction of model.

of flux density throughout the thesis. We mean that these distributions, observed and produced by our model, have two regimes : a lower non-power-law region and an upper steeper power-law or power-law-like region. We recall our schematic figure 5.7 illustrating this profile.

Schrijver & Harvey (1989) used synoptic magnetic field maps for the period 1975 to 1984 with resolution of 1° in longitude and 1/90 in sine-latitude. These maps were produced by smoothing 1″-resolution daily magnetograms in order to reduce noise. The data used by Schrijver & Harvey (1989) was obtained by discrete sampling, although of smoothed data. We would therefore expect the Isliker effect to be present and contribute at least partly towards the roll-over at the low end. Also, as discussed in section 3.4.6, our model-generated distributions of flux density are subject to the Isliker effect.

Thus, our conclusion here is that there is some limited evidence for agreement between the model and the observed changes in the distributions of $|B|$ with the Solar cycle.

5.5 How do the Power-law-like Distributions of Flux Density and Event-size Arise?

We will discuss the magnetic flux density and event-sizes together. The reason for this is that the spatial distribution of flux and the reconnection process feed into each other. Let's discuss in qualitative terms the relationships between the different processes in the model. Figure 5.9 summarises

schematically and in simple terms how the different aspects of the model interact qualitatively. The model produces power-law-like flux density distributions in the upper regions of the plots and arguably power-law-like event-size distributions over the majority of the x-range of plots. The figure illustrates that the fact of whether or not reconnection occurs, and (if it does occur) the rate of energy release, are both functions of the distribution of flux and its polarity. Reconnection will only occur where there is a meeting of anti-parallel flux at a boundary between cells. The reconnection affects the magnetic fields by the depletion of magnetic energy which results from reconnection. The magnetic field distribution affects the fluid behaviour by the presence of pressure resulting from the magnetic field. This magnetic pressure does not follow the adiabatic identity :

$$P_{\rm th}\, V^{\gamma} \;=\; \text{constant}$$

where $V \propto L$.

Instead,

$$P_{\rm mag} \propto B^2$$

and

$$|B| \propto \frac{1}{L}$$

therefore

$$P_{\rm mag} \propto \frac{1}{L^2}$$

We know that reconnection feeds directly into the thermodynamic properties of the cells by heating the material. We also know that the fluid motions of the cells affect the reconnection rate : the rate of reconnection is dependent upon B^2 and $C_{\rm A}$ (see section 5.2) and therefore upon B and ρ which both depend inversely upon L. The emergence and submergence processes affect the magnetic field density distributions and polarities, and the thermodynamic properties of the cells by creating and eliminating material which has magnetic field attached to it. In the extreme case, submergence will remove a cell and allow two cells to have a new common boundary at which reconnection will occur if the field polarities are antiparallel. Similarly, when emergence occurs to the point where the length of a cell, $L_{\rm i}$ is such that $L_{\rm i} > 1.5\ L_{\rm init}$, we have seen that the cell will be divided into two equal halves. The magnetic polarity of one of the two new cells will be random, and therefore reconnection will start if the polarity is anti-parallel. As we have already explained, this is equivalent to a new cell coming into being at the boundary between two pre-existing cells.

Now, given that there are no power-law distributions expressly input into the model we must conclude that scale free behaviour is being generated by the self-interaction of the model. Given the dependencies of event-size upon B : $|\dot{E}_{\text{peak}}| \propto |B|^3$ and $E_{\text{int}} \propto L\, B^2$, the power-law distributions in event-size may be caused by the power-law-like distributions in $|B|$, although these distributions are rarely smooth power-laws and only cover a small part of the upper x-range.

5.6 Can Features of Flaring Events, Sufficient Dynamic Range and Appropriate Power-law Indexes be Obtained with this Model?

In section 5.2 we compared the time-series of the energy release from the model with GOES X-ray photon flux time-series and find similarity in some features. Both have a stationary background level with many large events superimposed. These events exhibit an initial very rapid climb followed by a slower, though still rapid decay. We showed using figure 5.4 that the events generated by the model decay as :

$$|\dot{E}| \propto \frac{1}{(1+\frac{t}{\tau})^3}$$

and that it is plausible that the Solar flare events whose data were shown in table 1.2 also undergo this decay profile. Both have dynamic ranges of approximately two orders of magnitude, however Solar flares have so far been observed ranging in total integrated energy flux over eight orders of magnitude ($10^{17} \leftrightarrow 10^{25}$ J). Events generated by our model have been much smaller ($10^4 \leftrightarrow 10^{11}$ J) although the dynamic range generated was nevertheless large : approximately seven orders of magnitude. We could consider the model-generated flaring events to be equivalent to the unobservably small events which merge together to form the background X-ray flux. We must remember that the smallest events observed are limited by the time resolution of observing instruments. If the time interval between events is comparable or less than the time resolution of the instrument then these events will not be resolvable but will merge with the background. Also, if the time interval between events is comparable to the duration of the events then they won't be distinguishable from each other irrespective of spatial resolution but will appear to merge together to form a single event (i.e. see figure 5.10). Thus, when new instruments with higher time resolution are built we may find that these power-law distributions of Solar flare event-sizes continue down to smaller sizes and the dynamic range of the power-law is therefore greater than the observed eight orders of magnitude.

Regarding observed power-law indexes of flare size counted by peak energy release rate and integrated energy, SMM and ICE (table 1.2) found values for these in the range $-1.53 \leftrightarrow -1.92$. By

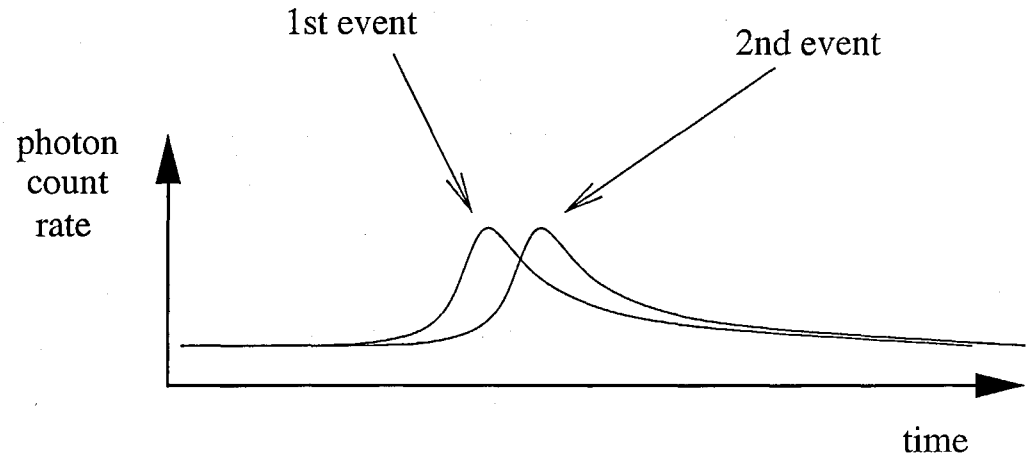

Figure 5.10: Schematic of flaring event photon count (energy release) time series where time interval is comparable to event duration.

	Peak energy release rate [J s^{-1}]	Integrated energy released [J]
Dynamic range	$10^5 \leftrightarrow 10^{12}$	$10^4 \leftrightarrow 10^{11}$
Gradient	-0.88 $\leftrightarrow$ -1.09	-0.83 $\leftrightarrow$ -0.91

Table 5.1: Power-law indexes in peak and integrated energy release.

contrast, our model produced values in the ranges given in table 5.1.

There may be many reasons for the relative flattening of our fit-lines compared with actual observations. The fact that our model has a finite cell size means that it cannot reproduce the large number of infinitesimal reconnections which are undoubtedly occurring in the Solar atmosphere. There may be a strong selection effect based upon the fact that by definition the model only counts the largest event at any one time, and therefore only large events will be counted in the distributions.

It is interesting that, as explained in section 3.6.2, we only find one very large event occuring at any one time, and this event is sufficiently large that it dominates the time-series for total energy release of the whole grid. It is accepted that there will occur in the Solar atmosphere only a single large event at any one time, as opposed for example to several comparably large simultaneous events.

The fact that these event-size gradients given in table 5.1 are all close to unity is some cause for concern. We must ask ourselves if there is a process or statistical feature within the model which naturally causes this. Given the complexity of the model it is difficult to see how this might come about.

We have found that the general features of observed flares are reproduced, i.e. power-law distri-

bution of event-sizes, qualitatively similar time-series profiles and large dynamic ranges. We have found that the profile and indexes of our distributions, in particular those of event-size are very robust, varying little regardless of the particular conditions of the run in question (see table 4.7). Our event-size results diverge from observed data in that the power-law indexes of the model-generated data are significantly less than those observed. The range of event-sizes examined by our model are smaller by $\sim 10^{14}$ however, the observed distributions are power-law which means they are scale free with no typical size, therefore we take the view that our model may effectively be looking at a part of the x-range below that of the observed flare-sizes.

5.7 How do the Results Depend Upon the Details of the Reconnection Mechanism?

5.7.1 Introduction.

In the exploration of this model we presupposed that the results are not dependent upon either the detailed spatial structure or physics of the important processes involved in the energy release. By using discrete cells and varying the parameters integral to emergence/submergence and reconnection we have sought to investigate this supposition. By examining the results generated by runs utilising variations in initial conditions and parameters we have attempted to determine the general profiles of the distributions of our results and the effects of these variations.

We recall that MHD modelling attempts realistic simulation of reconnection yet can neither effectively tackle complex problems with many null-points or current sheets, nor is MHD able to bridge the range of length scales between the metre scale necessary for reconnection (Foukal 1990) and 10^8 m over which the largest flares occur. Our continuous model attempts to obviate this problem by not concerning itself with the detailed spatial structure nor the detailed physics.

In this section we investigate the extent to which the structure of the reconnection process determine the distributions of event-sizes.

Now, we recall from section 3.3.4 that broadly the model's reconnection mechanism is designed such that the energy release rate is :

$$\begin{aligned} \dot{E} &\propto -C_{\mathrm{A}}\,\xi_{\mathrm{mag}} \\ &\propto -\frac{|B|}{\sqrt{\mu_0\,\rho}}\,\frac{\overline{B}^2}{2\mu_0} \\ &\propto -|B|^3 \end{aligned}$$

We can neglect density, ρ, because we find that this parameter varies very little throughout a run. Thus, counting by peak energy release rate we can say that the size of events depends as follows :

$$|\dot{E}_{\text{peak}}| \propto |B|^3 \tag{5.9}$$

We recall that $\dot{E}_{\text{peak}}$ is the maximum rate of energy release during a reconnection event, and we use this value when counting the events for the production of a distribution of event-sizes. Thus, our point is that in the model : $|\dot{E}| \propto C_{\text{A}} \, |B|^2$, which represents a proportionality to the Alfven speed and to the magnetic energy density. Our variations on the basic reconnection mechanism will not alter this property of the model at the level of calculation of the energy released prior to the modifications introduced in this section. These modifications consist of additional modules 'bolted on' to the model and, as will become obvious to us, because of the nature of these modules we will find that some cause deviation, in the final calculation of energy released, from the principle of : $|\dot{E}| \propto C_{\text{A}} \, |B|^2$. Thus, some of the changes in reconnection are severe and the results are therefore surprising insofar as the manifold variations in reconnection mechanism result generally in similar distributions.

We will show event-size distributions counted by peak energy release and integrated energy for runs using the typical conditions/initial parameter values (as per the Definition of Commonly Used Terms given at the beginning of the thesis). The runs incorporating variations in reconnection mechanism will be characterised by the following particular differences :

1. Standard reconnection method.

   Use mechanism detailed in chapter 3 unadulterated.

2. Partially randomised energy release: multiplied by random factor ζ, $(0.9 < \zeta < 1.1)$.

   Each time-step the total energy released within a cell by reconnection (using the standard mechanism) with one or both of the cell's neighbours is totalled and multiplied by the realisation of a random variable uniformly distributed within the range $0.9 \leftrightarrow 1.1$.

3. Completely randomised energy release: multiplied by random factor ζ, $(0 < \zeta < 1)$.

   Same as previous method, except we have : $0 < \zeta < 1$.

4. Energy release through a reconnection interaction between two cells is only recorded when the difference in magnetic field density between the two cells exceeds a threshold value of 20 G (in

addition to the usual requirement of flux being anti-parallel) at which point the energy release is calculated using the standard mechanism)

5. Same as immediately above, threshold value of 50 G.

We have already seen that the characteristics of energy release observed in flares is power-law distributed. Thus, the question is : while ensuring that the energy release rate remains broadly proportional to $C_A\ B^2$, is it likely that varying the details of the simulated reconnection process in the model will still result in power-law distributions in our event-sizes?

5.7.2 Results.

Following the precedent established by earlier figures in this thesis we will present figures of the following :

- distributions of size of unipolar field regions.
- distributions of magnetic field density.
- distributions of magnetic flux.
- event-size distributions counted by peak energy release rate.
- event-size distributions counted by integrated energy release.

Each of these figures will allow comparison between the distributions for the five different runs.

Unipolar Field Region Sizes.

Figure 5.11 shows us that the usual exponential distributions of unipolar region size are obtained with very typical gradients around the value -0.35.

Magnetic Field Density.

Figure 5.12 shows that the distributions of $|B|$ appear very typical with power-laws for the range greater than the initial flux density and gradients in the range $-2.7 \leftrightarrow -3.1$. This range is only slightly less than one decade but apart from the fourth plot the distributions are very close to power-law.

Magnetic Flux.

The distributions of magnetic flux shown by figure 5.13 are very similar to distributions shown in figure 5.12 therefore we conclude that there is poor correlation between B and L.

Event-Sizes.

The third, fourth and fifth plots of figure 5.14 show good power-law-like distributions with very similar gradients around -1.0. This value is of course a typical value given the other peak energy release rate event-size distributions we have already seen (see table 1.2). The third and fourth plots show data over approximately six orders of magnitude whereas data on the fifth plot ranges over approximately ten orders of magnitude. The second plot has an S-shaped profile.

5.7.3 Discussion.

The similarity between each of the different plots on figures 5.11, 5.12 and 5.13 indicates that the detail of the reconnection mechanism is not important in determining the distributions of L_{unipolar}, B and ϕ. Even the gradients hardly vary, ranging between -2.7 and -3.1 for B and ranging between -2.6 and -3.1 for ϕ.

Figures 5.14 and 5.15 again show similar power-law-like profiles for the distributions, apart from the second plot in each case. The gradients are very similar again, around -1.0 for peak energy release rate and -0.90 for integrated energy release. Regarding the second plots on each figure, we see close correspondence between them. The second plots are not power-law-like yet they are very similar between the peak and integrated energy release. Let's look closer at this.

In terms of peak energy release, we found (equation 5.9) that the size of an event depends as follows :

$$|\dot{E}_{\text{peak}}| \propto |B|^3$$

Similarly, the size of an event in terms of integrated energy release depends upon the total magnetic energy within a cell. Thus :

$$\begin{aligned} E_{\text{int}} &\propto L\,\xi_B \\ &\propto L\left(\frac{B^2}{2\,\mu_0}\right) \\ &\propto L\,B^2 \end{aligned}$$

Where as usual L is cell length. Thus, we have

$$|\dot{E}_{\text{peak}}| \propto |B|^3$$

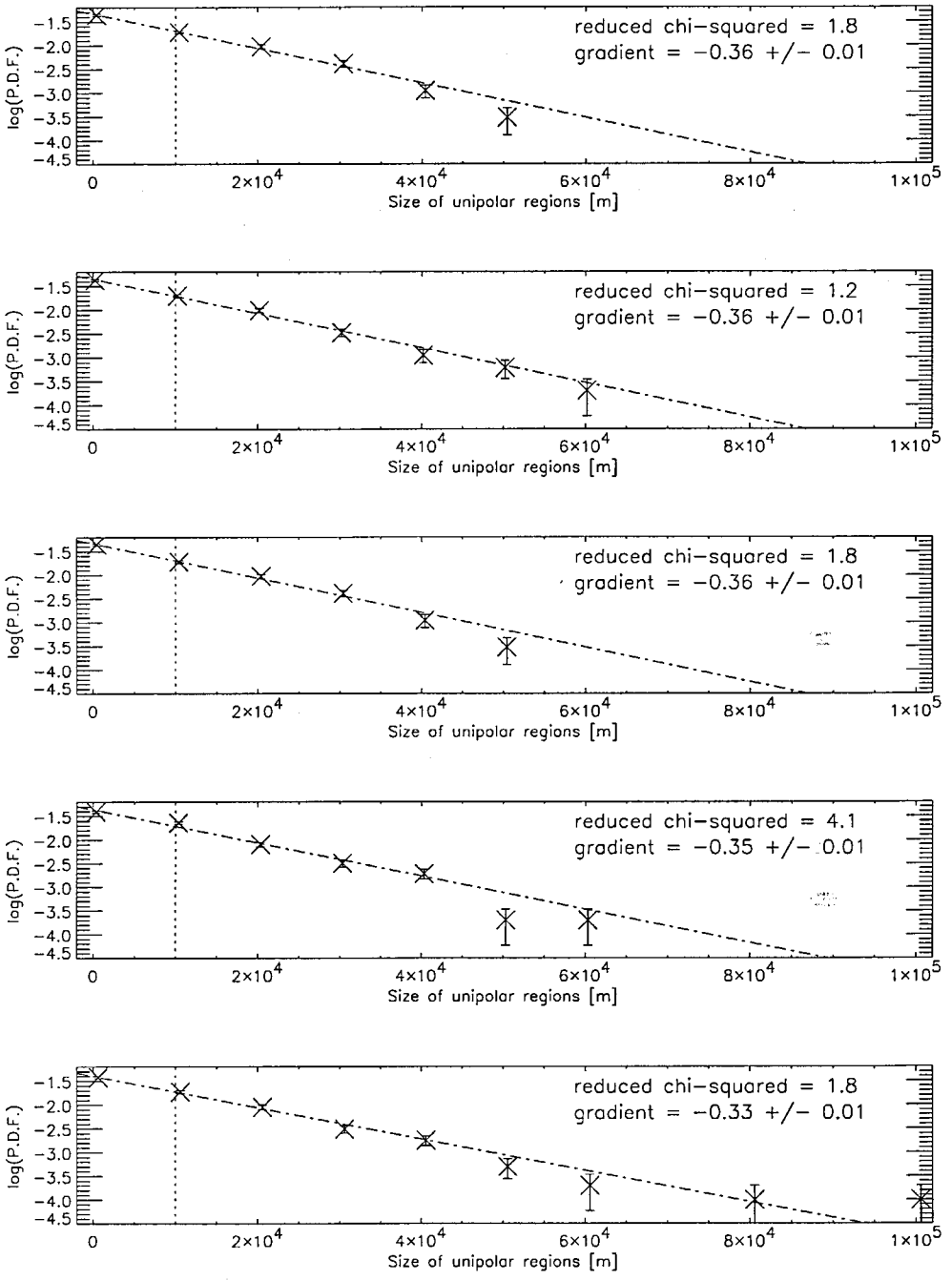

Figure 5.11: Distributions of size of regions of unipolar magnetic flux, using log-log axes; 10^3 cells; initial cell length = 10^4 m; bin-size = 10^4 m. Dotted line mark initial cell length. Top: typical conditions. Second: cell energy release multiplied by the realisation of a random variable in the range $0.9 \leftrightarrow 1.1$. Third: cell energy release multiplied by the realisation of a random variable in the range $0 \leftrightarrow 1$. Fourth: reconnection only allowed if difference in magnetic field density between adjacent cells exceeds 20 G ($|B_i - B_{i+1}| > 20$ G). Fifth: reconnection only allowed if difference in magnetic field density between adjacent cells exceeds 50 G ($|B_i - B_{i+1}| > 50$ G).

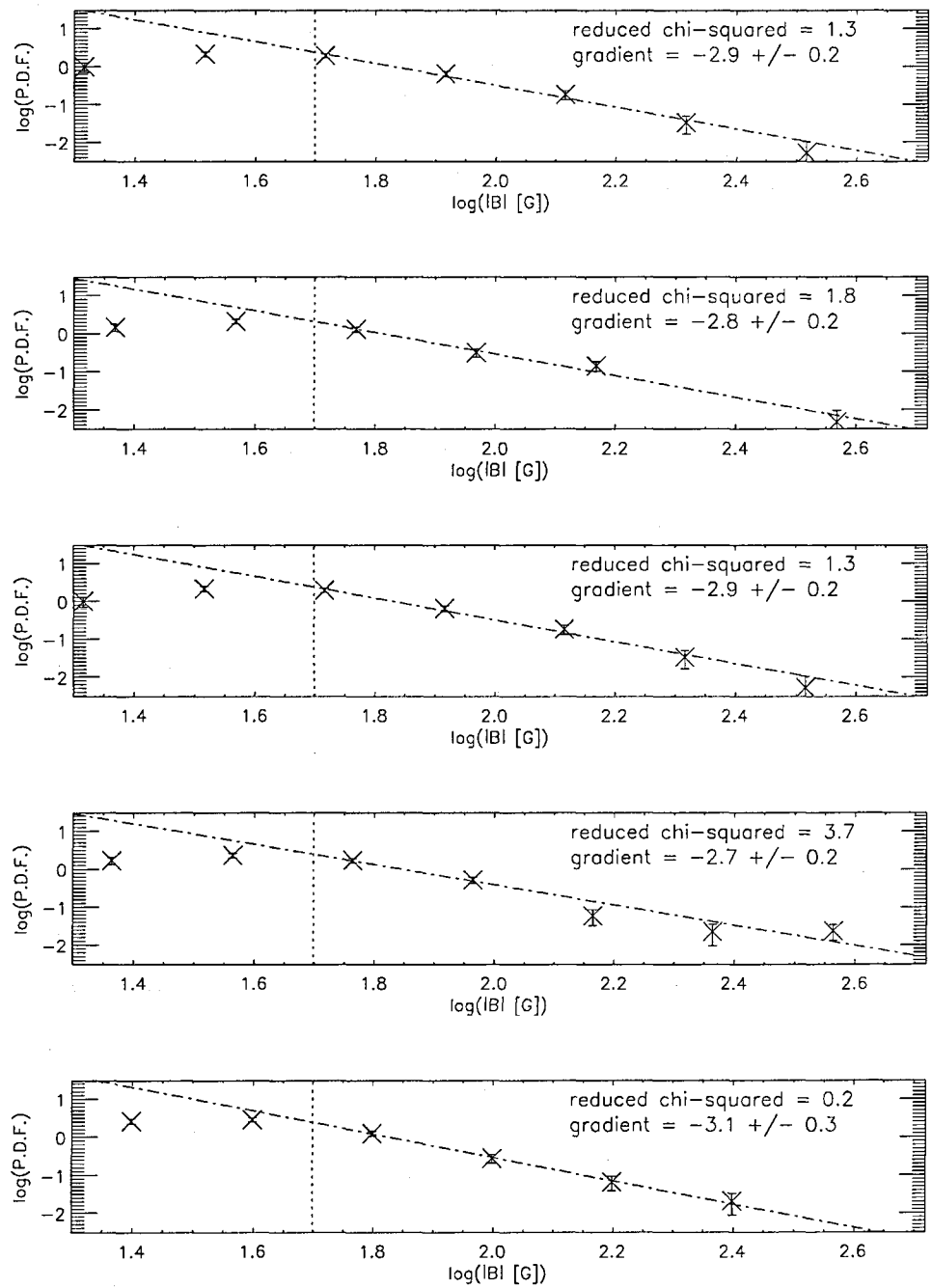

Figure 5.12: Evolved distribution of magnetic field density with initial mean absolute magnetic field density = 50 G. Bin-size = 0.2; 10^3 cells; initial cell length = 10^4 m. Dotted line marks mean initial magnetic flux density. Top: typical conditions. Second: cell energy release multiplied by the realisation of a random variable in the range $0.9 \leftrightarrow 1.1$. Third: cell energy release multiplied by the realisation of a random variable in the range $0 \leftrightarrow 1$. Fourth: reconnection only allowed if difference in magnetic field density between adjacent cells exceeds 20 G ($|B_i - B_{i+1}| > 20$ G). Fifth: reconnection only allowed if difference in magnetic field density between adjacent cells exceeds 50 G ($|B_i - B_{i+1}| > 50$ G).

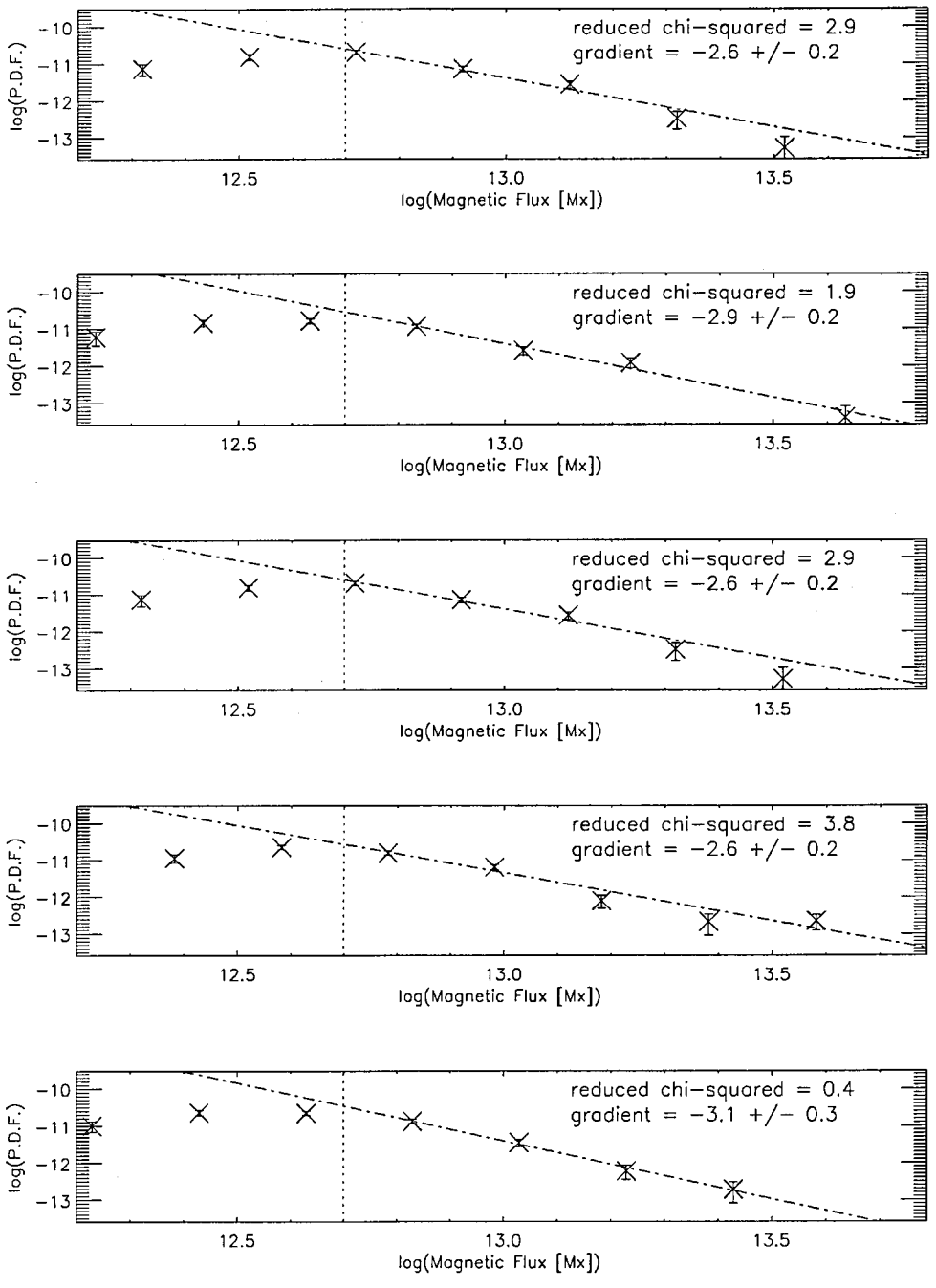

Figure 5.13: Distributions of magnetic flux with initial mean absolute magnetic field density = 50 G. Bin-size = 0.2; 10^3 cells; initial cell length = 10^4 m. Dotted line marks mean initial magnetic flux. Top: typical conditions. Second: cell energy release multiplied by the realisation of a random variable in the range $0.9 \leftrightarrow 1.1$. Third: cell energy release multiplied by the realisation of a random variable in the range $0 \leftrightarrow 1$. Fourth: reconnection only allowed if difference in magnetic field density between adjacent cells exceeds 20 G ($|B_i - B_{i+1}| > 20$ G). Fifth: reconnection only allowed if difference in magnetic field density between adjacent cells exceeds 50 G ($|B_i - B_{i+1}| > 50$ G).

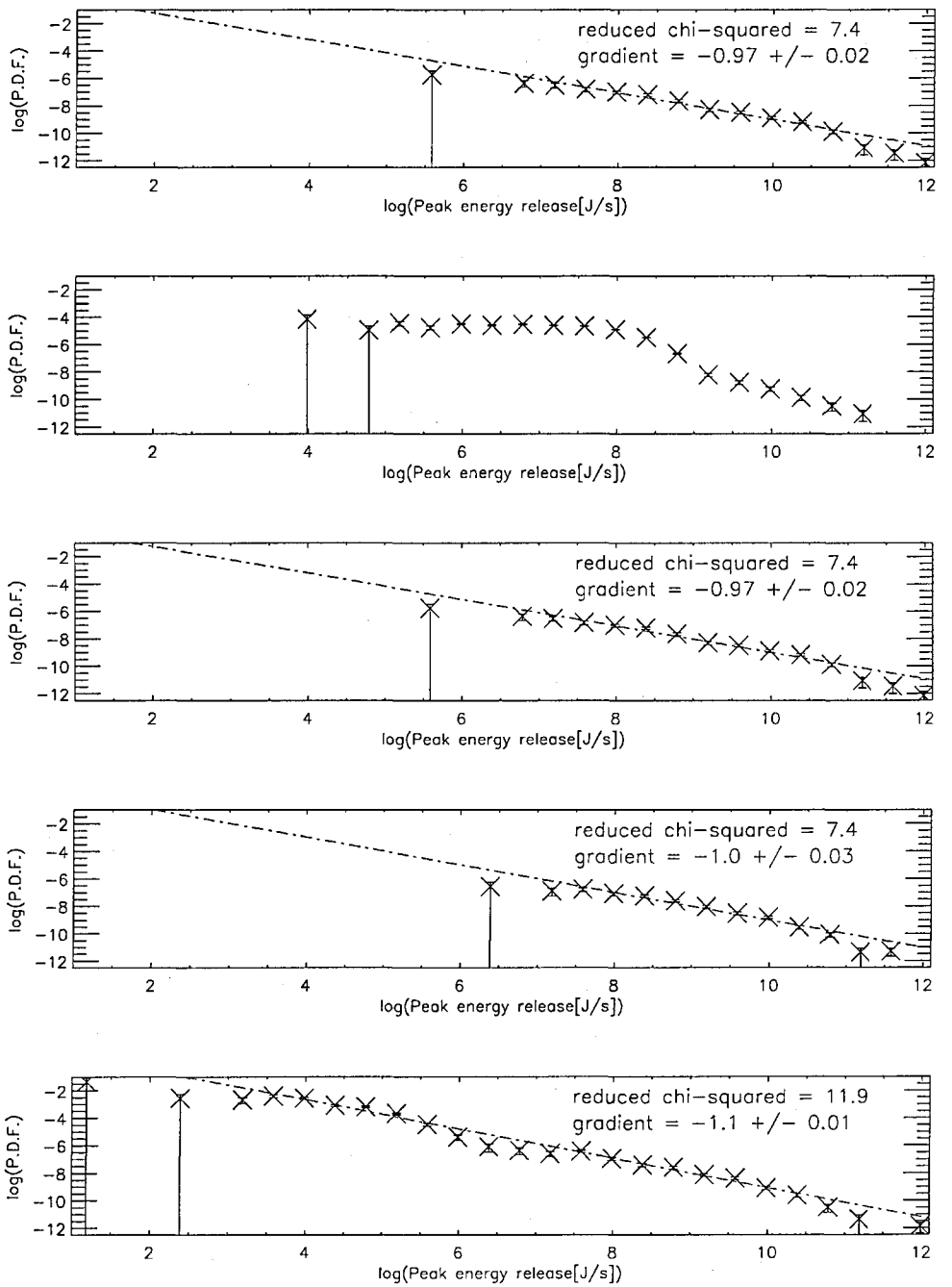

Figure 5.14: Distributions of sizes of events, counted by peak energy release rate. Initial cell length = 10^4 m; log-log axes; bin-size = 0.4; 10^3 cells. Top: typical conditions. Second: cell energy release multiplied by the realisation of a random variable in the range $0.9 \leftrightarrow 1.1$. Third: cell energy release multiplied by the realisation of a random variable in the range $0 \leftrightarrow 1$. Fourth: reconnection only allowed if difference in magnetic field density between adjacent cells exceeds 20 G ($|B_i - B_{i+1}| > 20$ G). Fifth: reconnection only allowed if difference in magnetic field density between adjacent cells exceeds 50 G ($|B_i - B_{i+1}| > 50$ G).

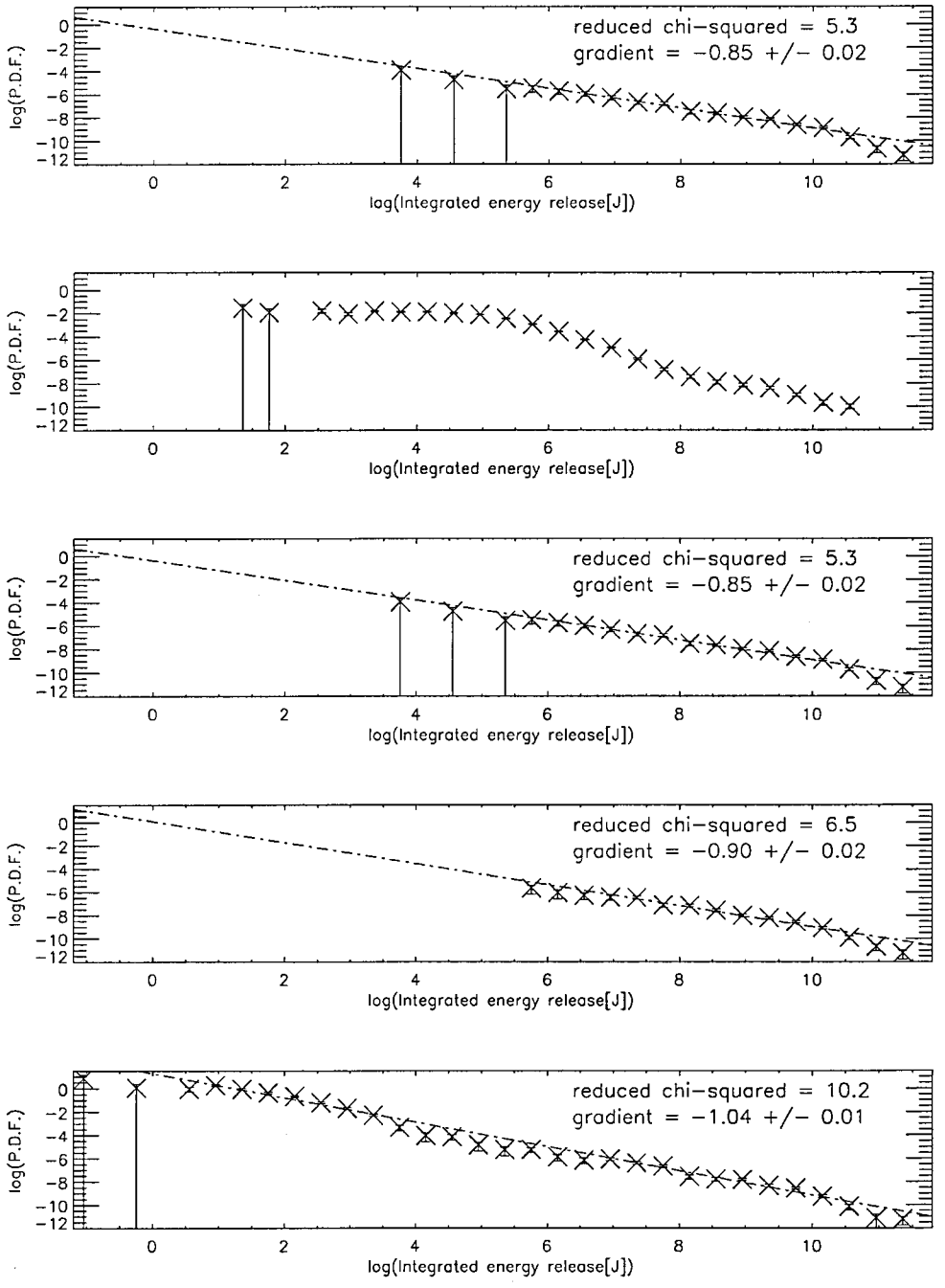

Figure 5.15: Distributions of sizes of events, counted by integrated energy release. Initial cell length = 10^4 m; log-log axes; bin-size = 0.4; 10^3 cells. Top: typical conditions. Second: cell energy release multiplied by the realisation of a random variable in the range $0.9 \leftrightarrow 1.1$. Third: cell energy release multiplied by the realisation of a random variable in the range $0 \leftrightarrow 1$. Fourth: reconnection only allowed if difference in magnetic field density between adjacent cells exceeds 20 G ($|B_i - B_{i+1}| > 20$ G). Fifth: reconnection only allowed if difference in magnetic field density between adjacent cells exceeds 50 G ($|B_i - B_{i+1}| > 50$ G).

and :

$$E_{\rm int} \propto B^2$$

Thus, we see that both have a component of B^2 and we also know that B and L are poorly correlated, therefore L is not a function of B. We expect therefore a strong correlation between $\dot{E}_{\rm peak}$ and $E_{\rm int}$ and it may be in this that we have found the reason for the close correspondence between the two distributions for each run.

It is interesting that the run which incorporates a B threshold of 50 G (fifth plot on each figure) shows a dynamic range of ten orders of magnitude. It seems very strange that this particular dynamic range is so much greater than the others. The events recorded for these distributions are by definition the largest events in the grid, and we know that there is a dependency upon B^2, therefore we expect $|B|$ to be large for these events. The neighbouring cells with which these cells are reconnecting will by definition have magnetic polarity opposite to the cells associated with the events. Therefore we do not expect that this threshold requirement would make very much difference in terms of field densities of the cells associated with the events recorded. We find however that a great many more very small events enter into the data, presumably substituted for other larger events which featured in the other four distributions on each of these two figures.

It must be emphasised that aside from event-size distributions produced by the run incorporating partially randomised energy release, the runs using: a random multiplier of $0 < \zeta < 1$, threshold of 20 G and 50 G produce power-law-like distributions with little variation between them. This tells us that the detail of the reconnection mechanism may not actually be very important and the determining feature of reconnection is that energy release is proportional to $C_{\rm A}\ B^2$.

We should ask why we use $|\dot{E}| \propto C_{\rm A}|B|^2$ as the basis of our energy release rate and not another formula? Petscheck (1964) suggested a mechanism where magnetic fields may reconnect at a rate approaching the Alfven speed. Certainly the Petschek Model (Petscheck 1964) involves an incompressible inflow of magnetic flux into an 'X'-point current-sheet region, as we saw in the Introduction. Considering the rate of flow of this flux into the 'X'-point diffusion region, the natural rate of propagation of magnetic waves along a magnetic field is the Alfven speed and we have already noted in section 3.3.4 that Dere (1996) find that the Alfven speed more appropriately accounts for the rate of reconnection than the timescales of resistive diffusion or tearing-mode reconnection. Certainly, the Alfven speed is considered to provide a natural timescale for the reorganisation of magnetic field within a magnetic structure of a given size (Roberts 1999) and we consider reconnection to be a process causing change to the topology of a field (Dere 1996). Also, it appears from Dere (1996) that the Alfven speed is considered the maximum limit upon the rate of propagation of reconnection

and Parker (1973) suggested that 'reconnection rates are universally of the order of 0.1 C_A'. Thus, we consider it sensible in the model that flux is being consumed by the reconnection process at the Alfven speed, and we therefore quantify the rate at which magnetic flux is destroyed as $C_A\ |B|\ W$ (equation 5.2) and the rate at which magnetic energy is destroyed : $A_{grid}\ C_A\ \xi_{mag}$. We find no grounds in the literature for any other basis expressing the rate of energy release.

5.8 What is the Relevance of Self-Organised Criticality?

In the Introduction we described the phenomenon of SOC. SOC is easier to describe than to define and there are many different interpretations of its fundamental features, therefore in this section we will only concern ourselves with the specific definition we give here. SOC has several components :

1. Stochastic excitation of a parameter within the system.
2. We can establish a gradient at each point in the system in relation to this parameter and there exists a critical threshold which the local gradient will eventually exceed somewhere in the model.
3. When the gradient reaches this threshold there will be a re-distribution, or relaxation of the system triggered such that the new gradients exceed the threshold at no point in the system.

There is no doubt that some researchers familiar with SOC would dispute these points, however we are not concerned here with precise abstract definitions but rather we must consider these as providing a working definition for our purposes.

Now, both the discrete and continuous models have produced many power-law and power-law-like distributions. We recall that regarding SOC, when a system has been excited to the point where it is everywhere in a minimally stable state any further excitation will produce relaxation events in accordance with point (3), with no intrinsic size scale. This scale-invariance will cause the relaxation events to have a power-law distribution. Thus, we may speculate that one or both of our models are fundamentally SOC in nature, or contain elements of SOC.

The classic example of such a system is the sand-pile model. Our model cannot be simply reduced to a sand-pile and is far more complex, yet it may be possible that it contains the relevant elements of the sand-pile model. The continuous model produces event-size distributions which are power-law except for edge effects. Therefore we must examine the question of whether these distributions can be attributed to any underlying SOC-like nature of our model, and to this end we will now examine these three points in relation to the model.

5.8.1 Stochastic Excitation.

We can view the emergence of magnetic flux as being a stochastic driving of the sustem. We recall that the flux emergence/submergence mechanism of the model varies the rate of emergence such that the total magnetic flux within the grid is maintained at a constant level. Flux is destroyed by magnetic reconnection. The sites of the emergence are random, and change frequently. Submergence causes cells to disappear from the model and cells will appear at cell boundaries as a result of emergence. These emerged cells have random magnetic polarity. Thus, there is a stochastic charging action upon the magnitude and polarity of the magnetic flux.

5.8.2 Gradient Threshold.

The model has no equivalent of the sand-pile's minimally stable state, where a small increase in a given parameter causes breach of the threshold and commencement of an event. Rather, we have a situation where the existence of anti-parallel flux at a cell boundary will allow an event to begin or continue. Thus, the threshold consists of the sign of the product of the two fluxes at a boundary. If $B_{\rm i}\ B_{\rm i+1} < 0$ then reconnection is allowed.

This is different however from the notion of threshold in the sand-pile model where the threshold prevents or allows the event, or 'avalanche', to continue and to propagate further through the system. We know from equation 5.9 that :

$$|\dot{E}_{\rm peak}| \propto |B|^3$$

and that :

$$E_{\rm int} \propto L\ B^2$$

Thus, in the case of integrated energy release, there is also a dependency upon L, the size of the cell. The size is a function of the initial length plus effects of emergence and submergence. In neither case is the size of the event related to the number of cells through which the event propagates. Whereas in the sand-pile model the size of an event is literally the number of cells through which the event/avalanche propagates, in our model there can be no propagation of an event beyond the immediate cell.

We carried out runs where the reconnection mechanism was only triggered if :
$|B_{\rm i} - B_{\rm i+1}| > 20$ G or 50 G, however these thresholds do not act as a gate upon the propagation of the event to another cell.

Thus even though there are runs which explicitly include a threshold it doesn't seem that there is triggering of events by the exceeding of a threshold in the sense necessary for SOC.

5.8.3 Re-distribution.

Re-distribution means a relaxation, in some sense, of the system (the grid in the model) such that parameter values in some cells are reduced and increased in others. This must be carried out such that (1) there is conservation of the total quantity of this parameter, and (2) there is reduction of the local gradient in this parameter-field.

The action of reconnection destroys magnetic flux, which is emerged the same time-step into one of the emerging-flux cells in the grid. Thus, the magnetic flux is made available again for reconnection, however there is no prohibition against flux emerging into a cell which already has a high flux density and thus increasing it further. In the sand-pile model the redistribution causes local increases in gradient at the periphery of a propagating event. This local gradient, if greater than the critical gradient, will produce more redistribution, and so on. Thus, the re-distribution is directly responsible for the continuing propagation of an event. We can agree that there is redistribution of some form caused by reconnection, however this will not obviously lead to further reconnection.

Conclusions.

In relation to the specific definition given above we have found that there is little evidence for SOC characteristics in the model, and if they exist they would be subtle. Any SOC effects would be very indirect and difficult to express analytically.

5.9 Future Work.

We have found that the continuous model is capable of producing power-law-like distributions over limited x-ranges, but not smooth power-law distributions. Nevertheless we have seen that in regard of the wide range of initial conditions and parameter values selected for running the model, it has robustly produced similar power-law-like distributions. To further test the robustness of the distributions we could perform further runs in the following manner. We might perform a number of runs, of the order of fifty perhaps, and for each we would randomly select each parameter value, although we would stipulate a reasonable range for each parameter. Thus, we can test the robustness of the power-law event-size distributions (simulated flare-size distributions) while ensuring that there is equal spacing of runs within the parameter space of the model with little clumping. These parameters would be : initial cell length, mean initial magnetic field density, standard deviation of

initial field density, initial number density, heating by energy released by reconnection, minimum cell length, maximum cell length, initial mean temperature, standard deviation of initial temperature, noise and field density threshold for reconnection. The production of similar distributions by this method would further support the suggestion that the details of the physics and/or specification of precise initial conditions are not critical for the production of self-similar flare-sizes.

Where distributions produced by the model are not power-law but we expect power-law distributions in observed data, this must mean one or more of the following (1) there is unknown or incompletely understood important physics, (2) power-law energy release of the Solar atmosphere is dependent on and driven by bulk flows emerging from below the photosphere, which are themselves in a power-law distribution, or (3) One or more features or mechanisms of the model do not match the physical reality as we understand it.

Regarding point (1), SOC behaviour causes power laws, and it may be that some type of SOC behaviour is responsible for causing the power-law event-size distributions. Certainly some workers in the field think so.

Regarding point (2), our model is designed to explore the self-interaction of the grid and the data produced arises solely from this self-interaction. Therefore, it may be that the solar convection drives the flare distributions, and by definition this cannot be explored by the model.

Regarding point (3), perhaps the dimensionality of the model is fatal to the generation of data in power-law form with correct indexes. It may be that non-local communication or the 3-D nature of the Solar atmosphere are essential features of any accurate model. Some researchers argue that secondary flaring events may be triggered remotely by fast particle beams emitted from the footpoints of primary flaring events. Litvinenko & Somov (1991) have determined that fast particle generation occurs as a result of magnetic energy dissipation by magnetic reconnection, and Khodachenko, Haerendel & Rieger (2000) have studied the reaction of a flux tube containing photospheric plasma when injected with a beam of fast non-thermal electrons and find that there is complex behaviour in the plasma-magnetic field system, which gradually returns to an equilibrium state. Triggering/communication processes like this may make possible some form of SOC in the Solar atmosphere and/or explain the very fast and sudden events observed such as the Bastille Day flare (a class M3 flare on 14 July 1998). In such flares there occurs a co-ordinated energy release over a large spatial scale, and communication occurs at speeds much higher than the Alfvenic speeds typically used in Solar flare models.

Communication between non-adjacent parts of the grid is in effect the introduction of a higher dimensionality therefore we can change the dimensionality of a model by incorporating non-local communication. Interestingly however Litvinenko (1998) applied branching theory methods to the

model by Macpherson & MacKinnon (1997) and proved that the distribution of flare energies produced by that model, power-law with index of -3/2, is independent of dimension. Therefore, if we believe that the mechanics of the model by Macpherson & MacKinnon (1997) is relevant to the size and propagation of flares then we must accept that the number of physical dimensions of any useful model should not be relevant.

However, we might yet explore the possibility of higher dimensionality by constructing a 2-D model with as far as possible similar concepts and mechanisms as the present continuous model. Such a model could contain cells which tessellate a 2-D surface, as shown in figure 5.16. Such tessellation would be simplest using triangular cells.

Such a grid would contain thermodynamic and magnetic properties. In the same way as we do in the 1-D model each time-step we would recalculate the parameter values, assuming adiabatic behaviour and a simple equation of motion. The model would be Lagrangian and therefore the distortion and motion of the triangular cells will reflect the velocity field of the material contained within the cells. Each vertex has a velocity associated with it and this is updated each time-step. The vertex velocities allow motion of the vertexes, which naturally will change the volume, and consequently the thermodynamic properties of each cell. Regarding the calculation each time-step of the new acceleration of each vertex, we can notionally partition each cell such that a polygon straddles each vertex and calculate its mass and the net force upon it and hence the acceleration of

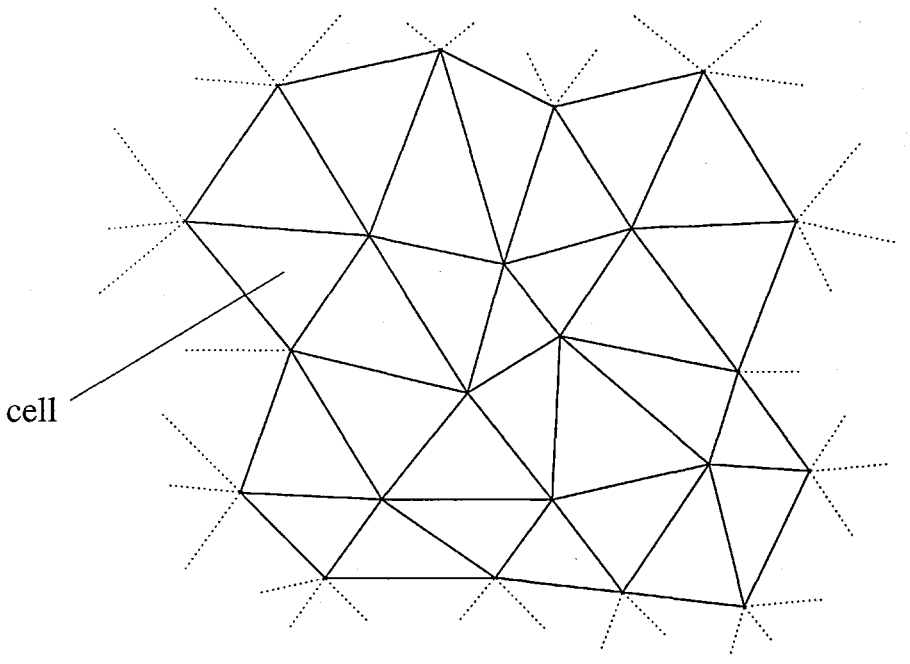

Figure 5.16: 2-D grid tessellated by triangular cells.

the polygon, which we can take to be a proxy for the vertex itself. This method is analogous to the method used in our present model.

Figure 5.17 shows a polygon formed from the centres of a group of cells ringing a vertex. For the purpose of finding the new velocity of the vertex in the figure we can determine the mass of such a polygon and calculate the pressure forces upon its sides. We may then find the acceleration during each timestep and assume the motion of the polygon is a proxy for the motion of the vertex.

We can use a simple parameterised mechanism for reconnection occurring at the cell boundaries.

If a triangular cell is within an expanding region and therefore is itself expanding, we can use an adaptive scheme analogous to the cell bifurcation used in the 1-D model. Such a scheme can increase the resolution in and around this triangle, as demonstrated in figure 5.18.

Such a model would be a 2-D version of our present model, which we can use to perform similar runs generating distributions of magnetic field density, magnetic flux, unipolar region sizes and event-sizes. We can simulate a variety of Solar phenomena including active regions and ephemeral regions, beginning the runs with magnetic field densities spatially distributed to represent those of ARs and ERs.

We know that the magnetic field dominates the behaviour of the Solar atmosphere and reconnection provides a useful mechanism for large and small scale reorganisation of the magnetic field in addition to heating of the corona. However, the process by which reconnection gives rise to the fast energy release observed in flares is not well understood despite nearly forty years of work in this area. Nor is it understood whether and/or how the observed characteristics of flares, and other Solar

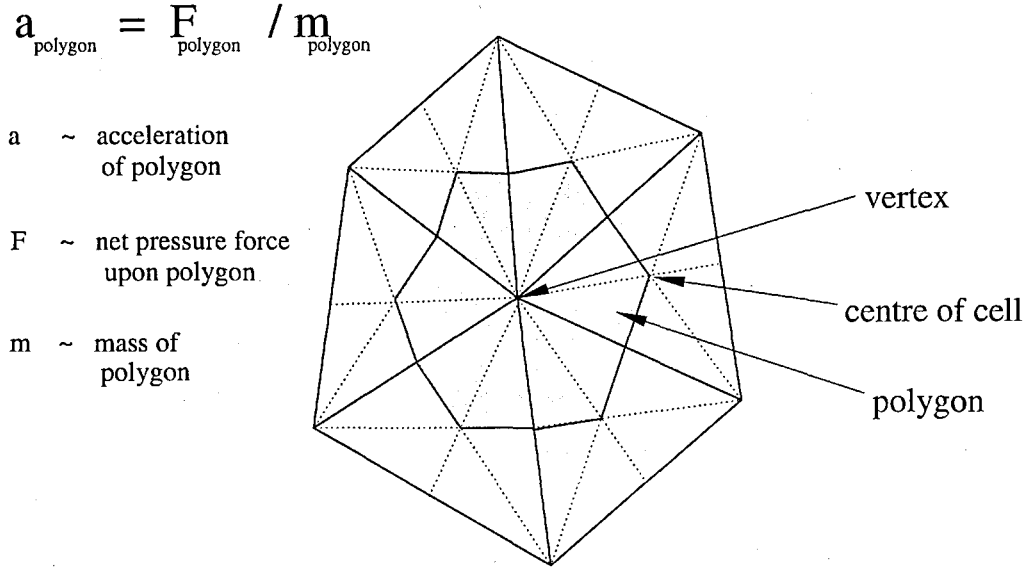

Figure 5.17: Polygon used with equation of motion for calculation of acceleration of vertex.

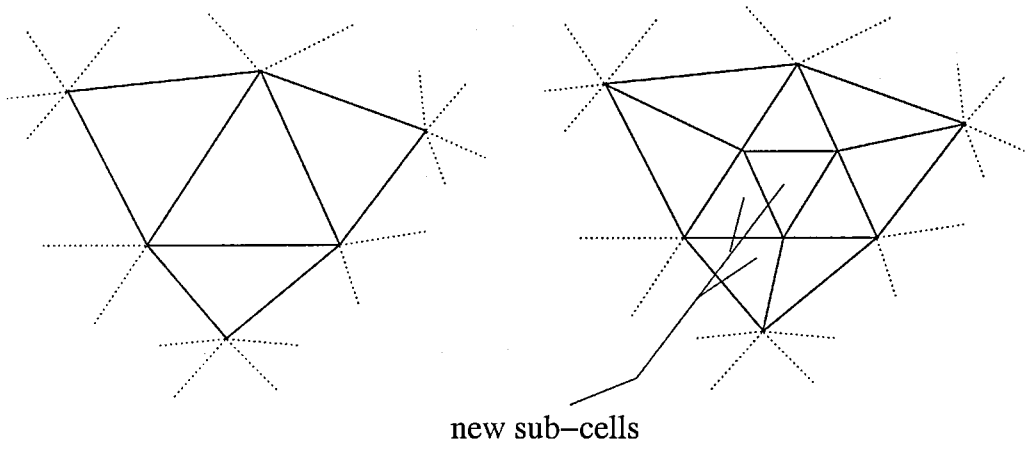

Figure 5.18: Adaptive subdividing of a tumescent cell.

activity such as sunspots and CMEs arise as a result of the reconnection. The models explored in this project (and also the 2-D model described above) provide mechanisms for the production of flaring events together with distributions of event-sizes and flux densities without relying upon the necessity of understanding the detailed physics of the emergence and reconnection processes nor on knowing the spatial distribution of the thermodynamic properties and magnetic fields within the model. The model also does not rely upon power-law emergence of fresh magnetic flux or input into the grid of any power-law distributions.

Full 3-D MHD is not yet possible over the eight orders of magnitude of length-scales from a few metres for reconnection diffusion region sizes to 10^8 m required for large flares. Our models occupy a different niche from MHD modelling in that they show that some of the statistical properties can broadly be reproduced and that therefore there may be correct principles within the model, such as the dependence of the energy release rate upon $C_{\mathrm{A}}B^2$, and the simplicity of the flux emergence mechanism, for example. The model will not in its present form allow exploration of large-scale time-dependent behaviour, such as the Solar cycle, nor other features such as CMEs, however the simplicity of the model means that additional modular features can easily be built into it. For example, we might include the notion of flux connectivity (from the discrete model). In the 2-D model, outlined above, we would then be able to make reconnection partially dependent upon simple formalised braiding and stretching of the field-lines, and where there are open field-lines these might lead to the shedding of plasma along the field-lines (if facility for this is built into the model).

A 2-D model allows for more possibilities for interaction between cells than our 1-D model. Non-local communication, justified as remote triggering of events, would also cause greater possibilities for interactions.

As already mentioned, a limitation of the model is the fact that an event consists of the interactions of a single cell with one or both neighbours. Therefore it is not possible to generate large extended events where a high level of reconnection is simultaneously occurring amongst many spatially localised cells. This places an upper limit upon the event-sizes. By using a suitable definition of reconnection events the 2-D model could incorporate this notion of spatially extended yet localised events.

It may be that the Solar convective motions feed flux into the magnetic carpet and photospheric fields with a particular distribution, exponential or power-law for example, and that this is important for the production via reconnection of event-sizes with the observed power-law indexes (~ 1.5 (Crosby et al. 1998)). The 1-D or 2-D model could include flux emergence with specifically power-law and exponential distributions however, if there is a specific index or profile to the Solar flux emergence distribution, this may change between Solar minimum and maximum. Therefore actual data concerning any such changing features of the Solar flux emergence will be required if an attempt is made to use an improved model to investigate whether, in accordance with observations, as we increase the flux emergence rate (as if moving towards Solar maximum) we obtain a changed flux density distribution power-law index, more complicated flaring events, CMEs along open field-lines, or global reversal of magnetic field polarities. A search of the literature has not revealed the existence of data regarding the detail of distributions of emerging Solar flux. We believe that modelling of any of these behaviours would require the inclusion of field connectivity into the model, and hence notions of field directionality between cells parallel to the grid. Thus, net toroidal and poloidal fields would be capable of representation within the model.

It was the intention during this project to never explicitly code into the model Solar behaviour nor supporting physical properties such as power-law flux emergence, granule or super-granule size, convective spreading/convergence or energy-release time-scales et al. The development of the 2-D model however would be a good environment for inclusion of features such as field connectivity, emergence of flux with particular distributions etc. Changes such as these would make the model more closely mimic real Solar physics and we could look for Solar-like behaviour and features such as sunspots, CMEs and global field reversal.

REFERENCES

Aschwanden A. J., Dennis B. R., Benz A. O., 1998, ApJ, 497, 972

Bak P., Tang C., Wiesenfeld K., 1987, Phys. Rev. Lett., 59, 381

Bak P., Tang C., Wiesenfeld K., 1988, Phys. Rev. A , 38, 364

Berger M. A., 1993, Phys. Rev. Lett., 70, 705

Biskamp D., 1986, Phys. Fluids., 29, 1520

Boffetta G., Carbone V., Giuliani P., Veltri P., Vulpiani A., 1999, Phys. Rev. Lett., 83, 4662

Bromund K. R., McTiernan J. M., Kane S. R., 1993, ApJ, 455, 733

Conway A. J., 1998, New Astr. Rev., 42, 343

Conway A. J., Brown K. P. Macpherson J., 1999, Astronomy & Geophysics, 39, 2.22

Crosby N., Vilmer N., Lund N., Sunyaev R., 1998, A&A, 334, 299

Crosby N. B., Aschwanden M. J., Dennis B. R., 1993, Solar Phys., 143, 275

Datlowe D. W., Elcan M. J., Hudson H. S., 1974, Solar Phys., 39, 155

Demoulin P., van Driel-Gesztelyi L., Schmieder B., Henoux J. C., Csepura G., Hagyard M. J., 1993, A&A, 271, 292

Dendy R., 1993, Plasma Physics, an Introductory Course, Cambridge University Press

Dere K. P., 1996, ApJ, 472, 864

Foukal P. V., 1990, Solar Astrophysics, Wiley Interscience

Galsgaard K., Roussev I., 2002, A&A, 383, 685

Galtier S., 2000, astro-ph/0003420

Gary G. A., 2001, Solar Phys., 203, 71

Gary G. A., Alexander D., 1999, Solar Phys., 186, 123

Georgoulis M. K., Vlahos L., 1996, ApJ, 469, L135

Hagenaar H. J., 2001, ApJ, 555, 448

Harvey K. L., Jones H. P., Scrijver C. J., Penn M. J., 1999, Solar Phys., 190, 35H

Hesse M., 1995, Reviews of Modern Astronomy, 8, 323

Hiei E., Hundhausen A. J., 1996, in IAU Colloq. 153: Magnetodynamic Phenomena in the Solar Atmosphere - Prototypes of Stellar Magnetic Activity, p. 125

Hudson H. S., 1991, Solar Phys., 133, 357

Isliker H., Anastasiadis A., Vassiliadis D., Vlahos L., 1998, A&A, 335, 1085

Isliker H., Benz A. O., 2001, A&A, 375, 1040

Jardine M., 1992, in 26th ESLAB Symposium, p. 141

Karttunen H., Kroger P., Oja H., Poutanen M., Donner K. J., 1996, Fundamental Astronomy, Springer-Verlag, Third Edition

Kaufmann P., Strauss F. M., Laporte C., Opher R., 1980, A&A, 87, 58

Kawaguchi T., Mineshige S., Machida M., 2000, Pubs. Astron. Soc. Japan., 52, L1

Khodachenko M. L., Haerendel G., Rieger E., 2000, A&AS, 32, 2

Kulsrud R. M., 2003, astro-ph/0007075

Lawrence J. K., Cadavid A. C., Ruzmaikin A., 2001, Solar Phys., 202, 27L

Litvinenko Y. E., 1998, A&A, 339, 57

Litvinenko Y. E., Somov B. V., 1991, PAZh, 17, 835

Lu E. T., Hamilton R. J., 1991, ApJ, 380, L89

Machida M., Matsumoto R., 2003, ApJ, 585, 429

MacKinnon A. L., Macpherson K. P., 1997, A&A, 326, 1228

MacKinnon A. L., Macpherson K. P., Vlahos L., 1996, A&A, 310, L9

Macpherson K. P., MacKinnon A. L., 1997, Physica A, 243, 1

Meunier N., 1999, ApJ, 515, 801

Mineshiga S., 1994, Pubs. Astron. Soc. Japan., 46, 97

Miroshnichenko L. I., Mendoza B., Enriquez R. P., 2001, Solar Phys., 202, 151

Moore R. L., LaRosa T. N., Orwig L. E., 1995, ApJ, 438, 985

Parker E. N., 1973, ApJ, 180, 247

Parker E. N., 1983, ApJ, 264, 642

Parker E. N., 1988, ApJ, 330, 474

Parker E. N., 1989, Solar Phys., 121, 271

Parnell C. E., 2001, Solar Phys., 200, 23

Pearce G., Rowe A. K., Yeung J., 1993, Ap&SS, 208, 99

Petscheck H. E., 1964, The Physics of Solar Flares, NASA

Petschek H. E., Thorne R. M., 1967, ApJ, 147, 1157

Priest E. R., Forbes T. G., 1992, J. Geophys. Res., 97, 16757

Rabin D., Moore R., Hagyard M. J., 1984, ApJ, 287, 404

Roberts B., 1999, Introductory Solar Physics, Lecture Notes

Saba J. L. R., Gaeng T., Tarbell T. D., 2002, A&AS, 200, 6809

Sano T., Inutsuka S., 2003, ApJ, 561, L179

Schrijver C. J., Harvey K. L., 1989, ApJ, 343, 481

Schrijver C. J., Title A. M., van Ballegooijen A. A., Hagenaar H. J., Shine R., 1997, ApJ, 487, 424

Simon G. W., Title A. M., Weiss N. O., 2001, ApJ, 561, 427S

Sornette D., 2000, Critical Phenomena in Natural Sciences, Springer-Verlag, First Edition

Spitzer L., 1962, Physics of Fully Ionized Gases, Interscience

Sweet P. A., 1958, in Lehnert B., ed, Electromagnetic Phenomena in Cosmical Physics, p. 124, Cambridge University Press

Tajima T., Gilden D., 1987, ApJ, 320, 741

Wheatland M. S., 2000, ApJ, 532, 1209

Wheatland M. S., Sturrock P. A., McTiernan J. M., 1998, ApJ, 509, 448

Wolfram S., 1984, Nat, 311, 419

Yamada M., 1998, Phys. Rev. Lett., 80, 3256

Zirin H., 1989, Astrophysics of the Sun, Cambridge University Press